Application de l'approche de mécanique de la rupture pour la tolérance aux dommages et la prédiction de la vie en fatigue de composants obtenus par fusion sélective au laser

par

Jean-René POULIN-MASSON

THÈSE PAR ARTICLE PRÉSENTÉE À L'ÉCOLE DE TECHNOLOGIE SUPÉRIEURE COMME EXIGENCE PARTIELLE À L'OBTENTION DU DU DOCTORAT EN GÉNIE
Ph. D.

MONTRÉAL, LE 13 JANVIER 2020

ÉCOLE DE TECHNOLOGIE SUPÉRIEURE
UNIVERSITÉ DU QUÉBEC

PRÉSENTATION DU JURY

CETTE THÈSE A ÉTÉ ÉVALUÉE

PAR UN JURY COMPOSÉ DE :

M. Vladimir Brailovski, directeur de thèse
Département de génie mécanique à l'École de technologie supérieure

M. Patrick Terriault codirecteur de thèse
Département de génie mécanique à l'École de technologie supérieure

M. Roland Maranzana, président du jury
Département de génie de la production automatisée à l'École de technologie supérieure

M. Vincent Demers, membre du jury
Département de génie mécanique à l'École de technologie supérieure

Mme Myriam Brochu, examinatrice externe
Département de génie mécanique à l'École de Polytechnique de Montréal

ELLE A FAIT L'OBJET D'UNE SOUTENANCE DEVANT JURY ET PUBLIC

LE 13 DÉCEMBRE 2019

À L'ÉCOLE DE TECHNOLOGIE SUPÉRIEURE

REMERCIEMENTS

Tout d'abord, j'aimerais adresser mes plus sincères remerciements à mon directeur et codirecteur de recherche, respectivement Vladimir Brailovski et Patrick Terriault. Vladimir, je tiens à souligner votre implication et votre support hors du commun, j'estime que vous m'avez accompagné à merveille dans la réalisation de ce projet et avez fait preuve d'une disponibilité extraordinaire. Au-delà de vos qualités de directeur, je ne peux passer sous silence vos qualités humaines. Merci pour la grande justesse dont vous avez fait preuve; vous avez su garder un niveau d'exigence raisonnable et m'avez aidé à l'atteindre en m'encourageant dans les moments plus difficiles. Merci à Patrick, ces dernières années, tu m'as donné un grand nombre d'opportunités de me développer à travers divers projets du PFE au Doctorat. Tu as cru en ma capacité d'entreprendre des études doctorales et a été l'instigateur de cette formidable expérience.

J'aimerais, en outre, remercier l'ensemble de mes collègues du LAMSI, pour leur collaboration et leur support dans la réalisation de ce projet. L'ambiance collaborative du laboratoire ainsi que le climat favorable à l'apprentissage qui y règne ont été déterminants dans la réalisation de ce projet. Au risque d'omettre certains collègues, j'aimerais adresser des remerciements plus spécifiquement à Morgan, Alena, Anatolie, Floriane, Karine, Mykhailo et Salah-Eddine pour leur support. Votre présence, vos idées et votre écoute ces dernières années ont été très appréciées, ce fut un élément facilitateur dans la réalisation de mes travaux. De surcroit, je dois remercier spécifiquement l'ensemble des stagiaires et étudiants ayant contribué directement à ces travaux dans le cadre d'un stage ou d'un projet. Merci à Fouad, Alexandre, Francisco, David, Alexis et Anthony. Je dois aussi remercier le personnel de l'ÉTS, en particulier Radu Romanica, Serge Plamondon et Éric Marcoux, le partage de vos compétences et expertises ont été plus qu'appréciés lors de la réalisation de la portion expérimentale de ce projet.

De surcroit, je désire remercier mes collègues de Pratt & Whitney Canada, avec qui je travaille depuis plus d'un an. J'aimerais adresser des remerciements plus spécifiques à Orlando Scalzo, gestionnaire de l'équipe de développement des procédés spéciaux. Premièrement, merci de m'avoir offert une telle opportunité malgré des restrictions considérables dans mon emploi du temps. Cette opportunité a une valeur inestimable pour moi et constitue un complément important à mes travaux académiques. Au-delà de ton rôle de gestionnaire, j'aimerais souligner tes qualités d'ingénieur et ton esprit scientifique, chaque échange constitue une opportunité d'apprentissage qui me permet de poser un regard plus critique sur mes travaux. J'aimerais également remercier Thomas George et Francesco d'Angelo, sans qui je n'aurais possiblement jamais eu cette opportunité. Merci également à Marjolaine Côté, tu as fait preuve d'une grande générosité et montré une belle confiance à mon égard en m'impliquant dans plusieurs de tes projets, lesquels ont grandement bonifié mon expérience chez P&WC. Finalement, merci aussi à Mathieu Fagnan, Guillaume Limoges, Dany Rasmussen, Ata Saeed et l'ensemble de l'équipe impliquée dans les projets de fabrication additive, chaque opportunité de travailler à vos côtés s'est avérée une occasion d'apprentissage très enrichissante.

Enfin, je ne peux passer sous silence le soutien indéfectible de ma famille. Merci à mes parents de m'avoir outillé pour mener mes projets à terme. Merci à ma conjointe, Paola, premièrement pour ton support, ton écoute et tes encouragements dans les moments plus difficiles. Merci d'être un modèle de persévérance, d'esprit critique et de dépassement. Merci également pour les sacrifices et compromis, sans toi, il m'aurait été impossible d'exécuter ces travaux.

Application de l'approche de mécanique de la rupture pour la tolérance aux dommages et la prédiction de la vie en fatigue de composants obtenus par fusion sélective au laser

Jean-René POULIN-MASSON

RÉSUMÉ

Les procédés de fabrication additive de matériaux métalliques suscitent de plus en plus d'intérêt dans différents secteurs industriels pour la fabrication de composants à forte valeur ajoutée. Parmi ces procédés, la fusion sélective au laser (LPBF pour laser powder bed fusion) permet de mettre en forme des alliages dont les propriétés mécaniques statiques sont similaires à celles de leurs contreparties corroyées. Toutefois, les défauts de fabrication leur confèrent un comportement moins enviable pour les applications en fatigue. En ce sens, pour élargir le champ d'application aux composants soumis à des chargements cycliques, il est nécessaire de développer une meilleure compréhension de l'impact de ces défauts sur le comportement en fatigue.

Cette thèse présente, en trois articles scientifiques, une proposition de démarche visant à établir une zone de conception sécuritaire pour des composants obtenus par LPBF, et ce, en considérant les défauts qui résultent de leur mise en forme. La démarche en question fait appel à la mécanique de la rupture et au modèle d'El-Haddad pour mettre en relation la taille de défaut tolérable à diverses amplitudes de contraintes.

Dans un premier temps, le comportement en fatigue de l'alliage d'Inconel 625 obtenu par fabrication additive est évalué selon l'approche de la mécanique de la rupture. L'effet de l'anisotropie résultant de la mise en forme est considéré et une comparaison avec un alliage corroyé de même composition est réalisée. La résistance à la propagation de fissure longue a été montrée dépendante de l'orientation de fabrication et de l'orientation de propagation de la fissure relativement à l'axe de fabrication. Toutefois, en excluant les mécanismes de fermeture de fissure, celle-ci s'est montrée comparable à celle de l'alliage corroyé de même composition (Inconel 625).

Par la suite, une méthode de création de défauts a été développée. Pour ce faire, des paramètres d'exposition laser non optimaux ont été développés. Dans le second article, des échantillons sont fabriqués en modifiant la vitesse du laser, ce qui a permis de générer différents taux de porosité (0.1 à 2.7%) et d'en évaluer l'impact sur le comportement quasi statique et en fatigue de l'Inconel 625. Les résultats obtenus mettent en évidence l'impact limité des défauts de fabrication sur les propriétés élastiques du matériau, mais une grande sensibilité de la ductilité

de la présence de ces défauts. De plus, l'impact des défauts a été montré fortement dépendant de l'orientation de fabrication. En propagation de fissure, la présence de défaut s'est avérée particulièrement importante lorsque le facteur d'intensité de contrainte est élevé, alors que l'impact sur le seuil de propagation de fissure est négligeable.

Dans un troisième temps, des échantillons de fatigue sont fabriqués avec des défauts induits dans la section de test en utilisant les paramètres laser déterminés au chapitre précédent lors de l'exposition des couches correspondantes. Un total de 4 ensembles d'échantillons sont étudiés, lesquels ont des taux de porosités compris entre ~0.1 et ~2.7%. La caractérisation des défauts sur un nombre restreint d'éprouvettes est réalisée et à partir de la taille mesurée, une prédiction de la limite de fatigue en vie infinie est effectuée en utilisant le modèle de El-Haddad. Pour valider la prédiction du modèle, des essais de fatigue sous force contrôlée sont réalisés et la limite de fatigue résultante est comparée à la prédiction du modèle d'El-Haddad. Les résultats expérimentaux montrent que le modèle est légèrement conservateur. L'erreur maximale entre la résistance en fatigue prédite par El-Haddad et celle estimée au moyen d'essais sous force contrôlée est d'environ 7%, ce qui est jugé acceptable.

Afin d'aller plus loin dans cette démarche et de manière préalable à l'application a une pièce, il est suggéré de réaliser des essais analogues sur des échantillons de tailles variables et de valider la possibilité de prédire la taille des défauts en utilisant les statistiques de l'extrême. Pour ce qui est des applications en vie finie, les résultats expérimentaux suggèrent qu'il est important de considérer la phase d'initiation de fissure, ainsi que celle de propagation afin d'avoir une prédiction adéquate puisqu'en présence de défauts, la phase de propagation s'étend sur un plus grand nombre de cycles.

Mots-Clés : Fabrication Additive, Fatigue, Mécanique de la rupture, Propagation de fissure, Superalliage, Tomographie à rayons X, porosité, défauts de fabrication.

Application of the fracture mechanics approach for damage tolerance design and fatigue life prediction of laser powder bed fusion processed alloys

Jean-Rene POULIN-MASSON

ABSTRACT

In the past years, metal additive manufacturing processes are gaining significant interest for many industrial applications due to the capacity to build complex components in a near net shape. Among these processes, laser powder bed fusion (LPBF) is particularly promising due to the capacity to manufacture a wide range of alloys with mechanical properties on par with their wrought counterparts. However, the fatigue properties are less appealing due to the presence of a significant amount of processing-induced defects. In this regard, in order to broaden the range of usage of LPBF built components in applications subjected to cyclical loading, there is a need to develop a better understanding and mitigate the impact of process-specific defects on their fatigue behavior. In this thesis, three scientific papers are presented. They constitute a procedure that allows relating the cyclic loading to be applied on LPBF built alloys while avoiding fatigue failure with respect to their process-induced defects.

To this end, in the first scientific paper, the fracture mechanics approach is employed to characterize the fatigue behavior of Inconel 625 alloy processed by LPBF. Additional wrought specimens of the same alloy are also tested. In addition, this paper investigates the effect of microstructural anisotropy resulting from the process. The fatigue crack propagation resistance is shown to be build-orientation dependant but similar to the wrought alloys in the worst case.

In the second paper, non-optimal laser exposure parameter sets are developed to manufacture Inconel 625 coupons with various levels of typical processing-induced defects. To this end, the laser scanning speed is modified and porosity typical of low-energy processing, known as lack-of-fusion defects, are generated (0.1 to 2.7%). The impact of such levels of porosity on the quasi-static mechanical behavior and on the fatigue crack propagation behavior is studied. The experimental results enlighten the limited impact of such porosity on the elastic properties, while the ductility of the material was strongly impacted by their presence. In addition, the reduction in ductility is found to be strongly build-orientation dependant. When it comes to the fatigue crack propagation behavior, the impact of defects is very limited in the near-threshold region. However, as the stress intensity factor range increases, the interaction of the porosity with the propagating crack becomes significant and strongly build-orientation dependant; the crack is retarded when propagating in the direction perpendicular to the build plane and accelerated when propagating in the parallel plane.

In the third paper, specimens are manufactured for conducting stress-controlled fatigue tests with porosity induced in their gauge section using the aforementioned laser exposure parameter sets (4 porosity levels ranging from 0.1 to 2.7%). Defects were characterized via computed tomography on a restricted number of specimens (3 per porosity level) to measure the pore size distribution using Murakami's parameter. The larges defects found for each porosity level were employed to predict the fatigue strength using El-Haddad's formulation of the Kitagawa Takahashi diagram. Stress-controlled fatigue testing was conducted on the specimens to evaluate their fatigue strength and experimental results were found in good agreement with the model's predicted fatigue strength, with a maximal error of 7%. Moving forward, we propose to apply this method to specimens with different gauge sections using the statistics of extreme to predict the defect size for various volumes of material.

Keywords: Additive manufacturing, Fatigue, Fracture mechanics, Fatigue crack propagation, Superalloys, Computed microtomography, porosity, processing-induced defects.

TABLE DES MATIÈRES

LISTE DES TABLEAUX

Page

LISTE DES FIGURES

Page

LISTE DES ABRÉVIATIONS, SIGLES ET ACRONYMES

CAD	Computer aided design
FA	Fabrication additive
AM	Additive Manufacturing
LEFM	Linear elastic fracture mechanics
EPFM	Elastic-Plastic fracture mechanics
HCF	High cycle fatigue
LCF	Low cycle fatigue
FCGR	Fatigue crack growth rate
SSY	Small scale yielding
SLM	Selective laser melting
YS	Limite d'élasticité (Yeild stress)
UTS	Résistance en traction (Ultimate tensile stress)
SR	Recuit de détente (Stress relieve thermal treatment)
HIP	Pressage isostatique à chaud (Hot isostatic pressing)
EBM	Electron beam melting
LPBF	Laser powder bed fusion
CT	Computed Tomography

LISTE DES SYMBOLES ET UNITÉS DE MESURE

a	Taille de défaut	$[mm]$
a_f	Taille finale de défaut	$[mm]$
a_0	Taille de défaut initiale	$[mm]$
$\sqrt{area}$	Paramètre de Murakami	$[mm]$
$\sqrt{area}_0$	Paramètre de Murakami intrinsèque	$[mm]$
C	Constante de la loi de Paris	$[-]$
m	Exposant de la loi de Paris	$[-]$
C_2	Constante du modèle de Forman	$[-]$
E	Module d'Young	$[GPa]$
m_2	Exposant du modèle de Forman	$[-]$
$\frac{da}{dN}$	vitesse de propagation de fissure	$[mm/cycle]$
N_f	Nombre final de cycle à la rupture	$[-]$
K_I	Facteur d'intensité de contrainte en mode I	$[MPa\sqrt{m}]$
ΔK	Variation du facteur d'intensité de contrainte	$[MPa\sqrt{m}]$
ΔK_{eff}	Variation efficace du facteur d'intensité de contrainte	$[MPa\sqrt{m}]$
ΔK_{th}	Seuil de propagation de fissure	$[MPa\sqrt{m}]$
$\Delta K_{th,eff}$	Seuil de propagation de fissure effectif	$[MPa\sqrt{m}]$
$\Delta K_{th,LC}$	Seuil de propagation de fissure longue=	$[MPa\sqrt{m}]$
K_{op}	Facteur d'intensité de contrainte à l'ouverture de fissure	$[MPa\sqrt{m}]$
K_{min}	Facteur d'intensité de contrainte minimum	$[MPa\sqrt{m}]$
K_{max}	Facteur d'intensité de contrainte maximum	$[MPa\sqrt{m}]$
K_{IC}	Ténacité en état plan de déformation	$[MPa\sqrt{m}]$
K_C	Ténacité	$[MPa\sqrt{m}]$
Y	Facteur de forme	$[-]$
σ	Contrainte nominale	$[MPa]$

$\Delta\sigma$	Contrainte distante alternée	$[MPa]$
$\Delta\sigma_f$	Limite de fatigue	$[MPa]$
$\Delta\sigma_{f,0}$	Limite de fatigue en absence de défauts à 10^7 cycles	$[MPa]$
$r_{0\varepsilon}$	Taille de la zone plastique monotone en déformation plane	$[mm]$
$r_{0\sigma}$	Taille de la zone plastique monotone en contrainte plane	$[mm]$
σ_{YS}	Limite d'élasticité	$[MPa]$
U	Rapport de facteur d'intensité de contrainte	$[-]$
UTS	Résistance mécanique	$[MPa]$
YS	Limite d'élasticité	$[MPa]$
f	Facteur de fermeture de fissure	$[-]$
R	Ratio de contrainte	$[-]$

INTRODUCTION

Les procédés de fabrication additive (FA) gagnent en popularité étant donné qu'ils permettent de fabriquer des composants avec un grand niveau de complexité tout en minimisant le nombre d'étapes de fabrication. En effet, le marché mondial de la fabrication additive croît à une vitesse fulgurante, comme le montre la Figure 0.1. Par exemple, entre 2011 et 2012, il a connu une croissance de 28,6% (Ford et Despeisse, 2016; Wohlers, 2016). Le rapport analogue de 2018 confirme la croissance soutenue et fait état d'une croissance de plus de 21% (Wohlers et al., 2018).

L'approche de FA consiste à lier successivement de nombreuses minces couches d'un matériau afin d'obtenir une géométrie finale en réduisant la matière consommée et les étapes de mise en forme. La géométrie de chacune des couches est déterminée à partir d'un modèle issu d'outils de conception assistée par ordinateur (CAO), déjà amplement utilisé en conception mécanique. De nombreux procédés peuvent être répertoriés; ils permettent de mettre en forme les différentes classes de matériaux (métaux, polymères, céramiques).

Figure 0.1 Marché actuel et projection du marché de la fabrication additive
Tirée de (Cotteleer et Joyce, 2014)

Les procédés de FA sont prometteurs et plusieurs bénéfices sont rapportés dans la littérature scientifique (Ford, 2014; Ford et Despeisse, 2016; Gao et al., 2015; Wohlers, 2016). Parmi les avantages envisagés, on distingue :

- Une réduction des couts excédentaires pour une modification au design,
- Des pertes de matières minimales,
- La réduction des couts associés au développement d'outillage,
- La réduction du temps de développement de produits.

Grâce aux avantages énoncés, de nombreux domaines d'applications pourraient tirer profit des procédés de fabrication additive. Les secteurs de l'aérospatiale, de l'énergie, ainsi que l'industrie biomédicale, constituent sans doute les champs d'application les plus prometteurs pour la FA étant donné que des composants à forte valeur ajoutée sont souvent fabriqués en petite ou moyenne séries. À titre d'exemple, la compagnie GE Aviation, qui fabrique des moteurs d'avion, a massivement investi dans ce domaine et fabrique de nombreux composants tels que des injecteurs de carburant (voir Figure 0.2). L'entreprise prévoit, en outre, fabriquer des ailettes de turbine et de nombreux autres composants.

Figure 0.2 Injecteur de carburant fabriqué
par GE Aviation

Dans le cas de l'injecteur, le choix de la FA est justifié par le fait que de nombreuses opérations de fabrication sont éliminées. Traditionnellement, la fabrication de ce composant requiert l'assemblage par brasage de nombreuses pièces usinées individuellement. La fabrication requiert de nombreuses étapes de brasage et donc plusieurs opérations manuelles et cycles de traitements thermiques sont évités en FA.

Dans le domaine biomédical, la FA permet de personnaliser les prothèses et implants pour un client spécifique sans en augmenter considérablement les couts de fabrication (Conner et al., 2014; Wohlers et Caffrey, 2013). Les procédés de FA pavent également la voie à la fabrication de composants structuraux aux géométries complexes obtenus par optimisation topologique

(Brackett, Ashcroft et Hague, 2011; Zegard et Paulino, 2016). Enfin, une nouvelle classe de matériaux semble émerger de cette technologie, soit, les structures architecturées. Ces structures sont obtenues en répétant une cellule unitaire ayant une morphologie et une porosité déterminée afin d'obtenir un matériau plus léger avec des propriétés mécaniques optimisées (Messner, 2016; Rehme et al., 2006; Zok, Latture et Begley, 2016).

De manière générale, les propriétés mécaniques des composants métalliques obtenues par FA, notamment par le procédé de fusion sélective au laser sur lit de poudre (LPBF ou LPBF pour laser powder bed fusion), sont comparables aux propriétés de pièces obtenues par d'autres procédés traditionnels (Simonelli, Tse et Tuck, 2014; Yadroitsev et al., 2009). Ceci a été rendu possible, entre autres, par les avancées technologiques en matière de laser qui permet d'avoir un contrôle accru des conditions de fusion et d'obtenir une porosité particulièrement faible (Kasperovich et al., 2016; Tammas-Williams et al., 2016a; Ziółkowski et al., 2014). Toutefois, certaines caractéristiques des matériaux obtenues par FA divergent de celles de leur contrepartie obtenue par procédés traditionnels, par exemple, la microstructure, les défauts surfaciques et volumiques. Si ces caractéristiques n'entravent pas l'emploi des technologies de FA dans certains secteurs d'applications, elles soulèvent toutefois des questions en ce qui concerne la possibilité d'employer ces technologies de fabrication pour des applications avec chargements cycliques (fatigue). En effet, la tenue d'un matériau en fatigue est fortement influencée par la microstructure, la présence de défauts de fabrication et toutes autres spécificités à l'échelle microstructurelle (Hertzberg, Vinci et Hertzberg, 2012; Krupp, 2007; Ritchie, 1999). Cette réalité se présente à l'heure actuelle comme une barrière d'importance significative à l'expansion des applications auxquelles se destine le procédé de LPBF, en particulier dans des industries hautement réglementées comme l'aérospatiale.

Pour aborder cette problématique, une connaissance approfondie des défauts induits par ce procédé ainsi que de leur impact sur les propriétés en fatigue est requise (Yadollahi et Shamsaei, 2017). La thèse présentée ici propose une contribution centrée sur la relation entre les défauts de fabrication typiquement observés en fabrication additive et le comportement en

fatigue avec une approche de mécanique de la rupture. Ainsi, les travaux devraient fournir des éléments de réponses aux questions entourant l'approche de tolérance aux dommages tels que la taille de défaut tolérable pour une application donnée.

Pour ce faire, le premier chapitre de la thèse s'intéresse à l'état des connaissances relatives aux caractéristiques et comportement des matériaux obtenus par fabrication additive, plus spécifiquement par LPBF. Dans ce même chapitre, des notions générales de fatigue, plus spécifiquement sur l'approche de mécanique de la rupture, sont présentées; elles constituent le fondement de la démarche expérimentale présentée dans la thèse. Ensuite, la thèse présente trois chapitres (2 à 4) qui prennent la forme d'articles scientifiques, lesquels portent, respectivement, sur les objectifs suivants :

- Évaluation de la résistance à la propagation de fissure de fatigue dans un alliage d'Inconel 625 obtenu par LPBF.
- Évaluation de l'influence de la porosité induite par le procédé de LPBF sur la propagation de fissure dans l'alliage d'Inconel 625.
- Prédiction de la limite de fatigue d'échantillons d'Inconel 625 imprimés avec différents niveaux de porosité, en appliquant le modèle d'El-Haddad.

CHAPITRE 1

ÉTAT DES CONNAISSANCES

1.1 Caractéristiques des matériaux obtenus par LPBF

L'avancement de la technologie de LPBF (laser powder bed fusion) ou EBM (electron beam melting) est à ce jour tel que des composants avec une densité supérieure à 99% peuvent être fabriqués (Jia et Gu, 2014; Kasperovich et al., 2016; Ziółkowski et al., 2014). Pour les composants obtenus par LPBF, en appliquant les traitements thermiques adéquats, les propriétés mécaniques statiques telles que la limite d'élasticité et la résistance mécanique observées sont généralement comparables aux propriétés obtenues par des procédés de fabrication traditionnels. Cette observation peut être vérifiée pour plusieurs alliages tels que l'Inconel 718 (Wang et al., 2012), l'alliage de titane Ti6Al4V (Gong et al., 2015; Rafi et al., 2013; Zhai, Galarraga et Lados, 2016), l'Inconel 625 (Kreitcberg, Brailovski et Turenne, 2017a; Yadroitsev et al., 2009), ainsi que des aciers inoxydables (Rafi, Starr et Stucker, 2013; Yadroitsev et al., 2009). Toutefois, outre ces propriétés, il est possible d'observer des différences notables entre les composants obtenus par LPBF et ceux obtenus par des procédés traditionnels, ces caractéristiques seront présentées dans le présent chapitre.

1.1.1 Description du procédé

Le procédé de LPBF est un des procédés de fabrication additive les plus prometteurs pour les matériaux métalliques, notamment parce que les propriétés mécaniques qui en découlent sont excellentes, un faible taux de porosité peut être obtenu et une précision dimensionnelle intéressante est aussi atteignable (Herzog et al., 2016; Wong et Hernandez, 2012).

Dans le procédé LPBF, présenté à la Figure 1.1, de fines couches de poudre métallique (20 à 100 μm) sont étendues successivement au moyen d'un système de balais mécanique sur une plaque de fabrication. La poudre est fusionnée, localement, grâce à l'énergie thermique fournie

par le faisceau laser. Il existe également un procédé similaire, la fusion sélective par faisceau d'électrons (EBM), où un faisceau d'électrons remplace le faisceau laser afin de fusionner les particules. Les zones à exposer sont définies à partir de tranches déterminées grâce à un modèle 3D de la pièce. Lors de l'exposition au faisceau laser, la température autour de la région exposée outrepasse la température de fusion de l'alliage. La région à l'état liquide, appelée bain de fusion, est fusionnée aux couches précédentes au refroidissement. Le procédé de fusion sélective au laser est réalisé dans une chambre contenant une atmosphère inerte d'argon ou d'azote afin d'éviter la création d'oxydes au sein du composant. En addition, une nomenclature normalisée est généralement employée concernant les axes dans une machine de fusion sélective au laser. Tel que montré à la Figure 1.1, l'axe X correspond à l'axe de déplacement du balai mécanique, l'axe Y est l'axe selon lequel le flux de gaz inerte s'écoule, alors que l'axe Z correspond à l'axe de déplacement de la plateforme de fabrication.

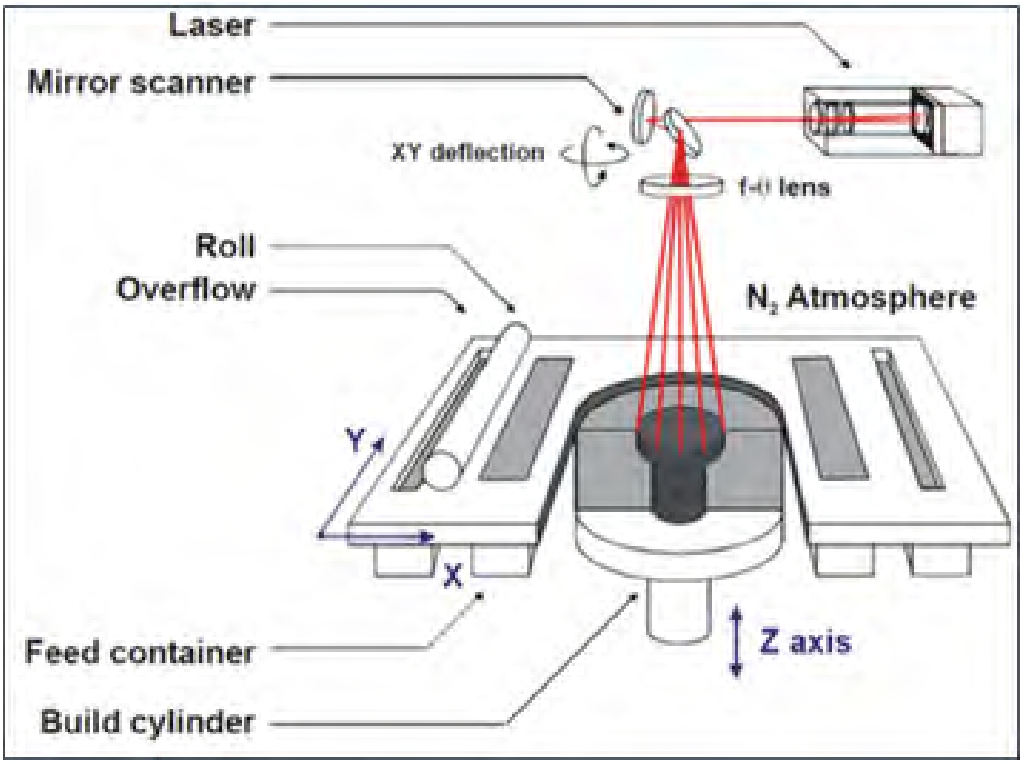

Figure 1.1 Schématisation du procédé de fusion sélective sur lit de poudre
Tirée et adapté de (Kruth et al., 2005)

Sans compter les paramètres de la poudre tels que sa composition chimique et sa granulométrie, ce procédé nécessite un choix judicieux de nombreux paramètres tels que l'épaisseur des couches de poudres métalliques, la puissance du faisceau laser, la vitesse du faisceau, le choix du parcours du laser, etc. Alors que l'épaisseur de couches est normalement constante pour la fabrication d'un composant, les paramètres de laser sont également ajustés pour faire certaines régions de la pièce telles que les surfaces supérieures, inférieures, les parois verticales afin notamment de minimiser la rugosité des surfaces. Les cycles thermiques répétitifs imposés lors de la fabrication par LPBF sont à l'origine d'une microstructure et des propriétés spécifiques au procédé qui ont une implication directe sur la vie en fatigue (Rafi et al., 2013). La présente section vise à faire une revue des caractéristiques des pièces obtenues par LPBF susceptibles d'affecter leur tenue en fatigue.

1.1.2 Microstructure

L'approche couche par couche employée dans le procédé de LPBF entraine un grand nombre de cycles de chauffage et de refroidissement rapides lors de la fabrication. Le bain de fusion créé par le faisceau laser est relativement concentré et l'énergie thermique emmagasinée se dissipe rapidement par conduction à travers les couches précédentes (Gusarov et al., 2009; Li et Gu, 2014). Or, la microstructure des matériaux est généralement déterminée par la vitesse de refroidissement et il se trouve qu'elle est extrêmement élevée (plus de 10^6 ºC/s) dans le procédé de LPBF (Li et Gu, 2014; Rafi et al., 2013). Il faut ajouter que les paramètres d'exposition au laser sont généralement sélectionnés afin d'assurer que quelques couches précédentes soient fusionnées de nouveau, ce qui affecte encore une fois la microstructure (Vilaro, Colin et Bartout, 2011).

Comme la tenue en fatigue d'un alliage métallique est fortement influencée par sa microstructure, il convient de s'intéresser aux éléments spécifiques au procédé de LPBF. Pour ce procédé de mise en forme, le refroidissement est extrêmement rapide et les gradients de températures sont fortement différents selon la direction. Ces particularités en termes de

transfert thermiques lors de la solidification sont à l'origine d'une microstructure relativement différente de celles des procédés plus traditionnels. En effet, suivant la mise en forme, la microstructure des alliages obtenus par LPBF est souvent caractérisée par une forte anisotropie, tel que l'illustre la Figure 1.2.

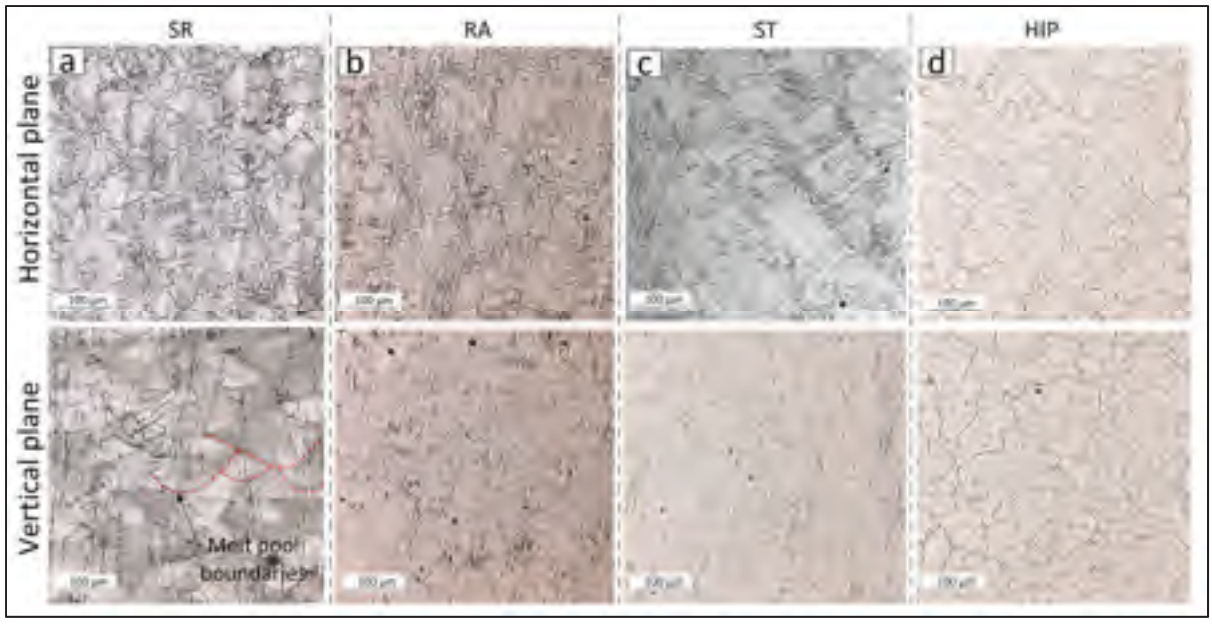

Figure 1.2 Microstructure de l'Inconel 625 obtenu par LPBF suivant : (a) un recuit de détente (SR), (b) un recuit de recristallisation (RA), (c) une mise en solution (ST) et (d) un traitement de pressage isostatique à chaud (HIP)
Tirée et adaptée de (Kreitcberg, Brailovski et Turenne, 2017a)

La Figure 1.2 (a) montre la microstructure suivant la mise en forme et un traitement de recuit de détente selon les plans principaux, soit le plan parallèle à la plaque de fabrication (plan horizontal, XY), et le plan normal à la plaque de fabrication (plan vertical, XZ). À l'état tel que fabriqué, il est possible de distinguer la forme des bains de fusion de manière analogue à ce qui est observé pour le soudage multi passes (traits rouges sur la Figure 1.2 a). À la Figure 1.2 (b) et (c), la microstructure suivant des traitements thermiques distincts, soient, respectivement, un recuit de recristallisation (SR) et une mise en solution (ST). Une forte anisotropie est notable sur le plan normal à la plaque de fabrication (XZ), les grains étant

allongés selon l'axe de fabrication (Z). Différents traitements thermiques peuvent être employés pour réduire l'anisotropie de la microstructure, par exemple, la Figure 1.2 (d) montre que le traitement de pressage isostatique à chaud (HIP pour hot isostatic pressing) est le plus efficace. Les observations concernant l'anisotropie microstructurelle observée pour l'alliage Inconel 625 sont corroborées par quelques études supplémentaires (Criales et al., 2017; Li et al., 2017; Li et al., 2015) et ce, sur différents alliages obtenus par LPBF.

Des études portant sur d'autres matériaux font également état d'une microstructure fortement anisotrope pour des alliages tels que l'alliage de titane Ti6Al4V (Rafi et al., 2013; Sallica-Leva, Jardini et Fogagnolo, 2013; Thijs et al., 2010; Vilaro, Colin et Bartout, 2011; Vrancken et al., 2012), l'Inconel 625 (Amato et al., 2012; Li et al., 2015), l'Inconel 718 (Jia et Gu, 2014; Wang et al., 2012) et l'alliage d'aluminium AlSi10Mg (Brandl et al., 2012; Yan et al., 2015).

1.1.3 Propriétés mécaniques

Il résulte des spécificités microstructurales décrites plus tôt un comportement anisotrope lorsque l'alliage est sollicité mécaniquement. Par exemple, le comportement en traction de l'alliage Inconel 625 obtenu par LPBF et suivant les divers traitements thermiques est comparé à celui d'un alliage corroyé (annealed-wrought) de même composition à la Figure 1.3.

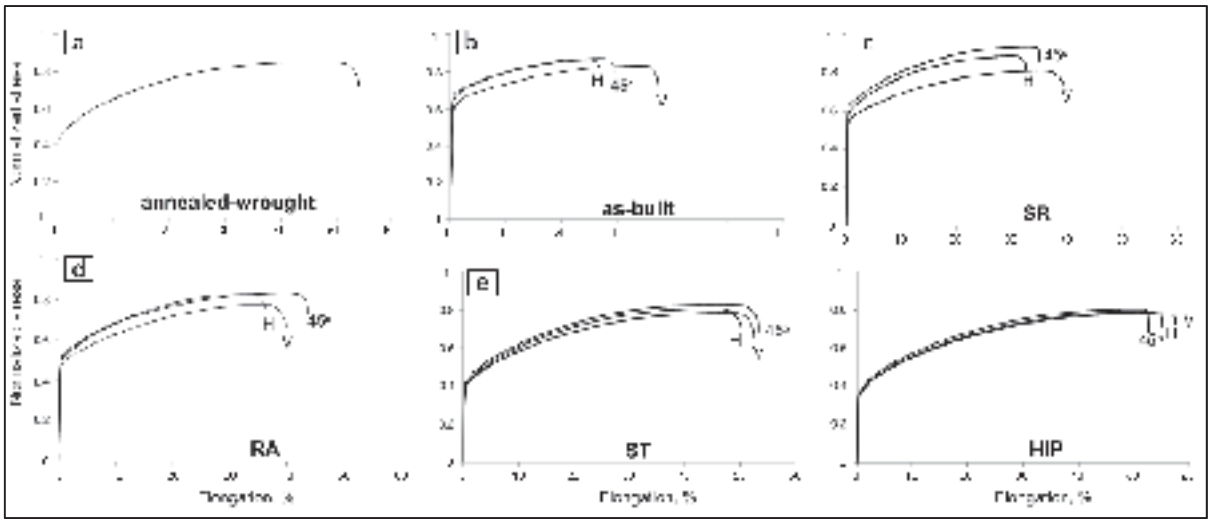

Figure 1.3 Courbes de traction d'un alliage Inconel 625 a) corroyé à l'état recuit, b) tel que fabriqué par LPBF, c) suivant un traitement de recuit de détente, d) suivant un traitement de recuit de recristallisation, e) suivant un traitement de mise en solution et f) suivant un traitement de HIP

Tirée de (Kreitcberg, Brailovski et Turenne, 2017a)

Les courbes de traction obtenues pour les échantillons tels que fabriqués (as-built) ont un comportement significativement différent du matériau de référence corroyé. Dans un premier temps, la limite d'élasticité est souvent plus élevée telle que montrée pour l'alliage d'Inconel 625 à la Figure 1.3 b) et c). Ici, ceci s'explique notamment par la finesse de la microstructure, un taux de dislocations élevé et la présence de la phase δ (Li et al., 2017). On note également que les propriétés sont fortement dépendantes de l'orientation de fabrication dans cet état, ainsi que suivant un recuit de détente (Figure 1.3 b et c). Par contre, les traitements thermiques de mise en solution (ST) ou de HIP sont efficaces pour homogénéiser la microstructure. Comme montrée à la section précédente, il en découle donc une plus faible anisotropie, ce qui se reflet dans les propriétés mécaniques (Figure 1.3 e et f). Typiquement, lorsque la résistance mécanique est plus élevée, la ductilité est inversement affectée (Figure 1.3 b, c et d). Les traitements de HIP et de mise en solution permettent néanmoins d'obtenir une ductilité et des propriétés mécaniques plus isotropes et proches des propriétés de l'alliage corroyé. Généralement, les propriétés mécaniques des alliages obtenus par LPBF sont dépendantes de

l'orientation de fabrication, ceci est rapporté également pour l'alliage de titane Ti6Al4V (Simonelli, Tse et Tuck, 2014), pour l'alliage Inconel 718 (Trosch et al., 2016) et pour différents alliages d'aluminium (Kimura et Nakamoto, 2016; Prashanth et al., 2014; Tradowsky et al., 2016).

L'anisotropie observée lors de ces essais de traction peut également être observée dans d'autres matériaux et pour d'autres essais tels que des essais d'impact sur un alliage de titane (Wu, Lai et Chen, 2016). Dans ce cas, la différence observée est encore plus marquante : alors que les échantillons bâtis à l'horizontale absorbent une énergie de 9,6 J contre 4,9 J pour les échantillons bâtis à la verticale, ce qui représente une variation du simple au double. Encore une fois, un traitement thermique de pressage isostatique à chaud permet de réduire significativement les anisotropies (Wu et Lai, 2016). Des essais de flexion 3 points (Transverse Rupture Strength, TRS) montrent la même tendance (Wu et Lai, 2016). Dans ce cas, il est montré que la différence est également attribuable à la réduction des porosités engendrée par le traitement de HIP, cet aspect sera discuté plus loin.

1.1.4 Contraintes résiduelles

Un autre phénomène observé lors de la fabrication par LPBF est la formation de contraintes résiduelles importantes causées par les gradients thermiques appréciables lors du refroidissement (Shiomi et al., 2004; Zaeh et Branner, 2010). Le matériau est chauffé à des températures passablement plus élevées que le point de fusion afin de minimiser la porosité (Kruth et al., 2012). Ceci fait en sorte qu'une grande quantité d'énergie doit se dissiper, principalement dans la direction de fabrication. La Figure 1.4 montre le mécanisme par lequel se créent les contraintes résiduelles lors du cycle thermique imposé à la pièce par la fusion au laser.

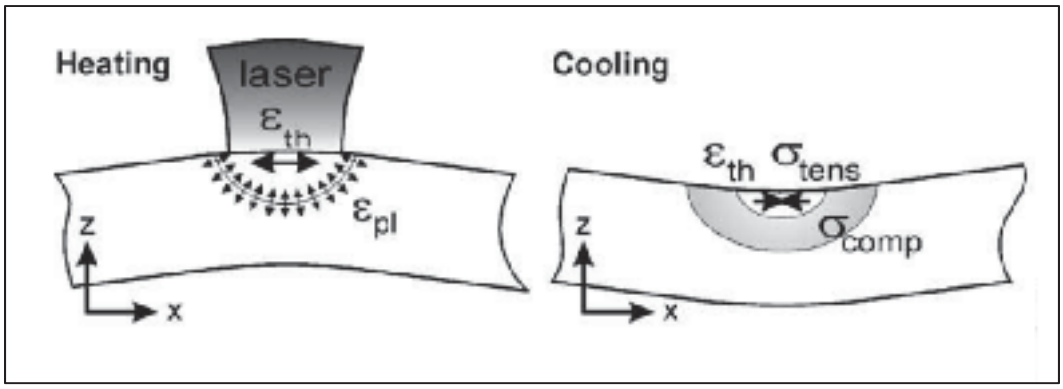

Figure 1.4 Schématisation du mécanisme par lequel se créent les contraintes résiduelles lors de la LPBF
Tirée de (Kruth et al., 2004)

Les contraintes résiduelles observées en LPBF font suite aux importants gradients thermiques engendrés par le chauffage rapide du matériau sur la couche supérieure. La dilatation thermique locale est importante et une zone de déformation plastique en compression est créée puisque le matériau avoisinant, n'étant pas fusionné, restreint l'expansion thermique. Suivant le passage du laser, le refroidissement s'accompagne d'un rétrécissement linéaire de la zone fusionnée et les régions demeurées solides reprennent les efforts engendrés par ce rétrécissement linéaire. Il en résulte des contraintes résiduelles importantes qui causent un effet de fléchissement dans les composants se traduisant par une concavité des pièces. Toutefois, lorsque des supports sont judicieusement employés, les déplacements sont contraints par ces derniers et le fléchissement est minimal.

Comme la superposition de milliers de couches est généralement requise pour obtenir une pièce, les contraintes résiduelles associées à chaque couche se superposent et affectent le composant à fabriquer dans son ensemble. L'emploi de couches plus épaisses semble augmenter les contraintes résiduelles (Mukherjee, Zhang et DebRoy, 2017). Lorsque la pièce est toujours retenue par les supports sur la plaque de fabrication, les contraintes résiduelles observées ont généralement une valeur qui avoisine la limite d'élasticité de matériau (Mercelis et Kruth, 2006). Un exemple de distribution d'amplitude des contraintes résiduelles selon l'axe

de fabrication (Z), avant et après le retrait de la plaque de fabrication est présenté à la Figure 1.5. On note que le retrait des composants de la plaque permet de relâcher en grande partie les contraintes, il est accompagné toutefois de distorsions importantes.

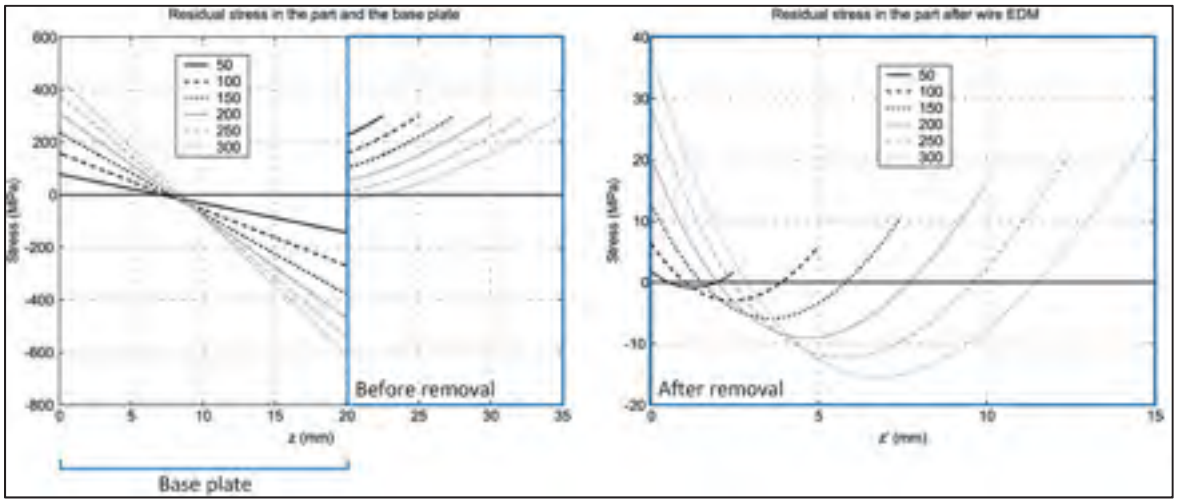

Figure 1.5 Contraintes résiduelles avant et après le retrait de la plaque pour différentes hauteurs de fabrication
Tirée et adaptée de (Mercelis et Kruth, 2006)

Afin de diminuer les contraintes résiduelles et éviter les distorsions, différentes approches ont été envisagées, par exemple: réaliser un traitement thermique à l'aide du laser, modifier la stratégie d'exposition du laser et chauffer la plaque de fabrication. Dans l'ensemble, chacune de ses approches permet de réduire les contraintes thermiques; la réduction observée est de l'ordre de 50% (Mercelis et Kruth, 2006; Shiomi et al., 2004). Un traitement thermique de recuit de détente, alors que les composants et la plaque de fabrication sont encore liés, demeure la meilleure façon d'éliminer les contraintes résiduelles tout en évitant les distorsions (Shiomi et al., 2004). De plus, un recuit de détente risque d'être moins couteux étant donné qu'il n'affecte pas le temps machine et requiert plutôt un four, moins dispendieux à opérer, dans lequel plusieurs plaques de fabrication peuvent être traitées simultanément.

1.1.5 État de surface

La rugosité des surfaces de pièces obtenues par le procédé de LPBF est un élément ayant été largement caractérisé. Dans un premier temps, l'approche de fabrication couche par couche apporte une certaine rugosité, laquelle est dépendante de l'angle d'inclinaison des surfaces relativement à la plaque de fabrication. La Figure 1.6 montre la relation entre l'orientation des surfaces et la rugosité obtenue.

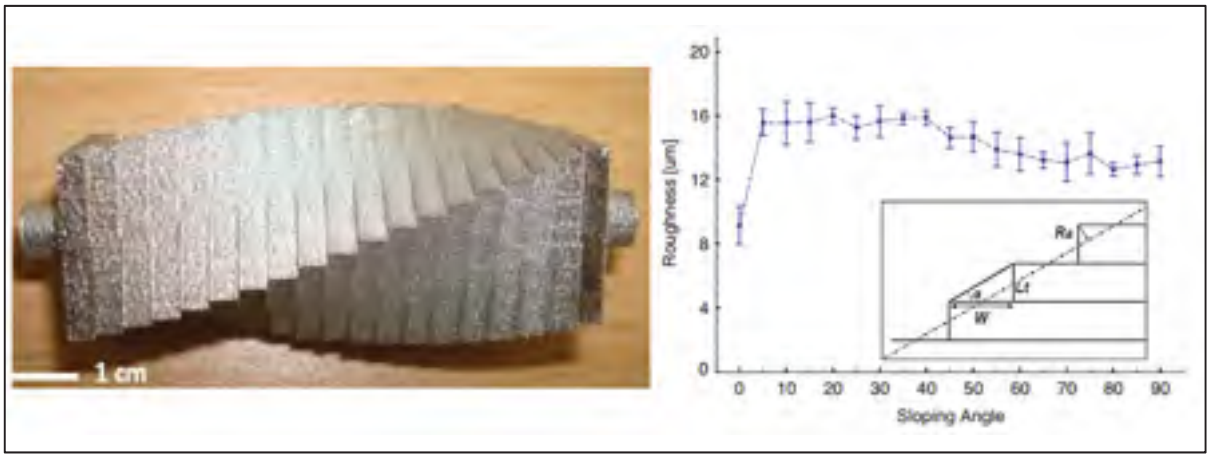

Figure 1.6 Rugosité de surface évaluée pour différentes orientations de fabrication
Tirée et adaptée de (Strano et al., 2013)

Bien que la distribution de rugosité présentée à la Figure 1.6 est dépendante de l'épaisseur de couche employée lors de la fabrication, elle fait état de certaines tendances intéressantes en regard de l'effet de l'orientation de la surface. Tout d'abord, les faces parallèles à la plaque de fabrication (orientation à 0°) présentent une rugosité moyenne nettement inférieure au reste des faces. Comme ces faces sont consolidées par une couche unique, il n'y a pas d'effet « d'escalier » et une rugosité d'environ 10 µm est obtenue. Pour les faces inclinées, la rugosité soit décroissante lorsque l'angle de la face se rapproche de la verticale (Figure 1.6a,b).

Certains traitements de surface permettent de réduire la rugosité des surfaces en fabrication additive. Le grenaillage est une technique largement documentée, qui en plus de modifier la rugosité de la surface, permet d'induire des contraintes résiduelles de compression à la surface des composants (Kobayashi, Matsui et Murakami, 1998). Le traitement de grenaillage est particulièrement intéressant puisqu'il peut, moyennant une sélection de paramètres étoffée, avoir des effets positifs sur la vie en fatigue en freinant les mécanismes d'endommagement dans la zone de contraintes résiduelles en compression (de los Rios et al., 1995; Torres et Voorwald, 2002). Enfin, l'enlèvement d'une surépaisseur de matière, par polissage mécanique, par polissage électrochimique ou par usinage peut aussi être envisagé. De nombreuses techniques d'enlèvement de matière permettent d'obtenir un état de surface comparable aux pièces obtenues par des procédés traditionnels.

1.1.6 Défauts de fabrication

En dehors des spécificités déjà énoncées, certains défauts tels que des microporosités, des inclusions, des microfissures et des zones partiellement frittées sont caractéristiques des matériaux obtenus par LPBF. Les défauts les plus couramment observés au sein de la majorité des pièces produites par des procédés impliquant les poudres métalliques sont sans aucun doute les pores. Comme il a été préalablement mentionné, le procédé de LPBF permet généralement d'obtenir une densité relative au-delà de 99% (Kasperovich et al., 2016; Tammas-Williams et al., 2016a; Ziółkowski et al., 2014), toutefois pour y parvenir, il faut employer des paramètres d'exposition au laser qui respectent certaines limites propres à chaque poudre. La Figure 1.7 met en évidence comment la porosité et la morphologie des pores sont affectées par la densité d'énergie employée pour la LPBF.

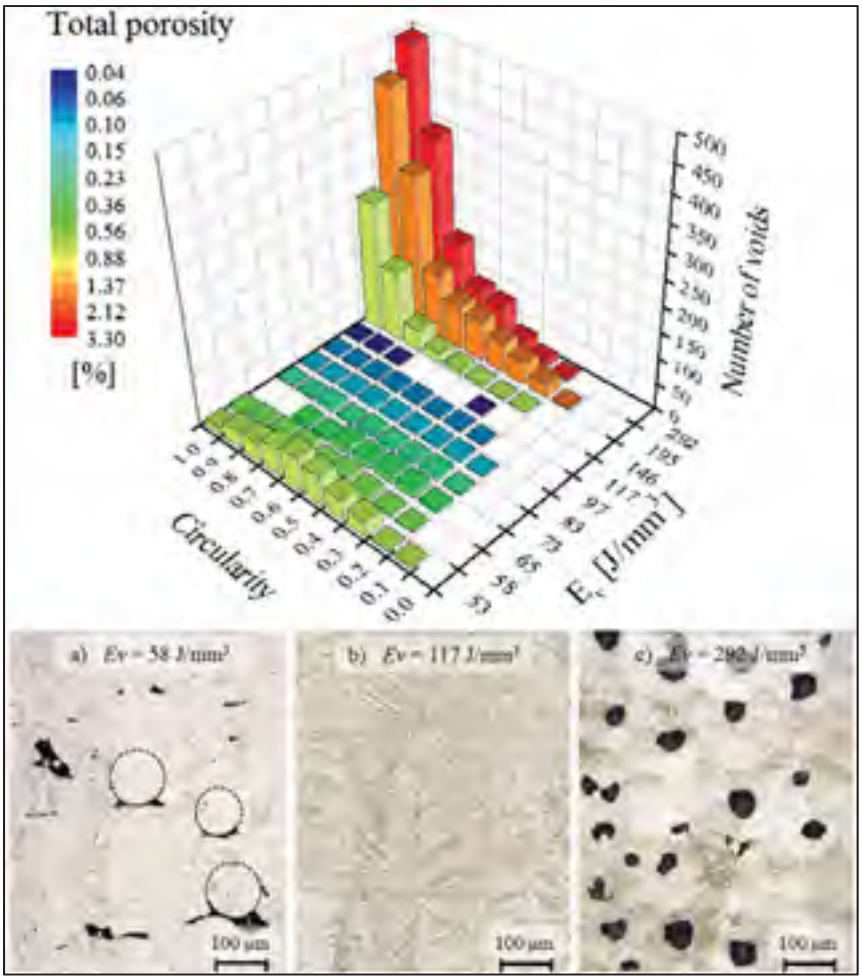

Figure 1.7 Porosité observée dans des échantillons de titane Ti6Al4V fabriqué par LPBF en fonction de la densité d'énergie
Tirée et adaptée de (Kasperovich et al., 2016)

En plus d'illustrer l'étroite relation existant entre le taux de porosité observé et le taux d'énergie employé dans la LPBF, il est possible de dégager certaines caractéristiques morphologiques des pores. On note que pour de faibles densités d'énergie (J/mm^3), la géométrie des pores est considérablement différente, ils ont une circularité beaucoup plus faible et sont allongés dans un axe. En opposition, lorsque la densité d'énergie employée est plus élevée, les pores sont beaucoup plus volumineux et plus sphériques. Si la sélection de la densité d'énergie permet de contrôler la porosité, il demeure pratiquement impossible d'obtenir une porosité nulle. Ces observations ont été confirmées à de nombreuses reprises et pour

différents alliages, autant obtenues par fusion sélective au laser que par fusion sélective au moyen d'un faisceau d'électrons (Mazur et al., 2015; Sallica-Leva, Jardini et Fogagnolo, 2013; Tammas-Williams et al., 2016a; Tang et Pistorius, 2017; Wan et al., 2016; Zhai, Galarraga et Lados, 2016; Ziółkowski et al., 2014).

Jusqu'ici, les pores ont été traités comme des entités similaires, toutefois, en s'intéressant un peu plus à la nature des défauts et à leur impact sur les propriétés des matériaux, il devient important de faire une distinction entre les différents types de pores. La littérature montre que les pores sphériques sont en fait des bulles de gaz ayant été emprisonnées dans le bain de fusion (Gong et al., 2014). L'observation plus détaillée des pores de faible sphéricité, obtenus lorsque la densité d'énergie est faible, révèle souvent la présence de poudre partiellement frittée. Dans de tels cas, l'énergie est insuffisante, ce qui ne permet pas d'assurer la stabilité du bain de fusion et de fusionner l'ensemble des particules. On retrouve alors souvent des particules non fusionnées à l'intérieur des composants. Ces particules affectent les propriétés mécaniques et sont souvent observées sur les surfaces de rupture comme montre la Figure 1.8.

Figure 1.8 Poudre non fusionnée observée sur les surfaces de ruptures d'échantillons obtenus par LPBF
Tirée et adaptée de (Siddique et al., 2015)

En addition aux pores, il est aussi possible de retrouver des inclusions suite à la mise en forme par LPBF. Ces particules sont en quelque sorte des contaminants qui se retrouvent dans le lit de poudre, leur nature peut varier et il a déjà été montré qu'ils ont aussi un impact sur le comportement du matériau (Jiang et al., 2016; Tang et Pistorius, 2017).

Enfin, un autre élément qui est important de retenir est la possibilité de fissuration dans le cas où des contraintes trop importantes sont créées lors de la fabrication. Ce type de défaut est souvent relié aux contraintes thermiques dont il a été question à la section précédente. La Figure 1.9 montre des exemples de pièces obtenues par LPBF au sein desquels des fissures sont observées. Dans ce cas, il n'est pas possible de régler le problème par traitement thermique, ceci illustre donc l'importance de choisir adéquatement des structures de support facilitant la diffusion de la chaleur vers la plaque de fabrication. Cette stratégie permet généralement de réduire les gradients de température.

Figure 1.9 Fissuration observée lors de la fabrication de composants par LPBF
Tirée et adaptée de (Kruth et al., 2012)

1.2 Endommagement par fatigue

Après avoir exposé les caractéristiques principales des matériaux obtenus par LPBF, il est maintenant possible de s'intéresser plus spécifiquement à l'état des connaissances concernant leur comportement en fatigue. La définition de la fatigue proposée par l'ASTM est la suivante:

« The process of progressive localized permanent structural change occuring in a material subjected to conditions that produce fluctuating stresses and strain at some point and that may culminate in cracks of complete fracture after a sufficient number of fluctuations ». Comme il a été montré dans les sections précédentes, dans le cas des alliages obtenus par LPBF, les défauts induits lors de la fabrication sont généralement le siège de l'endommagement par fatigue (initiation de fissure). Il importe donc de comprendre comment ces défauts affectent la vie en fatigue. Plusieurs publications sur le sujet sont répertoriées, mais la grande majorité porte sur l'alliage de titane Ti6Al4V. En se basant sur ce qui est observé pour ce matériau, il est possible de mettre en lumière les tendances qui se dégagent de la caractérisation du comportement en fatigue des matériaux métalliques obtenus par fusion sélective au laser. La Figure 1.10 montre le processus d'endommagement par fatigue.

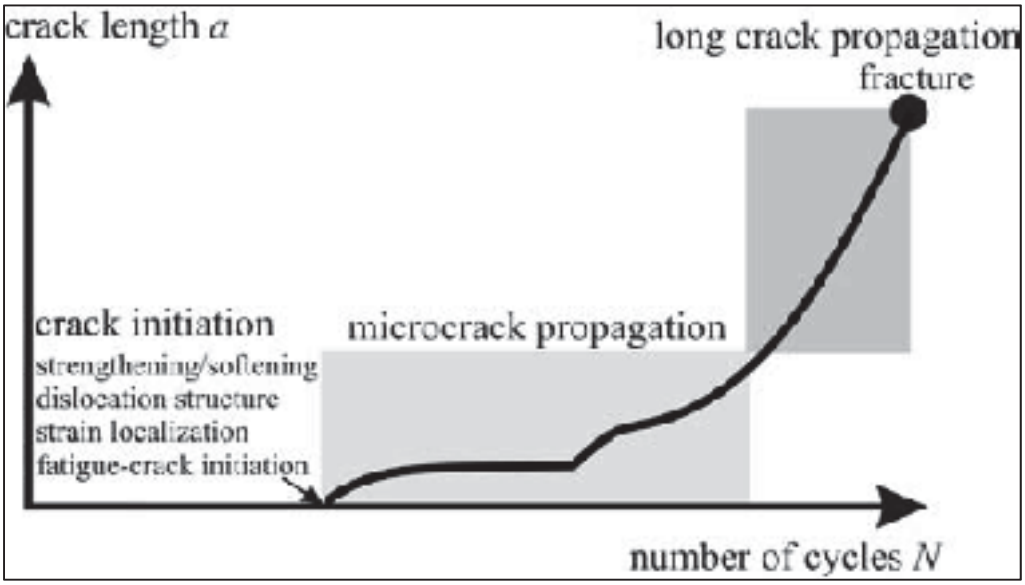

Figure 1.10 Exemple d'évolution d'un défaut, taille en fonction du nombre de cycles
Tirée de (Krupp, 2007)

Sur cette figure on distingue trois zones; la zone d'initiation de fissure, la zone de propagation d'une microfissure dite « courte » et la zone de propagation d'une fissure dite « longue ». Dans la première étape, le défaut est existant, mais il ne n'est pas mesurable, il s'agit plutôt de

changements microstructuraux tels que le développement de bandes de glissement. Lorsque ces défauts microstructuraux évoluent, il est possible de déceler une fissure dont la longueur est initialement comparable à la taille de grain; il s'agit d'une fissure « microstructurellement courte ».

À cette étape, la fissure, dite « courte », se propage d'une manière instable et difficilement prévisible puisque chaque discontinuité microstructurale affecte sa propagation. Par exemple, aux joints de grains, une fissure courte peut être freinée temporairement ou encore stoppée. Pour les alliages monophasés et lorsque la propagation est transgranulaire, la propagation est généralement réinitiée selon l'orientation des plans cristallographiques les plus denses dans le grain adjacent, selon lesquels les dislocations se déplacent plus facilement. Selon l'orientation cristallographique relative des grains adjacents, le nombre de cycles requis pour relancer la propagation varie. À ce stade, la microstructure joue donc un rôle considérable dans la cinétique de la propagation de fissure courte (Anderson, 2017; Krupp, 2007).

Toujours dans le régime de fissures courtes, on distingue une région caractérisée par une augmentation soudaine du taux de propagation, il s'agit du régime de propagation de fissure « mécaniquement courte ». Pour ce régime, la fissure a un comportement qui se distingue des fissures longues puisque la taille de la fissure est encore trop faible pour que les mécanismes de fermeture de fissure, dont il sera question plus loin, soient développés. La propagation est donc plus rapide que ce qui est anticipé pour des fissures longues sous un chargement analogue.

La troisième portion est la propagation d'une fissure dite « longue ». Le passage du comportement d'une fissure courte à longue s'observe généralement lorsque la taille de fissure atteint une longueur d'environ 10 fois la taille de grains (Krupp, 2007). Pour cette étape, la microstructure est moins déterminante et la propagation est plus facile à prédire au moyen de divers modèles basés sur la mécanique linéaire élastique de la rupture tels que la relation de Paris (Hertzberg, Vinci et Hertzberg, 2012). Dans de nombreuses applications d'ingénierie où l'on applique l'approche de tolérance aux dommages, ce sont ces fissures auxquels on

s'intéresse puisqu'elles ont des tailles permettant la détection au moyen de diverses méthodes de contrôle non destructif tel que l'inspection par liquide pénétrant (ressuage) ou l'inspection par courant de Foucault. De plus, le comportement de ces fissures est plus stable et divers modèles permettent le prévoir, à condition que les hypothèses de la mécanique de la rupture linéaire élastique présentées à la section 1.3 soient respectées.

Pour les matériaux obtenus par LPBF, les données expérimentales disponibles sont principalement le résultat d'essais de fatigue sous forces ou déformations contrôlées, sans faire distinction entre les étapes de l'endommagement. Ces essais visent plutôt à mettre en relation la contrainte ou la déformation alternées avec le nombre de cycles à la rupture. Il est également possible, pour certains alliages, de trouver des données relatives au comportement des fissures de fatigue longues. Il existe toutefois trop peu de données relatives au comportement des fissures courtes pour les métaux fabriqués par LPBF pour dresser un portrait intéressant. En ce sens, la présente section se limitera à la présentation de courbes de Wohler et de diagramme da/dN – ΔK pour illustrer le comportement des matériaux métalliques obtenus par LPBF.

1.2.1 Courbes de Wöhler

Les études portant sur la fatigue des matériaux obtenus par LPBF sont moins nombreuses que celles portant sur les propriétés statiques ou la microstructure. La majorité de ces études utilisent l'approche « Stress-Life », basée sur la courbe de Wöhler, aussi connue sous l'appellation « courbe S-N », comme l'outil de caractérisation et à des fins de comparaison. Pour l'alliage de titane Ti6Al4V, il est possible de trouver différentes publications concernant le comportement en fatigue d'échantillons fabriqués par LPBF qui permettent d'identifier certaines tendances comme l'impact des post-traitements sur la vie en fatigue. La Figure 1.11 est issue d'un article qui fait une revue assez complète des résultats publiés avant 2016.

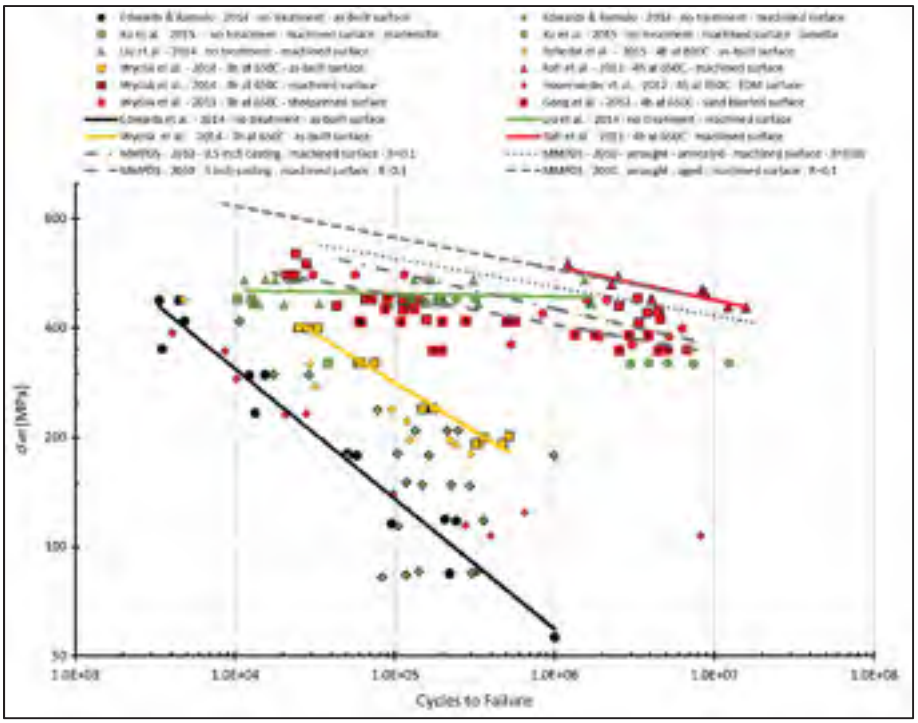

Figure 1.11 Courbes SN obtenues pour l'alliage de titane Ti6Al4V obtenu par LPBF testé à R≈0 avec différents posttraitements
Tirée de (Li et al., 2016)

Avant d'aller plus loin dans la comparaison, il est essentiel de prendre note que chaque courbe SN est obtenue pour les ratios de contraintes près de zéro, mais non identiques. Les contraintes reportées en ordonnée sont normalisées selon la contrainte maximale et le rapport de contrainte R exact reporté dans les articles originaux. Les posttraitements réalisés par chaque auteur diffèrent toutefois, ce qui met en évidence la sensibilité du comportement en fatigue au post-traitement. Ce constat est valable en ce qui concerne l'état de surface et on note que les pires résultats sont obtenus pour des échantillons testés tels que fabriqués (droite noire). Un traitement thermique de recuit de détente permet d'augmenter considérablement la durée de vie (droite jaune) en diminuant significativement les contraintes résiduelles (Kruth et al., 2012; Mercelis et Kruth, 2006). L'usinage des surfaces semble encore une fois augmenter de beaucoup la durée de vie (droite rouge et droite verte). Dans ce cas-ci, on peut ajouter que les durées de vie obtenues dépassent celles observées pour les spécimens coulés dont la surface

est usinée et se rapprochent des alliages forgés. Les résultats présentés ici suggèrent que l'obtention d'une résistance en fatigue s'approchant de l'alliage corroyé passe inévitablement par l'amélioration des conditions de surface. Il appert que cette variable est la plus déterminante, après quoi d'autres posttraitements permettant de diminuer la quantité de défauts apparaissent bénéfiques, comme le montre la Figure 1.12. À cet effet, le traitement de HIP a également été employé avec succès dans le cas de composants coulés dans des conditions de tests analogues à celles pour la Figure 1.11 (Li et al., 2016).

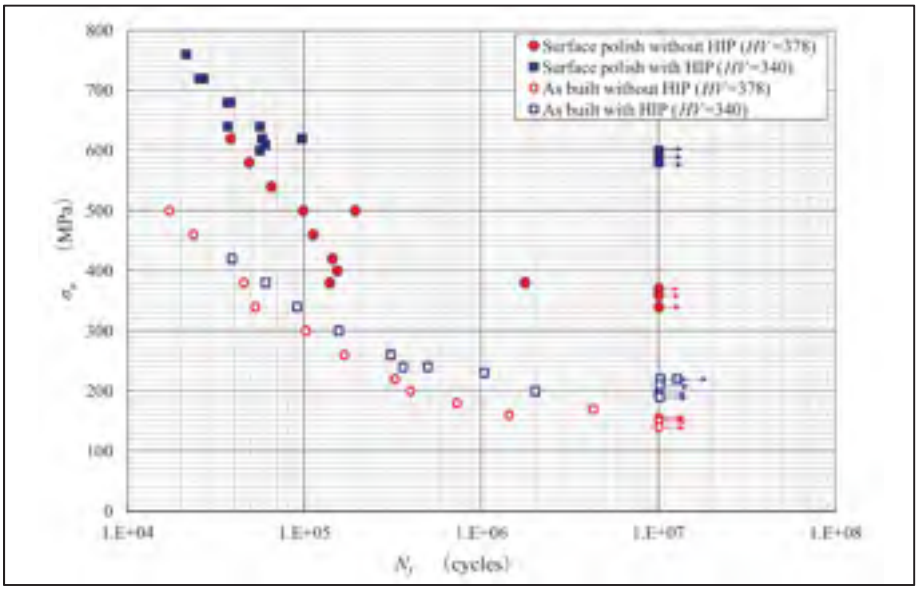

Figure 1.12 Courbes SN obtenues pour l'alliage de titane Ti6Al4V obtenu par LPBF testé à R=-1 suivant divers posttraitements
Tirée de (Masuo et al., 2018)

Toujours selon les résultats montrés à Figure 1.12, la réduction de la porosité qui découle du traitement de HIP améliore significativement la vie en fatigue. Toutefois, il est important de réitérer que l'effet positif du HIP n'est pleinement profitable que lorsque l'état de surface est adéquat puisqu'il s'agit de la propriété la plus déterminante en ce qui concerne l'initiation de fissure. Une rugosité trop importante peut provoquer une diminution du nombre de cycles à la rupture d'environ 75% (Edwards et Ramulu, 2014; Kasperovich et Hausmann, 2015). Lorsqu'un HIP est employé, il est possible de noter que les défauts près des surfaces demeurent

des sites d'initiation de fissures courants (Wycisk et al., 2014; Yadollahi et Shamsaei, 2017). En addition, l'effet délétère des pores résultant d'un procédé ayant un niveau d'énergie trop élevé n'est pas aussi important que lorsque les pores résultent d'un niveau d'énergie insuffisant (Gong et al., 2015). Enfin, il a aussi été démontré que l'orientation du chargement cyclique par rapport au plan de fabrication est également un aspect déterminant pour la vie en fatigue de pièces obtenues par LPBF (Edwards et Ramulu, 2014).

1.2.2 Faciès de rupture par fatigue d'échantillons obtenus par LPBF

L'observation de surfaces de rupture au moyen d'un microscope à balayage permet de dégager des informations importantes pour complémenter les résultats d'essais de fatigue. Dans le cas de la majorité des analyses portant sur des matériaux obtenus par LPBF, les défauts de fabrication sont identifiés comme site d'amorçage des fissures de fatigue culminant en rupture. Parmi les différents défauts répertoriés, il semble que les pores de faible sphéricité associés à un manque de fusion soient les plus dommageables. On retrouve également régulièrement des particules non fusionnées près des régions d'initiation de fissures, qui témoignent d'un manque d'énergie lors de la fusion. Ces observations sont vérifiées pour différents alliages, dont l'aluminium (Siddique, Imran et Walther, 2017), le titane (Edwards et Ramulu, 2014; Greitemeier et al., 2017) et l'acier inoxydable (Schönbauer, Yanase et Endo, 2017). En addition, comme le montre la Figure 1.13 même suivant un post-traitement de HIP, le site d'initiation de fissures de fatigue peut être un défaut de fabrication, ce qui indique que le procédé possède certaines limites (Masuo et al., 2018).

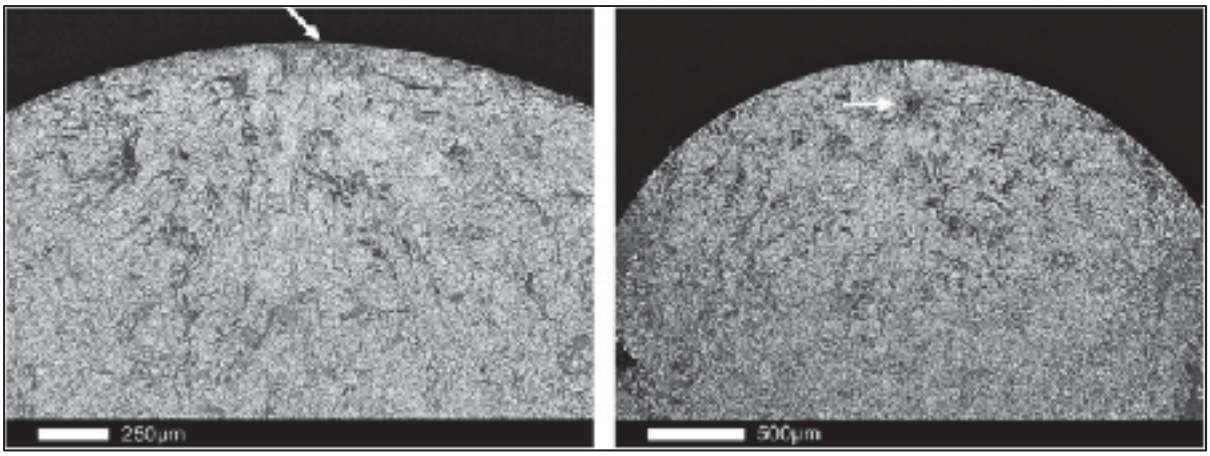

Figure 1.13 Surface de rupture en fatigue d'un spécimen de Ti6Al4V obtenu par LPBF et soumis à un post-traitement de HIP
Tirée de (Masuo et al., 2018)

1.2.3 Comportement en propagation de fissure de fatigue

La norme ASTM E-647-13a est couramment employée afin d'évaluer la vitesse de propagation de fissure au sein d'échantillons obtenus par LPBF et ce, malgré leur anisotropie. Cette méthode est toutefois limitée à la caractérisation du comportement en propagation de fissures dits « longues », lequel est généralement obtenu lorsqu'une fissure dépasse une longueur de 10 fois la taille de grains (Krupp, 2007). Les résultats sont reportés dans un diagramme da/dN - ΔK, tel qu'illustré à la Figure 1.14. Pour ce cas, deux directions de propagation de fissure ont été considérées dans un alliage de titane Ti6Al4V obtenu par LPBF, et ce, pour différents traitements thermiques, afin de voir l'influence de l'anisotropie sur cette propriété.

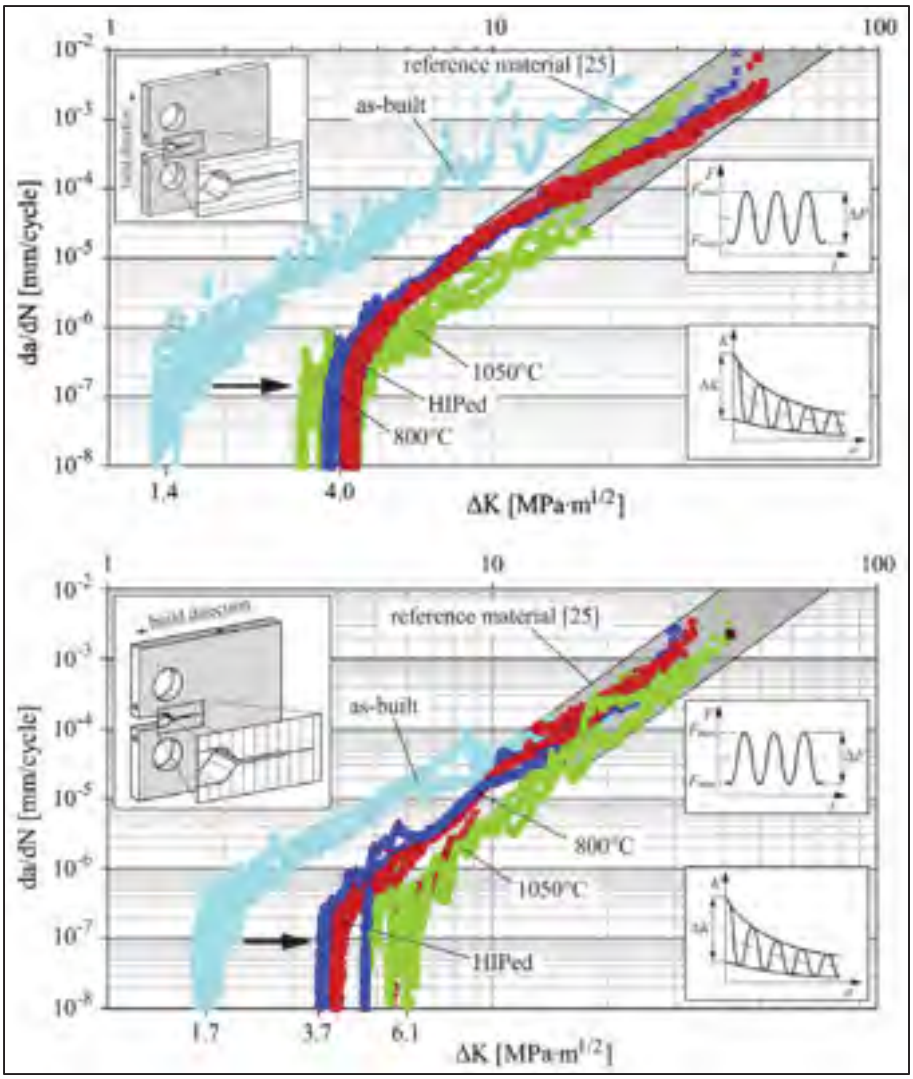

Figure 1.14 Courbes de propagation de fissure pour l'alliage Ti6Al4V obtenu par LPBF a) Fissure dans le plan de fabrication et b) Fissure normale au plan de fabrication
Tirée de (Leuders et al., 2013)

Des résultats analogues peuvent être trouvés pour d'autres alliages incluant ceux d'aluminium (Siddique, Imran et Walther, 2017), d'acier inoxydable (Riemer et al., 2014), et Inconel 718 (Konečná et al., 2016). Les diagrammes de Paris trouvés dans la littérature pour des alliages obtenus par LPBF montrent certaines tendances sur le comportement en propagation de fissure pour de nombreux cas et on peut tirer les conclusions suivantes :

- La propagation de fissure pour les échantillons « As-built » est beaucoup plus rapide et le facteur d'intensité de contraintes seuil est très faible,
- Pour ces mêmes échantillons, une fissure dans le plan de fabrication se propage plus rapidement qu'une fissure transversale,
- Pour les échantillons traités thermiquement, la propagation de fissure se fait à des vitesses comparables aux matériaux de référence corroyés,

En plus de ces résultats, il a été rapporté dans la littérature que la ténacité est généralement plus élevée lorsque la fissure est normale aux plans de fabrication (Edwards et Ramulu, 2015), mais de manière générale, elle demeure plus faible que pour un matériau mis en forme par des procédés traditionnels à cause de la microstructure (Van Hooreweder et al., 2012). Également, au niveau des surfaces de rupture, on note que les fissures se propagent de manière transgranulaire tant pour les matériaux obtenus par LPBF que pour ceux corroyés.

1.3 Mécanique de la rupture linéaire élastique

L'approche de tolérance aux dommages part de la prémisse que tout composant mécanique, quels que soient le matériau et le procédé de fabrication, comporte des défauts, lesquels sont souvent attribuables à leur mise en forme ou leur utilisation. Pour le procédé de fusion sélective au laser, il a été montré que les défauts de fabrication ont un impact significatif sur la vie en fatigue. Étant donné leurs caractéristiques géométriques, il apparait que leur présence accélère la phase d'initiation des fissures de fatigue et diminue la durabilité des spécimens ou parts. En ce sens, pour ce procédé de fabrication, il convient d'aborder le comportement en fatigue selon l'approche de la mécanique de la rupture linéaire élastique. Une revue non exhaustive des principales notions de la mécanique de la rupture linéaire élastique est présentée à cette section.

1.3.1 Modes de propagation de fissure

On distingue trois modes de sollicitation de fissure selon le type de chargement illustré à la Figure 1.15. Pour le mode I, la fissure est sollicitée en tension alors que le mode II et le mode III sont des modes où la fissure est sollicitée en cisaillement. Dans le cas du mode II, le cisaillement est dans l'axe longitudinal de la fissure alors que pour le mode III, chaque côté de la fissure se déplace dans une direction opposée dans l'axe perpendiculaire à la fissure, on parle plutôt de déchirement. Pour un cas de chargement complexe, une fissure peut être sollicitée dans deux ou trois modes simultanément. Il est donc possible de calculer des facteurs d'intensité de contrainte pour chacun des modes (K_I, K_{II}, K_{III}). Toutefois, pour la majorité des cas de rupture par fatigue, la sollicitation en mode I (tension) est responsable de la rupture du composant.

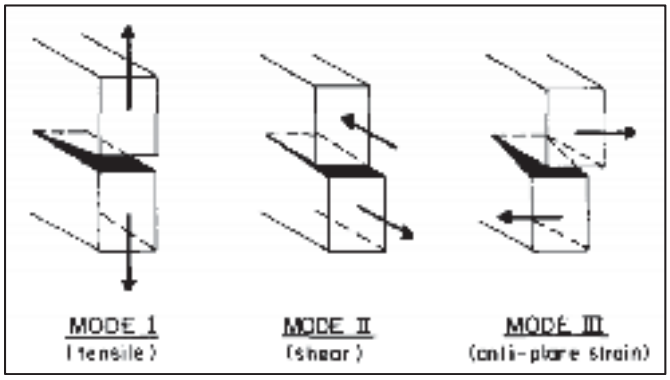

Figure 1.15 Modes de propagation de fissure
Tirée de (Ritchie et al., 1982)

Comme le mode I est le mode critique menant à la rupture, il est plus largement documenté et caractérisé afin d'obtenir des critères de conception en tolérance aux dommages. La norme ASTM E647 et la norme ISO 12108 proposent toutes deux une méthode qui permet de caractériser la propagation de fissure en mode I afin d'obtenir un diagramme da/dN - ΔK dont il a été question à la Section 1.2.3.

1.3.2 Comportement des fissures longues

Lorsqu'un corps sujet à un champ de contrainte linéaire élastique comporte une surface plane libre (fissure), les modèles d'analyse basée sur le facteur de concentration de contrainte sont inadéquats pour évaluer le niveau de contrainte en fond de fissure. Comme la valeur de rayon tend vers zéro pour un tel cas, une singularité est obtenue. Ceci suggère que la contrainte est infinie en fond de fissure, or il est impossible d'obtenir une telle contrainte. Les travaux de Griffith (Griffith, 1921), réalisés au début 20^{e} siècle, ont été une avancée significative pour la mécanique de la rupture. Ce dernier s'est intéressé a mis en relation l'équilibre énergétique associé à la création de surfaces lors de la fissuration dans une plaque et le changement d'énergie potentielle du corps. Par la suite, Irwin (Irwin, 1957), à partir des travaux de Westergaard (Westergaard, 1939) a développé le facteur d'intensité de contrainte K qui évalue la sévérité du champ de contraintes en fond de fissure pour un matériau linéaire élastique isotrope. Ce facteur, calculé à l'aide de l'équation 1.1, met en relation la contrainte nominale appliquée sur un corps fissuré et la taille de la fissure.

$$K_I = Y * \sigma\sqrt{\pi a} \tag{1.1}$$

Dans cette équation, K_I est le facteur d'intensité de contrainte en mode I, Y est un facteur de forme associé à la géométrie de la fissure, de la pièce et le type de chargement qui peut être évalué analytiquement pour des cas simples. Pour des cas complexes, il est possible d'avoir recours à la méthode des éléments finis pour l'évaluer. Ensuite, σ est la contrainte appliquée dans l'axe normal à la fissure et a est la profondeur du défaut. Les composantes différentes de zéro du tenseur de contrainte en fond de fissure sont toutes proportionnelles au facteur K et inversement proportionnelles à la racine carrée de leur coordonnée radiale en considérant l'origine au fond de la fissure. Cette distribution est représentée en ligne pointillée sur la Figure 1.16.

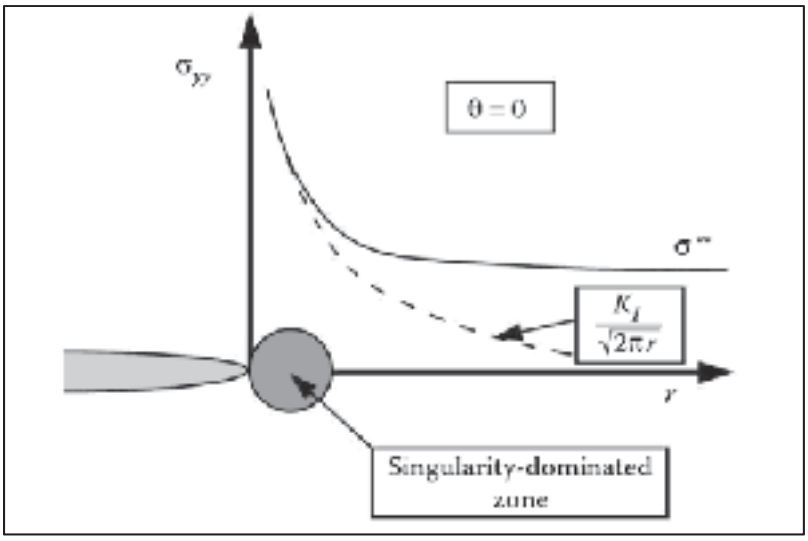

Figure 1.16 Distribution des contraintes en fond de fissure

Il faut préciser que cette approche suggère toutefois l'existence d'une contrainte infinie en fond de fissure (singularité). Or, ce modèle est basé sur l'hypothèse d'un matériau linéaire élastique tandis que les matériaux métalliques sont ductiles et donc manifestent un comportement élastoplastique. En réalité, lorsque la contrainte en fond de fissure excède la valeur de la limite d'élasticité, une zone plastique est générée en fond de fissure.

1.3.3 Plasticité en fond de fissure

À la Figure 1.16, il est possible d'identifier une zone dominée par la singularité, la plasticité est observée dans cette région située à la pointe de la fissure. Lorsque la charge est augmentée, la taille de la région déformée plastiquement augmente. En connaissant le facteur d'intensité de contrainte maximal (K_{max}), il est possible d'estimer la taille de la zone plastique, dite monotone, grâce aux équations 1.2 et 1.3 (Anderson, 2017).

$$r_{0\sigma} \approx \frac{1}{2\pi}\left(\frac{K_{max}}{\sigma_{YS}}\right)^2 \tag{1.2}$$

$$r_{0\varepsilon} \approx \frac{1}{6\pi}\left(\frac{K_{max}}{\sigma_{YS}}\right)^2 \tag{1.3}$$

La première relation est valide lorsque le chargement est en contrainte plane alors que la seconde prévaut pour les cas de déformation plane. Dans ces équations, la taille de la zone plastique $r_{0\sigma}$ ou $r_{0\varepsilon}$ est relié à la limite d'écoulement du matériau σ_{YS} et au facteur d'intensité de contrainte K_{max}. On utilise K_{max} étant donné qu'en fatigue, la valeur du facteur d'intensité de contrainte fluctue et c'est sa valeur maximale qui définit la taille de la zone plastique dite monotone. Il existe également une zone plastique cyclique, cette zone est causée par le retour élastique qui accompagne la phase de déchargement, lequel entraine un effort de compression sur la région en fond de fissure. Comme le montre la Figure 1.17, immédiatement en fond de fissure, l'amplitude de contrainte locale est alors équivalente à la limite d'élasticité du matériau. Bien entendu, ce modèle suppose un matériau parfaitement plastique, l'effet de durcissement par écrouissage est alors négligé. La taille et la forme réelle de la zone plastique sont en réalité différentes de ce qui est schématisé.

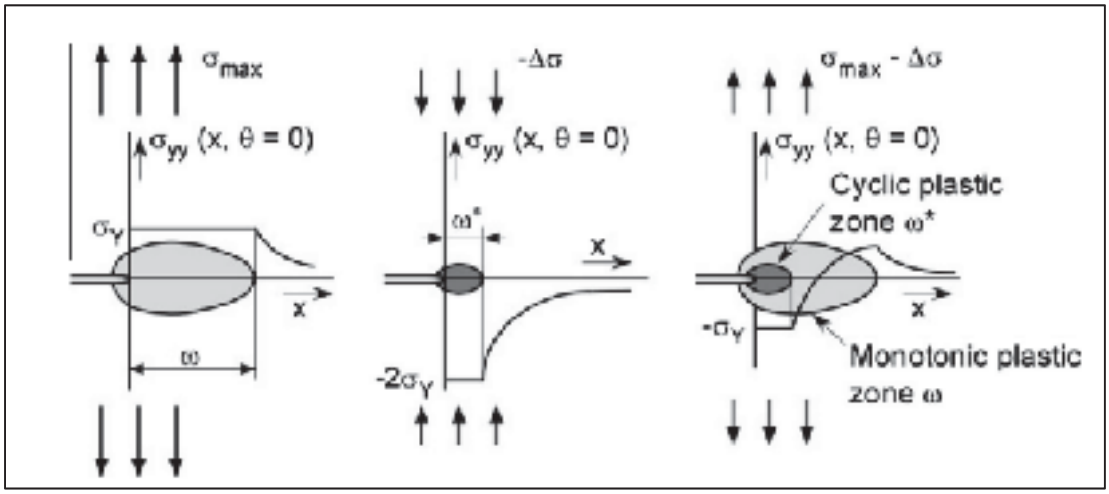

Figure 1.17 Schématisation du développement des zones plastiques monotones et cycliques en fond de fissure.
Tirée de (Zerbst et al., 2016)

1.3.4 Validité de la mécanique de la rupture linéaire élastique

Malgré la présence de la région déformée plastiquement en fond de fissure, la mécanique de la rupture linéaire permet de décrire le comportement en propagation de fissure des alliages métalliques ductiles. Il faut cependant respecter la condition selon laquelle la région plastique doit être plus petite que la taille de fissure ou de toute autre dimension caractéristique de l'échantillon de propagation de fissure ou de la composante. Cette condition est connue sous l'appellation small scale yielding (SSY) en anglais. Dans le cas d'un essai de propagation de fissure sur un échantillon de type compact tel que définit par la norme ASTM E647, on définit la limite de validité d'un échantillon après l'équation 1.4 (*Standard Test Method for Measurement of Fatigue Crack Growth Rates*, 2015) :

$$(W-a), b, a\ et\ h\ \geq \frac{4}{\pi}\left(\frac{K_{max}}{\sigma_{YS}}\right)^2 \tag{1.4}$$

Dans cette équation, $(W-a)$ correspond à la taille du ligament d'un échantillon compact ayant comme dimension caractéristique W. Les termes a, b et h sont respectivement la taille de fissure, la largeur de l'échantillon et sa hauteur. Pour les cas qui violent le critère de SSY, il existe quelques modèles de correction de la LEFM qui permettent d'étendre son application, dont les modèles de Irwin et Dugdale, qui ajuste la taille de fissure d'après la taille de la région plastique. Il est toutefois préférable dans ce cas d'avoir recours au modèle de mécanique de la rupture élastoplastique dont la théorie n'est pas abordée dans cette thèse.

1.3.5 Mécanismes de fermeture de fissure

Jusqu'ici, la discussion sur la propagation des fissures n'a pas tenu compte des mécanismes de fermeture de fissure, qui peuvent pourtant jouer un rôle prépondérant dans le comportement de ces dernières. Il existe trois principaux mécanismes de fermeture de fissure, à savoir, la fermeture induite par la plasticité, la fermeture induite par la rugosité et la fermeture induite par la présence d'oxydes, qui ont été schématisés à la Figure 1.18 par (Zerbst et al., 2016).

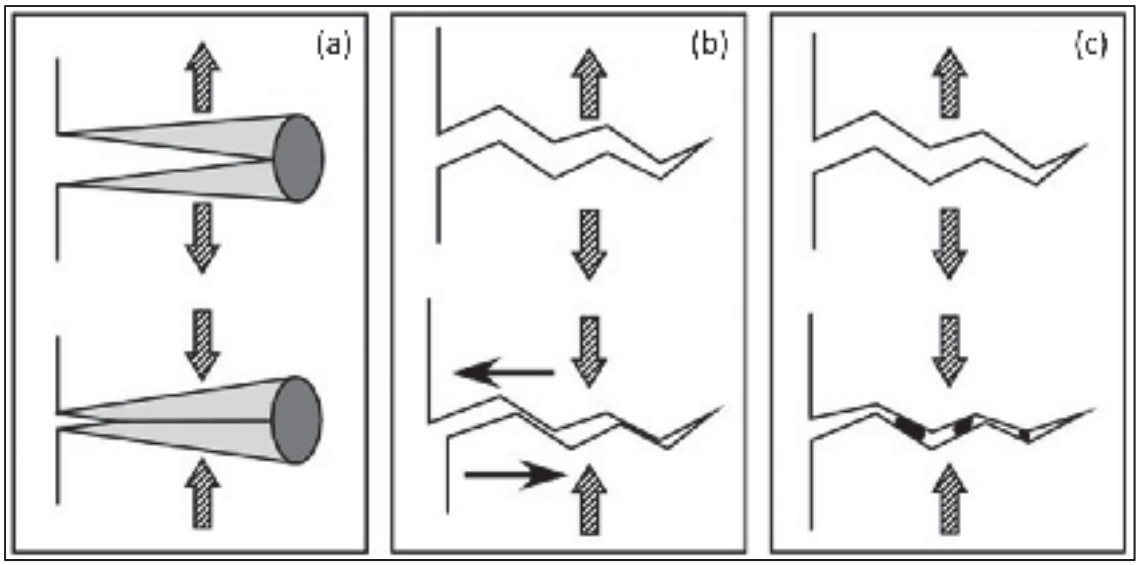

Figure 1.18 Schématisation des mécanismes de fermeture de fissure (a) Induite par la plasticité, (b) induite par la rugosité et (c) induite par la présence d'oxydes
Tirée de (Zerbst et al., 2016)

La fermeture de la fissure induite par la plasticité est directement reliée à l'existence de la zone plastique en fond de fissure. Lorsque la fissure avance, elle scinde cette région en deux et les contraintes résiduelles présentant en fond de fissure ont pour effet de gonfler les nouvelles surfaces, ce qui cause une fermeture précoce de la fissure avant que la charge minimale atteigne zéro. Le ratio de contrainte joue un rôle important dans l'ensemble des mécanismes de fermeture de fissure. Pour un ratio de contrainte qui s'approche de 1, il est possible que la fermeture de la fissure ne soit jamais observable.

Dans le cas de la fermeture induite par la rugosité, elle est particulièrement observable lorsque la fissure suit un chemin tortueux. Ceci s'observe notamment sous des conditions de chargement près du seuil, lorsque la taille de grain du matériau est élevée. Elle est observée à plus forte raison lorsque la fissure est sollicitée en mode mixte. Des aspérités plus ou moins grandes et même des ramifications sont parfois observées. Lorsque les surfaces fissurées s'approchent une de l'autre, elles entrent en contact avant que la charge soit entièrement relâchée

Enfin, la fermeture induite par les oxydes s'observe souvent dans des milieux particulièrement agressifs et pour des matériaux sensibles à la corrosion. L'ouverture de la fissure met en contact les surfaces fraichement produites par l'avancement de la fissure avec l'environnement, ce qui permet aux oxydes de se former. Leur présence entraine un contact prématuré des surfaces de la fissure et donc une diminution de l'amplitude de la variation de la charge reprise par la région avoisinant le fond de la fissure.

Ces mécanismes sont particulièrement importants puisqu'ils ont pour effet de réduire le chargement effectif en fond de fissure. L'observation de ce phénomène peut se faire au moyen d'une courbe de souplesse, telle que montrée à la Figure 1.19, qui met en relation la force appliquée sur l'échantillon et l'ouverture des lèvres de la fissure.

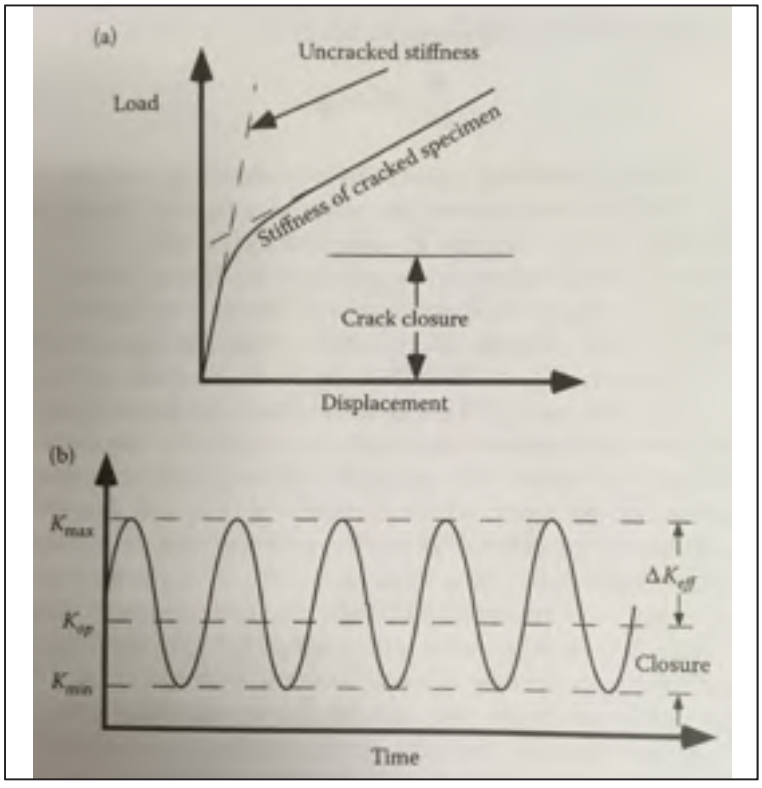

Figure 1.19 Fermeture de fissure (a) Mesure à partir de la courbe de souplesse et (b) Facteurs d'intensité de contraintes efficace en présence de fermetures
Tirée de (Anderson, 2017)

Lorsque l'on mesure une fissure de fatigue par la méthode de souplesse, on utilise la pente de la courbe reliant la force et l'ouverture des lèvres de la fissure. Il faut noter que la présence de fermeture de fissure induit une non-linéarité dans cette relation. Par exemple, lors du déchargement, on observe généralement un changement de pente à une charge intermédiaire dénotée K_{cl}, qui correspond au facteur d'intensité de contrainte à la fermeture de la fissure Entre la charge de fermeture K_{cl} et minimale K_{min}, on peut considérer que la fissure est fermée et que cette portion de la sollicitation ne cause pas d'endommagement en fond de fissure. Tel que montré à la Figure 1.19, on peut définir ΔK_{eff} comme la variation efficace du facteur d'intensité de contraintes qui contribue à l'endommagement par fatigue (K_{min}-K_{cl}).

1.3.6 Modèles de propagation de fissure

Le diagramme da/dN - ΔK, tel que présenté à la Figure 1.20, est un outil précieux en mécanique de la rupture. Il met en relation le facteur d'intensité de contrainte, en abscisse et l'avancement de la fissure par cycle en ordonné. La norme ASTM E647-13a présente la méthode pour obtenir cette courbe (*Standard Test Method for Measurement of Fatigue Crack Growth Rates*, 2015), la norme ISO12108 présente également une méthode similaire à quelques exceptions près (ISO 12108, 2002). De nombreux modèles empiriques sont dérivés du diagramme da/dN - ΔK afin de prédire la durée de vie en fatigue d'un composant étant donné les défauts observables. Certains de ces modèles seront présentés dans cette section, plus spécifiquement ceux pour un chargement cyclique a amplitude de force constante.

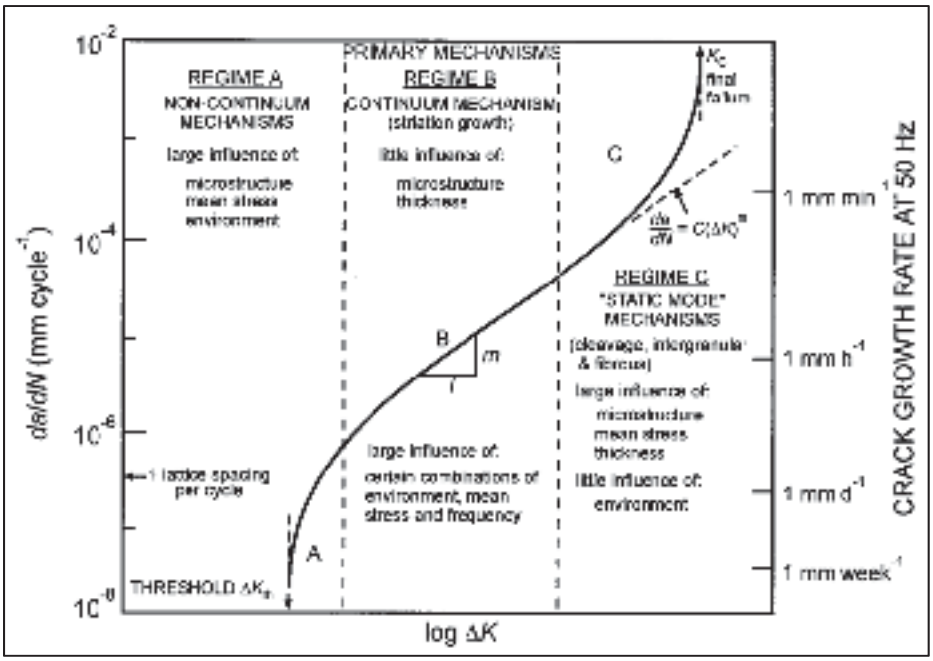

Figure 1.20 Exemple de diagramme da/dN - ΔK
Tirée de (Krupp, 2007)

Trois régimes distincts sont identifiés dans le diagramme da/dN - ΔK; pour le premier, la propagation de la fissure est très lente et plus difficilement prévisible. Il y a toutefois un paramètre d'importance, soit le facteur d'intensité de contrainte seuil ΔK_{th}. Lorsque la variation du facteur d'intensité de contrainte est en deçà de cette valeur, on considère que la fissure « longue » ne dispose pas de la force motrice suffisante pour avancer. En ce sens, le facteur d'intensité de contrainte seuil est en quelque sorte analogue à la limite d'endurance employée dans l'approche de conception « Stress-life ».

Dans la seconde région, la propagation de fissure est stable et prévisible, elle se caractérise par une droite sur le diagramme da/dN - ΔK. Finalement, la troisième région du diagramme da/dN - ΔK se désigne comme la région de propagation instable. Le paramètre important pour cette région est la valeur de ténacité K_c puisque lorsque cette intensité de contrainte est atteinte, la fissure se propage catastrophiquement et il y a rupture brutale du composant. La valeur de K_c est fortement liée à la ténacité en état plan de déformation K_{IC}. La valeur K_{IC} est une

propriété du matériau qui peut être évalué à l'aide de la norme ASTM E399-12 (*Standard Test Method for Linear-Elastic Plane-Strain Fracture Toughness of Metallic Materials*, 2012). Dans le cas de K_c, la valeur est différente étant donné qu'elle dépend de la géométrie de l'échantillon.

Modèle de Paris : La seconde région du diagramme da/dN - ΔK est particulièrement intéressante puisqu'on peut appliquer le modèle de Paris afin de prédire la vitesse de propagation de la fissure (Paris, 1961). Ce modèle, qui présente l'avantage d'être le plus simple qui puisse être employé en mécanique de la rupture, est basé sur l'équation 1.5.

$$\frac{da}{dN} = C\Delta K^m \tag{1.5}$$

Pour cette équation, $\frac{da}{dN}$ représente le taux d'avancement de la fissure en mm/cycle, C est une constante du matériau, ΔK est la variation du facteur d'intensité de contrainte et m est une constante du matériau. La relation de Paris à quelques applications intéressantes; par exemple, on peut estimer le nombre de cycles requis pour propager un défaut d'une taille initiale connue à une taille finale donnée en intégrant l'équation 1.5 afin d'obtenir l'équation 1.6.

$$N_f = \frac{a_f^{1-\frac{m}{2}} - a_i^{1-\frac{m}{2}}}{C * \left(Y * \Delta\sigma * \sqrt{\pi a}\right)^m * \left(1 - \frac{m}{2}\right)} \quad avec\ m \neq 2 \tag{1.6}$$

Ici, N_f est le nombre de cycles requis pour propager la fissure de la taille initiale (a_o) à la taille finale (a_f), C est une constante du matériau, $\Delta\sigma$ est la contrainte alternée appliquée et Y le facteur de forme pour la fissure considérée. Le paramètre Y est un paramètre qui varie en fonction de la géométrie de la fissure et de la pièce ainsi qu'en fonction du type de chargement auquel elle est soumise. Bien que la résolution de cette équation semble simple, il faut préciser que la valeur du facteur de forme Y varie en fonction de l'avancement de la fissure et des

méthodes numériques sont généralement requises pour évaluer le nombre de cycles à la rupture avec une meilleure précision. Également, comme la relation de Paris possède plusieurs limitations, d'autres modèles sont généralement employés afin de tenir compte de l'effet du rapport de contrainte R, de la fermeture de fissure ou encore des régions de la courbe da/dN – ΔK ou la relation de Paris ne s'applique pas. Certains de ces modèles sont présentés ici.

Modèle de Forman : Le modèle qui vient tout juste d'être présenté est basé sur l'équation de Paris. Il est assez simple, toutefois, il ne permet pas de prendre en compte l'effet de la contrainte moyenne, qui est déterminant pour la vie en fatigue. Forman a donc proposé une généralisation permettant de prédire le comportement d'une fissure pour diverses contraintes moyennes, en employant le ratio de contrainte R comme paramètre (Forman, Kearney et Engle, 1967), tel que le montre l'équation 1.7.

$$\frac{da}{dN} = \frac{C_2(\Delta K)^{m2}}{(1-R)(K_c - K_{max})} \tag{1.7}$$

Dans son modèle, Forman emploie les constantes C_2 et m_2 qui sont des constantes du matériau que l'on peut déterminer, comme C et m, à partir d'une courbe de Paris. La valeur de ténacité du matériau K_c est également employée, il faut savoir que cette valeur est variable selon l'épaisseur du matériau. Enfin en la comparant à K_{max}, le modèle est alors sensible à la troisième section de la courbe de Paris puisque, lorsque K_{max} tend vers K_c, une propagation catastrophique est prédite

Modèle de Elber : Une méthode simple a été proposée par Elber (Elber, 1971) afin de tenir en compte la fermeture de fissure induite par la plasticité. Il s'agit essentiellement d'une modification à apporter à la loi de Paris, alors qu'on remplace la variation du facteur d'intensité de contrainte ΔK par sa valeur effective ΔK_{eff} tel qu'indiqué à l'équation 1.8.

$$\frac{da}{dN} = C\Delta K_{eff}{}^{m} \tag{1.8}$$

Elber définit également un paramètre U qui est un rapport entre le la variation du facteur d'intensité de contrainte efficace ΔK_{eff} et la variation du facteur d'intensité de contrainte nominal ΔK, tel que montré par l'équation 1.9.

$$U = \frac{\Delta K_{eff}}{\Delta K} \tag{1.9}$$

Le paramètre U est fortement influencé par la longueur de fissure. Dans les régimes de fissure microstructurellement et mécaniquement courtes, les mécanismes de fermeture de fissure ne sont pas observables. Lorsque la fissure se propage, la valeur de U évolue et se stabilise dans le régime de fissures longues et à ce stade, elle est principalement influencée par la valeur du rapport de contrainte R. Tel que présenté, le terme U est le résultat de mesures expérimentales, il existe toutefois des modèles permettant de prédire ce facteur, tel que celui proposé par Newman (Newman, 1984). À défaut de décrire ce modèle, il est important de mentionner que la relation entre U et R est fortement dépendante d'un matériau à l'autre. De plus, la valeur de K_{max} joue également un rôle important dans la relation entre les variations efficaces et nominales du facteur d'intensité de contrainte puisque la taille de la zone plastique monotone en fond de fissure est tributaire de la valeur K_{max} (équation 1.2 et 1.3).

Modèle NASGRO Forman et Meettu : Un autre modèle intéressant a été développé à la NASA par Forman et Meettu, il s'agit du modèle NASGRO (Forman et al., 2000). Ce modèle semi-empirique permet, à l'aide d'une seule équation, de représenter le comportement dans les trois régions de la courbe de Paris. De plus, ce modèle introduit le paramètre R qui permet de prendre en compte la contrainte moyenne, ainsi qu'un paramètre f qui permet de considérer l'impact de la fermeture de fissure d'après le modèle de Newman (Newman, 1984) . L'équation 1.10 est celle proposée par Forman et Meettu (Forman et al., 2000).

$$\frac{da}{dN} = C\left[\frac{1-f}{1-R}\Delta K\right]^m \frac{1-(\Delta K_{th}/\Delta K)^p}{1-(K_{max}-K_c)^q} \tag{1.10}$$

Le modèle de Forman et Meetu fait intervenir un grand nombre de paramètres de matériaux, soient, $C, m, p, q, \Delta K_{th}\ et\ K_c$, ce qui le rend relativement complexe. Le paramètre f est un paramètre qui permet de considérer la charge d'ouverture de la fissure et ainsi considérer les mécanismes de fermeture de fissure dans la prédiction du taux de propagation de fissure.

1.3.7 Approche de Kitagawa-Takahashi

Le diagramme de Kitagawa-Takahashi est un outil intéressant qui permet de définir une région sécuritaire pour la mise en service de composants comprenant des défauts. Pour construire ce diagramme, la limite de fatigue du matériau obtenue par une approche « Stress-Life » peut être employée, ainsi que le seuil de propagation de fissure obtenue par l'approche de la mécanique de la rupture. Il s'agit en quelque sorte d'une approche combinée qui permet d'obtenir le diagramme montré à la Figure 1.21. Le diagramme met en relation la taille de défaut qui peut être toléré et la contrainte alternée qui peut être appliquée à un matériau pour demeurer en condition de fissure non propageante.

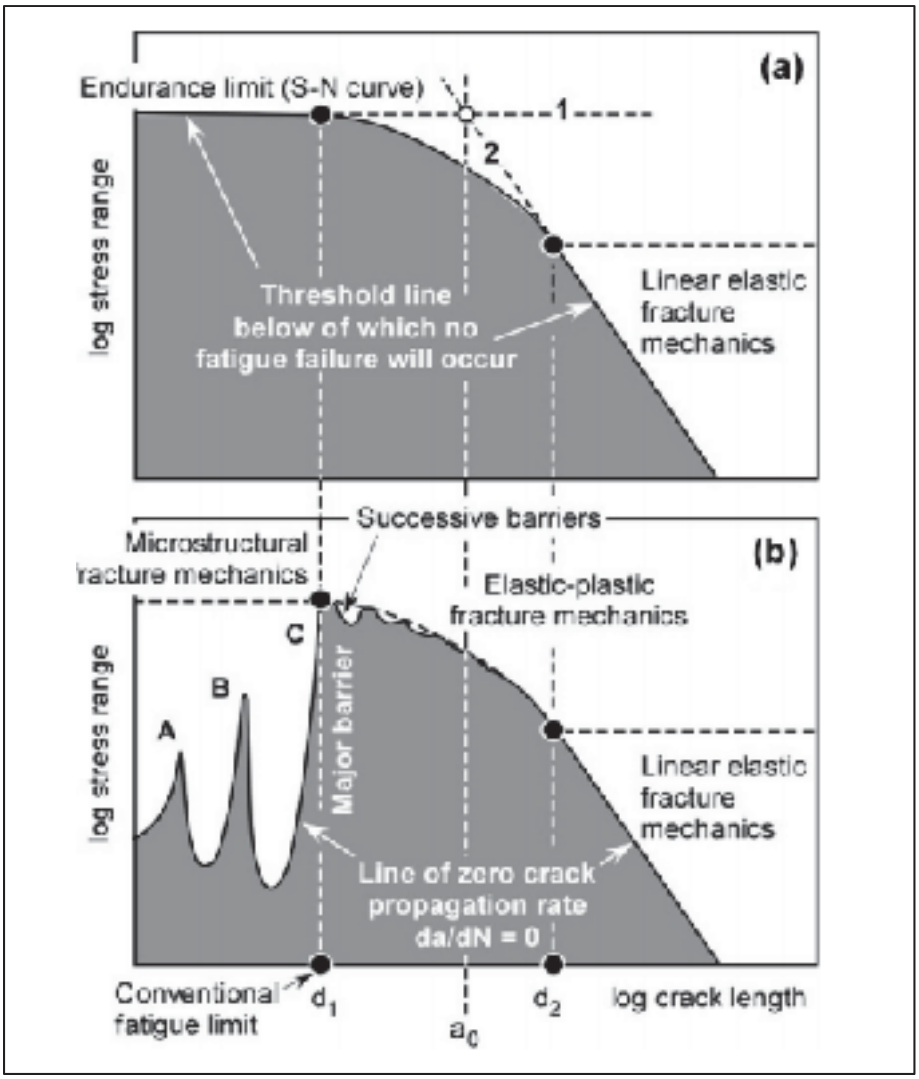

Figure 1.21 Représentation du diagramme de Kitagawa-Takahashi à
Tirée de (Zerbst et al., 2016)

Il est cependant important de mentionner que le diagramme de Kitagawa-Takahashi, dans la formulation initiale, repose sur les hypothèses de la mécanique de la rupture linéaire élastique. En ce sens, la formulation originale emploie donc le seuil de propagation de fissure longue. Toutefois, le diagramme à la Figure 1.21 montre très bien qu'il couvre plusieurs ordres de grandeur en termes de taille de fissure, allant ainsi en deçà de ce qu'il convient de traiter au moyen de relations basées sur le comportement des fissures longues. Le comportement réel

des fissures courtes se distingue et le diagramme de la Figure 1.21 b) l'illustre bien. Pour la région de fissures dont la taille est inférieure à la barrière microstructurale, il est possible qu'une fissure soit initiée sous de très faibles chargements (région identifiée comme région de mécanique de la rupture microstructurale à la Figure 1.21). En de telles circonstances, le comportement de la fissure est fortement lié à son interaction avec les éléments microstructuraux, tels que les joints de grains, qui peuvent freiner la propagation. Ensuite, pour les fissures dites mécaniquement courtes (région de mécanique de la rupture élastoplastique), les mécanismes de fermeture dont il a été question à la section 1.3.5 ne sont pas observables. Ceci contribue également à conférer aux fissures de cet ordre de grandeur un comportement distinct de celui des fissures longues caractérisées au moyen de la LEFM.

Néanmoins, d'autres approches dérivées de ce diagramme permettent d'étendre son application malgré l'emploi de métriques relevant de la LEFM tels que le facteur d'intensité de contrainte seuil ΔK_{th}. C'est notamment le cas de l'approche proposée par El-Haddad, qui évalue une taille de défaut intrinsèque à partir de l'équation 1.11 afin de mieux représenter la région de fissures courtes. La contrainte alternée qui peut être admissible en fonction de la taille de défaut (a) est ensuite donnée par l'équation 1.12.

$$a_0 = \frac{1}{\pi} * \left(\frac{\Delta K_{th}}{Y * \Delta \sigma_{f,0}} \right)^2 \tag{1.11}$$

$$\Delta \sigma_f = \frac{\Delta K_{th}}{Y * \sqrt{\pi (a + a_0)}} \tag{1.12}$$

En outre, le diagramme peut également être construit en utilisant le seuil de propagation de fissure effectif (ΔK_{eff}), qui correspond à un seuil défini en absence de mécanismes de retardation de fissure tel que la fermeture.

1.4 Discussion

L'état des connaissances portant sur la fatigue des alliages obtenus par LPBF permet de montrer que l'approche de fabrication couche par couche leur confèrent des caractéristiques et défauts qui soulèvent des questions relativement à leur capacité à résister à des chargements cycliques. Tel que discuté préalablement, en considérant ces caractéristiques, l'approche de mécanique de la rupture reposant sur la courbe da/dN – ΔK apparait intéressant pour relier le comportement en fatigue des matériaux obtenus par LPBF à leur défaut de fabrication. Bien que ces courbes soient disponibles pour l'alliage de titane Ti6Al4V ou les alliages aluminium-silicium-magnésium, les données pour certains superalliages tels que l'Inconel 625 sont très peu abondantes ou complètement absentes de la littérature.

En ce sens, il existe un besoin de caractériser le comportement en propagation de fissure d'autres alliages que le titane et l'aluminium. De surcroit, il importe de caractériser les défauts de fabrication induits par le procédé de LPBF et corréler leur impact le comportement en fatigue pour d'autres alliages. De plus, il serait important de vérifier la possibilité d'employer les outils de mécanique de la rupture pour permettre la tolérance aux dommages sur des échantillons comprenant un niveau de défaut variable. En outre, il est important de valider l'impact des défauts typiques du procédé sur la phase de propagation de fissure. Pour l'instant, les données portant sur la propagation de fissure dans les matériaux obtenus par LPBF se concentrent sur deux orientations de fissures sans considérer le niveau de défauts comme une variable, or il serait souhaitable de savoir quelles sont les limites à travers desquelles il est possible d'employer la mécanique de la rupture linéaire élastique pour faire une prédiction de la vie en fatigue.

1.5 Problématique de recherche

Le survol des caractéristiques des alliages obtenus par LPBF a permis de montrer que, moyennant un choix judicieux de post-traitements, certaines propriétés mécaniques statiques sont comparables à celles observées pour des procédés de fabrication traditionnels. Également,

il est possible de réduire significativement la présence de défauts moyennant l'emploi de paramètres laser optimaux. Un post-traitement de HIP permet également de réduire significativement la quantité et les dimensions des pores. Toutefois, certains défauts tels que des inclusions, des porosités résiduelles ou encore l'anisotropie ne peuvent être complètement corrigés et ils influencent le comportement en fatigue. En ce sens, il semble acquis que le développement de composants assujettis à des chargements cycliques et fabriqués par LPBF passe inévitablement par une approche de tolérance aux dommages et aux inhomogénéités associés au procédé. Il est également essentiel de comprendre l'importance de l'anisotropie dans un tel contexte. Il existe un manque d'information dans la littérature afin de mettre en relation les défauts induits par le procédé LPBF et le comportement en fatigue, comme requiert l'approche de conception basée sur la tolérance aux dommages. Pour certains alliages, comme l'Inconel 625, ces données sont tout simplement absentes de la littérature, malgré un certain nombre d'études portant sur les caractéristiques microstructurales. De surcroit, cet alliage est largement employé en aérospatiale pour la fabrication de composants de turbine à gaz et il possède de nombreuses caractéristiques prometteuses pour l'application d'une telle approche, par exemple, une ductilité élevée.

1.6 Objectifs de recherche

L'objectif principal du projet de recherche consiste à évaluer l'influence des défauts induits par le procédé LPBF sur le comportement en fatigue des composants fabriqués en se concentrant sur le comportement des fissures longues. En ce sens, le présent projet vise à valider la possibilité d'employer cette approche pour guider la tolérance aux dommages lors de la mise en service de composants obtenus par fabrication additive. Il est donc nécessaire de s'intéresser aux défauts de fabrication inhérents à la mise en forme par LPBF et évaluer leur impact sur le comportement du matériau. Pour ce faire, trois objectifs spécifiques ont été identifiés :

1. Évaluer l'influence de l'anisotropie sur le comportement en propagation de fissures au sein d'un alliage obtenu par LPBF et le comparer à celui d'un alliage obtenu par un procédé traditionnel.

2. Développer une méthode pour générer différents niveaux de défauts typiques au procédé LPBF et évaluer leur impact sur le comportement en propagation de fissures.

3. Évaluer expérimentalement la vie en fatigue par une approche « Stress-Life » et valider la possibilité de prédire la limite de fatigue d'échantillons contenant des défauts induits intentionnellement à partir de l'approche de Kitagawa-Takahashi.

CHAPITRE 2

LONG FATIGUE CRACK PROPAGATION BEHAVIOR OF INCONEL 625 PROCESSED BY LASER POWDER BED FUSION: INFLUENCE OF BUILD ORIENTATION AND POST PROCESSING CONDITIONS

J-R. Poulin[1], V. Brailovski[1,*], P. Terriault[1]

[1]Department of Mechanical Engineering, École de technologie supérieure,

*Corresponding author: Vladimir Brailovski, Department of Mechanical Engineering, École de technologie supérieure, 1100 Notre-Dame Street West, Montreal, Quebec, Canada, H3C 1K3 (vladimir.brailovksi@etsmtl.ca, tel: 514-396-8594)

Article publié dans la revue « International Journal of Fatigue », vol. 116. pp. 634-647, 2018.

2.1 Avant-Propos

En premier lieu, dans le cadre de ce projet, il est nécessaire d'évaluer le comportement en propagation de fissure d'un alliage obtenu par LPBF. Il est particulièrement important de considérer l'impact de l'anisotropie résultant de sa mise en forme sur le comportement des fissures de fatigue longues. Pour ce faire, l'alliage d'Inconel 625 a été retenu puisqu'il n'existe pas de données relatives à son comportement en propagation de fissure de cet alliage obtenu par LPBF. Dans cet article, sa résistance à la propagation de fissure est caractérisée en considérant 4 différentes configurations (orientation de fabrication et orientation de propagation de la fissure). En addition, la résistance à la propagation de fissures de fatigue longue est comparée à celui d'un alliage corroyé de même composition.

2.2 Résumé

Dans l'article présenté à ce chapitre, la résistance à la propagation de fissure de fatigue de l'alliage d'Inconel 625 obtenu par fabrication additive est évaluée et comparée à celle d'un alliage corroyé de même composition (R = 0.1, f = 20 Hz). Les défauts de fabrication induits

par le procédé de LPBF sont également évalués, ainsi que les propriétés mécaniques statiques, qui sont mesurées au moyen d'essais de tractions monotones. Quatre configurations sont considérées pour évaluer la propagation de fissure, ainsi que deux traitements thermiques. La moitié des échantillons sont caractérisés suivant un traitement thermique de relaxation de contraintes alors que l'autre moitié est en plus soumise à un traitement thermique sous pression isostatique. L'impact de l'orientation de fabrication et du post-traitment thermique sont discutés et dans l'ensemble, la résistance à la propagation de fissures de fatigues dites ''longues'' s'avère être équivalente à celle de l'alliage corroyé.

2.3 Abstract

In this paper, the room temperature fatigue crack propagation behavior of Inconel 625 alloy processed by laser powder bed fusion was studied and compared to that of a wrought alloy of the same composition. First, the processing-induced defects distribution and the build orientation-dependent tensile properties of the laser powder bed-processed specimens were analysed. Next, crack propagation testing specimens were manufactured with four build orientations, some were subjected to stress relief annealing, while the others were subjected to stress relief annealing followed by hot isostatic pressing. The impact of the build orientation and the post-processing conditions on the long fatigue crack propagation behavior at low R ratio (R=0.1) was evaluated. The resistance to crack propagation of the laser powder bed-processed IN625 specimens was found to be similar to that of a wrought alloy.

Keywords: Additive manufacturing, Laser powder bed fusion, Selective laser melting, Nickel-based superalloy, Fatigue crack propagation, Damage tolerance

2.4 Introduction

Additive manufacturing (AM) technologies are gaining a lot of interest in the aerospace industry due to their potential benefits, such as the possibility of tooling-free (Gao et al., 2015) near net shape manufacturing of complex components (DebRoy et al., 2018; Herzog et al.,

2016). AM metal technologies usually employ feedstocks in the form of pre-alloyed powders, and their specificity lies in the way the energy is delivered to powdered material. In the laser powder bed fusion AM technology (LPBF), a thin layer of powder is spread on a platform and a laser beam selectively fuses powder particles to form one layer of the component at a time, in conformity with a 3D model of the component.

The LPBF technology is a promising AM process (Herzog et al., 2016; Murr et al., 2012), since it provides mechanical properties similar to those of the conventional processes (DebRoy et al., 2018; Herzog et al., 2016), a surface roughness (R_a) ranging from 7 to 20 μm (DebRoy et al., 2018), and a dimensional accuracy, from 40 to 200 μm (Herzog et al., 2016; Wong et Hernandez, 2012). A wide range of metallic materials, such as stainless steel, aluminium, titanium, and nickel-based alloys, have been successfully manufactured using LPBF, and their mechanical properties, microstructure, and processing-induced defects (spherical pores, crack-like elongated voids and inclusions) have been widely documented (Mazur et al., 2015; Sallica-Leva, Jardini et Fogagnolo, 2013; Tammas-Williams et al., 2016a; Tang et Pistorius, 2017; Wan et al., 2016; Zhai, Galarraga et Lados, 2016; Ziółkowski et al., 2014). Laser exposure parameters, such as laser power, scanning speed and hatching distance, have been proven to play a determinant role in the development of processing-induced defects (Gong et al., 2014; Kasperovich et al., 2016; Li et al., 2017). When optimal laser exposure parameters were used, relative densities close to 99.9% were obtained in the LPBF-processed components (Kasperovich et al., 2016), thus resulting in the mechanical properties close to those of the conventionally-processed materials of the same composition.

Due to a repeated melting and re-melting of the material caused by laser heating, the microstructure resulting from the LPBF process bears a complex thermal history (Gusarov et al., 2009; Li et Gu, 2014). During LPBF, thermal energy is diffused directionally from a rapidly moving laser spot towards the build plate, and this localized melting is responsible for very high cooling rates (up to $\approx 10^6$ °C/s (Li et Gu, 2014)) and, therefore, for a nonequilibrium solidification of the material (Rafi et al., 2013). The high temperature gradients are also

responsible for significant levels of residual stresses. Elongated grains are generally formed along the build direction (normal to the build plane), which causes the resulting microstructure and mechanical properties to be strongly build orientation-dependent (Criales et al., 2017; Li et al., 2017; Li et al., 2015). The surface finish of LPBF components is also build orientation-dependent: the layer-by-layer approach produces a stair-like arrangement on the inclined surfaces and the appearance of partially bonded particles, especially on downward facing surfaces (Strano et al., 2013). Several post-LPBF treatments have been shown to improve the bulk properties of LPBF components. An adequate selection of these treatments can get the mechanical properties of a given alloy to match those of its conventionally manufactured equivalent (Kreitcberg, Brailovski et Turenne, 2017a). Stress relief (SR) annealing represents an effective method to ensure dimensional stability of LPBF components by diminishing the level of residual stresses (Shiomi et al., 2004), even though it is unable to reduce the anisotropy of the microstructure. A more complex treatment, hot isostatic pressing (HIP), has been shown to be more effective for this purpose (Kreitcberg, Brailovski et Turenne, 2017a). It has also been demonstrated that a simultaneous application of elevated temperatures and pressures during HIP can assist in decreasing the level of processing-induced porosity (Tammas-Williams et al., 2016a).

Since many engineering component are used in applications in which cyclic loading prevails, the fatigue behavior of LPBF-built components is of a particular concern (Gao et al., 2015; Yadollahi et Shamsaei, 2017). So far, the studies supporting the suitability of LPBF components for fatigue resistant applications are relatively scarce, and the few that exist focus mainly on lightweight alloys. For titanium alloys, which are the most extensively studied, the post-processing treatments have been shown to play a significant role in improving the fatigue life of LPBF components (Li et al., 2016), with surface post-processing being the most determinant factor, followed by bulk post-processing (heat and HIP treatments).

Examinations of the fatigue fracture surfaces of LPBF components reveal that crack initiation typically occurs in the vicinity of surface and subsurface processing-induced defects (Akita et al., 2016; Edwards et Ramulu, 2014; Günther et al., 2017; Kasperovich et Hausmann, 2015; Liu et al., 2014; Siddique, Imran et Walther, 2017; Wycisk et al., 2013; Wycisk et al., 2014; Yadollahi et al., 2017). The existence of such defects and their obvious impact on the fatigue life suggest that a damage-tolerant approach should be used, when commissioning LPBF components for critical applications.

Even though the literature on crack propagation in AM-built components is still limited, aluminium alloys 7075 and AlSi12Mg, 316L stainless steel, Inconel 718 and, more extensively, Ti6Al4V alloys, have already been studied. For the aluminium alloys, the resistance of LPBF components to fatigue crack growth was found to be inferior to that of conventionally built specimens, and also to be highly sensitive to build orientation and post-processing conditions (Reschetnik et al., 2016; Siddique, Imran et Walther, 2017). In the case of Ti6Al4V alloy, the as-built LPBF components showed relatively poor mechanical performances (Leuders et al., 2013) due to a microstructure predominantly composed of α phase (Rafi et al., 2013; Vrancken et al., 2012), whereas the properties of stress-relieved and HIP-ed LPBF Ti6Al4V components were found similar to those of their conventionally-manufactured counterparts (Leuders et al., 2013). In the case of 316L stainless steel, as-built and stress-relieved components showed similar crack propagation behavior (Riemer et al., 2014). For this alloy, only HIP treatment appeared to have a positive influence on crack propagation behavior, especially at the extremities of the Paris diagram (low and high stress intensity factors, SIFs) (Riemer et al., 2014).

As far as the nickel-based superalloys are concerned, the crack propagation behavior of as-built LPBF Inconel 718 components was found to be similar to that of their wrought counterparts in the case of intermediate SIFs, whereas in the near threshold region, a lower boron content, a finer microstructure and a higher level of residual stresses all led to a lower resistance of LPBF Inconel 718 components to crack propagation (Konečná et al., 2016).

The case of LPBF Inconel 625 (IN625) is especially compelling, given its extensive use in aircraft engine components. Publications dealing with the LPBF processing of this alloy offer guidelines for manufacturing IN625 parts with an extremely low level of processing-induced porosity (Caiazzo et al., 2017; Criales et al., 2017; Li et al., 2015). The effects of different post-treatments on the microstructure and static mechanical properties of this alloy are also well documented (Kreitcberg, Brailovski et Turenne, 2017a; 2017b; Li et al., 2017). According to these papers, IN625 can be produced with almost 100% density, and manifests a good ductility and a high isotropy of mechanical properties, following a stress relief post-treatment and a subsequent heat treatment promoting grain growth (Kreitcberg, Brailovski et Turenne, 2017a; Li et al., 2017). All these suggest that LPBF IN625 alloy components might be excellent candidates for aircraft engine applications, but, to the best of the authors' knowledge, information on the fatigue resistance of this alloy is still very limited. To start filling this gap, the present work focuses on the fatigue crack propagation behavior of LPBF IN625 alloy as a function of build orientation and post-processing conditions. Although this alloy is generally reserved for service at elevated temperatures, the current study is limited to ambient temperature testing conditions, in order to establish a starting point for further investigations.

2.5 Materials and Methods

2.5.1 Specimens manufacturing and post-processing

All the specimens used in this study were manufactured under argon protective atmosphere using an EOSINT M 280 system equipped with a 400W Yttrium laser. An EOS IN625 powder, whose composition corresponds to the UNS N06625 specifications (weight %: ≥58%Ni, 20-23%Cr, 8-10%Mo, 3.15-4.15%Nb, ≤5%Fe, ≤0.40%Ti, ≤0.40%Al, ≤ 1%Co, ≤0.10%C, ≤0.05%Ta, ≤0.50%Si, ≤0.50%Mn, ≤0.15%P. ≤0.15%S), was used. Since processing optimization was not within the scope of this work, the EOS IN625 Performance Parameters Set (laser power ~300 W, scanning speed ~1000 mm/s, hatching space ~0.1 mm, layer thickness 40 μm) was employed.

To measure the monotonic and fatigue crack propagation properties, specimens for tensile testing and crack propagation testing were manufactured with different build orientations (Figure 2.1 a to c). After printing, according to the powder manufacturer's recommendations, stress relief (SR) annealing was performed on the build plate with specimens (870 ºC for 1h, under argon atmosphere). Next, the specimens were cut off the build plate and machined to their final dimensions. Half of the specimens were tested in this state (SR), while the other half were additionally subjected to HIP, according to the procedure proposed in (Kreitcberg, Brailovski et Turenne, 2017a): 1120 ºC and 100 MPa for 4 hours, under argon atmosphere.

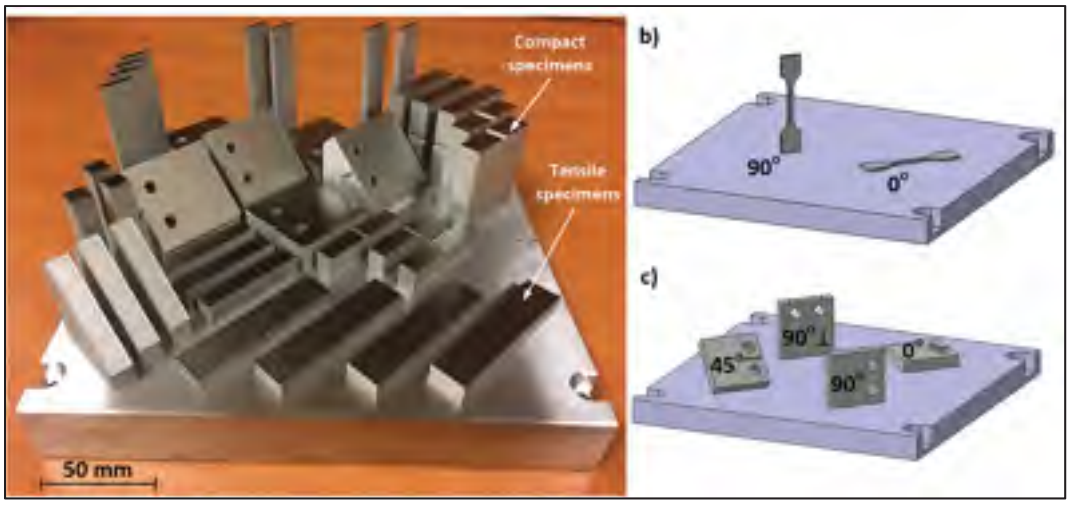

Figure 2.1 a) Photo of one of the build plates with specimens before their machining; schematic representation of each set of specimens with different build orientations: b) tensile specimens, and c) crack propagation specimens

First, sixteen 85 x 18 x 4 (mm) rectangular coupons were manufactured with 0º and 90º orientations relatively to the build plane and then machined to obtain the tensile specimens shown in Figure 2.1b. For each orientation, eight tensile specimens with a gauge cross-section of 2 x 4 mm^2 and a gauge length of 27 mm were manufactured.

Fatigue crack propagations specimens were manufactured with four different configurations shown in Figure 2.1c. The compact crack propagation specimens were manufactured according to ASTM E647-13a standard, with a characteristic length (W) of 38 mm and a thickness (b) of 9.5 mm. All external surfaces of the specimens were manufactured with 1 to 1.5 mm of machining allowances, which were removed by milling, except for the starter notch which was formed by electrical discharge machining. For one of the configurations ($90^{o}\perp$), three additional specimens were produced and kept as-built (unmachined) in order to compare the effect of machining on the fatigue crack initiation and propagation behavior. In all cases, to help with the visual observations of cracks, the side surfaces were polished with silicon carbide paper up to grit 1200 before each test. Three crack propagation specimens were manufactured for each configuration.

From the four crack propagation specimen configurations, three configurations corresponded to build orientations of 0, 45 and 90^{o} and contained starter notches oriented parallel to the build plane (Figure 2.1d). The fourth configuration was obtained in 90^{o} specimens by orienting their starter notches perpendicular to the build orientation ($90^{o}\perp$ specimen in Figure 1d).

As a reference, tensile and crack propagation specimens were also manufactured from a wrought IN625 alloy (VDM Metals); they were machined from a 12.5 mm thick plate with cracks in the T-L (transversal-longitudinal) and L-T (longitudinal-transversal) directions, as referred to in ASTM E647-13a standard

2.5.2 Defect analysis

Computed tomography was used for defect detection: gauge sections of tensile specimens were inspected first, as shown in Figure 2.2. Moreover, 2 x 2 x 10 (mm) samples were cut from the top end of tensile specimens. For these samples, one of the surfaces was in the as-built instead of the machined conditions (see Figure 2.2). The specimens were scanned with a 180 kV transmission X-Ray source providing a resolution of 2.5 µm and a detection threshold of 6 µm.

The scans were performed with a beam energy of 150 kV and a current of 10 μA. A total of 2634 projections were acquired with an exposure time of two seconds. The scans were performed on 6 specimens: two for each manufacturing condition (SR, HIP and wrought). Equivalent diameters of pores were used as metrics of their size; ORS Dragonfly image processing software was used for image processing.

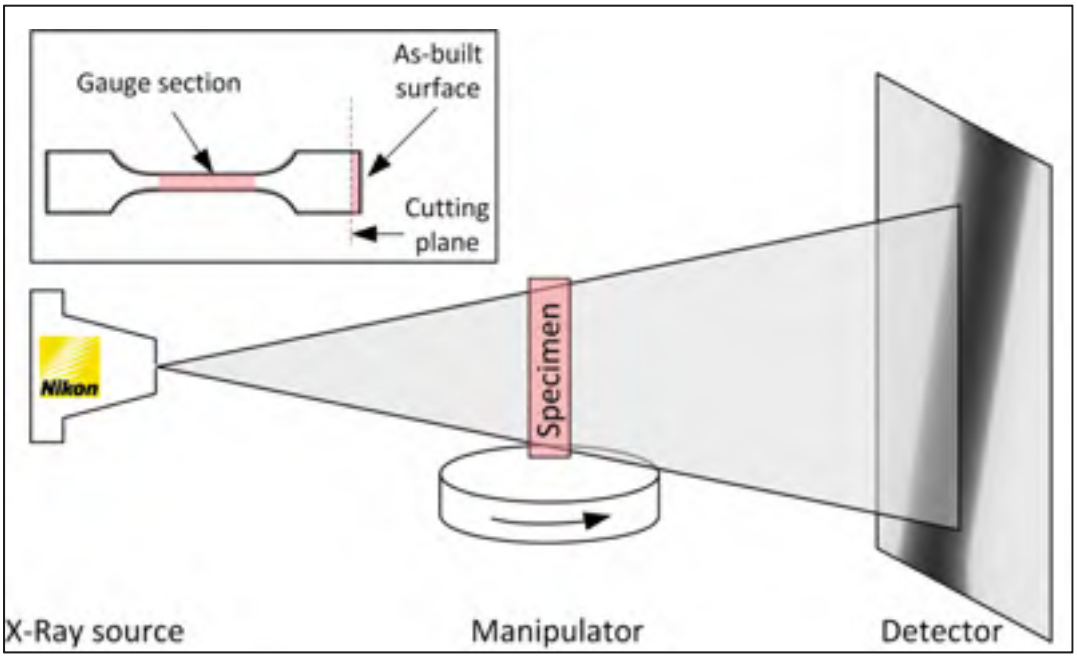

Figure 2.2 Schematic representations of two inspection zones for X-Ray microtomography

2.5.3 Tensile testing

Tensile testing was performed on a 15 kN MTS 810 servo hydraulic tensile machine equipped with an MTS 634.12 mechanical extensometer. The tests were conducted at a constant strain rate of 10^{-3} s^{-1} to specimen failure.

2.5.4 Fatigue crack propagation testing

Stress-controlled fatigue crack propagation testing with a stress ratio of R=0.1 were conducted in accordance with the ASTM E647 standard (*Standard Test Method for Measurement of Fatigue Crack Growth Rates*, 2015), using a 15 kN MTS 810 servo hydraulic tensile machine (see the testing setup in Figure 2.3). In order to build a Paris diagram, the entire testing procedure was divided into three sequential steps:

1. Pre-cracking of the specimens,
2. Stepdown (K-decreasing) procedure (near-threshold region),
3. K-increasing procedure (Paris regime).

Pre-cracking of the specimens was conducted at a frequency of 20 Hz with K_{max} = 12-14 MPa*$m^{1/2}$. Up to 3 million cycles were required to obtain a pre-crack with a length exceeding 1.5 mm on both faces of machined specimens (note that the crack propagation rate for this part of the procedure was not considered when building crack growth diagrams).

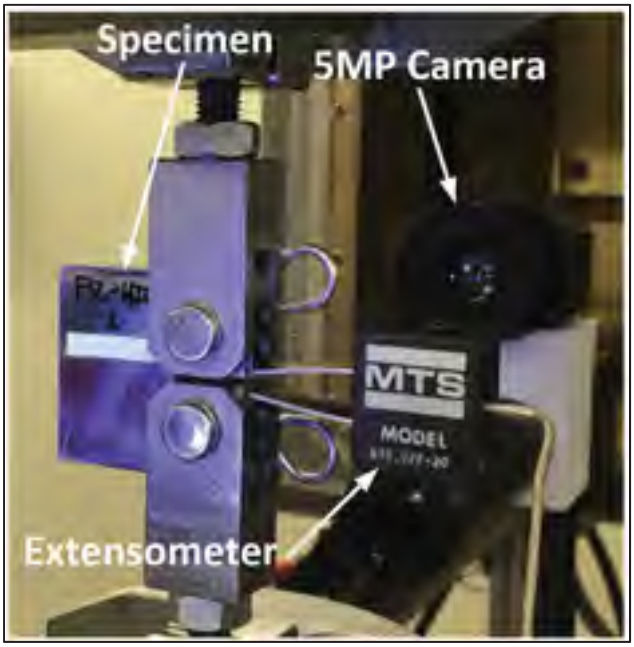

Figure 2.3 Image of the fatigue crack propagation testing setup

As shown in Figure 2.3, the force applied on the specimens was measured using an MTS 662.20D-0415kN load cell, while the crack opening displacement (COD) was measured using an MTS 632.02F clip gauge. Both parameters were recorded at an acquisition rate of 1025 Hz (pre-cracking, stepdown or K-increasing), to allow the compliance (inverse of stiffness)-based measurements of the crack length (Figure 2.4). For these calculations, a special Matlab post-processing routine was developed and calibrated using an ANSYS APDL model of crack propagation (see Annexe 1). For validation purposes, visual data acquisition was also conducted during testing using two external 5 MP cameras (GOM Aramis digital image correlation system), each directed towards one face of the specimen, and the average optically-measured crack lengths were periodically compared to those calculated using the compliance method. The visual crack propagation measurement technique was preliminary calibrated using an Olympus 3D laser microscope at a magnification ratio of 50.

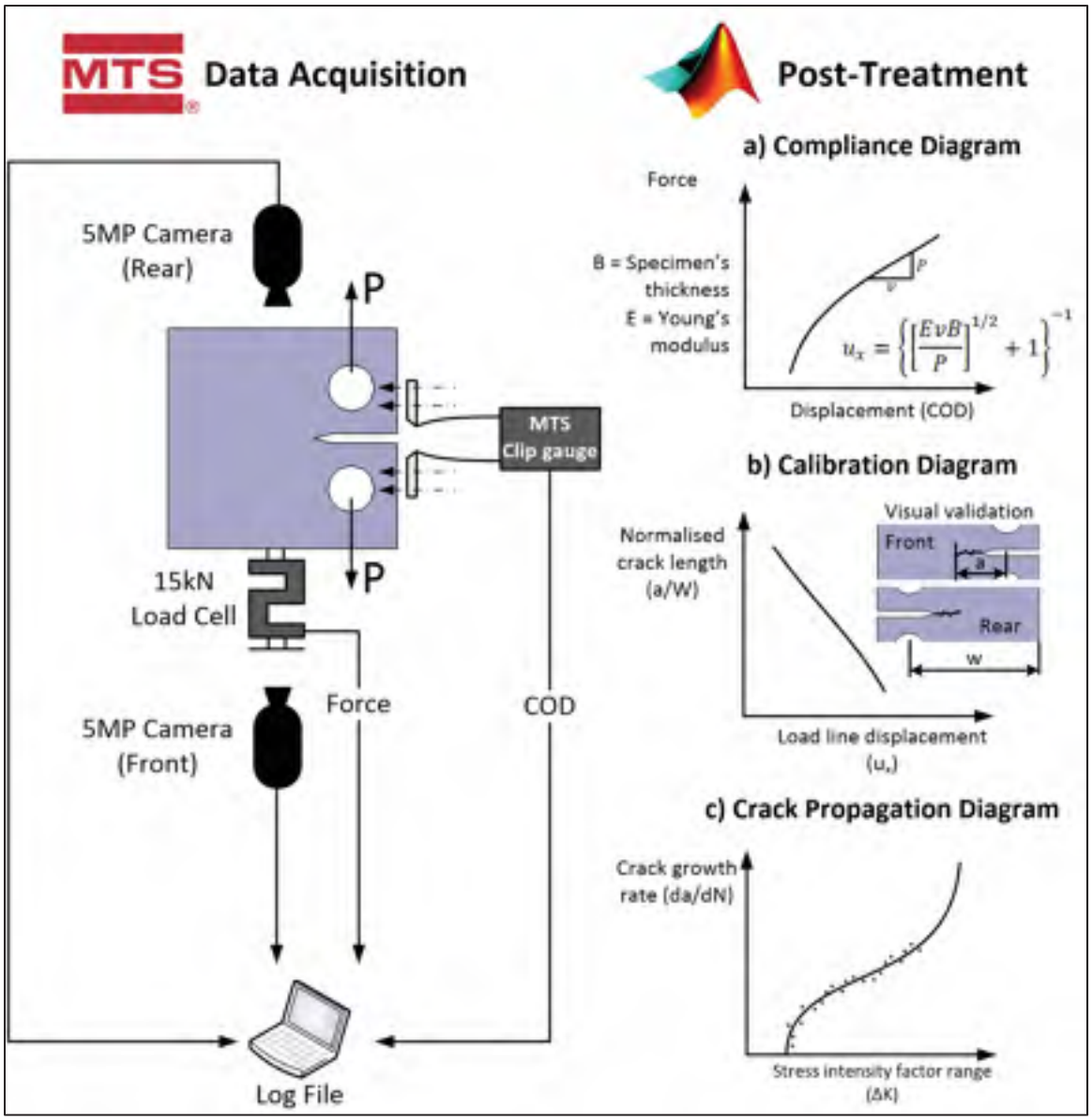

Figure 2.4 Schematic representation of the experimental setup and the post-treatment procedure; a) compliance curve, b) calibration curve, and c) crack propagation curve (Paris diagram)

The threshold SIF (ΔK_{th}) was estimated using the stepdown (K-decreasing) approach in conformity with ISO 12108 and ASTM E647 standards (ISO 12108, 2002; *Standard Test Method for Measurement of Fatigue Crack Growth Rates*, 2015). Following the pre-cracking procedure, each step of the stepdown procedure implied a 10% decrease in the maximum and

minimum forces in a cycle (F_{max} and F_{min}), and testing under these conditions to lengthen the crack for at least 0.5 mm. This procedure was repeated until no such crack growth was obtained within 5 million cycles. This situation corresponds to a crack propagation rate below 10^{-7} mm/cycle, which is in agreement with the ASTM threshold SIF range definition. Prior to testing, the starter notch length a_o was measured optically, and during the procedure, the crack lengthening was evaluated using the compliance-based measurement technique and validated by periodical visual observations (Figure 2.4b). A typical example of the evolution of the crack length during the pre-cracking and the stepdown procedure is shown in Figure 2.5.

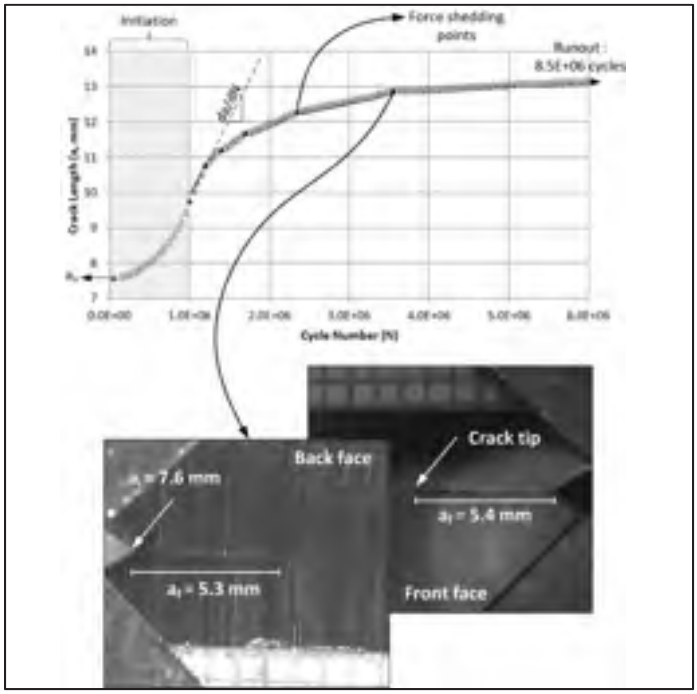

Figure 2.5 Schematization of the stepdown procedure preceded by the crack initiation procedure; results are from a 90°-oriented HIP LPBF specimen

Following the runout of the stepdown procedure, the K-increasing procedure (Paris regime) testing was conducted with the same frequency, using the ASTM E647 standard approach. To ensure an overlap between the data from the K-decreasing and the K-increasing procedures, the forces necessary to re-initiate the tests were calculated for the final crack length of the

stepdown procedure (ΔK=10 to 12 MPa*m$^{1/2}$). The tests were carried out until the compliance of the specimens was high enough to cause saturation of the clip gauge. Typical compliance curves for the K-increasing portion of the tests are shown in Figure 2.6. The above-mentioned compliance-based crack measurements from the K-decreasing and the K-increasing routines were combined to build the ΔK – da/dN crack propagation diagram shown in Figure 2.4c.

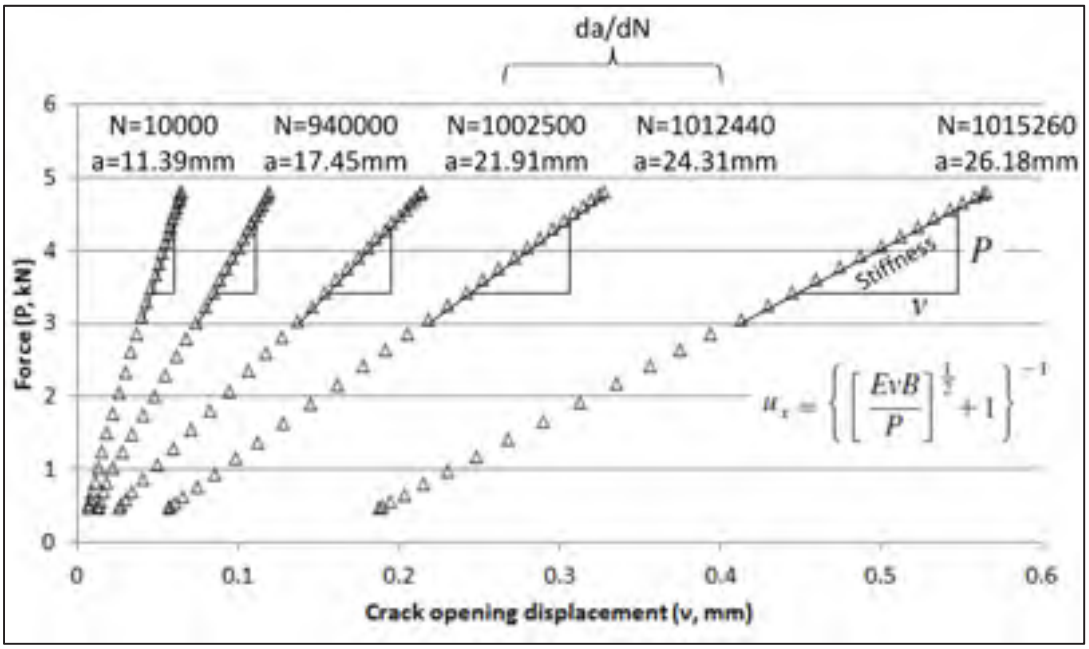

Figure 2.6 Typical stiffness curves (ν-P) obtained for the fatigue crack growth test at SIFs ranges of ≈ 12, 20, 30, 40 and 50 MPa*m$^{1/2}$; results are from a 90^{o}-oriented HIP LPBF specimen

Finally, the contributions to the near-threshold crack propagation measurements from a so-called “crack closure effect” were determined using the compliance offset method described in ASTM E647 standard (*Standard Test Method for Measurement of Fatigue Crack Growth Rates*, 2015). To this end, the unloading part of force-displacement curve was divided into segments corresponding to approximately 10% of the total amplitude, and compliance of each such segment was compared to that of the specimen with a fully open crack. (The fully open crack compliance was established for the upper 25% of the force range.) The force

corresponding to 4% offset in measured compliances was considered to be the onset of crack closure, according to the ASTM E647-13a standard procedure. The effective threshold SIF ($\Delta K_{th.eff}$) was then calculated using the maximum force in a cycle and the closure force at a crack arrest.

It must be emphasised, however, that given the high frequency of the test, the sinusoidal waveform and the low acquisition rate, the samplings obtained did not entirely satisfy the requirements of ASTM E647 standard. In order to obtain more data points, three consecutive unloading cycles were used (we applied this procedure since the propagation rate was very low at this stage of testing). As a result, the compliance offset method provided only a rough assessment of the offset to the threshold SIF caused by crack closure. A typical example of a compliance offset curve is shown in Figure 2.7a, and the corresponding offset of the near-threshold part of the Paris diagram, in Figure 2.7b.

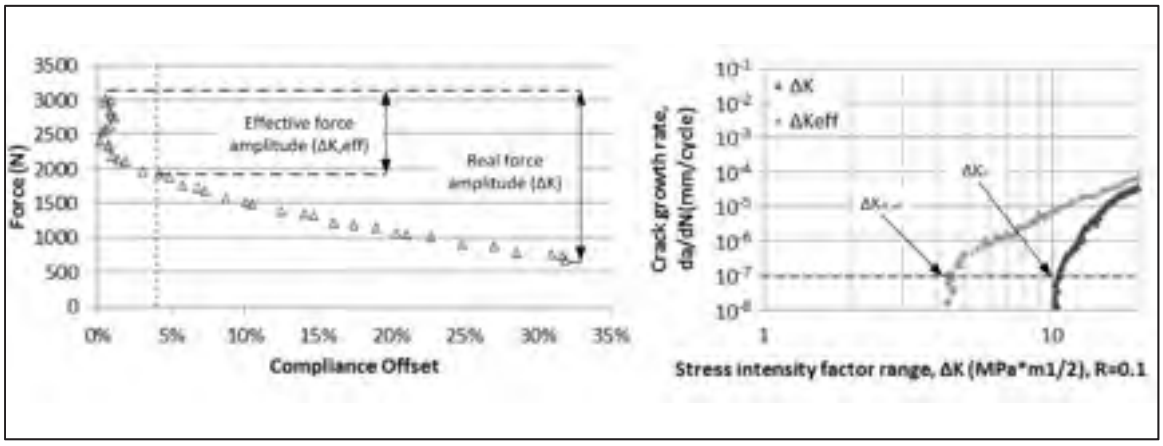

Figure 2.7 a) Compliance offset curve at a threshold for a specimen exhibiting crack closure at ≈1900N, b) Example of Paris curve using effective force amplitude (ΔK_{eff}) compared to real force amplitude (ΔK). Results are from a 90°-oriented HIP LPBF specimen.

To consider the crack closure contribution to the Paris diagram offset (Figure 2.7 b), the dimensionless parameter $U=\Delta K_{th,eff}/\Delta K_{th}$ can be introduced (Zerbst et al., 2016). When no crack closure occurs, U is equal to 1, which is generally the case of a short crack regime. For long cracks, as those studied in this work, the parameter U ranges between 0 and 1, and the smaller the value, the more pronounced the effect of crack closure on the threshold value (closure occurs at a higher decreasing force).

2.6 Results

2.6.1 Defects analysis

The total number of 10 to 50 µm-diameter pores observed in the printed specimens prior to their machining corresponded to 47 for the SR and 24 for the HIP specimens; these pores were present in the vicinity of the as-built surfaces (Figure 2.8). The presence of such subsurface pores resulted from laser contouring was also reported in the literature for Inconel 625 (Koutiri et al., 2018) and Inconel 718 (Seede et al., 2018).

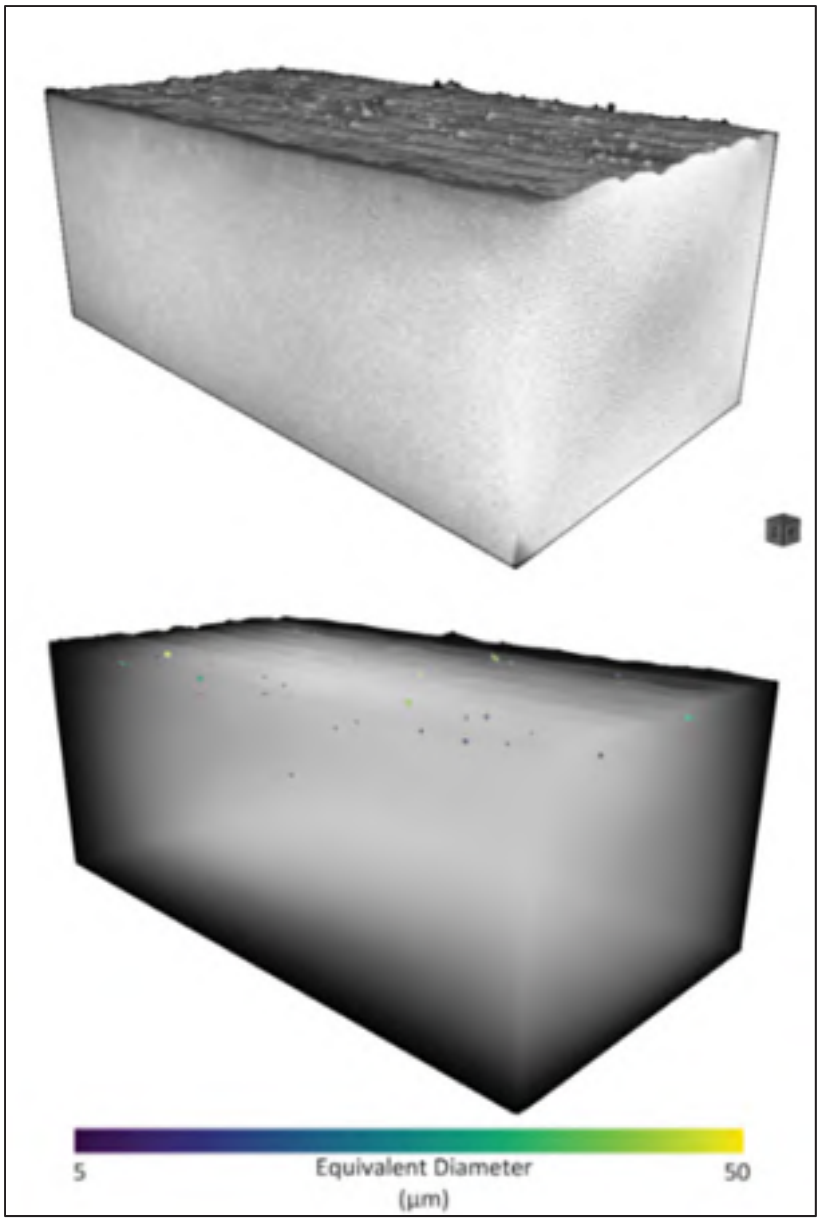

Figure 2.8 Results from the porosity analysis of a sub-section of a 90°-oriented LPBF SR tensile specimen before machining

Next, the obtained quantitative data on the porosity distribution in the SR and HIP LPBF specimens were compared in Figure 2.9: Figure 2.9a illustrates the number of detected pores as a function of their equivalent diameter, Figure 2.9b, the distance of pores from the as-built surface, and Figure 2.9c, the pores sphericity. As shown in Figure 2.9a, the number of pores

detected in the HIP specimens is half of that of the SR specimens, and their average and maximum equivalent diameters are smaller: 20.3 and 33.7 μm as compared to 26.7 and 47.8 μm. It is clear from Figure 2.9b, that those pores are almost exclusively located near the as-built surface. Finally, the aspect ratio of the pores seems to be distributed from 0.5 to 0.9, and pores in the SR specimens tend to be more spherical (Figure 2.9c). After machining, no such pores were detected in the gauge sections of the tensile specimens.

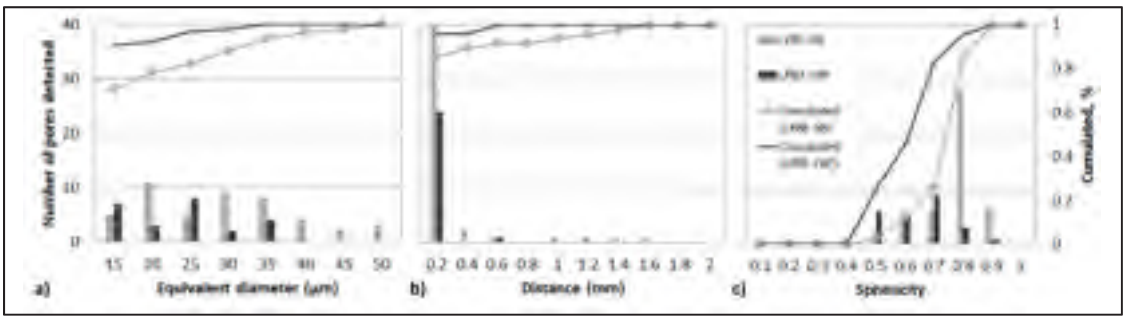

Figure 2.9 Number of detected pores (equivalent diameter ≥ 10 μm) as a function of: a) equivalent diameter, b) distance from the as-built surface, and c) sphericity; Grey – SR and Black – HIP 90°-oriented specimens

2.6.2 Mechanical properties

Typical stress-strain tensile diagrams for the SR and HIP LPBF, as well as for the wrought specimens, are shown in Figure 2.10. For the wrought material, only one diagram is shown, since no difference was observed between the L-T and T-L wrought specimens. The mechanical properties evaluated from these diagrams in conformity with ASTM E8-15a standard (*Standard Test Methods for Tension Testing of Metallic Materials*, 2016) are summarized in Table 2.1Table 2.1 Mechanical properties of IN625 specimens of different configurations, where the deviations are calculated assuming a t-student distribution with a confidence interval of 95%. The measurements of these properties, more specifically, the values of E and YS, are necessary to establish the crack propagation testing conditions (see below). For the 45° specimens, the Young's modulus and Yeild Stress were considered equivalent to that of the 0° specimens.

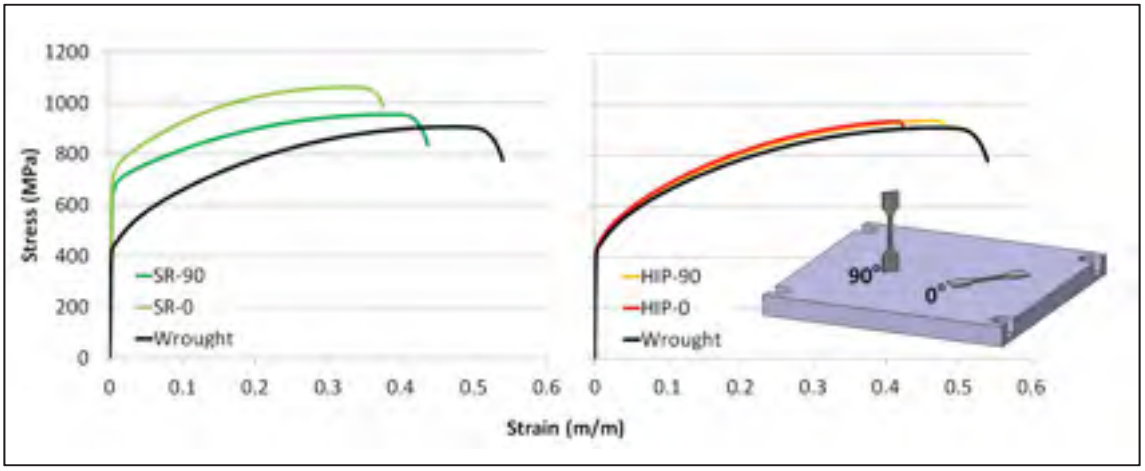

Figure 2.10 a) Typical stress-strain diagrams for the 0 and 90°-oriented LPBF specimens a) SR and b) HIP states; the diagrams for the wrought specimens are in black

Table 2.1 Mechanical properties of IN625 specimens of different configurations

Property	SR-0 °	SR-90 °	HIP-0 °	HIP-90°	Wrought
E (GPa)	202 ± 3	195 ± 12	212 ± 7	214 ± 7	205 ± 5
YS (MPa)	718 ± 13	685 ± 87	442 ± 6	425 ± 9	440 ± 27
UTS (MPa)	1069 ± 11	1009 ± 56	933 ± 14	923 ± 21	899 ± 19
Elongation (%)	37 ± 2	43 ± 5	43 ± 4	46 ± 5	52 ± 3

The SR LPBF specimens showed notably higher yield strength (YS) and ultimate tensile strength (UTS) values, but lower elongations to failure, than the wrought material. The Young's modulus (E) of the HIP specimens was found to be slightly higher than that of the SR specimens. The HIP post-processing also led to a slight increase in the elongation to failure, but this improvement was not sufficient to reach the ductility level of the wrought material. The YS and UTS values of the HIP specimens were found to be identical to those of their wrought counterparts, whereas their Young's modulus was slightly higher than that of the wrought material.

2.6.3 Fatigue crack propagation testing

The results of crack propagation testing of the 0º-oriented SR and HIP LPBF specimens and their wrought counterparts are collected in Figure 2.11. Since no difference was observed between the specimens of the wrought material cut in the L-T and T-L directions, only one diagram is shown in Figure 2.11, and this diagram was found to be in a good agreement with the literature (Ganesh et al., 2010). The threshold value for the wrought alloy was also found to be close to that of the annealed Inconel 600 (7.1 MPa*$m^{1/2}$ according to ASM (Lampman, DiMatteo et Committee, 1996)). The threshold SIFs of the LPBF SR and HIP specimens were considerably higher than that of the wrought alloy: 11, as compared to 7.2 MPa*$m^{1/2}$. In the Paris regime, however, all the specimens demonstrated similar behavior up to SIFs of 40 MPa*$m^{1/2}$, from which point the SR specimens started to display a better resistance to crack propagation than their HIP LPBF and wrought counterparts.

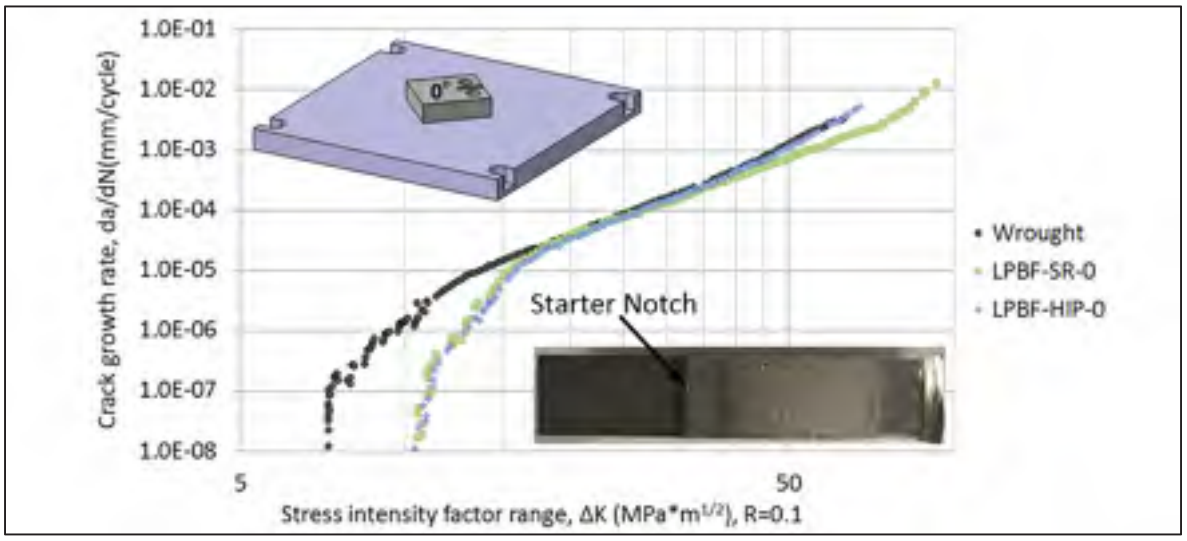

Figure 2.11 Fatigue crack propagation diagrams of the wrought and 0º-oriented SR and HIP LPBF specimens; an image of a fractured 0º-oriented LPBF-HIP specimen is inserted

Figure 2.12 a and Figure 2.12 b show, respectively, the crack propagation diagrams for the SR and HIP specimens with three different build orientations (0, 45 and 90º) and cracks propagating parallel to the build plane. The SR specimens showed a strong build orientation-

dependent crack growth rate in the near-threshold region (Figure 12a), while being build orientation-independent in the Paris regime. The values of the threshold SIFs confirm the anisotropic crack growth behavior in the SR specimens, with ΔK_{th} of 7.1, 8.6 and 11.2 MPa*m$^{1/2}$ for the 90, 45 and 0^{o}-oriented specimens, respectively. In the worst case, the threshold SIF was on par with that of the wrought alloy (7.2 MPa*m$^{1/2}$), while in the best case, it was equivalent to that of the HIP specimens (11.2 MPa*m$^{1/2}$). The crack growth behavior in HIP specimens was found to be build orientation-independent across the entire tested range of stress intensity.

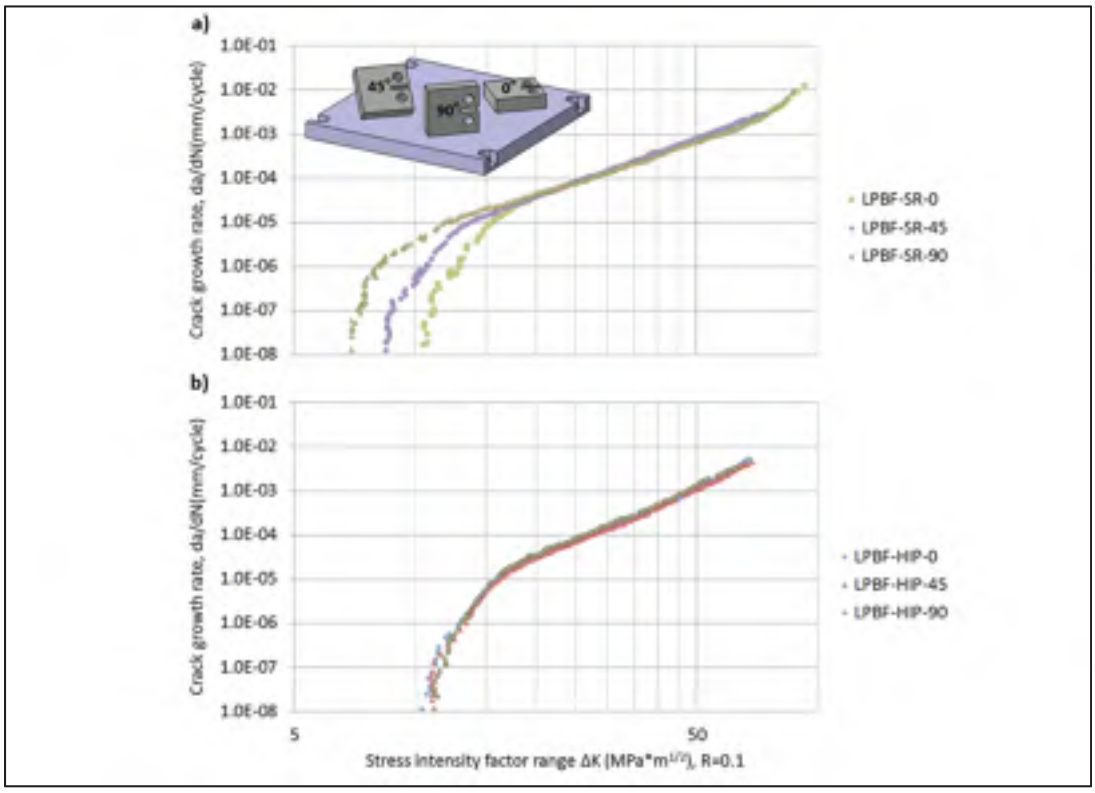

Figure 2.12 Fatigue crack propagation diagrams for a) SR and b) HIP LPBF specimens built with orientations 0, 45 and 90^{o}

In Figure 2.13a and Figure 2.13b, the crack growth diagrams of the 90^{o}-oriented LPBF specimens with cracks propagating parallel (90^{o}) and perpendicular (90$^{o}\perp$) to the build plane are compared for the SR and HIP states. The ΔK_{th} of the SR specimens with two crack

orientations were equivalent to that of the wrought alloy (compare Figure 2.13a and Figure 2.11a). For the HIP specimens however, ΔK_{th} for the cracks propagating perpendicular to the build plane (90°⊥) appeared to be slightly lower than for the cracks propagating parallel to the build plane (90°): 10.4 versus 11.1 MPa*m$^{1/2}$. In the Paris regime, no significant differences were noticed.

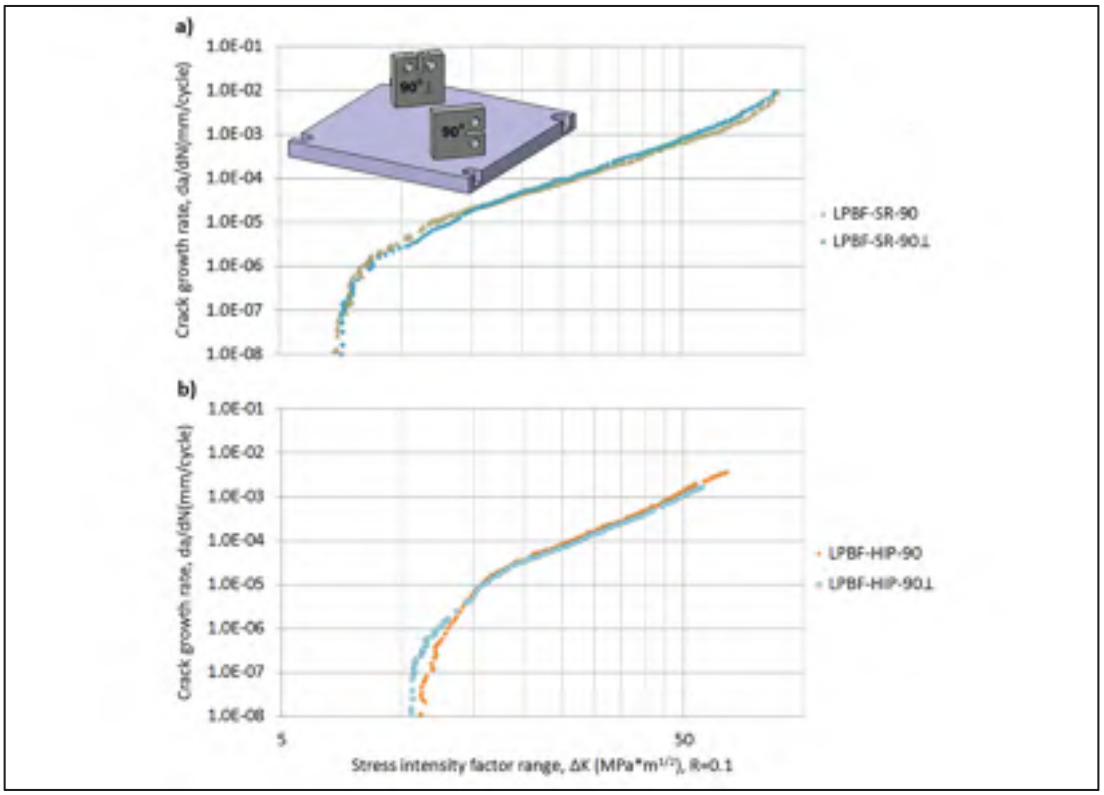

Figure 2.13 Fatigue crack propagation diagrams for the LPBF specimens: a) SR and b) HIP 90° specimens with cracks parallel and perpendicular to the build plane

2.7 Discussion

2.7.1 Defect analysis

The porosity level was evaluated at 0.05% for the SR specimens as compared to 0.03% for the HIP specimens. Our findings also suggest that the HIP post-processing does not entirely remove the processing-induced porosity, but rather reduces the average pore size, a phenomenon already observed in LPBF-processed Inconel 718 (Tillmann et al., 2017) and 316L stainless steel (Lavery et al., 2017) components. Additional scans are required to entirely validate this hypothesis; this work is however out the scope of this publication.

It was also shown that 85% of pores are located in close vicinity to the as-built surface (subsurface porosity), i.e., at a distance less than 0.2 mm from this surface, which explains why no pores were detected in machined specimens. To evaluate the impact of the as built surface, which is characterized by a combination of a relatively high surface roughness (Ra=9-19 μm, Rz=46-91 μm (Urlea et Brailovski, 2017) and subsurface porosity, on the crack initiation and propagation behavior, as-built (unmachined) specimens were subjected to crack propagation testing, and it was observed that unmachined specimens required ~$0.25 \cdot 10^6$ cycles to form a crack prior to testing, as compared to ~$1.25 \cdot 10^6$ cycles for their machined counterparts with identical orientation and post-processing (for both cases, however, the Paris diagrams of the machined and unmachined specimens were found identical)These results appear to be of a significant practical importance since they clearly demonstrate a much greater vulnerability to crack initiation of as-built components as compared to their machined counterparts. More work is definitely needed to individually assess how surface roughness and subsurface porosity impact the crack initiation behavior.

That said, the presence of any near-the-surface defects, which promote fatigue crack initiation in LPBF built components (Akita et al., 2016; Liu et al., 2014; Yadollahi et al., 2017), must be avoided. This goal may be reached by two means: by optimizing contouring-related laser processing parameters or by adding at least 0.2 mm of extra material, which must be removed

using an appropriate finishing technique. Although this post-processing would increase the total manufacturing cost, it could be partially compensated by an eventual removal of laser contouring from the LPBF processing routine (the contouring time amounts to approximately 10% of the total time of LPBF processing).

2.7.2 Static mechanical behavior

When compared to the wrought alloy, the SR LPBF specimens manifest higher YS and UTS and lower ductility than their wrought counterparts, which is in agreement with the literature on the topic (Kreitcberg, Brailovski et Turenne, 2017a). According to Table 2.1, YS is 55-60% higher, UTS is 12-18% higher, whereas the elongation at break is 17-29% lower than the corresponding parameters for the wrought alloy. There is also a strong anisotropy following the SR annealing, the horizontal (0^o) coupons having 5% higher YS and 7% higher UTS, and a 16% lower elongation at break than their vertically (90^o)-oriented counterparts. This behavior is attributed to a highly anisotropic microstructure of SR LPBF specimens, which is inherited from the as-built material (Kreitcberg, Brailovski et Turenne, 2017a). The elongated grains oriented along the testing directions are responsible for the higher ductility of the 90^o-oriented specimens, while finer microstructure in the build plane enhances the mechanical properties of their 0^o-oriented counterparts.

After HIP, the mechanical properties of LPBF specimens do not manifest any significant build orientation dependence, which is a direct consequence of the isotropic microstructure development during this processing. When compared to the wrought specimens, the elongations at break of the 90^o and 0^o-oriented HIP specimens are, respectively, 11 and 17% lower than that of the wrought material. Other papers suggest however that the elongation at break may be almost identical for the HIP LPBF and the wrought specimens (Kreitcberg, Brailovski et Turenne, 2017a).

The measurements of the Young's modulus of the LPBF-processed specimens showed that the Young's modulus of the HIP specimens (212-214 GPa) is slightly higher than that of the SR specimens (195-202 GPa). This slight increase in the Young's modulus values after HIP can be attributed to two concurrent phenomena: a) the HIP-induced densification [51] and b) the changes in the chemical composition of the matrix which occur during post-processing. Since the porosity level in IN625 specimens is very low (under 0.5%), the observed increase in Young's modulus cannot be explained by the HIP-induced densification only. In this context, it may be supposed that the dissolution of carbide particles during HIP resulting in larger amounts of Mo and Nb atoms in the matrix (Kreitcberg, Brailovski et Turenne, 2017b) could contribute to this phenomenon. Similar variations in the Young's modulus values were also observed after aging and solution treatment of LPBF IN625 components [52].

2.7.3 Crack propagation behavior

2.7.3.1 Results overview

Several parameters characterizing the crack growth behavior are retrieved from the Paris diagrams and collected in Table 2.2. The threshold SIFs (ΔK_{th}), corresponding to a crack growth rate of 10^{-7}mm/cycle, are calculated first, following the effective threshold SIFs ($\Delta K_{th,eff}$) estimated using the compliance offset method presented in section 2.5.

To validate the values of $\Delta K_{th,eff}$ reported in Table 2.2. an additional crack propagation test was performed on a wrought specimen at a higher R ratio of 0.5, to avoid any crack closure during testing. Since, for this specimen, the resulting ΔK_{th}=5.2 (R=0.5) was nearly identical to the $\Delta K_{th,eff}$ =5.1 (R=0.1), we can state that the ratio $U=\Delta K_{th,eff}/\Delta K_{th}$ introduced earlier reflects a true contribution of the crack closure effect to the threshold SIF at R=0.1.

Next, for the linear portion of the Paris diagram, excluding the data points violating the small scale yielding criterion (*Standard Test Method for Measurement of Fatigue Crack Growth Rates*, 2015), the constant C and m of the Paris law are estimated. The average values for all the specimen configurations are also presented in Table 2.2.

Table 2.2 Fatigue crack propagation thresholds ΔK_{th} and Paris law constants for all tested specimens

Material	**Wrought**	**LPBF built - Stress Relief (SR) annealing**				**LPBF built - Hot Isostatic Pressing (HIP)**			
	T-L and L-T	0°	45°	90°	90°⊥	0°	45°	90°	90°⊥
ΔK_{th} (MPa*m$^{1/2}$)	7.2	10.6	8.8	7.5	7.1	11.1	11.1	10.9	10.4
$\Delta K_{th,eff}$ (MPa*m$^{1/2}$)	5.1	4.1	4.7	4.5	4.5	4.3	4.6	4.2	4.5
U at threshold	0.71	0.39	0.53	0.60	0.63	0.39	0.42	0.39	0.43
M	3.48	3.23	3.25	2.95	3.22	3.62	3.69	3.67	3.64
C (*10^{-9})	1.38	2.37	2.02	4.66	3.02	6.6	4.85	4.90	6.43

2.7.3.2 Effects of the processing conditions

When comparing the crack propagation behavior of the wrought IN625 specimens to that of the SR and HIP LPBF specimens (Figure 2.11), a striking difference can be seen in the near-threshold region of the Paris diagrams. The SR and HIP LPBF specimens demonstrate a much higher fatigue crack propagation threshold than their wrought counterparts. When considering the crack closure phenomenon, using the compliance offset method described in section 2.5, the effective crack propagation threshold ($\Delta K_{th,eff}$) is indeed significantly lower and similar to that of the wrought specimens. As a result of these observations, the better resistance to fatigue crack propagation of the LPBF IN625 specimens in the near-threshold crack propagation regime at a low stress ratio of R=0.1 can be attributed to the roughness-induced crack closure phenomenon.

It has been proven that the coarser the microstructure, the higher the crack propagation threshold at low stress ratio, thanks to the roughness-induced crack closure effect (Liaw, 1988; Pippan, 1991). These observations were also confirmed for a specific case of the Nickel-based superalloy tested at ambient temperature (Gao et al., 2005). The observed differences in the crack propagation behavior of the LPBF and wrought specimens are in accordance with more tortuous crack paths in the former specimens as compared to the latter ones (see Figure 2.14).

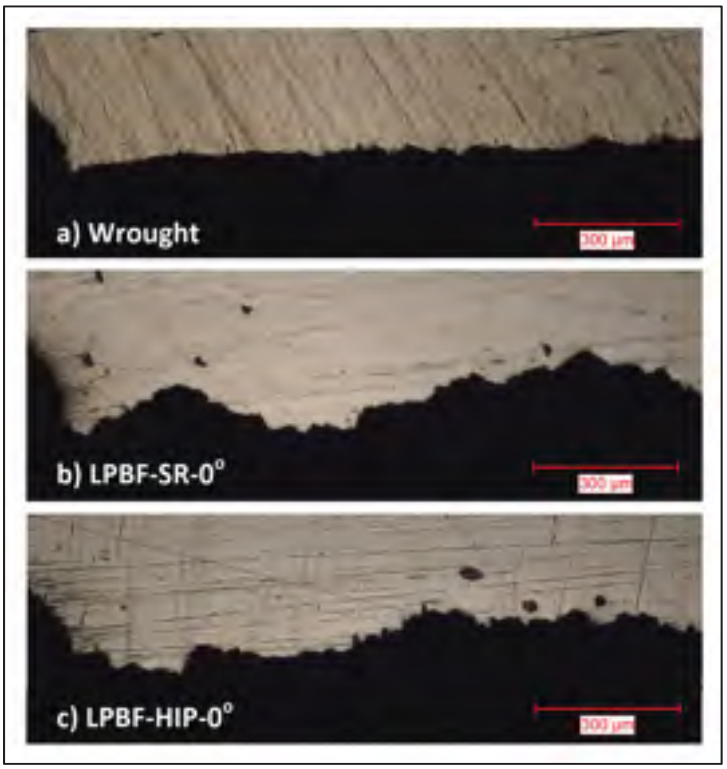

Figure 2.14 Crack profiles for a) wrought material,
b) SR and c) HIP 0°-oriented specimens

At intermediate SIFs, the behavior of all the specimens was nearly identical. Differences were only observed in the higher Paris regime and could be attributed to the considerably higher static mechanical properties of the SR specimens as compared to their HIP counterparts (Figure 10). This translates to a Paris law exponent of 3.2 for the SR specimens as compared to 3.5 for the wrought alloy and 3.6 for the HIP specimens. Although variations in the microstructure and mechanical properties are known to be less significant in the Paris regime (Krupp, 2007),

the YS of the HIP and wrought specimen was 40% lower than for the SR specimens, which could have significant effects on the growth mechanisms influenced by plasticity such as crack tip blunting (Hertzberg, Vinci et Hertzberg, 2012). When compared to other LPBF-processed alloys, such as Ti6Al4V or 316L, the Paris regime behavior of LPBF IN625 appears to be less affected by these post-treatments. The constants of the Paris law for all the specimens in this study range from 2.95 to 3.69, while for the 316L alloy, these values range from 3.15 to 4.30 (Leuders et al., 2013; Riemer et al., 2014).

2.7.3.3 Effect of the build and crack orientations

For the SR specimens, crack propagation in the near-threshold regime is strongly orientation-dependent (see Figure 2.12 a) at low stress ratio (R=0.1). The highly anisotropic microstructure resulting from the powder bed processing can explain this dependence (Hack et al., 2017; Li et al., 2017). According to (Kreitcberg, Brailovski et Turenne, 2017b), in the plane parallel to the build plate, the SR specimens manifest mostly equiaxed microstructure with an average grain size of 20 μm. In the normal plane, these specimens manifest columnar structure with grain length more than twice the layer thickness. That being said, as shown in Figure 2.15a, the crack oriented perpendicularly to the build plane (0°-oriented specimens) faces fewer grain boundaries than the cracks oriented parallel to the build plane (90°-oriented specimens). In the case of the 45° specimen, the near-threshold crack propagation value lies between those of the 0 and 90° specimens; this translates to a threshold SIF ΔK_{th} of 10.6, 8.8 and 7.5 MPa*m$^{1/2}$ for the 0, 45 and 90° specimens, respectively. When considering crack closure, the effective stress intensity factor $\Delta K_{th,eff}$ is comprised between 4 and 5 MPa*m$^{1/2}$ for all the specimens.

What might come as a surprise is that the near-threshold behavior for the two crack orientations (90° and 90°⊥) was nearly identical although the crack propagating in the 90°⊥ specimen faces fewer grain boundaries (see in Figure 2.15b). Based on the grain size alone, the 90°⊥ specimens were expected to behave more like the 0° specimens. However, the resulting crack profile of the 0°-oriented specimens being more tortious than that of their 90°⊥-oriented counterparts,

the crack closure effect in the former is less pronounced than in the latter (U=0.63 versus U=0.39 in Table 2.2). This indicates that the elongated grains in the propagation direction offer less resistance to crack growth, which is in accordance with the behavior of LPBF 316L components in (Riemer et al., 2014).

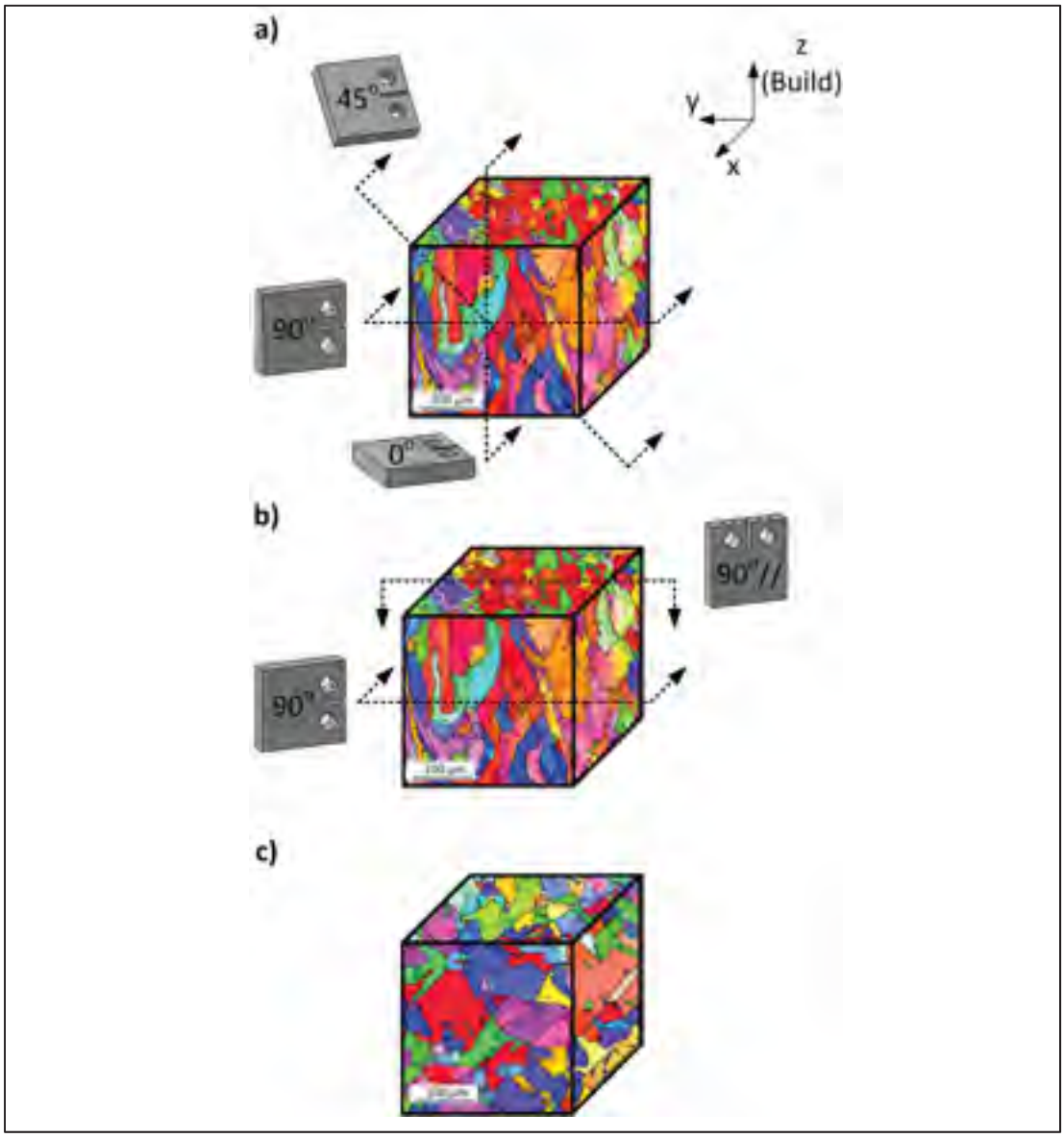

Figure 2.15 Representation of the specimens microstructures versus crack propagation directions: a) SR specimens with different build orientations (0°, 45° and 90°); b) SR specimens with different crack orientations (90° and 90°⊥), and c) specimens microstructure after HIP; (all microstructures adapted from (Kreitcberg, Brailovski et Turenne, 2017b))

In the Paris regime, the most of the SR LPBF specimens showed no crack orientation dependence, with the exception of the 90° specimen performing better at higher SIF (Paris law exponent m ≈3.0) than the 0, 45 and 90°⊥ specimens (m≈3.2). The underlying mechanisms for the better resistance to crack growth of the 90° specimen should be related to extensive crack tip blunting promoted by the higher ductility and toughness of this specimen displayed in tensile tests (Figure 2.10). The three other specimens demonstrated identical behavior in this regime.

After HIP, for all the build and crack orientations, a nearly identical threshold value of ~10 to 11 MPa*$m^{1/2}$ was obtained (Figure 2.13b), this value being close to the highest K_{th} obtained for the 0°-oriented SR specimens (Figure 2.12a). This outcome is explained by a coarser and more isotropic microstructure resulting from the HIP treatment (Kreitcberg, Brailovski et Turenne, 2017b; Li et al., 2017). During the HIP process, grain growth causes the microstructure to become nearly equiaxed (random texture) with a certain quantity of annealing twins (Kreitcberg, Brailovski et Turenne, 2017b). Neglecting the annealing twins, the grain size varied from 10 to 200 μm with an average size of ~40 μm in the build plane as shown in Figure 2.15c. A similar variation in size was observed in the normal plane, with an average size of ~50 μm. This microstructure promotes the roughness-induced crack closure in all directions as opposed to the SR specimen microstructure. In the Paris regime, the HIP specimens crack propagation behavior was also independent of the build orientation and close to that of the wrought alloy, with the Paris law exponent m ranging from 3.6 to 3.7, as compared to 3.5 for the wrought IN625.

2.7.4 Summary

A strong microstructural anisotropy observed in the SR specimens significantly influenced their static mechanical properties, while only moderately impacting their crack propagation behavior. The near-threshold behavior of the crack growth regime in the SR specimens was affected by the build orientation, while the Paris regime was affected by the crack orientation.

The first observation relates to the microstructure, which promotes the roughness-induced crack closure phenomenon to a different extent, depending on the specimen orientations. This effect disappears when the SIF exceeds ≈ 15-17MPa*$m^{1/2}$. The crack propagation behavior of the HIP specimens was almost insensitive to the build and the crack orientations, and the coarse microstructure promoted the roughness crack closure effect for all the specimen configurations. Therefore, for low stress ratio applications, the coarser microstructure of the HIP LPBF built IN625 components has a positive effect; roughness-induced crack closure can help shielding fatigue cracks and prevent their propagation. It should be emphasised however, that this effect was observed only for the 0° and, to a lower extent, the 45°-oriented SR LPBF IN625 specimen. Under higher stress ratios R, however, this effect is expected to vanish (Dubey, Soboyejo et Soboyejo, 1997), and, according to our results, the threshold SIF of the LPBF specimens will be within the 4 to 5 MPa*$m^{1/2}$ range, which is similar to that of the wrought specimens.

2.8 Conclusions

In this paper, LPBF-built IN625 alloy was characterized from the processing-induced flaw and mechanical resistance points of views. The X-Ray computed microtomography revealed pores smaller than 50 µm in diameter and almost entirely confined to the zones close to the surface. Fatigue crack propagation testing of unmachined specimens revealed an accelerated crack initiation phenomenon. It is therefore reasonable to suppose that surface finishing of LPBF specimens must yield a longer fatigue life, thanks to the reduction of the surface roughness and the number of subsurface defects. In our case, thickness of the material layer containing the majority of pores was ~0,2 mm; this value being directly related to the scanning strategy and contouring processing parameters of an EOS M280 system. Next, the crack propagation behavior of LPBF-built IN625 alloy was studied and compared to that of its wrought counterpart: the behaviors of both materials were found to be similar. Specifically, following the HIP, the LPBF built IN625 showed an isotropic mechanical behavior and the microstructure promoted a higher damage tolerance when compared to the wrought material

in the near-threshold region under low stress ratios, which was found to be independent on the build or crack orientations. The findings of this study are however limited to ambient temperature; further research should focus on the high temperature fatigue crack propagation behavior of LPBF built IN625, since concerns about a relatively low elevated-temperature ductility of this material as compared to the wrought material of the same composition have already been raised in (Kreitcberg, Brailovski et Turenne, 2017a; 2017b) .

2.9 Acknowledgment

The author would like to thank the Fonds de Recherche du Québec - Nature et Technologie (FRQNT), and the National Science and Engineering Research Council of Canada (NSERC) for their support in financing the present study. The author would also like to thank Alena Kreitcberg, Pierre-Antony Deschênes, Alexis de la Fuente and Serge Plamondon for their supporting the experimentation performed for this publication.

2.10 Annex: Definition of the calibration curve

Several correlations (calibration curves) are proposed in the ASTM E647 standard to evaluate the fatigue crack length using remote crack opening displacement (COD) measurements. Each calibration curve is given for a specific clip gauge attachment point. In this experimental setup, external knife edges were fixed on the specimen, and therefore, COD readings were taken at an intermediate position for which the ASTM standard did not provide a calibration curve. Therefore, a calibration curve was established via An ANSYS APDL model reflecting our setup to ensure a valid relation between the compliance and the crack length for this specific condition.

In this 2D model, a plane stress behavior was assumed, and the compact specimen (W=38, b=9.5mm) was meshed with 12676 PLANE182 elements having a nominal size of 0.5 mm and 0.1 mm in the vicinity of the crack and arc length of 3^{o} at the mounting hole edges. A linear elastic material was assumed, with a Young’s modulus of 205GPa and a Poisson ratio of 0.3

in plane stress conditions. In order to avoid dealing with contact elements, the external knife edges were considered as a part of the specimen since their material has nearly identical linear elastic constants (Young's modulus and Poisson ratio). Equal and opposite nodal forces were applied to the upper 120^{o} arc of the top mounting hole edge and on the lower 120^{o} arc of the lower mounting hole edge.

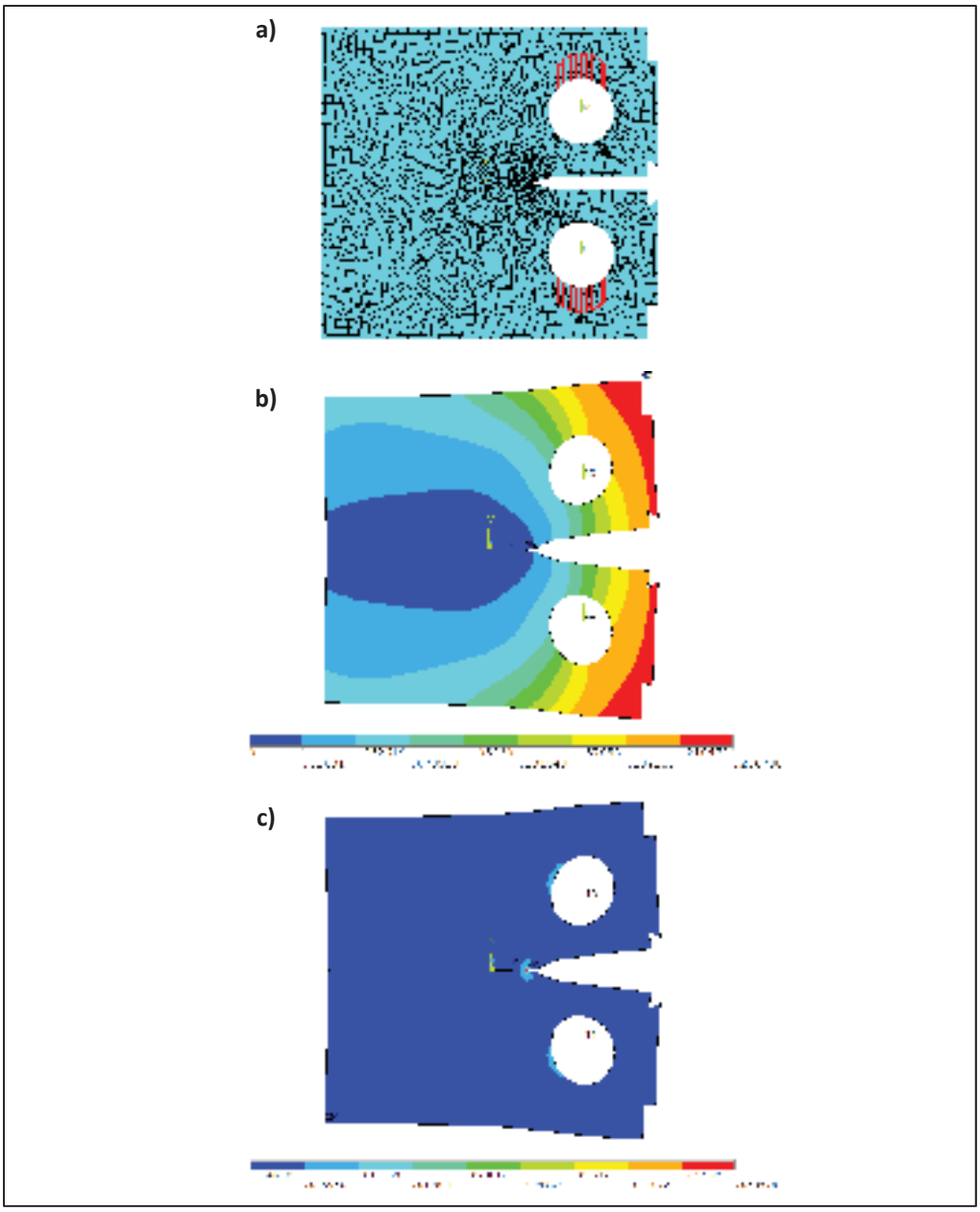

Figure 2.16 a) ANSYS APDL model with mesh and boundary conditions, b) solution for nodal displacement and c) solution for nodal elastic strain

The model above was solved for crack length increments of 0.5 mm from an initial crack length of 7.6 mm to a final length of 29.6 mm. This corresponds to an adimensional crack length a/W range of 0.2 to 0.8. The nodal displacement of the two points corresponding to the mounting

locations of the clip gauge was recorded at each crack length simulated to retrieve the COD value ν for each crack length. The compliance for all crack lengths was tabulated and a 5-degree polynomial curve (Equation A1.1) was fitted through the data. The values of the constant C_0 through C5 are shown in Table 2.3 and compared against the values suggested by the ASTM standard.

$$\frac{a}{W} = C_0 + C_1 u_x + C_2 {u_x}^2 + C_3 {u_x}^3 + C_4 {u_x}^4 + C_5 {u_x}^5 \qquad \text{(A2.1)}$$

Table 2.3 Constants of the calibration curve compared to the ASTM values

	Normalised COD measurement position (x/W)	C_0	C_1	C_2	C_3	C_4	C_5
ASTM Vx1	-0.345	1.0012	-4.9165	23.057	-323.91	1798.3	-3513.2
APDL	***-0.293***	***1.0009***	***-4.6037***	***13.726***	***-176.51***	***885.45***	***-1469.2***
ASTM Vo	-0.250	1.0010	-4.6695	15.400	-180.55	870.92	-2143.4

CHAPITRE 3

LONG FATIGUE CRACK PROPAGATION BEHAVIOR OF LASER POWDER BED FUSED INCONEL 625 WITH INTENTIONNALY SEEDED POROSITY

J-R. Poulin[1], A. Kreitcberg, P[1]. Terriault[1], V. Brailovski[1,*]

[1]Department of Mechanical Engineering, École de technologie supérieure,

*Corresponding author: Vladimir Brailovski, Department of Mechanical Engineering, École de technologie supérieure, 1100 Notre-Dame Street West, Montreal, Quebec, Canada, H3C 1K3 (vladimir.brailovksi@etsmtl.ca, tel: 514-396-8594)

Article publié dans la revue « International Journal of Fatigue », vol. 127. p. 144-156, 2019.

3.1 Avant-Propos

Dans un second temps, afin de donner suite aux travaux présentés dans le chapitre précédent, le chapitre 3 vise à vérifier l'impact de la porosité sur le comportement des fissures de fatigue. Cette validation est particulièrement importante pour l'implémentation de l'approche de Kitagawa-Takahashi afin d'assurer que le seuil de propagation de fissure obtenu pour un matériau dense se transpose en présence de porosité, plus spécifiquement des défauts spécifiques au procédé de LPBF. Dans ce cas précis, les défauts générés sont des régions partiellement fusionnées découlant d'un apport d'énergie insuffisant, leurs caractéristiques géométriques s'apparentent à celle d'une fissure. De surcroit, l'obtention des courbes de Paris en présence de différents niveaux de porosité permettra de saisir l'importance de l'interaction des défauts avec les fissures de fatigue en situation de vie finie (propagation).

3.2 Résumé

Dans cet article, différents échantillons d'Inconel 625 sont fabriqués avec des paramètres laser altérés afin de générer différents niveaux de porosité, cette dernière étant caractérisée au moyen de la méthode d'Archimède et de la microtomographie à rayons X. Un total de 4 niveaux de

porosités (entre 0.1 et 2.7%) sont retenus pour évaluer l'influence de la porosité induite sur le comportement statique ainsi qu'en propagation de fissure. Les résultats montrent que les propriétés élastiques de l'alliage sont très faiblement influencées par la présence de porosité alors que l'allongement à la rupture est fortement diminué, en particulier pour des échantillons fabriqués à la verticale. En ce qui concerne la propagation de fissure, le seuil et la région à faible facteur d'intensité de contrainte sont également peu influencés par la porosité. Toutefois, à un facteur d'intensité de contrainte plus élevé, la porosité joue un rôle prépondérant et son influence est également dépendante de l'orientation de la fissure.

3.3 Abstract

Inconel 625 coupons were manufactured via laser powder bed fusion with different levels of intentionally-seeded porosity (up to 2.7%). The processing-induced porosities, morphologies and distributions were measured via Archimedes method and computed tomography. Tensile tests were performed, followed by fatigue crack propagation characterization. The static strength characteristics were not strongly affected by the levels of porosity, but the elongation at break was severely impacted. In the near threshold region of the Paris diagram, porous specimens were unaffected by porosity and build orientation. However, under higher stress intensity factors, the effect of porosity was found to be significant and build orientation-dependent.

Keywords: Additive manufacturing, Laser powder bed fusion, Selective laser melting, Nickel-based superalloy, Fatigue crack propagation, Damage tolerance, Porosity

3.4 Introduction

Metal additive manufacturing (AM) technologies are increasingly used for manufacturing complex metallic components from various alloys, including aluminum, titanium and nickel-based alloys, and different grades of stainless steel (DebRoy et al., 2018; Herzog et al., 2016; Murr et al., 2012). The laser powder bed fusion technology (LPBF) has attracted significant

attention due to its inherent capacity to build complex components with mechanical properties comparable to those produced using conventional manufacturing techniques (Hanzl et al., 2015; Vrancken et al., 2012). In this process, a thin layer (~20 to 100 μm) of prealloyed powder is spread on a build plate, and then a laser is used to locally melt the powder (Wong et Hernandez, 2012). The regions to be fused are then generated by slicing a CAD file of the part to build. These steps are repeated thousands of times until the part is completely fabricated.

The LPBF is of particular interest to the aerospace industry where complex geometries can be obtained in near net shapes without tooling and in the just-in-time manner (McLouth et al., 2018). This is even more compelling in the case of Inconel 718, Waspalloy, Inconel 625 and other superalloys which are expensive to machine due to their extensive work hardening (Rahman, Seah et Teo, 1997). Furthermore, the design freedom enabled by AM also opens a window for manufacturing topology optimized structures which can provide significant weight savings (Brackett, Ashcroft et Hague, 2011; Zegard et Paulino, 2016). With all these benefits, AM has proven to be competitive against traditional machining for small or medium productions as encountered in the aerospace industry (Atzeni et Salmi, 2012; Thomas et Gilbert, 2014).

Commissioning AM-built components in such a highly regulated industry as aerospace requires a thorough understanding of the mechanical behavior of the materials, especially of their fatigue resistance. So far, the literature has shown that the fatigue properties of LPBF-built components are strongly dependent on processing and post-processing conditions (Li et al., 2016). The main artifacts that can affect the fatigue life of LPBF components are residual stresses, highly heterogeneous microstructures, rough surface finishes, and processing-induced defects (pores, cracks, inclusions). The residual stresses and microstructure heterogeneity arise from the fast repeated heating and cooling cycles inducing non-uniform thermal dilatation in the heat affected zone near the melt pool (Mukherjee, Zhang et DebRoy, 2017; Parry, Ashcroft et Wildman, 2016). Typically rough and build orientation-dependent surfaces of LPBF components are due to the so-called rippling effect, the staircase effect, and the presence of

partially bonded particles, the latter being dominant on unsupported down-facing surfaces (Mumtaz et Hopkinson, 2009; Strano et al., 2013). The most commonly observed volumetric processing-induced defects are lack-of-fusion defects, gas-contained pores, inclusions and cracks (Kasperovich et al., 2016; Koutiri et al., 2018; Ziółkowski et al., 2014). Some of these defects are LPBF-specific, while the others can also be encountered in different manufacturing processes. For example, the lack-of-fusion defects, which are typically low-sphericity crack-like elongated voids sometimes containing unfused powder, result from the layer-by-layer manufacturing approach, whereas gas-contained pores, cracks and keyhole-induced pores are also observed in metal injection molding (Hwang, 2012) and welding (Katayama, 2013).

In LPBF, the occurrence of volumetric defects is a result of complex interactions between the powder-related parameters (layer thickness and powder bed density), the laser-related parameters (power, wavelength and spot size), and the scan-related parameters (scanning speed, hatching space and scanning strategy) (Kasperovich et al., 2016; Koutiri et al., 2018). For a given scanning strategy, the main processing parameters can be combined into a single metric called the volumetric energy density (VED=P/vht, where P is the laser power; v, the scanning speed; h, the hatching distance, and t, the layer thickness) (Letenneur et al., 2017). This metric is generally well correlated with the porosity level of LPBF components (Kasperovich et al., 2016), and the lowest porosity is obtained when the energy level is in its optimum range, i.e. where multiple (up to 3 times) material remelting occurs (Tang, Pistorius et Beuth, 2017). In this case, it is possible to obtain almost fully dense components (porosity below 0.1%), as reported for Ti6Al4V (Kasperovich et al., 2016), Inconel 625 (Koutiri et al., 2018) and Inconel 718 (Sheridan et al., 2018) alloys, among others.

If the energy density is above its optimum range, the keyhole effect has been shown to be responsible for creating spherical pores (Criales et al., 2017; Montgomery et al., 2015; Simonelli et al., 2015). Conversely, lower energy densities tend to produce lack-of-fusion defects (Khairallah et al., 2016; Qiu et al., 2015). Finally, similarly to welding, melt pool instabilities during the LPBF process can also cause spattering, balling or unmelt, which can

also generate volumetric defects in the final build (Bidare et al., 2018; Criales et al., 2017; Khairallah et al., 2016). Other variables affecting the quality of the build are the uniformity of the powder layer and the protective gas flow (Ferrar et al., 2012). Because of the complex interactions of all these phenomena, the problem of finding LPBF parameters which would provide optimal processing conditions in all the locations of a complex part becomes almost unsolvable; rather, parameters are defined within certain processing windows and can therefore be suboptimal in some regions of a component being built, thus resulting in some residual porosity.

The fatigue resistance of as-built LPBF components has been extensively reported for several alloys, such as Ti6Al4V, AlSi10Mg and 316L stainless steel, and has often been found to be lower than that of their wrought counterparts (Li et al., 2016). Several surface and bulk post-processing treatments can be applied to LPBF-built components with the objective of improving their surface finish, reducing the level of residual stresses, optimizing the material microstructure and reducing the processing-induced porosity (Baicheng et al., 2017; Lavery et al., 2017; Tillmann et al., 2017; Witkin et al., 2019; Wu et Lai, 2016). However, even after such treatments, the fatigue life of LPBF components has frequently been found to be shorter than that of their conventionally-built counterparts (Li et al., 2016). It is generally agreed that in such a case, residual processing-induced flaws, such as pores and inclusions, start playing a decisive role in the fatigue life limitations (Akita et al., 2016; Sheridan et al., 2018; Wycisk et al., 2014; Yadollahi et Shamsaei, 2017; Yamashita et al., 2018), as these sites are preferential areas for the fatigue crack nucleation (Gong et al., 2015; Koutiri et al., 2018; Liu et al., 2014; Prithivirajan et Sangid, 2018; Sheridan et al., 2018). To define the safe design space for LPBF parts, a damage tolerance design approach, as proposed by Kitagawa-Takahashi (Kitagawa, 1976) which considers the fatigue life of components containing processing-induced defects, can be employed (Biswal et al., 2019; Romano et al., 2018; Wycisk et al., 2014). Using El-Haddad's formulation (El Haddad, Smith et Topper, 1979; El Haddad, Topper et Smith, 1979), it is possible to obtain a safe zone for fatigue which accounts for defects smaller than the typical long crack thresholds. This approach combines the stress life and fracture mechanics

approaches, i.e., the S-N and Paris diagrams, the latter providing threshold stress intensity factors determined from fatigue crack propagation testing (Garb et al., 2018; Peters et al., 2002; Tenkamp et al., 2018). The influence of processing-induced porosity on crack propagation behavior has already been studied for steel components produced by powder metallurgy. A decrease in their relative density (inverse of porosity) has been shown to lower threshold stress intensity factors, increasing the crack propagation rate in the Paris regime (Fleck et Smith, 1981a; 1981b; Hadrboletz et Weiss, 1997), and decreasing the fracture toughness (Stephens et al., 1998). However, the porosity studied was in the 5% to 20% range, which is significantly higher than the porosity expected after LPBF. In LPBF, the layer-by-layer manufacturing approach and the lack-of-fusion defects are both responsible for peculiar pores arrangements and morphologies, which differ from the porosity in pressed-and-sintered powder metallurgy products.

This study is focused on the fatigue crack propagation behavior of an Inconel 625 (IN625) alloy widely used in the aerospace industry. The fatigue crack propagation behavior of fully dense LPBF IN625 components was previously studied, and appeared to be similar to that of their wrought counterpart (Poulin, Brailovski et Terriault, 2018). However, how this resistance will be affected by the LPBF-induced porosity is still unknown. In order to help fill this gap and thus support the damage-tolerant design approach, the present study focuses on the evaluation of the impact of processing-induced porosity on the fatigue crack propagation behavior of IN625 alloy processed by laser powder bed fusion. In this manuscript, the methods employed to manufacture and characterize the defects, as well as the microstructure and mechanical behavior of specimens with various levels of porosity are described first. The results are presented in the next sections and are analyzed in an attempt to link the processing parameters with the structure, properties and performance of LPBF IN625 components.

3.5 Materials and methods

3.5.1 Manufacture, porosity and microstructure analyses of specimens with intentionally-seeded porosity

All specimens of this study were manufactured under argon protective atmosphere, using an EOSINT M 280 system equipped with a 400 W Yttrium laser. An IN625 powder, whose composition corresponds to the UNS N06625 specifications (weight %: ≥58%Ni; 20-23%Cr; 8-10%Mo; 3.15-4.15%Nb; ≤5%Fe; ≤0.40%Ti; ≤0.40%Al; ≤ 1%Co; ≤0.10%C; ≤0.05%Ta; ≤0.50%Si; ≤0.50%Mn; ≤0.15%P; ≤0.15%S) provided by EOS was used.

A melt pool model (Letenneur, Kreitcberg et Brailovski, 2019) was employed to calculate several sets of processing parameters capable of generating distributed porosities ranging from 0.1 to ~13 %. This porosity variation range was ensured by varying the laser scanning speed from 720 to 3840 mm/s (see parameter sets V1-V8 in Table 3.1). The laser power P, the layer thickness t, the hatching space h, and the scanning strategy remained constant for all specimens, the latter consisting of a 67° hatch rotation between layers. The same sets of printing parameters are also plotted on the density distribution map of Figure 3.1 in the Volumetric Energy Density (E-P/vth) – Build Rate (BR=vht) coordinates.

Table 3.1 Parameter sets employed for the manufacture of LPBF IN625 specimens; results of calculations using model (Letenneur, Kreitcberg et Brailovski, 2019).

Parameter Set ID	Laser power (W)	Scanning speed (mm/s)	Hatching space (mm)	Layer thickness (mm)	Build rate (cm^3/h)	Energy density (J/mm^3)	Calculated porosity (%)
V1	285	**720**	0.11	0.04	11.4	90.0	0.1
V2		**960**			15.2	67.5	0.4
V3		**1200**			19.0	54.0	1.4
V4		**1440**			22.8	45.0	2.9
V5		**1680**			26.6	38.5	4.5
V6		**1920**			30.4	33.8	5.5
V7		**2880**			45.6	22.5	9.2
V8		**3840**			60.8	16.9	12.9

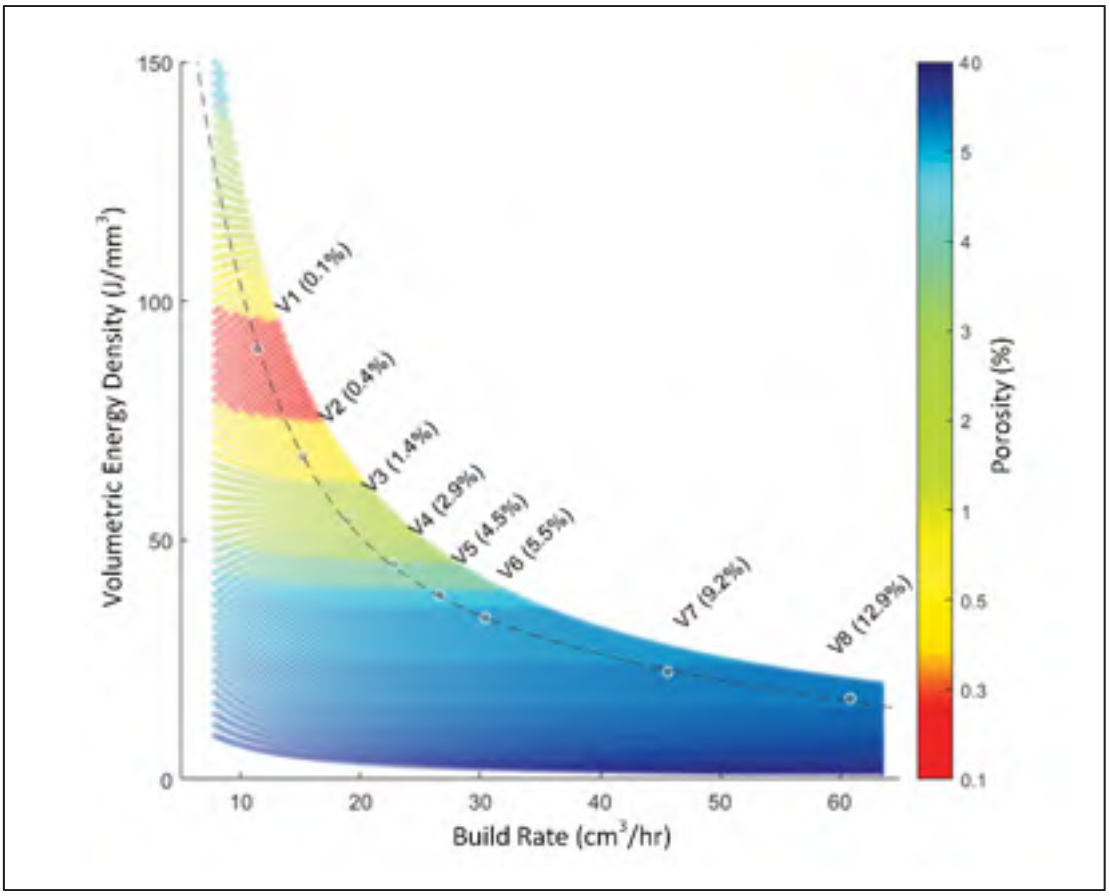

Figure 3.1 Density distribution map with 8 parameter sets used for the porosity evaluation; colors indicate the porosity levels predicted using a melt pool model in [58]

Three sets of specimens were built for this study. First, 6 mm-diameter, 40 mm-long cylindrical specimens (Figure 3.2a) were built to validate the levels of porosity generated using the calculated parameter sets of Table 3.1 (two specimens per set). The Archimedes and Computed Tomography (CT) techniques were applied to assess the processing-induced porosity levels as well as the pore size, shape and distributions.

Second, 8 mm-diameter x 80 mm-long cylindrical blanks (Figure 3.2b) for small standard tensile testing specimens (ASTM E8) were built with porosities of up to 3%, which is typical for LPBF components. Half of the 32 blanks for tensile testing were manufactured in the

vertical (90^{o}) orientation while the other half were built horizontally (0^{o}). Four specimens in total were manufactured for each build orientation. CT analyses were also carried out on the top and lower sections of the selected specimens to ensure the uniformity of the porosity distribution across the build plate.

Third, prismatic specimens with overall dimensions of 47 x 45 x 9.5 (mm^3) (Figure 3.2 c) for crack propagation testing (ASTM E647) were built with the same porosity levels as for tensile testing (0 to 3%). 24 blanks were built, half with a starter notch parallel to the build plate and the other half with a starter notch normal to the build plane. In this manuscript, the orientation of the compact specimens (0^{o} or 90^{o}) is given according to the orientation of the starter notch plane. Therefore, 0^{o} specimens have a starter notch along the build direction, while 90o specimens have a starter notch normal to the build direction. To ensure that the pore size, shape and distributions in compact specimens were equivalent to those in cylindrical specimens, cubic samples were cut from the compact specimens after their testing (the Archimedes technique was used in this case for porosity measurements). The microstructure analysis was also performed on these cubic samples. The specimens' characteristic dimensions are provided in Figure 3.2, whereas a complete test matrix for density measurements, tensile and crack propagation testing is given in Table 3.2.

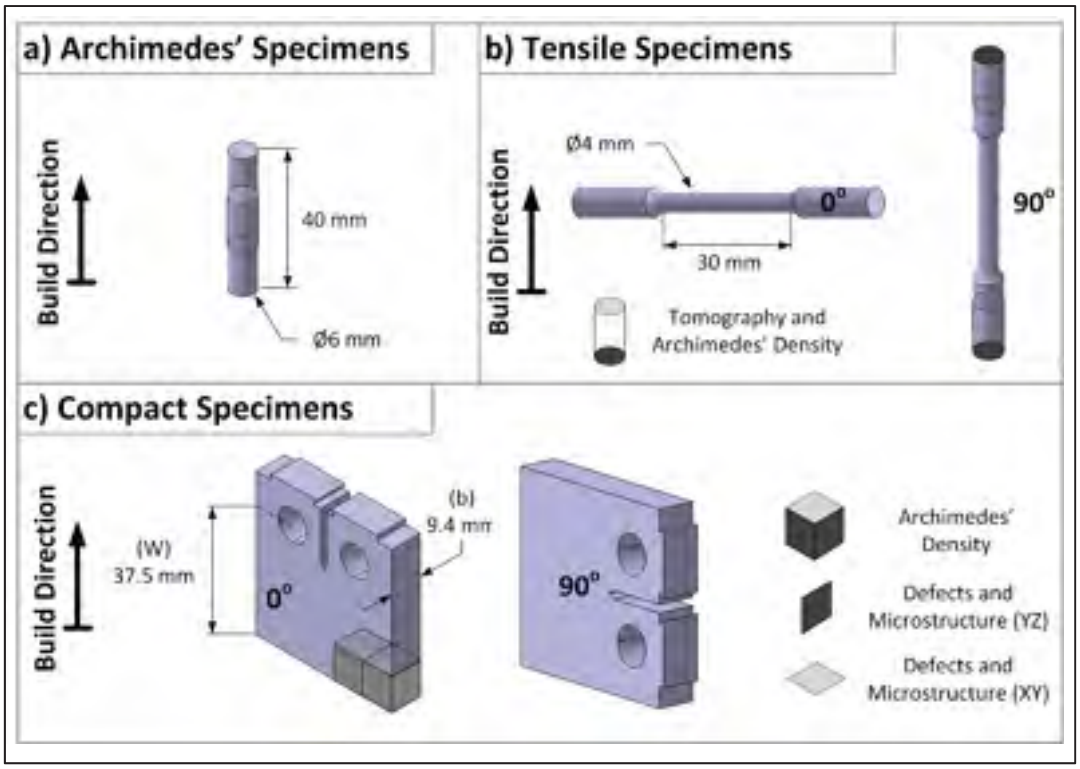

Figure 3.2 a) Cylindrical specimens for porosity evaluation experiment; b) tensile specimens for static mechanical testing, and c) compact specimens for fatigue crack propagation testing

Table 3.2 List of specimens for the porosity, tensile and fatigue crack propagation experiments

Specimen designation	Orientation, (°)	Maximum porosity, (%)	Replications
Density specimens (custom)	90	~13	16 (2 x 8)
Tensile specimens (ASTM E8)	0	~ 3.0	16 (4 x 4)
	90	~ 3.0	16 (4 x 4)
Fatigue crack propagation specimen (compact, ASTM E647)	0	~ 3.0	12 (3 x 4)
	90	~ 3.0	12 (3 x 4)

An example of the build plate containing compact specimens is shown in Figure 3.3a. Following each build, a stress relief (SR) annealing was performed on the build plates according to the manufacturer recommendations (870ºC for 1h, under argon atmosphere). Next, the porosity, tensile and compact specimens were cut off the build plates to be machined to final dimensions and then tested.

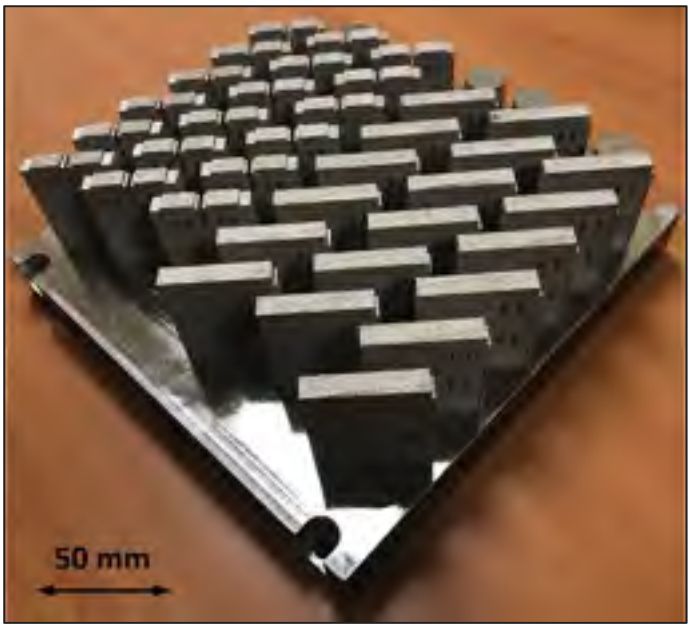

Figure 3.3 a) Image of the build plate with 0º and 90º blanks for fatigue crack propagation testing

3.5.2 Porosity evaluation procedures

Porosity measurements using the Archimedes technique were performed according to the ASTM B962-17 standard using a Sartorius YDK03 density determination kit with an uncertainty of 0.05% on the density measurements. For each specimen, the measure was repeated twice. Next, computed tomography observations were carried out on at least one specimen for each parameter set. These analysis were performed using a Nikon XT-H225 computed tomography system with a 225 kV reflection X-Ray source on at least one 6 mm-diameter x 5 mm-long sections of the coupons belonging to each parameter set. The specimens

were scanned with a voxel size of 5 µm, a beam energy of 200 kV and a current of 50 mA, using a 1 mm-thick copper sheet filter. A total of 2634 projections with an exposure time of 2.83 seconds were acquired. The images were reconstructed using the CT PRO 3D software provided by Nikon Metrology, and their post-processing performed using the ORS Dragonfly image processing software. To avoid false detections associated with noise, a detection threshold of 8 contiguous voxels was considered.

3.5.3 Metallography and Microstructure analyses

As shown in Figure 3.2 c), cubic samples in the direction parallel (XY plane) and normal (YZ plane) to the build plane were cut from compact specimens for metallography analysis. They were mounted in Bakelite and polished manually using SiC paper up to grit 1200. Polishing was done with Alumina Oxide particles of 9 µm followed by particles of 1 µm, and a final polishing was performed with 0.05 µm particles. After polishing, the samples were cleaned with ethanol, dried and observed using an Olympus 3D laser microscope at magnification ratios of 50, 100 and 200x to qualitatively compare the microscopically-observed distribution of processing-induced porosity to the results of CT observations.

Following the optical microscope (OM) observations, the same samples were used for the microstructure analysis using a scanning electron microscope (SEM, Hitachi SU8230) equipped with an electron backscatter diffraction (EBSD) unit. The parallel (XY) and normal plane (YZ) faces of the cubic specimens were examined. The texture evolution was characterized using contrast imaging and integrated ARGUS FES/BSE imaging. Specimens were tilted by 70° and scanned at 20 kV, with a 1 µm step. These analyses were conducted using 4×3 mm^2 mapping areas for horizontal and vertical planes, respectively.

3.5.4 Tensile testing procedure

Room-temperature tensile testing to failure was conducted in accordance with the ASTM E8 standard at a constant strain rate of 10^{-3} s^{-1} on a 15 kN MTS 810 servo-hydraulic tensile machine. It is worth mentioning that the gauge length of specimens tested had to be increased above the ASTM recommendations in order to mount an MTS 634.12 mechanical extensometer with a gauge length of 25 mm. During testing, the time, strain and force were recorded at an acquisition rate of 20 Hz. The Young's modulus was calculated in the 100-250 MPa stress range, the yield stress (YS) was determined based on a 0.2% offset strain. The ultimate tensile strength (UTS) and the elongation at break (δ) correspond to the maximum stress and strain (without elastic component) reached during testing.

3.5.5 Fatigue crack propagation testing procedure

Room temperature fatigue crack propagation testing was conducted according to the procedure described in (Poulin, Brailovski et Terriault, 2018). Prior to testing, a manual polishing was performed with SiC paper up to grit 1200 on the external surfaces to allow a visual observation of the crack. A stress-controlled approach was employed with a stress ratio of R=0.1 and a frequency of 20 Hz using a 15 kN MTS 810 servo hydraulic tensile machine. A three-step procedure was used which involved pre-cracking the specimen, followed by a stepdown method to evaluate the near-threshold behavior, and finally, the test was carried out with a K-increasing procedure under constant loads to evaluate the Paris regime behavior. The force applied on the specimens was measured using an MTS 662.20D-0415kN load cell, and the crack opening displacement (COD), using an MTS 632.02F clip gauge. Both parameters were recorded at an acquisition rate of 1025 Hz. A Matlab routine was employed to obtain the Paris diagram using the Force and COD data obtained during the test. More details on the procedure are given in (Poulin, Brailovski et Terriault, 2018).

3.6 Results

3.6.1 Porosity evaluation

The calculated and the measured (Archimedes and CT) porosities are plotted in Figure 3.4 as functions of the laser scanning speed (see Table 3.2 for numerical values). It is worth mentioning that the calculated, CT- and Archimedes-measured porosity values differ. First, the calculated values are systematically higher than those measured experimentally, with the level of discrepancy being smaller for the lowest and highest scanning speeds (V1, V2 and V7, V8). That nonwithstanding, the calculated porosity level does not account for powder entrapment.

Next, for specimens having porosity levels below 2%, the Archimedes porosity was consistently higher than that measured using the CT technique, while it was the opposite for specimens having porosity levels exceeding 2%. Many factors can be invoked to explain these differences: first, variations in the alloy compositions could result in density levels differing from the theoretical value for this alloy used in the Archimedes calculations. Secondly, completely wetting the rough as-built surfaces is difficult, and water can also impregnate specimens with greater porosities due to capillary action in pores connected to the surface, which would also affect the Archimedes measurements. Thirdly, the presence of a significant amount of partially fused and tightly packed particles inside large pores would affect the CT analyses results.

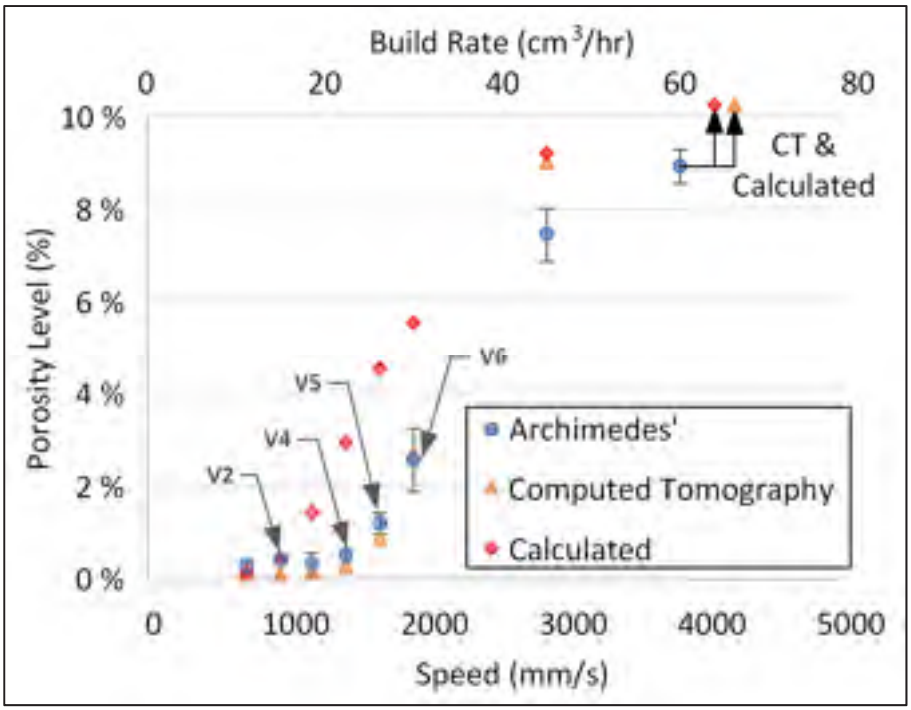

Figure 3.4 Calculated and experimentally-measured (Archimedes and CT) porosities as functions of the laser scanning speed; parameter sets V2, V4, V5 and V6 selected for mechanical testing

Table 3.3 Porosity levels: calculated and measured (Archimedes and CT); parameter sets V2, V4, V5 and V6 were selected for mechanical testing

Parameter Set	Porosity, %		
	Calculated	Measured	
		Archimedes	CT
V1	0.1	0.26 +/- 0.18	0.08
V2	0.4	0.39 +/- 0.08	0.06
V3	1.4	0.30 +/- 0.24	0.11
V4	2.9	0.50 +/- 0.08	0.25
V5	4.5	1.18 +/- 0.23	0.87
V6	5.5	2.53 +/- 0.69	2.67
V7	9.2	7.42 +/- 0.29	8.99
V8	12.9	8.90 +/- 0.38	19.32

Nevertheless, the trends depicted by the Archimedes and the CT techniques regarding the porosity-laser scanning speed relationship are identical, especially in the region of interest (0-3% porosity). According to these experiments, using a fixed power of 285 W, a hatching space of 0.11 mm, and a layer thickness of 40 μm, but varying the scanning speed from 720 to 1440 mm/s, LPBF IN625 can be manufactured with porosity levels below 0.5% (Parameter sets V1, V2 and V3). Above this speed, the porosity increases exponentially with respect to the scanning speed.

A T-test with a confidence level of 95% revealed that the difference in the porosity levels estimated by the Archimedes method was not statistically significant between specimens V1, V2 and V3. Based on these observations, it was deemed reasonable to select one of three "density-equivalent" parameter sets as a reference (high-density) parameter set. This set corresponds to the V2 processing conditions and it was used to manufacture specimens for microstructure analyses and mechanical testing. The additional parameter sets V4, V5 and V6, for which the experimental porosity levels gradually increase up to ~3%, were also selected, and are identified with lead lines in Figure 3.4.

Note that the porosity levels in larger specimens (tensile and compact) were found identical to those measured in smaller specimens (density), within the margins of measurement error. For visual assessment, the CT and metallographic images selected are shown in Figure 3.5 for the build (XY) and normal (YZ) planes. The regions presented here are limited to cubic subsections having a width equivalent to the metallography images (2.75 mm). Note that for the remainder of this manuscript, the CT porosity levels were rounded to 1 tenth of a %, and they were reported as 0.1, 0.3, 0.9 and 2.7% for specimens V2, V4, V5 and V6, respectively.

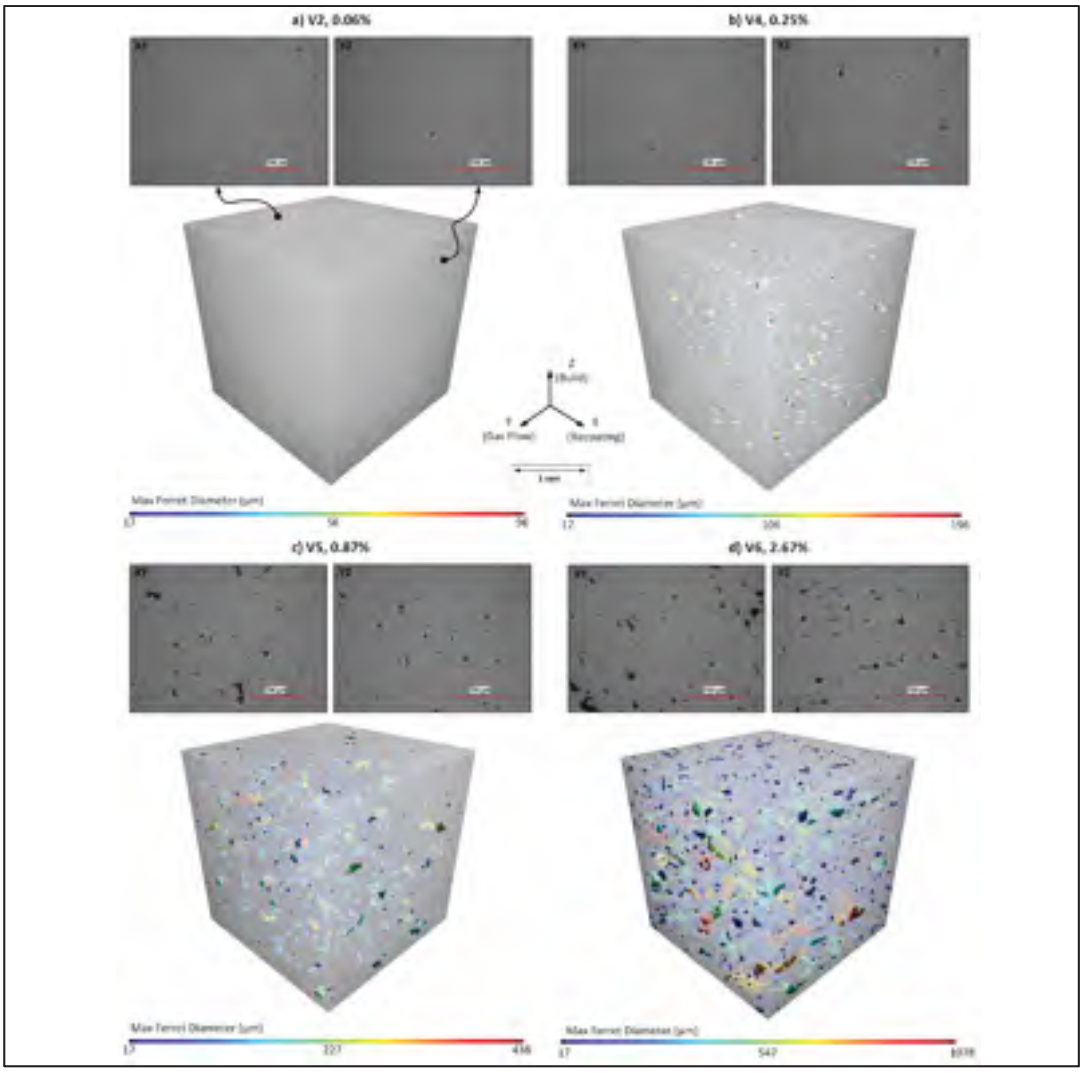

Figure 3.5 Processing-induced porosity observations using the CT and metallography techniques on LPBF IN625 specimens with parameter sets a) V2, b) V4, c) V5, and d) V6

3.6.2 Microstructure analysis

For the parameter sets identified in Section 3.1 (V2, V4, V5 and V6), the microstructures observed in the normal (YZ and XZ) and build (XY) planes are shown respectively in Figure 3.6 a) to d). Note that for a given parameter set, YZ and XZ maps correspond to different areas of the same EBSD map, and they were not taken from two different vertical planes. This simplification was deemed reasonable since the processing maps span across approximately

12 layers, rotated one to another by 67° (Criales et al., 2016). Also, an average grain size for specimens V2, V4, V5 and V6 was evaluated using the linear interception method on the EBSD map, the measures are reported in the Appendix.

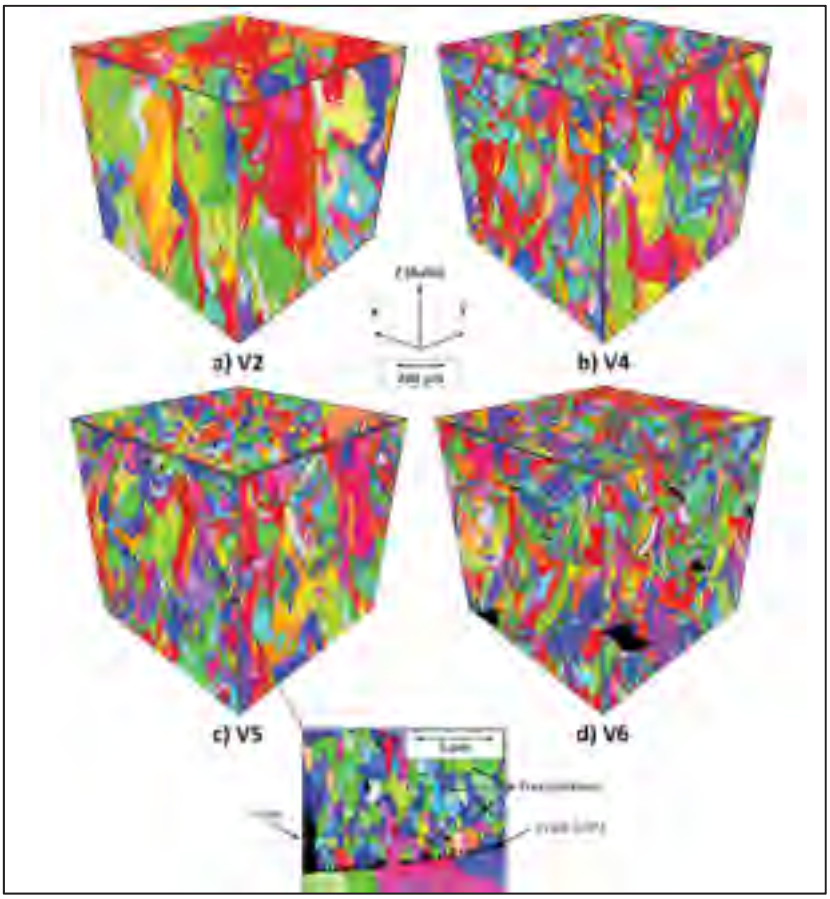

Figure 3.6 EBSD analysis results showing microstructure of specimens a) V2, b) V4, c) V5, and d) V6

3.6.3 Tensile mechanical properties

Typical stress-strain tensile diagrams of the 0 and 90°-oriented V2, V4, V5 and V6 specimens with porosities ranging from 0.1 to 2.7 % (V varies from 960 to 1920 m/s, P=285 W, h=0.11 mm, and t=40 µm) are shown in Figure 3.7. The mechanical properties and the porosity levels of all the tested specimens are presented in the Appendix (Table 3.6Table 3.5).

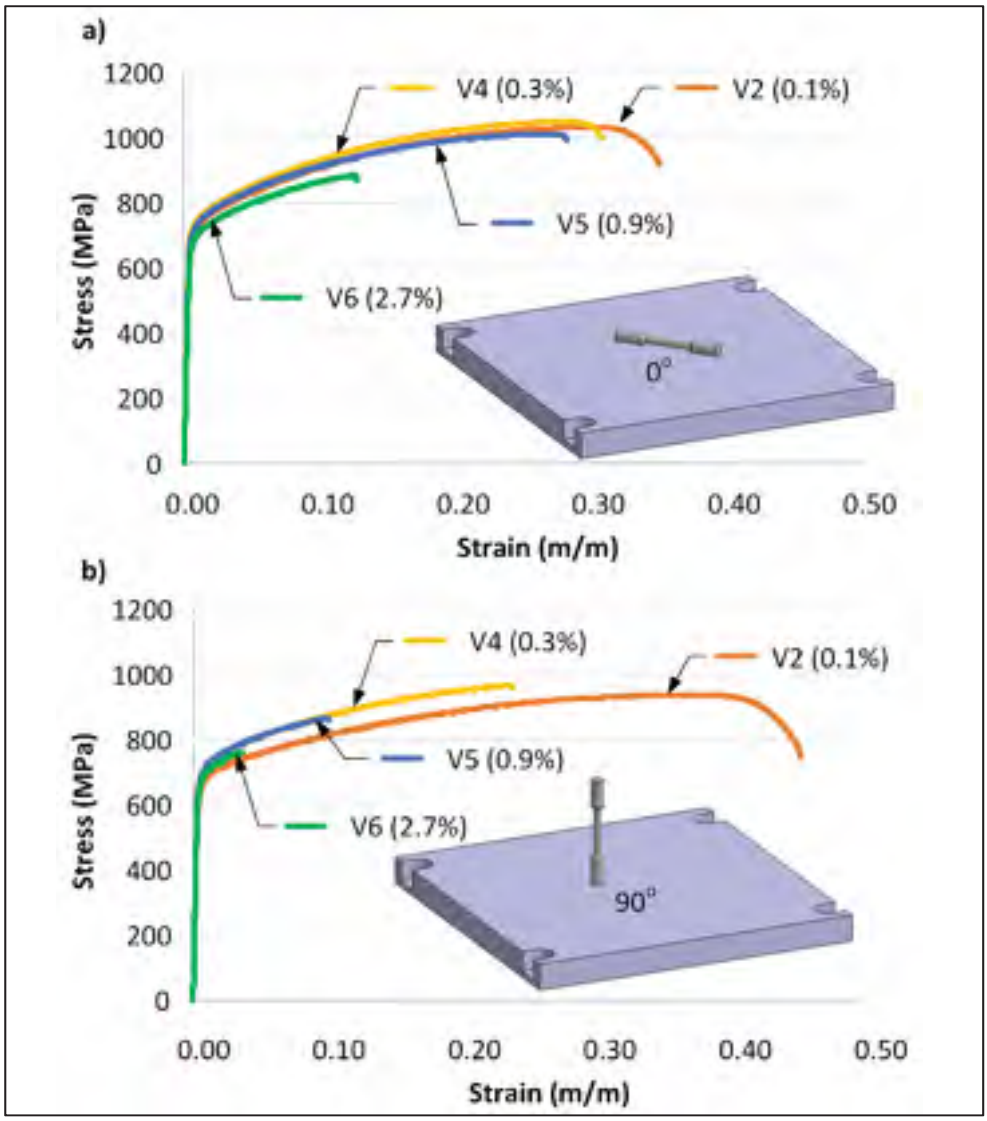

Figure 3.7 Typical tensile stress-strain diagrams obtained for the V2, V4, V5 and V6 parameter sets for the build orientations: a) 0º and b) 90º

3.6.4 Fatigue crack propagation behavior

Typical fatigue crack propagation diagrams obtained for specimens V2, V4, V5, V6 according to the plan described in Section 2 are shown in Figure 3.8a for the 90º-oriented specimens and in Figure 3.8b, for the 0º-oriented specimens. For each parameter set and orientation, the

Young's modulus was corrected for the initial compliance of uncracked specimens. It is worth mentioning that the results for the specimens with low porosity are in good agreement with our previous work (Poulin, Brailovski et Terriault, 2018).

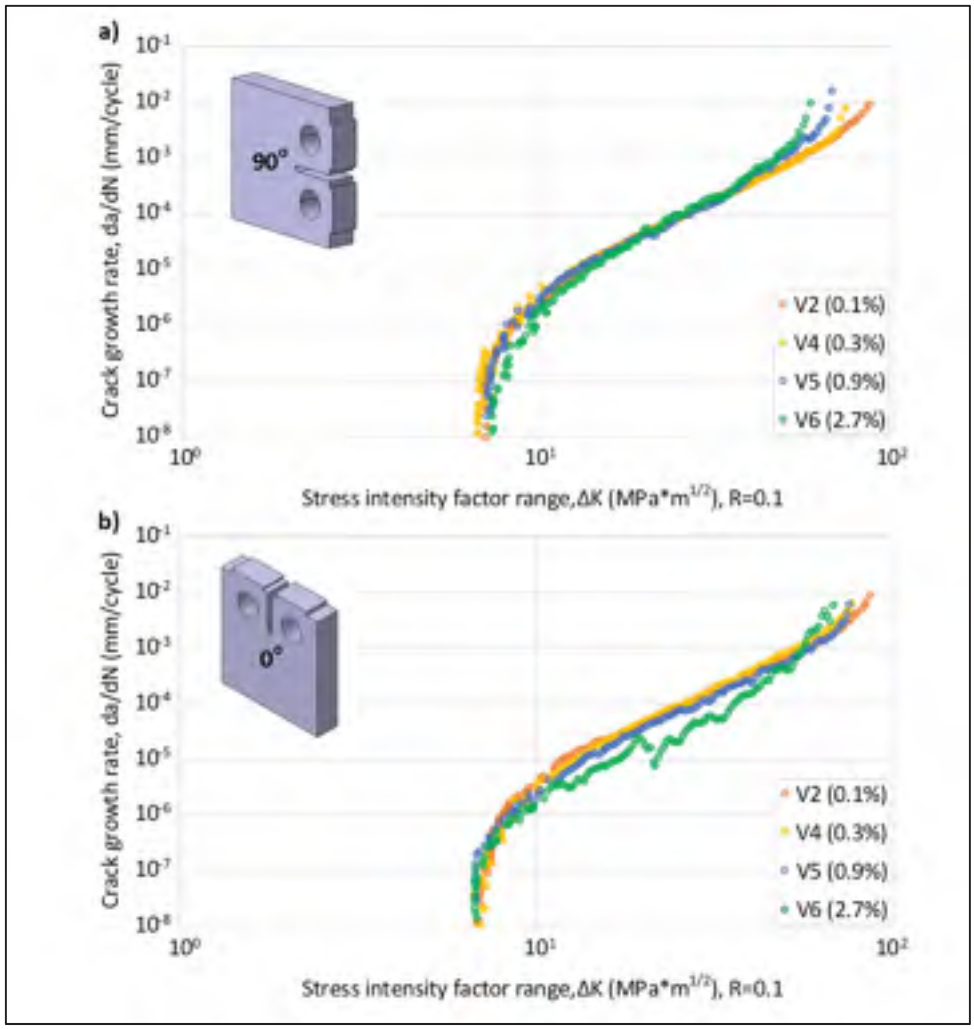

Figure 3.8 Fatigue crack propagation diagrams of the V2, V4, V5 and V6 IN625 LPBF specimens: a) 90°-oriented, b) 0°-oriented

Typical fracture surfaces of the compact specimens are also shown in Figure 3.9, for the 90° orientation, and in Figure 3.9b, for the 0° orientation. It is worth mentioning that even though they are generally not symmetrical in the near-threshold region, they meet the ASTM E647

specification criterion (difference in length below 0.25B) with the exception of the 0º-oriented V6 specimen. The resulting Paris diagrams for the V6 specimens were however in good agreement with other results, and they were therefore kept for this presentation.

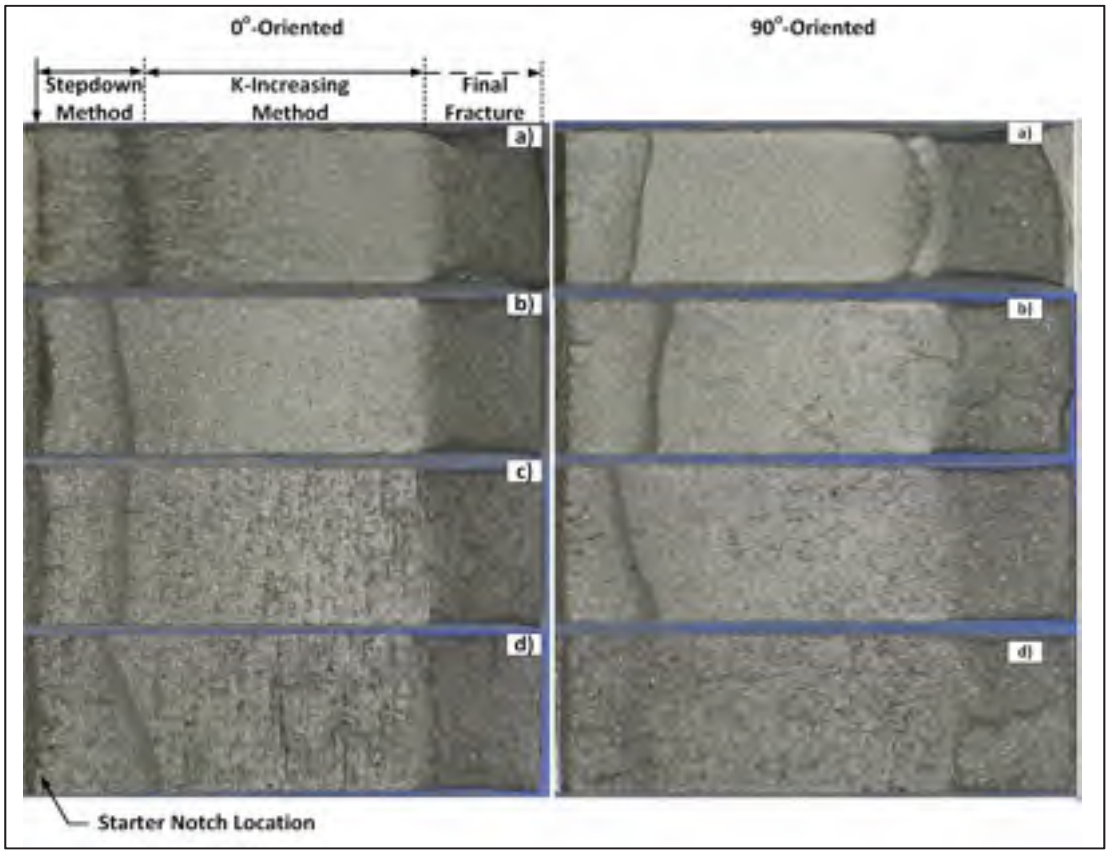

Figure 3.9 Fracture surface of the 0º and 90º-oriented compact specimens: a) V2, b) V4, c) V5 and d) V6

As depicted in Figure 3.8 a) and b), the crack propagation behavior does not appear to be strongly affected by the porosity level in the low SIF range. It is also the case in the Paris regime, with the exception of the 0º-oriented V5 and V6 specimens (Figure 3.8b). The crack growth in this case appears to be more erratic, with this effect being even more compelling in the case of V6 specimens (2.7%). Surprisingly, in the Paris regime, for these specimens, the crack growth rate was lower for specimens with higher porosity levels. When approaching the final fracture however (ΔK above ~40 MPa*$m^{1/2}$), the situation was reversed: the higher the

porosity level, the greater the crack growth and the lower the SIF at fracture. For high SIF ranges (above 50 MPa*$m^{1/2}$), where the small-scale yielding criterion is not met, there is an abrupt increase in the crack growth rate for specimens V5 and V6. The estimated fracture toughness K_c is found lower for increasing porosity. This is in agreement with the tensile testing results showing a lower elongation for these specimens.

Given the roughness of the fracture surface in the presence of porosity, additional tests were conducted at R=0.5 on 0°-oriented specimens to evaluate the crack growth rate with a minimum of roughness-induced crack closure. The Paris diagrams for the 0°-oriented specimens are shown in Figure 3.10 and depict a similar behavior: in the near-threshold region, all specimens have an equivalent behavior as well as in the Paris regime, with the exception of specimen V6, for which the crack growth rate evolution is more erratic.

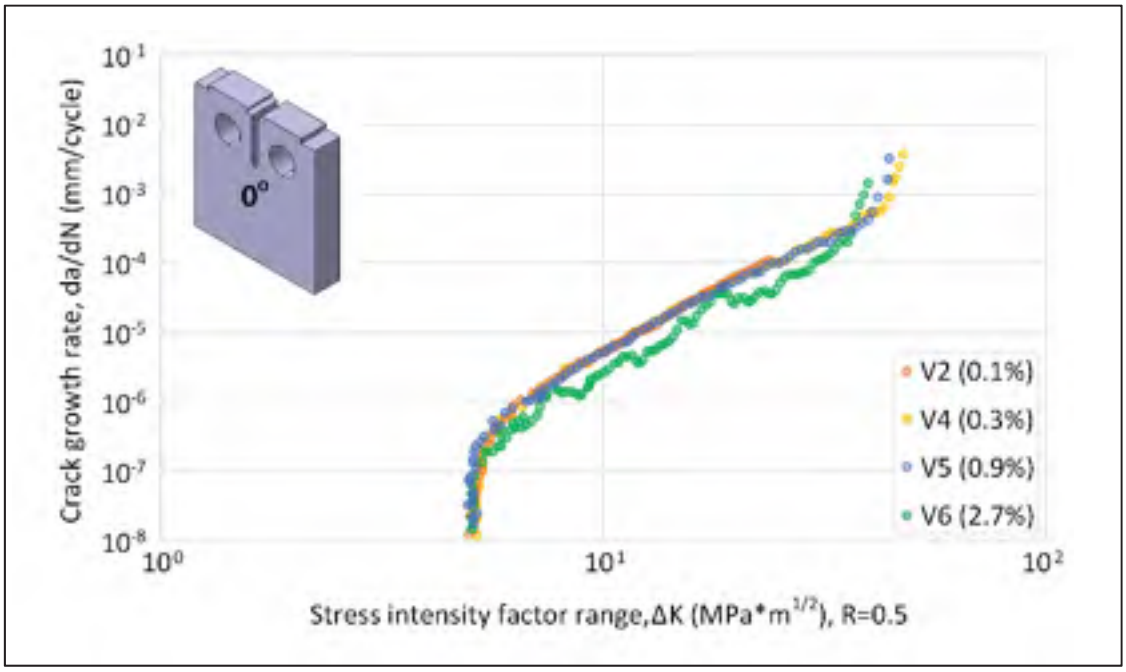

Figure 3.10 Fatigue crack propagation diagrams of the 0°-oriented V2, V4, V5 and V6 IN625 LPBF specimens for a stress ratio of R=0.5

Finally, using the Paris diagram obtained at R=0.1, the Paris Law's constants (C and m) were evaluated using the data points in the 15-50 MPa*$m^{1/2}$ SIF range. The threshold SIF range ΔK_{th} was also measured according to the ASTM E647 method, using the value corresponding to a crack growth rate of 10^{-7} mm/cycle. In addition, the SIF range at fracture was measured, and was used to calculate the toughness value (K_c). The K_c value should however be regarded as a comparative value between specimens since it was obtained under conditions where the small-scale yielding criterion was not met. The complete table of results is given in Table 3.4.

Table 3.4 Average fatigue properties measured from the fatigue crack propagation tests

Specimens		Porosity, %	C, E-09	m	ΔK_{th}, MPa·m ½	ΔK_{fc}, MPa·m ½	K_c, MPa·m ½
V2	0°	0.1	4.71	3.07	7.5	85.3	94.8
	90°		7.23	2.91	7.1	86.8	96.4
V4	0°	0.3	4.00	3.11	7.0	79.9	88.7
	90°		3.79	3.15	7.1	74.3	82.5
V5	0°	0.9	3.90	3.07	6.8	73.8	82.0
	90°		1.06	3.53	7.2	69.0	76.7
V6	0°	2.7	0.6	3.21	7.3	70.3	78.1
	90°		0.50	3.67	7.5	59.0	65.5

3.7 Analysis

3.7.1 Effect of laser scanning speed on porosity

An increase in bulk porosity levels with respect to the scanning speed was clearly indicated by the CT and Archimedes porosity analyses. The defect count and their size increase accordingly. A more detailed analysis was conducted to compare the pore size distributions of specimens V2, V4, V5 and V6. From the CT results, several metrics were obtained, namely, the max ferret diameter (Figure 3.11a) and the skewness factor evaluated by dividing the projected surface located in the build plane by the projected surface located in the normal plane (Figure 3.11b).

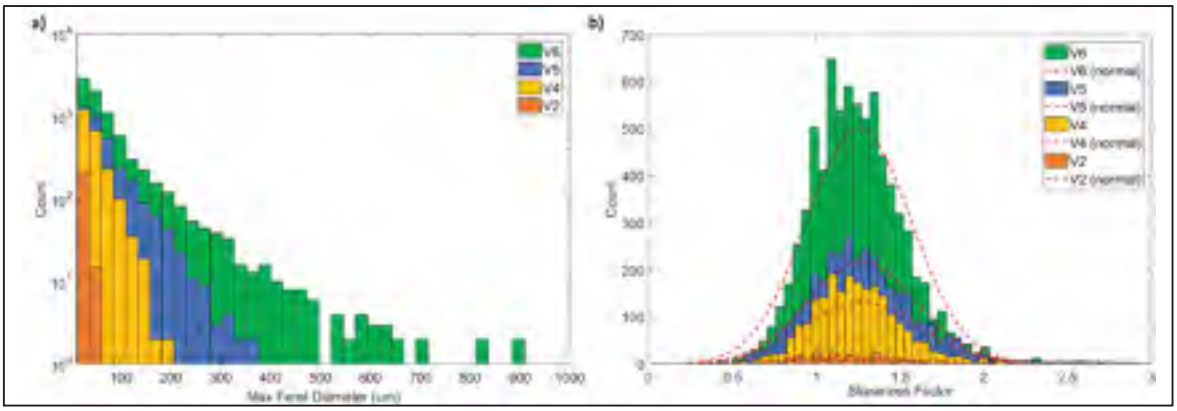

Figure 3.11 Results of CT analysis of specimens V2, V4, V5 and V6, a) Max ferret diameter and b) square root of projected surface in the build and normal planes

As seen in Figure 3.11 a), the higher the porosity level, the larger the defect size and the greater the number of large defects. For example, the maximum ferret diameter distribution varies significantly with respect to the scanning speed. For specimens V2, V4, V5 and V6, their maximum values are 96, 196, 438 and 1067 µm, respectively. Furthermore, from Figure 3.11 b), the skewness factor distributions confirm the fact that pores are elongated along the build plane. For all the datasets, the skewness factors range from ~0.5 to ~4, with an average value corresponding to 1.27 ± 0.3. Based on the metallographic observations, this type of pores corresponds mainly to that of lack-of-fusion defects caused by an insufficient size of the melt pool, as depicted in (Mukherjee et DebRoy, 2018). It can be expected from these observations that the lack-of-fusion porosity with pores being skewed along the build plane will have a more significant effect for 90°-oriented than for 0°-oriented specimens, since in the former case, the effective load-bearing surface is smaller, while the stress concentration is higher, than the same characteristics in the latter case.

3.7.2 Effect of laser scanning speed on the material microstructure

In LPBF built IN625 alloy processed with a higher scanning speed, or lower energy density, an irregular mixture of coarse columnar and fine equiaxed grains was developed as a result of two main concurrent solidification-related phenomena, more specifically, strong temperature gradients and high cooling rates. In the case of an adequate energy density, the columnar grain structure appears as a result of epitaxial grain growth from the melt pool boundaries caused by strong temperature gradients from the melting zone towards the build plate (see Figure 3.6a). In the case of insufficient power density and weak temperature gradients, heterogeneous nucleation of clustered fine near-equiaxed grains occurs (Blackwell, 2005; Liu et al., 2013; Wang et al., 2015) (see Figure 3.6c). The EBSD map for these regions reveals that these equiaxed grains are very fine (their size ranges from ~0.3 to ~1 μm) and they are mostly clustered around defects (pores) where columnar grain growth is suppressed. It is worth mentioning that the higher the scanning speed, the greater the number of pores and the greater the fraction of these equiaxed grains. According to the grain size estimation from Annex (Table 3.5), with an increasing scanning speed, the sizes of both the columnar and equiaxed grains decrease due to higher cooling rates (Li, Guo et Zhao, 2017; Yadroitsev et al., 2013). With the increasing scanning speed, the grain size anisotropy is reduced significantly, and the texture becomes more random.

It is generally agreed that fatigue crack propagation becomes strongly microstructure-sensitive in the near-threshold region (Stage I), and this impact is diminished in the Paris regime (Stage II) (Hertzberg, Vinci et Hertzberg, 2012; Krupp, 2007; Suresh, 1998). The literature shows that early in the fatigue crack formation (Stage I), the crack grows along slip bands that form in the direction of active slip systems (Balachandramurthi et al., 2019). On the one hand, a coarser microstructure has been shown to increase the slip band length, thus increasing the threshold SIF by promoting the roughness-induced crack closure effect (Morrison et Moosbrugger, 1997; Poulin, Brailovski et Terriault, 2018). In addition, the texture can also contribute to a similar effect: higher angle grain boundaries generate a more effective microstructural barrier to crack

propagation at Stage I, when cracks have to change their direction when propagating into adjacent grains (Gao et al., 2007; Miao, Pollock et Wayne Jones, 2012; Wilkinson, 2001; Wilson et Dunne, 2019), especially at room temperature when less slip systems are active. The same trend can be expected at elevated temperatures, when the fracture mode for this material changes from intergranular to transgranular (Caton et Jha, 2010; Suave et al., 2016), and cracks can propagate along the interface between the columnar and equiaxed regions (Liu et al., 2013).

3.7.3 Effect of laser scanning speed on the mechanical properties

In Figure 3.12, normalised mechanical properties from Table 3.6, namely the Young's modulus E, the Yield stress YS, the ultimate tensile strength UTS, and the elongation at break δ are plotted as functions of the build orientation for different porosity levels studied in this work. In this figure, the mechanical properties are normalised using the corresponding values of V2 specimens.

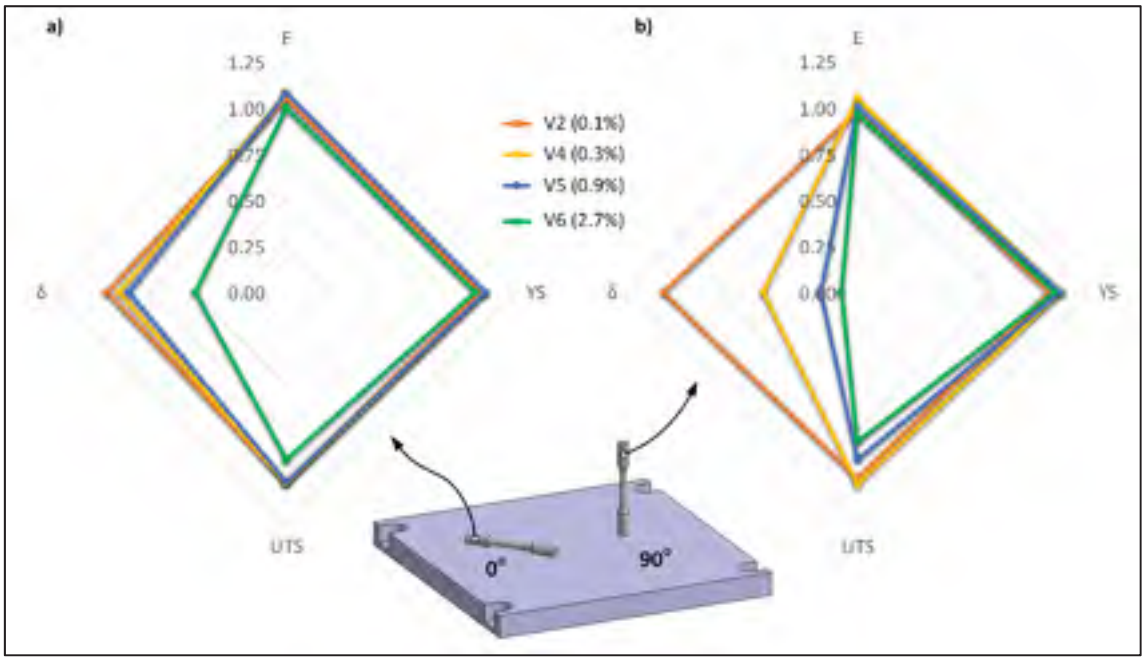

Figure 3.12 Normalised mechanical properties (V2) for two build orientations: a) 0° and b) 90°

When comparing the properties for specimens manufactured with various laser scanning speeds (Figure 3.12a) and b)), it can be seen that the E and YS values remain similar for all the porosity levels tested. Surprisingly, YS is even slightly higher for specimens V4 and V5 as compared to specimens V2, despite the higher porosity levels of the formers (see Table 3.3). In this case, as indicated by the EBSD analysis, an increase in laser scanning speed (V2, V4, V5 and V6) results in higher cooling rates and finer microstructures (Kreitcberg et al., 2017). It means that for these relatively small porosities, the material strengthening caused by grain refinement (Hall-Petch effect (Kozar et al., 2009)) outweighs the material weakening caused by the presence of pores, as far as the YS values are concerned.

In the plastic deformation regime however, a significant drop in elongation at break indicates that the mechanical behavior of most specimens is strongly affected by porosities. In the case of specimens built at 0^{o} (Figure 3.12a), the reduction in elongation at break for low porosities is limited (V4 and V5), while for those built at 90^{o}, the ductility decreases significantly even at the lowest porosity levels (see Figure 3.12b).

Lightly flawed specimens showed very limited loss in UTS since their strain hardening capacity remained high (see Figure 3.7a). As indicated in Figure 3.12, the presence of pores has a stronger impact for specimens built at 90^{o}. In this case, there is a strong decrease in elongation at break for each scanning speed increment. The UTS is also more defect-sensitive for this orientation. As a result, the mechanical behavior of the LPBF IN625 becomes highly anisotropic when the scanning speed is increased. While the increase in scanning speed appears to promote the development of a finer, more equiaxed microstructure, the presence of pores which are skewed along the build plane appears to be responsible for a higher anisotropy of the mechanical behavior of porous specimens.

3.7.4 Fatigue crack propagation behavior

In this study, the strategy employed to generate defects resulted in two somewhat contradictory trends: the higher the porosity, the finer and less textured the microstructure, the former trend weakening the material whereas the latter trend, strengthened it. This notwithstanding, the microstructure evolution resulting from scanning speed variations did not significantly affect the threshold SIF. For the orientations considered, they were all found equivalent to the cases reported in (Poulin, Brailovski et Terriault, 2018).

All the parameter sets and orientations considered in this study resulted in a threshold SIF ranging from 6.8 to 7.5 MPa*$m^{1/2}$. Given the testing method for threshold SIF estimation (stepdown with 10% load shedding), these differences are not considered significant. The additional tests conducted at higher stress ratios (R=0.5) confirmed these observations. For this last condition, the threshold SIF was estimated at 5.1-5.3 MPa*$m^{1/2}$ for all the parameter sets. Above threshold, when comparing the fatigue crack propagation diagrams from Section 3.4, there appears to be a limited effect of porosity on the long crack propagation behavior in the near threshold region. As a result, we believe the threshold SIF could be an interesting design and quality control criterion (Riemer et al., 2014) for the acceptance of LPBF-built IN625 components. In comparison, works on powder metallurgy showed that when porosity was at a lower bound of the process (5%), the threshold intensity factor was only slightly lower than that in the case of porosity-free specimens (Hadrboletz et Weiss, 1997); it started to be affected significantly when porosity approached 10%. It can therefore be hypothesized that in our work, the critical porosity level affecting the threshold for fatigue crack propagation was not reached. In the Paris regime (Stage II), as the SIF range was increased, the crack propagation behavior appeared to be sensitive to the presence of defects. Surprisingly, for 0^{o}-oriented specimens, above the threshold value (from $\Delta K \sim 10$ MPa*$m^{1/2}$), specimens V5 and V6 showed lower crack propagation rates. There appears to be an interaction of the crack front with defects which translates to a lower, while more erratic, growth rate in the Paris regime. To illustrate this, a fatigue crack growth curve was plotted as a function of the crack length and superimposed on

the matching fracture surface in Figure 3.13. The red arrows indicate that the regions where the crack growth decreases or remains constant correspond to those where the crack front meets large defects.

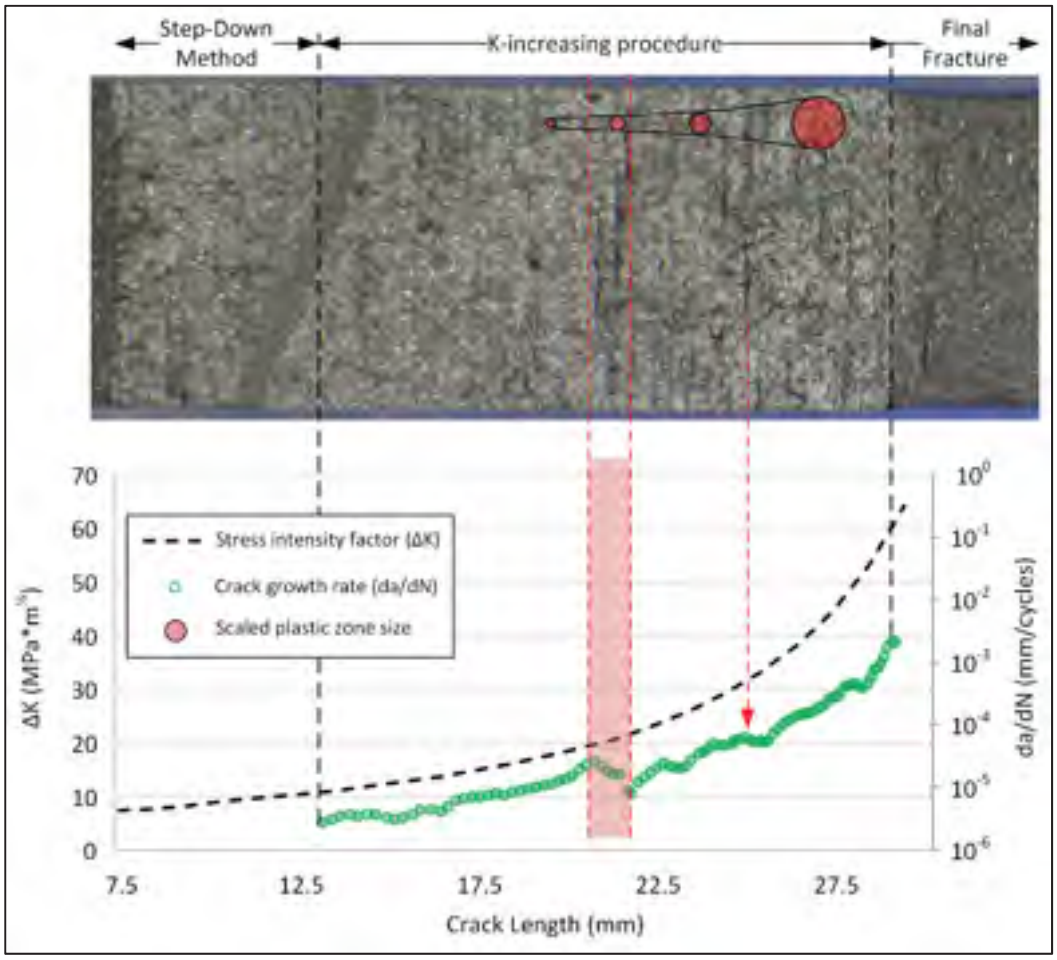

Figure 3.13 Crack growth rate and SIF as functions of the crack length for specimen V6-0°, superimposed on the crack surface

In Figure 3.14a, Paris diagrams for 0° and 90°-oriented V6 specimens are compared and they illustrate a strongly anisotropic crack growth behavior for highly-porous specimens. This occurs despite the more isotropic microstructure resulting from this parameter set, suggesting that in our case, the effect of microstructure on the crack growth rate is less significant than the effect of porosity. Regarding the properties, this corresponds to a strong increase in constant

m with respect to the porosity level for 0º-oriented specimens (from 2.9 to 3.6 for 0.1 to 2.7% porosity). Conversely, the m constants of 90º-oriented specimens are close for all porosity levels (3.1 to 3.2)

It is hypothesized that the defects act as crack-retardants in the 0º-oriented specimens due to the crack branching mechanism. This mechanism is known to reduce the crack growth rate and it was demonstrated, using FEA modeling and experimental observations, to be insignificant for branches below 45º, and maximum, when branches approach 90º (Meggiolaro et al., 2005; Pavlou et al., 2004). This is in agreement with our experimental results, showing a strong retardation effect for the 0º-oriented V6 specimens, for which the branches are perpendicular to the main crack (see Figure 3.14 b), and a very limited effect for the 90º-oriented V6 specimens, for which the branches propagate parallel to the main crack (see Figure 3.14 c). Because of random distribution of the defects and their relatively small size as compared to the specimen thickness, this mechanism is believed to take place locally and, as a result, it is not observed for specimens with low porosity. In addition, when fatigue branching occurs as the crack bridges a pre-existing crack-like defect, an overload may appear in other regions of the specimen contributing to crack retardation; this mechanism being well documented in the literature (Pereira et al., 2007; Skorupa, 1998; Yuen et Taheri, 2006). That notwithstanding, the crack retardation observed in the highly-porous specimens could be the result of a combined effect of these two mechanisms.

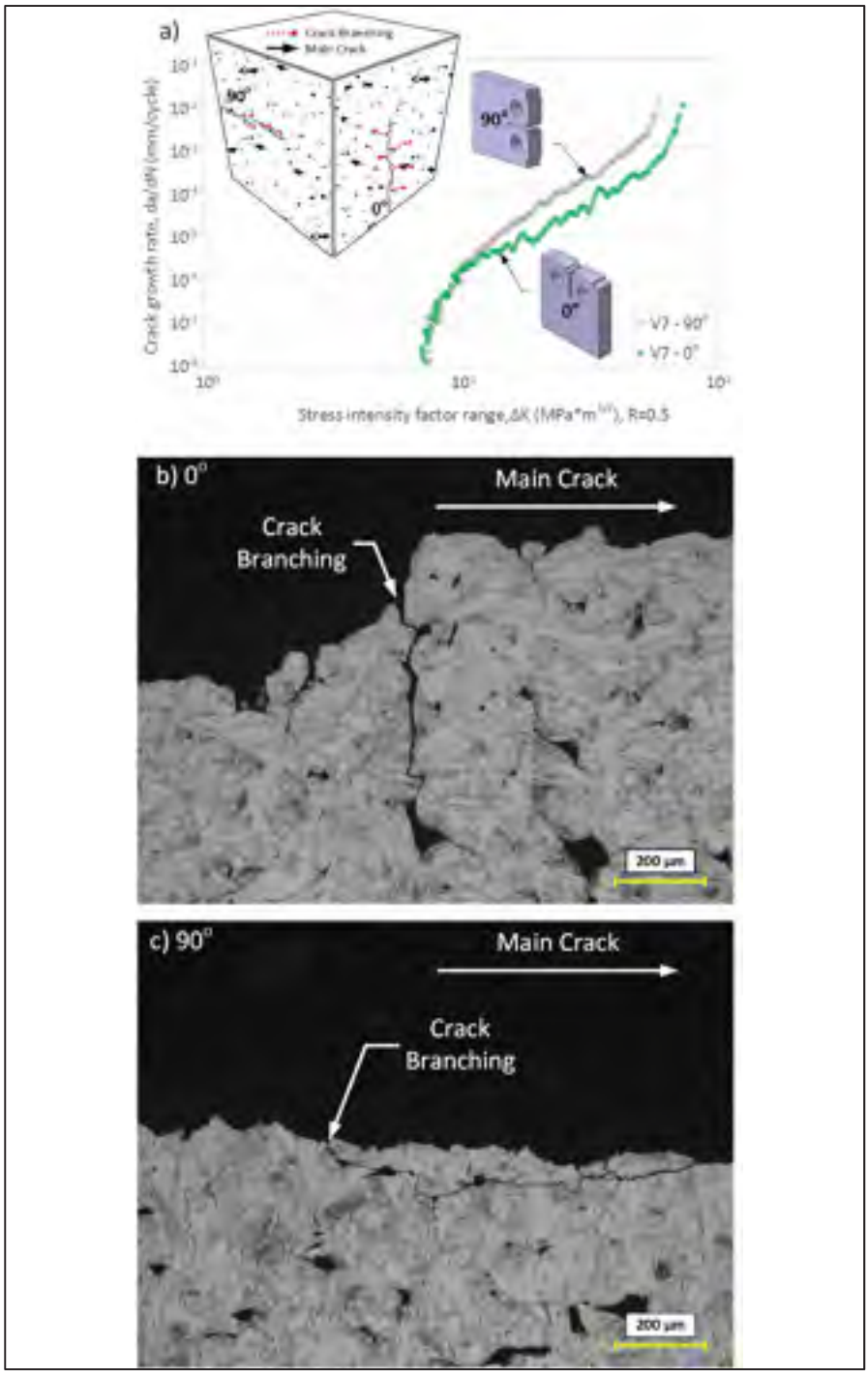

Figure 3.14 a) Paris curves for 0° and 90°-oriented V6 specimens, R=0.1, b) typical crack branching for 0°-oriented V6 specimens and c) typical crack branching observed on 90°-oriented specimen

Finally, using the Paris diagram obtained at R=0.1, the Paris Law's constants (C and m) were evaluated using the data points in the 15-50 MPa*m1/2 SIF range. The threshold SIF range ΔKth was also measured according to the ASTM E647 method, using the value corresponding to a crack growth rate of 10-7 mm/cycle. In addition, the SIF range at fracture was measured, and was used to calculate the toughness value (Kc). The Kc value should however be regarded as a comparative value between specimens since it was obtained under conditions where the small-scale yielding criterion was not met. The complete table of results is given inFinally, using the Paris diagram obtained at R=0.1, the Paris Law's constants (C and m) were evaluated using the data points in the 15-50 MPa*$m1^{/2}$ SIF range. The threshold SIF range ΔKth was also measured according to the ASTM E647 method, using the value corresponding to a crack growth rate of 10-7 mm/cycle. In addition, the SIF range at fracture was measured, and was used to calculate the toughness value (Kc). The Kc value should however be regarded as a comparative value between specimens since it was obtained under conditions where the small-scale yielding criterion was not met. The complete table of results is given in Table 3.4.

Table 3.4 depicts strong porosity and build orientation dependencies. In all the cases, the higher the porosity, the lower the SIF of the specimens at final fracture. This behavior is in good agreement with the results from tensile tests, which highlighted the lack of ductility resulting from the presence of pores, especially for the 90^{o}-oriented tensile specimens. Interesting fact is that a critical level of porosity significantly affecting the mechanical behavior of LPBF alloy is much lower in the case of static tensile testing than in the case of crack propagation testing, which is probably the result of differences in related mechanisms of damage accumulation and propagation: one occurring on global scale (in the entire body of tensile specimens) while the other, on local scale (in the vicinity of the crack tip of compact specimens for crack propagation testing). The crack propagation diagrams also depict this trend, as the impact of porosity becomes more apparent when the stress intensity factor, and therefore the plastic zone in the vicinity of the crack tip, increase.

3.8 Conclusion

In this study, porosities of up to ~10% were generated in LPBF Inconel 625 specimens by varying the laser scanning speed from 720 to 3840 mm/s. Next, specimens with intentionally-seeded porosities of 0.1, 0.3, 0.9 and 2.7% resulting from scanning speeds of 960, 1440, 1680 and 1920 mm/s, respectively, were subjected to defect and microstructure analyses, and to mechanical testing. The CT observations of defects revealed that pores resulting from this increase in scanning speed are significantly skewed along the build plane. Furthermore, the microstructures observations revealed than this increase in scanning speed results in a finer and more equiaxed microstructure with clusters of fine sub-micrometer grains along the lack-of-fusion defects. Next, tensile mechanical properties (ASTM-E8) of porous specimens built in two orientations (0 and 90^{o}) were measured, and while the material resistance was not strongly affected, a significant loss of ductility was seen when increasing the porosity, especially for the 90^{o}-oriented specimens. Finally, fatigue crack propagations testing showed that the 0.1-2.7% porosity has a very limited effect on the near-threshold fatigue crack propagation behavior of LPBF IN625 alloy: all threshold values situated in the 6.8-7.5 MPa*m$^{1/2}$ range (R=0.1); this effect being more pronounced for high SIF values.

According to these findings, a threshold SIF defined by means of the linear elastic fracture mechanics could be used to guide the commissioning of LPBF parts containing gas filled pores and lack-of-fusion defects. This approach was shown to be promising for conditions where linear elasticity assumptions are verified (when small scale yielding prevails) and for a relatively wide range of porosities and microstructures. Furthermore, this fracture mechanics approach could be combined with the widely implemented in the industry stress-life approach -- to correlate the fatigue life of LPBF components with the level of processing-induced defects (Kitagawa-Takahashi method (Kitagawa, 1976), using El-Haddad's formulation (El Haddad, Topper et Smith, 1979)). With this objective in mind, future work must be conducted to use the findings presented in this manuscript and support the implementation of the damage tolerance approach for the design and quality control of LPBF parts

3.9 Acknowledgement

The authors would like to thank the Fonds de Recherche du Québec - Nature et Technologie (FRQNT), and the National Science and Engineering Research Council of Canada (NSERC) for their support in financing the present study. In addition, thanks also go to Morgan Letteneur, David Guévremont and Alexandre Boucher for their contributions in the experimental phase of this project

3.10 Annex

Table 3.5 Grain size evaluated by linear interception method for specimens V2, V4, V5, V6

Parameter Set	Orientation	Grain size range (µm)	Average size (µm)	ASTM #	Max size (µm)
V2	XZ	25-40	30	7	150
V4	XY	15-20	18	8.5	120
V5	XY	12-16	14	9	100
V6	XY	10-15	12	10	75
V2	YZ	75-150	100	3.5	600
V4	YZ	40-50	45	6	300
V5	YZ	30-50	35	7	300
V6	YZ	15-25	18	8.5	150

Table 3.6 Mechanical properties of specimens V2, V4, V5 and V6

Parameter Set	Porosity (%)	E (GPa)	YS (MPa)	UTS (MPa)	Elongation (%)
SR Specimens					
V2 – 0°	0.1	194 ± 5	689 ± 4	1035 ± 7	33.4 ± 2
V4 – 0°	0.3	199 ± 1	704 ± 2	1036 ± 3	31.0 ± 2
V5 – 0°	0.9	198 ± 5	707 ± 4	1030 ± 18	29.3 ± 5
V6 – 0°	2.7	184 ± 3	672 ± 4	909 ± 16	16.9 ± 1
V2 – 90°	0.1	189 ± 3	637 ± 1	934 ± 2	46.0 ± 1
V4 – 90°	0.3	202 ± 5	676 ± 4	966 ± 18	22.3 ± 5
V5 – 90°	0.9	193 ± 4	673 ± 3	840 ± 58	8.8 ± 4
V6 – 90°	2.7	185 ± 4	651 ± 4	749 ± 17	4.3 ± 1

CHAPITRE 4

FATIGUE STRENGTH PREDICTION OF LASER POWDER BED FUSION PROCESSED INCONEL 625 PARTS WITH INTENTIONNALY SEEDED POROSITY: FEASABILITY STUDY

J-R. Poulin[1], A. Kreitcberg, P[1]. Terriault[1], V. Brailovski[1,*]

[1]Department of Mechanical Engineering, École de technologie supérieure,

*Corresponding author: Vladimir Brailovski, Department of Mechanical Engineering, École de technologie supérieure, 1100 Notre-Dame Street West, Montreal, Quebec, Canada, H3C 1K3 (vladimir.brailovksi@etsmtl.ca, tel: 514-396-8594)

Article publié dans la revue « International Journal of Fatigue », vol. 132., 2020.

4.1 Avant-Propos

Les travaux présentés au chapitre précédent ont montré que le seuil de propagation de fissure est peu affecté par la porosité obtenue lors de la mise en forme par LPBF avec un niveau d'énergie sous-optimal (0 à 2.7%). Pour la troisième portion de ce projet, les courbes da/dN - ΔK (seuil de propagation de fissure) sont employés pour mettre en relation la taille des défauts et l'amplitude de contrainte cyclique qui peut être appliquer. Pour ce faire, des échantillons de fatigue ayant divers taux de porosité sont produits à partir de la méthode proposée au Chapitre 3. Des essais de fatigue sous force contrôlée sont réalisés sur ces échantillons pour valider l'applicabilité du modèle d'El-Haddad aux matériaux obtenus par LPBF.

4.2 Résumé

Dans cet article, des échantillons de fatigue sont fabriqués par LPBF avec différents niveaux de porosité dans la section d'essai (≤0.1 à 2.7%) et assujettis à un traitement thermique de relaxation de contraintes. Le nombre et la distribution de taille de défauts induits sont évalués

par microtomographie aux rayons X. Pour étudier l'effet des défauts de fabrication sur la vie en fatigue, des essais de fatigue à température ambiante, contrôlés en force, sont réalisés sur les échantillons les moins poreux (fréquence 30 Hz, R = 0.1). La limite de fatigue des échantillons avec la plus faible porosité a été identifiée à 590 MPa. Par la suite, en employant le modèle de El-Haddad et la description de taille de défauts proposés par Murakami, la limite de fatigue des échantillons ayant des taux de porosité supérieure est évaluée. La limite de fatigue prédite est légèrement conservatrice, mais l'écart maximal montre une prédiction intéressante du modèle avec un maximal de moins de 8%.

4.3 Abstract

(≤ 0.1, 0.3, 0.9 and 2.7%) were manufactured by laser powder bed fusion and subjected to stress relief annealing. The morphology, number and distribution of seeded defects were characterized using the micro-computed tomography technique. The effect of the different levels of porosity on the high cycle fatigue behavior of these specimens was studied using room temperature force-controlled fatigue testing according to the ASTM E466 standard (frequency of 30 Hz; R=0.1) with a runout at 10^7 cycles. The fatigue strength of specimens with the lowest level of porosity (≤0.1%) was found to be 590 MPa. Next, using El-Haddad's formulation of the Kitagawa-Takahashi model defining the limiting conditions for fatigue failure in the presence of defects and Murakami's parameter for defect size rating, the fatigue strengths of specimens with 0.3, 0.9 and 2.7% porosity were predicted at 280, 190 and 160 MPa, respectively. The predicted values were found to deviate by less than 8% from the experimental results, which were, respectively, 288, 207 and 170 MPa.

Keywords: Additive manufacturing, Laser powder bed fusion, Selective laser melting, Nickel-based superalloy, Fatigue behavior, Porosity

4.4 Introduction

In recent years, the fatigue behavior of laser powder bed fusion (LPBF) manufactured metallic components has attracted a lot of interest from the research community. This interest is caused by the uncertainty related to the ability of LPBF-built metallic components to sustain cyclic loading conditions, which is especially important for critical components (Gorelik, 2017; Seifi et al., 2017; Seifi et al., 2016). Indeed, despite the fact that the quasi-static mechanical properties of LPBF components are on par with those of their wrought counterparts, scatter in the fatigue life of the LPBF components has been found to be significantly higher than of the wrought components (Luo et al., 2019; Sterling et al., 2015; Tammas-Williams et al., 2017). This scatter is attributable to the presence of a significant number of defects and heterogeneities of various nature in the LPBF material, which are detrimental to fatigue life (Hrabe, Gnäupel-Herold et Quinn, 2017a; Murakami et Endo, 1994; Prithivirajan et Sangid, 2018). As a result, the microstructure and integrity, and, thus, the fatigue properties of LPBF components, are strongly dependent on processing and post-processing conditions (Li et al., 2016).

As far as the fatigue behavior is concerned, the quality of LPBF-built surfaces is particularly detrimental to fatigue life. The layer-by-layer approach employed during LPBF causes a staircase effect, which results in a relatively rough and orientation-dependent surface finish: surface roughness values (R_a) ranging from 7 to 20 μm are typically obtained (DebRoy et al., 2018). Additionally, the presence of partially bonded particles is often reported, especially on unsupported down-facing surfaces (Mumtaz et Hopkinson, 2009; Strano et al., 2013). These surface artifacts ease crack nucleation by acting as strain concentrators. Moreover, fast and directional cooling during LPBF yields very specific microstructures, often reported to be anisotropic, and generates significant residual stresses, which also affect the fatigue behavior of materials (Deng et al., 2017; Nicoletto, 2017). Surface post-processing and heat treatments of LPBF components are therefore critical as they can improve the fatigue behavior by reducing the negative influence of surface artifacts, anisotropic microstructure and residual stresses (Li et al., 2016; Yadollahi et Shamsaei, 2017).

However, even in LPBF components subjected to adequate heat treatment and surface finishing operations, fractographic examinations often identify internal or volumetric defects that play the role of the fatigue crack nucleation sites (Biswal et al., 2019; Brandl et al., 2012; Hrabe, Gnäupel-Herold et Quinn, 2017b; Meneghetti, Rigon et Gennari, 2019). These defects have been shown to be particularly detrimental in the high cycle fatigue (HCF) domain (Hertzberg, Vinci et Hertzberg, 2012). In such cases, processing-induced defects act as stress raisers and promote crack nucleation, which typically accounts for up to ~80% of the total life in the HCF regime (Hertzberg, Vinci et Hertzberg, 2012; Krupp, 2007).

The most commonly observed volumetric LPBF-induced flaws are lack-of-fusion (LOF) defects, gas-containing pores, inclusions and cracks (Kasperovich et al., 2016; Koutiri et al., 2018; Ziółkowski et al., 2014). As far as the fatigue properties are concerned, the LOF defects appear to be the most threatening. They are typically described as high aspect ratio voids, often containing a mix of unfused powder and gas from the build atmosphere with sharp crack tips acting as powerful stress raisers (Masuo et al., 2018). Although hot isostatic pressing (HIP) post-processing has been shown to be effective in reducing porosity in LPBF components, many concerns remain regarding the limits of efficiency of this technique for the LOF defects (Shao et al., 2017; Tammas-Williams et al., 2016a; Tammas-Williams et al., 2016b).

Given the challenges posed by the presence of defects in LPBF components, there is a need to correlate the life of cyclically loaded LPBF components with the defects inherent in their manufacture (Gorelik, 2017). The onset of fractures in LPBF components can be studied at different length scales, spanning from the level of crystal plasticity to that of the elastic-plastic fracture mechanics (EPFM) or linear-elastic fracture mechanics (LEFM), every of the levels of modeling having different underlying hypotheses, simplifications and applications (Miller, 1997). On the one hand, models based on crystal plasticity deal with microstructure-sensitive behaviors, such as crack nucleation and microstructurally short crack growth, using virtual models representing statistically representative volumes matching the material's

microstructural features (Chen, Jiang et Dunne, 2017; Han et al., 2018; Prithivirajan et Sangid, 2018). On the other hand, while it does not apply to very small defects, the LEFM models can predict the behavior of cracks typically one order of magnitude larger than grain size.

The LPBF approach is also convenient for engineering applications since the long crack growth behavior can be readily evaluated by means of standardized procedures such as those described in ASTM E647 (*Standard Test Method for Measurement of Fatigue Crack Growth Rates*, 2015) or ISO 12108 (ISO 12108, 2002). Given the fact that LOFs are often significantly larger than grain or subgrain size, applying LEFM for the evaluation of the fatigue resistance of LPBF components seems reasonable. It was already shown that the fracture mechanics-based approach can be employed to predict conditions ensuring non-propagation of processing-induced LOF defects under cyclic loading, using experimentally-measured fatigue crack propagation thresholds and defect size (Masuo et al., 2017). The application of classic fracture mechanics to the assessment of the fatigue resistance of LPBF-built aluminium and titanium alloys has been shown to be as effective as it is for their wrought counterparts (Beretta et Romano, 2017).

Furthermore, an intrinsic threshold SIF (ΔK_{eff}) can be evaluated by this technique and applied to short cracks (Zerbst et al., 2016). The ΔK_{eff} value can be estimated by performing typical long crack propagation testing in the absence of crack closure, by using high stress ratios (R), with the minimum SIF being higher than the crack closure SIF (McCarver et Ritchie, 1982). Moreover, stress intensity factor (SIF) calculations are relatively simple, since analytical solutions can be employed for simple cases, and many calculation routines are already implemented in commercial FEA packages.

In addition, LEFM holds true when the material remains predominantly elastic (i.e., small plastic zone size), which is often verified in engineering applications designed to serve in the HCF domain. Next, hypothesizing that the LPBF-generated LOF defects can be treated as cracks due to their high aspect ratio and sharpness, the Kitagawa-Takahashi diagram

(Kitagawa, 1976), as shown in Figure 4.1, appears to be an interesting tool for evaluating the safe design zone for infinite life (zone of non-propagating cracks (Beretta et Romano, 2017; Patriarca, Filippini et Beretta, 2018; Romano et al., 2018; Torries et al., 2018)).

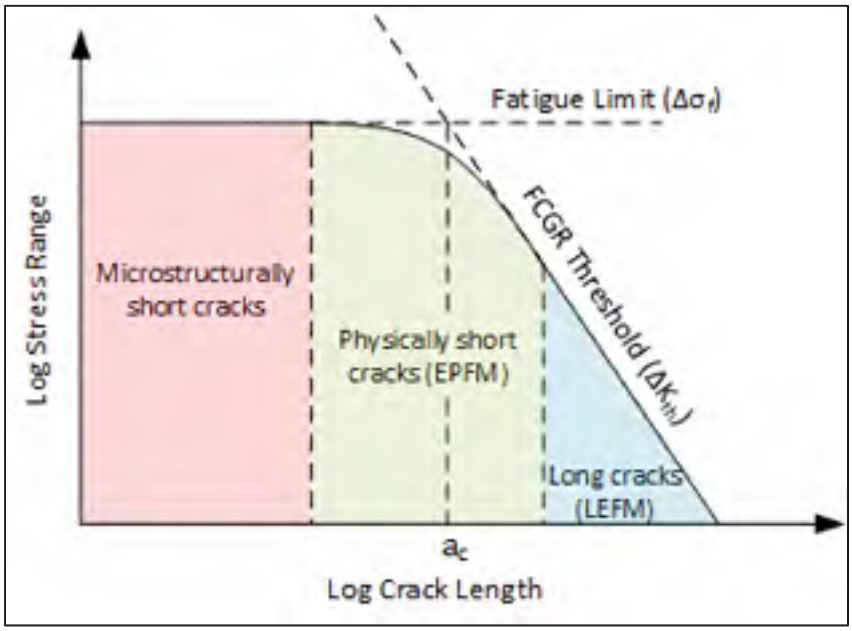

Figure 4.1 Representation of the Kitagawa-Takahashi diagram, adapted from (Zerbst et al., 2016)

In this approach, the fatigue strength evaluated by the stress-life approach is combined with the threshold stress intensity factor from fracture mechanics to evaluate the permissible stress range ($\Delta\sigma$), depending on size of processing-induced defects. In the original approach proposed by Kitagawa-Takahashi (Kitagawa, 1976), a threshold SIF for long cracks was employed to evaluate a critical flaw size. This method has been shown to be non-conservative, since short cracks are known to propagate at lower SIF ranges than those predicted by Paris diagrams obtained for long cracks (Miller, 1982; Spagnoli, 2004). To account for these limitations, El Haddad and Topper (El Haddad, Smith et Topper, 1979) proposed to calculate the size of an intrinsic defect using the classic LEFM relationship between the stress intensity factor and the applied stress (Equation 1).

$$\Delta K = Y * \Delta\sigma * \sqrt{\pi * a} \qquad \text{Equation 1}$$

Using a fatigue strength defined in the absence of defects ($\Delta\sigma_{f,0}$) or independent from them, El-Haddad's model is based on the hypothesis that there exists an intrinsic flaw size a_0 which makes the stress intensity factor equal to the long crack propagation threshold defined by means of LEFM ($\Delta K_{th,LC}$).

Taking into account the above-mentioned considerations, the initial flaw size can be calculated as follows.

$$a_0 = \frac{1}{\pi} * \left(\frac{\Delta K_{th,LC}}{Y * \Delta\sigma_{f,0}}\right)^2 \qquad \text{Equation 2}$$

The fatigue strength in the presence of defects ($\Delta\sigma_f$) can, therefore, be estimated as follows, with the flaw size given by the sum of the measured flaw (a) and the calculated intrinsic flaw size (a_0).

$$\Delta\sigma_f = \frac{\Delta K_{th,LC}}{Y * \sqrt{\pi(a + a_0)}} \qquad \text{Equation 3}$$

While the initial flaw size (a_0) proposed by El-Haddad and Topper is an empirically correlated parameter and not a direct material property measure, (a_0) translates many complex aspects affecting the fatigue strength, including phases, texture, and size of structural elements. Experimental results on cast specimens containing gas and shrinkage pores smaller than 0.5 mm in size, which is below the typical LEFM threshold size, have shown a good correlation with the predictions from this approach (El Haddad, Topper et Smith, 1979; Tenkamp et al., 2018).

In the subsequent developments, Murakami and Endo proposed to use as the defect size metric a square root of the defect surface area ($\sqrt{area_o}$) instead of a crack length (a_0). The Murakami approach has advantages since it is easier to apply for cracks of different shapes. El-Haddad's model can therefore be reformulated using Murakami's parameter and the following equation (Beretta, Carboni et Madia, 2009).

$$\sqrt{area}_0 = \frac{1}{\pi} * \left(\frac{\Delta K_{th}}{Y * \Delta\sigma_{f,0}}\right)^2 \qquad \text{Equation 4}$$

And the fatigue strength can be rewritten as follows:

$$\Delta\sigma_f = \frac{\Delta K_{th,LC}}{Y * \sqrt{\pi\left(\sqrt{area} + \sqrt{area}_0\right)}} \qquad \text{Equation 5}$$

Note that Murakami's shape factor Y depends on the defect location; it is suggested to use $Y = 0.65$ for surface defects and $Y = 0.50$, for internal defects (Murakami, 2019).

Considering that Kitagawa-Takahashi's approach and El-Haddad model are very much in line with the damage tolerance design techniques supporting the commissioning of critical LPBF components, this work assesses the possibility of implementing this approach to predict the fatigue strength of LPBF Inconel 625 components. It is necessary to remind in this context, that the fatigue crack propagation behavior of LPBF IN625 alloy was already studied in our previous work, and that the fatigue crack propagation threshold of LPBF components was found to be close to that of their wrought counterparts (Poulin, Brailovski et Terriault, 2018). Subsequent work revealed that the crack growth rates in the near-threshold region of LPBF IN625 components are relatively insensitive to the presence of processing-induced defects (Poulin et al., 2019). On the contrary, it has been shown that these defects could play a role of crack nucleation sites, thus leading to reduced fatigue strengths in LPBF IN625 alloys (Koutiri

et al., 2018) as compared to their wrought counterparts (Trester, Kaae et Gallix, 1985). It can therefore be hypothesized that El-Haddad's model, which relies on a set of properties corresponding to different levels of LPBF processing-induced porosity, could be used for fatigue strength prediction, and therefore, for design and quality control purposes (Kolitsch et al., 2016; Zerbst et al., 2016).

To this end, the methodology used to build, characterize and mechanically test LPBF specimens with various levels of intentionally-seeded porosity is presented first. Next, El-Haddad's model is used to combine the fatigue strength of fully dense specimens obtained in this work with the fatigue crack propagation threshold of fully dense specimens taken from our previous work (Poulin et al., 2019), in order to predict the fatigue strengths for specimens with various levels of processing-induced porosity.

4.5 Materials and Methods

4.5.1 Manufacture of specimens

High cycle fatigue (HCF) specimens were manufactured from 15 mm-diameter x 108 mm-long cylindrical blanks, all produced in a single build. The build was conducted under argon protective atmosphere, using an EOSINT M280 system equipped with a 400W Yttrium laser and IN625 powder provided by EOS, whose composition corresponds to ASTM B443-00, as shown in Table 4.1.

Table 4.1 Chemical composition of the IN625 powder used for this study (wt%)

IN625	Ni	Cr	Mo	Nb	Fe	Ti	Al	Co	C	Ta	Si	S	Mn
ASTM B443-00	Bal.	21.0-23.0	8.0-10.0	3.15-4.15	≤5.0	≤0.4	≤0.4	≤1.0	≤0.1	≤0.05	≤0.5	≤0.015	-
Powder	Bal	21.81	9.33	4.06	0.78	0.39	0.34	0.19	0.013	<0.02	0.15	0.002	0.04

A total of 48 blanks were manufactured with four different levels of porosity generated in their central (gauge) part extending from 5 mm below to 5 mm above the center line; the end parts of the blanks were built with the highest possible level of density (≥99.9%) (see Figure 4.2). To generate porosities ranging from ≤0.1 to ~3%, four different laser exposure parameter sets, P_0, P_1, P_2 and P_3, were used (see Table 4.2). These parameter sets were generated by varying the laser scanning speed from 960 to 1920 mm/s, while keeping other processing parameters (laser power, layer thickness and hatching space) constant.

Among the 48 specimens, 24 were built with the highest density (lowest porosity) in their gauge sections (parameter set P_0) to generate a reference Wohler curve. Three additional sets of 8 specimens were built with parameter sets P_1, P_2 and P_3, respectively. Following the build, the specimens were heat treated on the build plate as per the EOS recommendation (870ºC for 1h under argon protective atmosphere followed by air forced cooling). Next, the specimens were removed from the build plate, using a saw. Finally, a CNC lathe was used to machine fatigue testing specimens with 6 mm-diameter, 12 mm-long gauge sections and 12 mm-diameter, 48 mm-blend radius grip sections, in compliance with ASTM E466 standard (see Figure 4.3 a) (*Standard Practice for Conducting Force Controlled Constant Amplitude Axial Fatigue Tests of Metallic Materials*, 2015). Following machining, the specimens' gauge sections were polished manually on a lathe to obtain a surface finish of R_a~0.5µm.

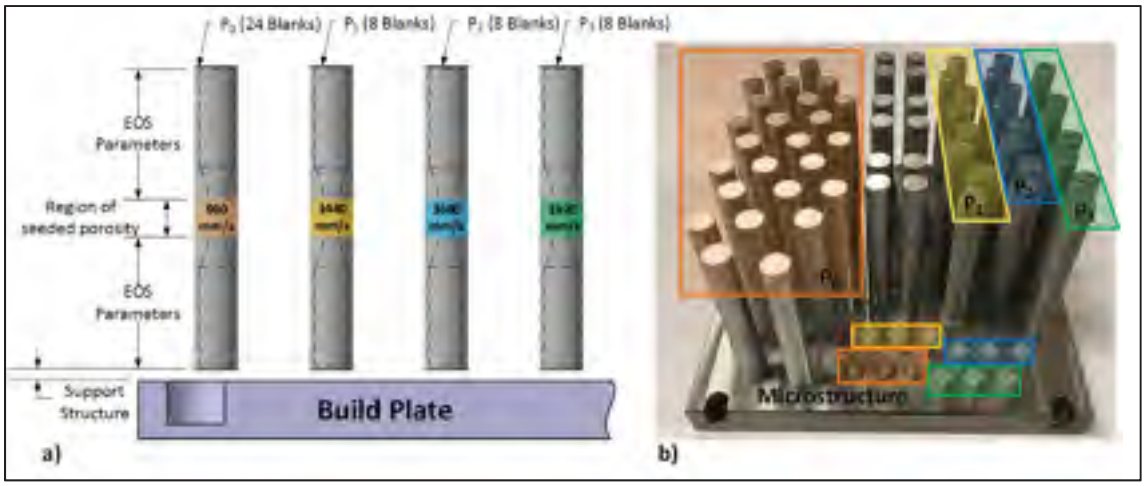

Figure 4.2 a) Schematic representation of the strategy to manufacture fatigue specimens with intentionally-seeded porosity in their gauge section and b) actual build plate

Table 4.2 Processing parameter sets and list of fatigue specimens in this study

Parameters	**Speed (mm/s)**	**Power (W)**	**Hatching Space (mm)**	**Replications**	**Expected Porosity** (Poulin et al., 2019)
P_0	960	285	0.11	24	≤ 0.1%
P_1	1440	285	0.11	8	0.3%
P_2	1680	285	0.11	8	0.9%
P_3	1920	285	0.11	8	2.7%

4.5.2 Characterization of defects

Following machining and polishing, computed tomography (CT) inspections were carried out on the gauge sections of at least three specimens for each parameter set (P_0, P_1, P_2, P_3). These analyses were performed using a Nikon XT-H225 computed tomography system with a 225 kV reflection X-Ray source (Figure 4.3). The specimens were scanned with a voxel size of 7 µm, a beam energy of 200 kV and a current of 50 mA using a 0.5 mm-thick copper sheet filter.

A total of ~2000 projections, with an exposure time of 2.83 seconds, were acquired. The images were reconstructed, using the CT PRO 3D software (Nikon Metrology), and the post-treatment was performed using the ORS Dragonfly image treatment software. With this voxel size, defect detectability was approximately 20 µm. However, in order to focus on relevant defects, i.e., those larger than the grain size, a detection threshold of ~40 µm, or 100 contiguous voxels, was applied.

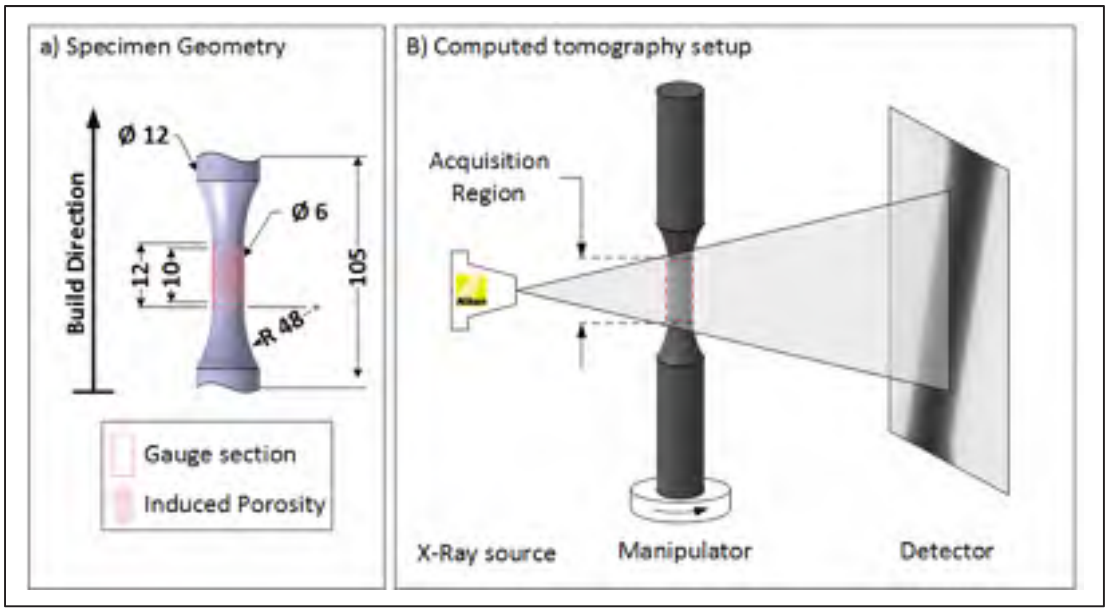

Figure 4.3 a) Dimensions of the as-machined fatigue specimens, b) Schematic representation of the computed tomography setup

Using three CT scans for each specimen set and the above-mentioned threshold, defects were identified and treated as separate regions of interest (ROI). For example, the defect sizes reported in Figure 4.4 were measured by projecting each ROI on the plane perpendicular to the specimen's loading axis and calculating their Murakami's parameters ($\sqrt{area_0}$). It is worth mentioning that within the scope of this work, the clustering effect was not considered, although it could definitely affect the measurement results, especially with increasing levels of porosity, when the spacing between pores becomes close to the defect size (Zerbst et Klinger, 2019). Note also that the CT-detected porosity for P_0 specimens was omitted from the

presentation, since the largest Murakami's parameter for these specimens was comparable to the grain size (~40 μm) and, therefore, considered too small to affect the fatigue strength in the HCF regime (Poulin et al., 2019).

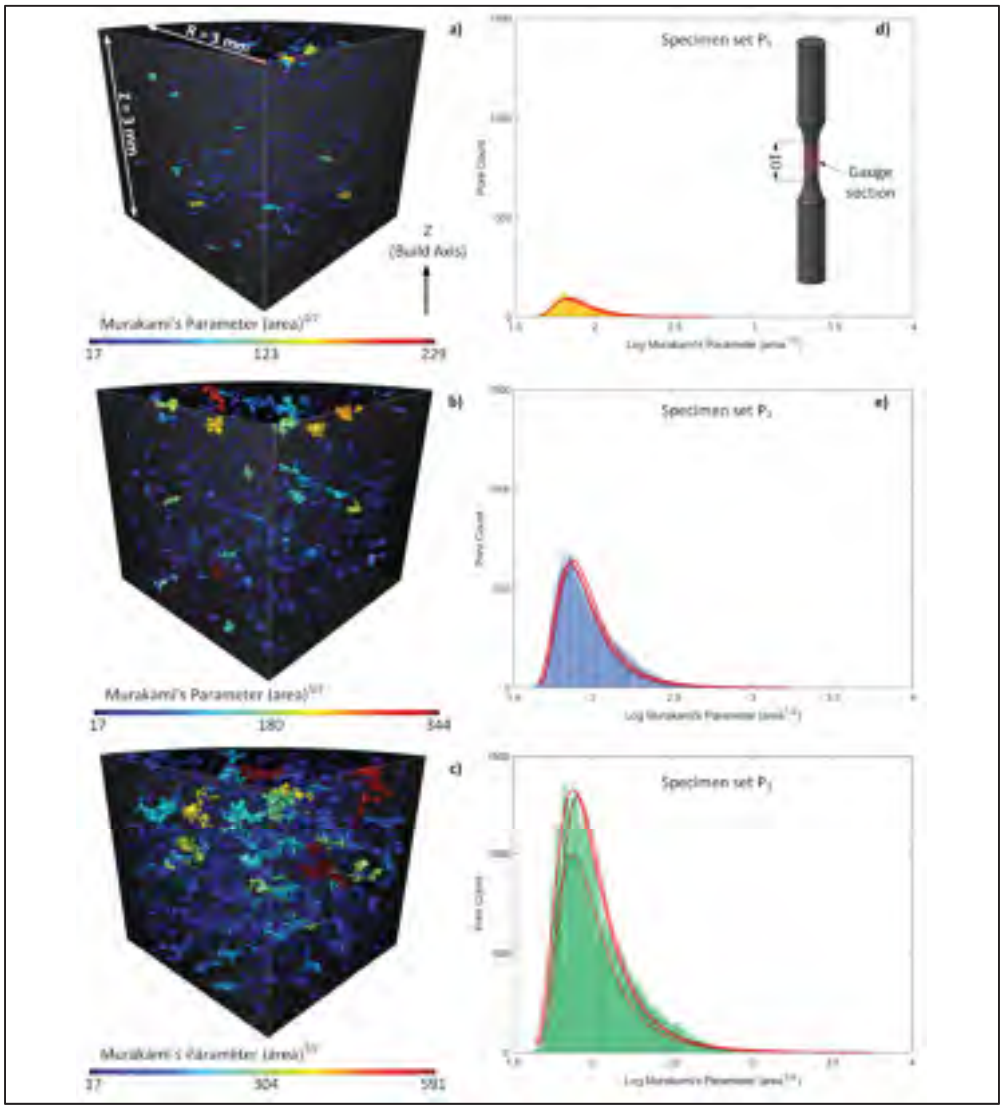

Figure 4.4 Representation of the porosity distribution in the sub-sections ($\Delta\theta$=90°, R=3mm, ΔZ=3mm) of fatigue specimens after their machining: a) P_1, b) P_2 and c) P_3; Murakami's parameter distribution for two repeated CT scans of the entire gauge sections: d) P_1, e) P_2 and f) P_3

To evaluate the consistency of the porosity control method used in this work (amount and size distribution), the CT inspection routine was extended to a region larger than the gauge section, and this inspection confirmed that the induced porosity was restricted to the designated sub-region (10 mm). The porosity levels estimated via CT are shown in Table 4.3, and found to be in good agreement with values obtained in the previous work (Poulin et al., 2019). The number of defects in specimens and their maximal Murakami's parameters rounded to 10 µm are also reported in Table 4.3.

Table 4.3 Summary of the porosity detection for all specimen sets

Parameter Set	**Expected Porosity** (Poulin et al., 2019) **(%)**	***Gauge Section Porosity (%)***	***Max size*** $\sqrt{\mathbf{area}}$ ***(µm)***	***Pore count ≥ 100 voxels***
P_0	≤ 0.1%	≤ 0.1%	60	6
P_1	0.3 %	0.3 %	350	1826
P_2	0.9 %	0.9 %	900	9824
P_3	2.7 %	3.1 %	1400	19161

The pore size distributions are combined in Figure 4.5, with the defect count for each processing parameter set corresponding to the sum of detections in all inspected specimens belonging to this set. It is worth mentioning that P_0 specimens do not appear in this graph, due to an insufficient number of defects in the size range of interest to gather a relevant distribution.

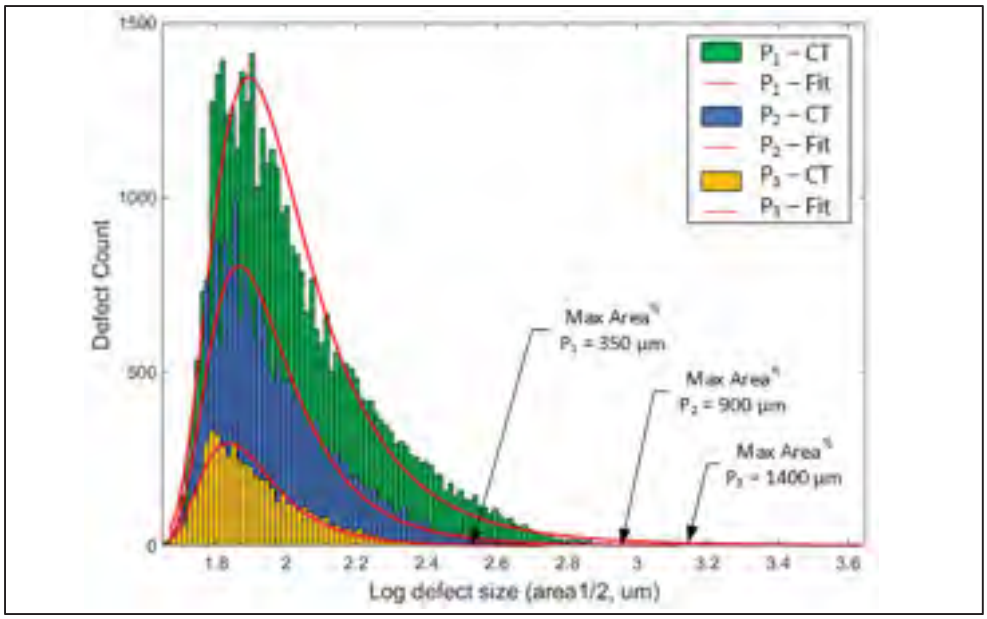

Figure 4.5 Defect size distribution (Murakami's parameter, $\sqrt{\text{area}}$ projected in the plane normal to the loading axis and generalized extreme value distribution distribution for all CT detection above threshold size

4.5.3 Fatigue testing protocole

To obtain the reference S-N curve (specimens P_0), a total of 18 specimens among 24 specimens built with the lowest level of porosity (≤0.1%) were tested using 6 distinct load levels with 3 replications, corresponding to a replication level of 66%, as defined by the ASTM E466 standard. The load levels and test plan are given in Table 4.4.

Table 4.4 Fatigue test plan for LPBF IN625 specimen set P_0

Step	Alternated Stress (Δσ, MPa)	Replications
1	590	3
2	605	3
3	620	3
4	650	3
5	680	3
6	740	3
Total		18

Fatigue testing was performed on an MTS 810 servo hydraulic machine using a stress-controlled approach (ASTM E466). The tests were conducted at a frequency of 30 Hz using a stress ratio of R=0.1 applied in a sinusoidal waveform. Forces and displacements were monitored using an MTS 661.20H-03 force transducer and an MTS LVDT (10 cycles for each 10^3 cycles were recorded), to ensure a constant force and waveform throughout the tests. The number of cycles to failure was also recorded with a runout set at 10^7 cycles.

Figure 4.6 Fatigue specimen mounted for testing

A Wohler curve for the reference specimen set P_0 is presented in Figure 4.7; among the results obtained, two data points were excluded for establishing the fitted curve, and they are represented by empty diamonds. The first exclusion had fatigue crack nucleation site in the

vicinity of a large subsurface defect located in the blend section, which resulted in a very short fatigue life. The second specimen had a fatigue life significantly greater than the expected values at this alternated stress level ($\Delta\sigma$ = 620 MPa), and considered as an outlier. All other specimens fractured in their gauge sections, and the crack initiation sites were localized near the surface.

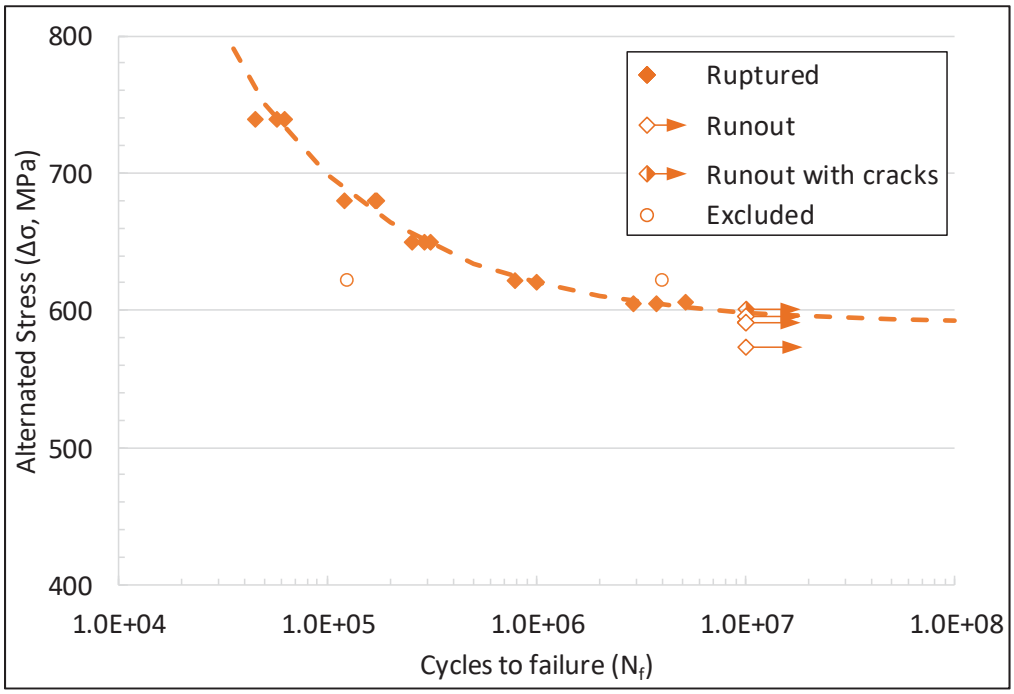

Figure 4.7 Wohler curve obtained for specimens with very low porosity (parameter set P_0); arrows indicate runouts, R=0.1

A second-order exponential trendline was plotted using Matlab for all but two the aforementioned specimens (see Figure 4.7). The trendline indicates that the fatigue strength of this material (asymptote) can be estimated at 590 MPa. This evaluation is backed up by experimental data since all three specimens tested at this stress level resulted in runouts (one having a visible crack on the surface at runout). Although there is very limited information on the room temperature mechanical properties of this specific alloy, the measured fatigue strength of LPBF IN625 alloy was found to be significantly higher than the ~470 MPa reported

for the annealed wrought IN625 specimens with much larger sections (Boyer, 1985), but comparable to the ~550 MPa reported for wrought IN625 specimens with thin sections (Theriault, Xue et Dryden, 2009).

Three monotonic tensile tests were also conducted on P_0 specimens, and the results obtained are provided in Table 4.5. Similar quasi-static mechanical properties were found when compared to previous publications on LPBF IN625 manufactured using EOS LPBF systems (Kreitcberg, Brailovski et Turenne, 2017a; Poulin, Brailovski et Terriault, 2018), except for the elongation at break, the latter being higher in the test carried out in this work; the difference is believed to be related to the difference in the specimens' geometry (fatigue specimens have a lower slimness ratio than their static counterparts (Sergueeva et al., 2009)). This higher static mechanical resistance is expected to have a positive effect on the fatigue life in the HCF regime (Stephens et al., 2000).

Table 4.5 Mechanical properties reported in the literature for stress relieved LPBF IN625 built on EOS M280

Study	Parameter Set	Porosity (%)	E (GPa)	YS (MPa)	UTS (MPa)	Elongation (%)
This Study	P_0	≤ 0.1	191.4 ± 1	654 ± 3	955 ± 5	56.3 ± 1
(Poulin, Brailovski et Terriault, 2018)	P_0	≤ 0.1	195 ± 4	685 ± 27	1009 ± 18	43.0 ± 2
(Poulin et al., 2019)	P_0	≤ 0.1	189 ± 3	637 ± 1	934 ± 2	46.0 ± 1
(Poulin et al., 2019)	P_1	0.3	202 ± 5	676 ± 4	966 ± 18	22.3 ± 5
(Poulin et al., 2019)	P_2	0.9	193 ± 4	673 ± 3	840 ± 58	8.8 ± 4
(Poulin et al., 2019)	P_3	2.7	185 ± 4	651 ± 4	749 ± 17	4.3 ± 1

It was already shown that LPBF IN625 alloy subjected to stress relief heat treatment manifests a significantly higher yield stress than annealed wrought IN625 alloy (Kreitcberg, Brailovski et Turenne, 2017a; Poulin, Brailovski et Terriault, 2018), but comparable to that of as-rolled IN625 alloy (Products). This was already shown to be caused by a very fine dendritic microstructure, a high density of dislocations in addition to the presence of very fine MC carbides in LPBF IN625 alloys, when heat treatment temperatures were not high enough to

lead to material recrystallization (Marchese et al., 2018b). Moreover, after stress relief annealing, the presence of delta phase has been reported (Lass et al., 2018; Marchese et al., 2018a), and is expected to significantly increase the room temperature mechanical properties, while negatively affecting those at elevated temperatures (Marchese et al., 2018a).

4.5.4 Prediction of the fatigue strength

In order to build the Kitagawa-Takahashi diagram, the fatigue strength from specimen set P_0 ($\Delta\sigma_{f,P0} = 590\ MPa$) and the lower bound of the fatigue crack propagation threshold obtained on identical specimens in our previous work ($\Delta K_{th,P0} = 7.1\ \pm 0.1\ MPa * m^{1/2}$) (Poulin et al., 2019) are employed first (the average thresholds and Paris law constants obtained in our previous work are given in Table 4.6). It is deemed acceptable to combine the threshold SIFs measured at 20 Hz (previous study) with the fatigue strengths measured at 30 Hz (this study), since the fatigue crack growth behavior for nickel alloys does not exhibit a strong frequency dependency in this range of frequencies and environmental conditions (Makhlouf et Jones, 1993; Mayer, 1999).

Table 4.6 Average fatigue crack propagation thresholds SIF and Paris law constants for various porosity levels (Poulin et al., 2019)

Parameter Set	Porosity (%)	ΔK_{th} (MPa·m ^{½})	C, E^{-09} (-)	m (-)	K_c (MPa·m ^{½})
P_0	≤ 0.1	7.1	7.23	2.91	96.4
P_1	0.3	7.1	3.79	3.15	83.5
P_2	0.9	7.2	1.06	3.53	76.7
P_3	2.7	7.5	0.50	3.67	65.5

Combining the aforementioned threshold SIFs measured at 20 Hz (previous study) with the fatigue strengths measured at 30 Hz (this study) is deemed acceptable, since the fatigue crack growth behavior for nickel alloys does not exhibit a strong frequency dependency in this range of frequencies and environmental conditions (Makhlouf et Jones, 1993; Mayer, 1999).

Using the fatigue strength of P0 specimens ($\Delta\sigma_{f,P0}$) and the LPBF-predicted fatigue strength calculated with the known threshold stress intensity factors (ΔK_{th}) (Equation 1), the Kitagawa-Takahashi diagram for LPBF IN625 alloy can now be plotted. To this end, the initial flaw size is evaluated using Equation 4 as $\sqrt{area_0} \approx 100\ \mu m$. Next, El-Haddad's fatigue strengths are calculated using Equation 5, and plotted in Figure 4.8 as functions of the defect size. The region below the El-Haddad curve corresponds to that of non-propagating cracks. Each colored arrow depicts the maximum defect size measured by CT and reported in Table 4.3.

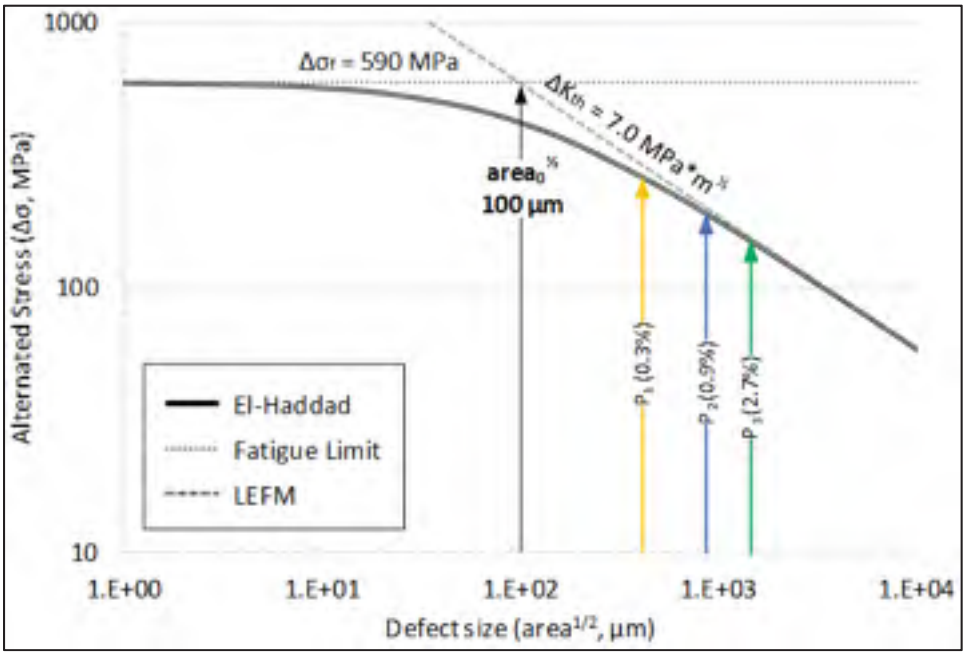

Figure 4.8 Kitagawa-Takahashi diagram with El-Haddad's prediction for fatigue life of intentionally-flawed specimen sets

4.5.5 Fatigue strength validation method

In order to validate the predicted fatigue strengths, stress-controlled fatigue testing of specimens with induced porosity (P_1, P_2 and P_3) was carried out. For these specimens, due to their reduced number (8), five different load levels were employed (see Table 4.7). This corresponds to a replication level of 37.5% and can be considered adequate for research

purposes or exploratory studies according to ASTM (*Standard Practice for Conducting Force Controlled Constant Amplitude Axial Fatigue Tests of Metallic Materials*, 2015; *Standard Practice for Statistical Analysis of Linear or Linearized Stress-Life (S-N) and Strain-Life (ε-N) Fatigue Data*, 2015). The initial load levels (Load step 1 in Table 4.7) corresponded to the fatigue strengths predicted by El-Haddad's model and rounded to 10 MPa. Load steps 2 and 3 were obtained by incrementally increasing the load applied by ~10%, while steps 4 and 5, by incrementally increasing the load applied by ~20%. When one runout was obtained, the remaining specimens were tested at the same and higher loads to obtain a Wohler curve.

Table 4.7 Fatigue test plan for LPBF IN625 specimen set P_1, P_2, P_3

Specimen Set Step	P_1 (Δσ, MPa)	P_2 (Δσ, MPa)	P_3 (Δσ, MPa)	Replications
1	280 ($\Delta\sigma_f$)	200 ($\Delta\sigma_f$)	160 ($\Delta\sigma_f$)	1
2	310	220	180	2
3	340	240	200	2
4	400	280	240	2
5	520	400	280	1
Total				8

4.5.6 Fractography and microstructure analysis

The microstructure analysis was carried out using a scanning electron microscope (SEM, Hitachi SU8230) equipped with an electron backscatter diffraction (EBSD) unit. The analysis was conducted in the parallel (XY) and normal (YZ) plane of our specimens. Specimens were tilted by 70° and scanned at 20 kV, with a 1 μm step. These analyses were conducted using 4×3 mm^2 mapping areas for the horizontal and vertical planes, respectively. The orientation maps were generated using Channel 5-Tango software. A misorientation criterion of 15° was employed to highlight high-angle grain boundaries.

After failure, specimens were prepared for fractographic examination. To this end, their gauge section was cut out using a Struers Labotom 5, and the specimens were cleaned using ethanol in an ultrasonic bath and dried before examination. To identify the fatigue crack initiation sites and the different features appearing on their fractured surface, this fracture surfaces were observed using a Hitachi S3400-N SEM in secondary electron mode at 20kV. Fracture surface analysis was conducted on at least two specimens with the lowest stress ratios leading to failure, and on at least two additional specimens tested at higher stress ratios**.** However, the results are reported for only two specimens (P_0-19 and P_2-2) to avoid including additional figures to the present manuscript.

4.6 Results

4.6.1 Fatigue diagrams of LPBF IN625 specimens

S-N diagrams obtained for all LPBF IN625 specimen sets are shown in Figure 4.9 and the corresponding data, including a full specimen list, can be found in the appendix. Despite the small sample size, all data confirm that increasing porosity significantly reduces the fatigue resistance of this alloy. For instance, at an alternated stress of 280 MPa, specimens P_1 (0.3% porosity) has an expected life well above the conventional HCF limit of 10^7 cycles, while specimens P_2 (0.9% porosity) and P_3 (~3% porosity) have an average life of, respectively, ~$5*10^5$ and ~$1.2*10^5$ cycles. The loss of fatigue resistance is even more significant at lower stress levels; when comparing specimens P_2 to P_3 at an alternated stress of 240 MPa, we see that the fatigue life is reduced by more than one order of magnitude. In addition, a higher scatter is observed in the fatigue life of specimens with seeded porosity.

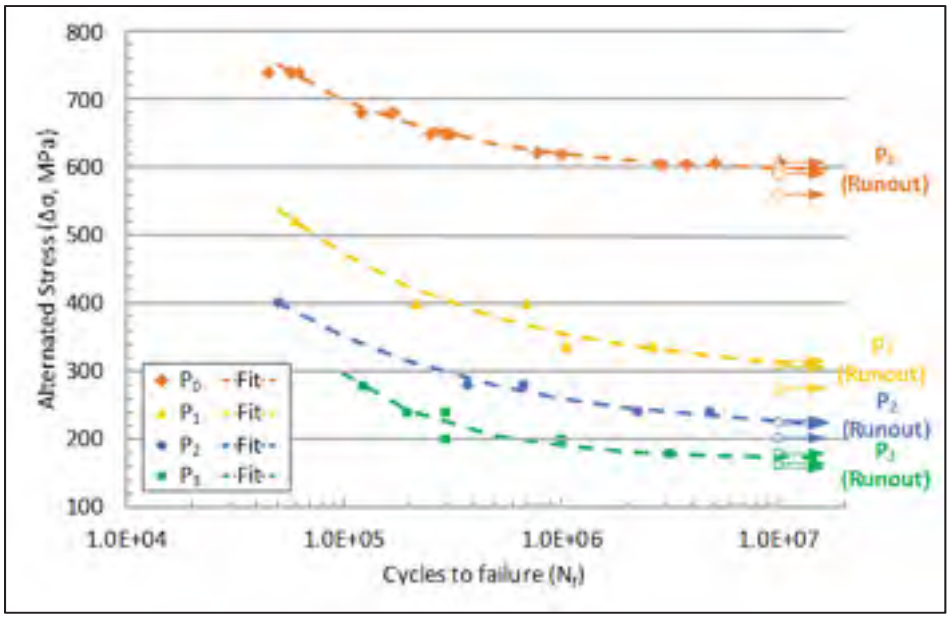

Figure 4.9 Wohler curves obtained for all specimens set

However, despite a significant loss of fatigue resistance in the finite-life region, the impact of porosity on the estimated fatigue strength at 10^7 cycles is less pronounced and runouts are obtained at alternated stress levels of respectively 310 MPa (0.3%), 220 MPa (0.9%) and 180 MPa (2.7%). As an example, one of the specimens with a level of porosity well above 1% (P_3) tested at a stress level of 180 MPa resulted in a runout, while the other resulted in ~$3 \cdot 10^6$ cycles of life.

Fatigue testing results are also superposed on the Kitagawa-Takahashi diagram (Figure 4.10) and, although slightly conservative, they are in good agreement with the model, since indicate runouts at stresses above the safe-life predicted region. Fatigue strength comparisons are made in Table 4.8 and show that the maximum discrepancy between the predicted and measured values corresponds to 7.2% (P_2 specimens). It is worth mentioning that in Figure 4.10, the depicted defect size corresponds to the microstructural barrier's estimated size, i.e. to a grain size of ~25 µm (Kreitcberg, Brailovski et Turenne, 2017a).

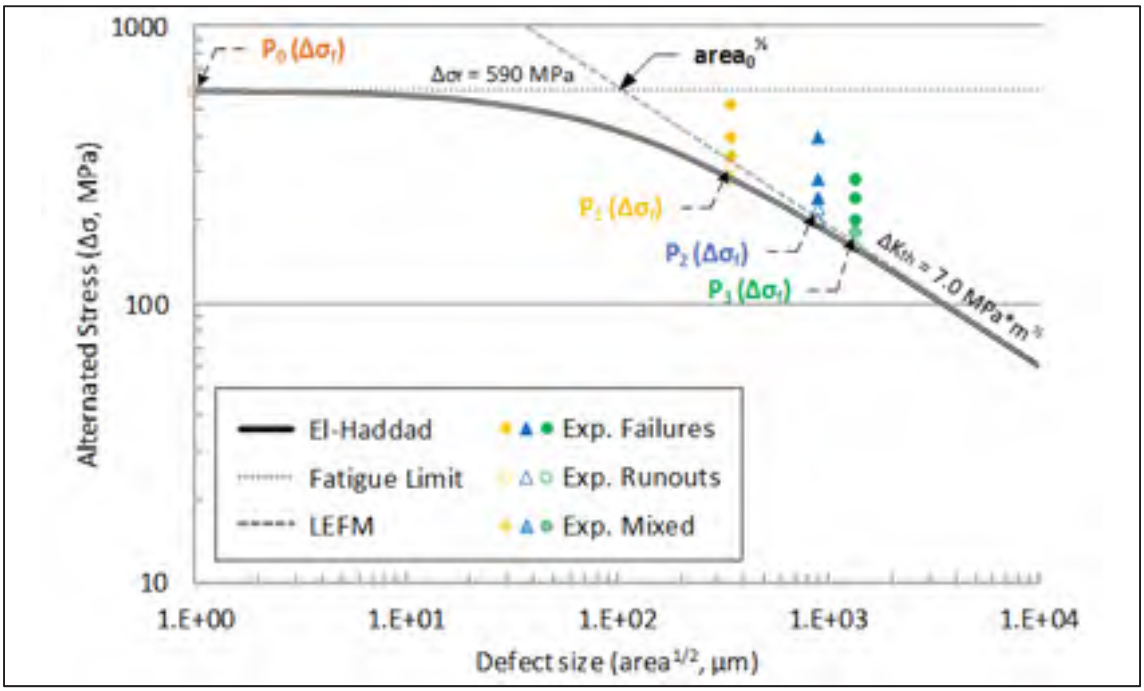

Figure 4.10 El-Haddad's model prediction of fatigue strength with experimental data

Table 4.8 Fatigue strength prediction vs. Experimental results

Specimen Set	*Prediction: El-Haddad (MPa)*	*Measured' Stress-Life (MPa)*	*Error (%)*
P_1	284	288	1.4
P_2	192	207	7.2
P_3	158	170	7.0

4.6.2 Microstructure

In addition to defects, different microstructures were obtained for each laser exposure parameter set. These microstructural variations can also have an effect on the fatigue behavior, which is not taken into account in El-Haddad's model. While the aim of this manuscript was not to carry out detailed microstructure analyses, typical EBSD maps for specimens P_0 and P_2 after their stress relief heat treatment are shown in Figure 4.11 and will be used to support the fractographic examination discussion.

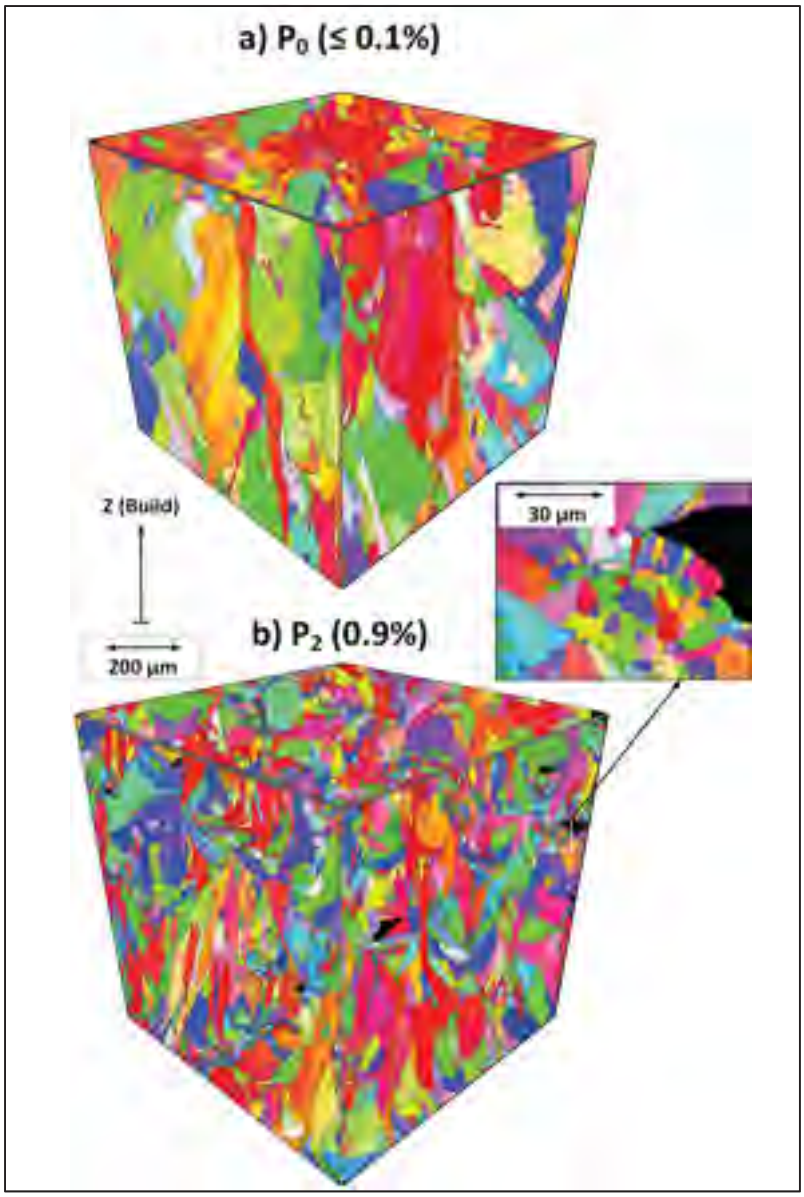

Figure 4.11 EBSD maps of a) P_0 and b) P_2 LPBF IN625 specimens, after their stress relieve heat treatment (adapted from (Poulin et al., 2019))

It can be seen that specimens P_2 produced with higher scanning speeds manifest a finer and less anisotropic microstructure than specimens P_0 due to their higher cooling rates (Li, Guo et Zhao, 2017; Yadroitsev et al., 2013). In addition to a generally smaller grain size of specimens P_2 (~50 µm along the build axis and ~20 µm along the build plane), grain regions, containing

grains as small as ~5 μm, are found near the defects. It seems that an increase in scanning speed results in combination of both 1) epitaxial growth of columnar grains from the melt pool bottom and 2) a heterogeneous nucleation of fine near-equiaxed grains from pores, unmelted powder etc., where epitaxial grain growth is supressed.

4.6.3 Fractographic observations

For each specimen set, stress intensity factors are plotted with respect to the crack length in Figure 4.12 a. To build this diagram, an initial SIF range applied for each specimen set was calculated using Equation 1; the assumed initial crack size taken from the CT analysis. The alternated stress considered in building this diagram was respectively 605, 340 240 and 180 MPa for specimens $P_{0,}$ $P_{1,}$ 2 and P_3, which all correspond to the lowest alternated stress levels inducing a failure. The final SIF range was estimated using the crack size in the overload region, where the remaining section becomes too small to handle the maximum load applied during the fatigue cycle (see Figure 4.12 b, c, d, e with typical fatigue fracture surfaces). It can be seen that due to lower levels of stress applied on the fatigue specimens with higher porosity, most of their life was spent in the low SIF region.

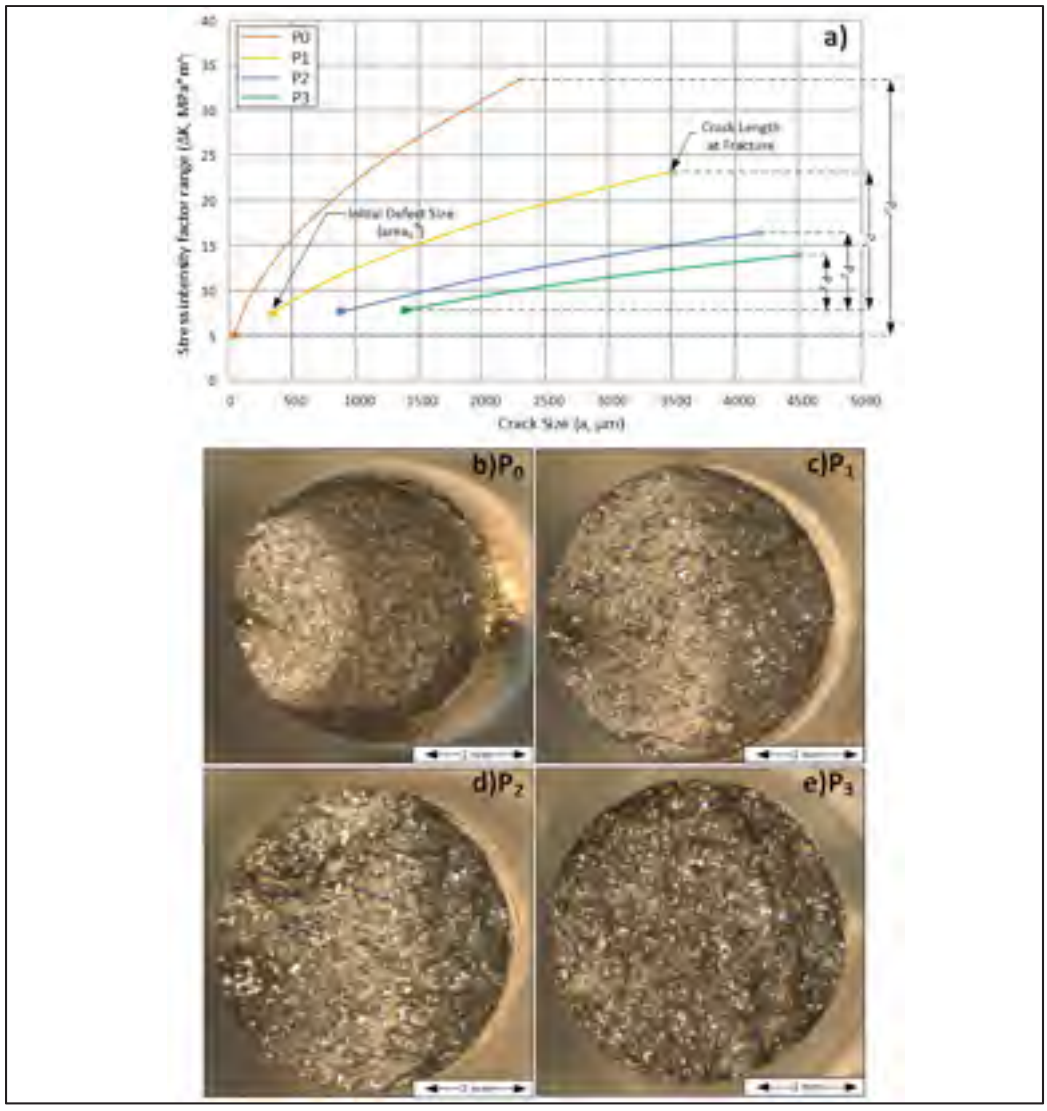

Figure 4.12 a) Stress intensity factor evolution with respect to crack length for stress-controlled fatigue tests (lowest load level with failures), b), c), d) and e) are typical fatigue fracture surfaces for the corresponding specimens

Reference specimen set (density ≥ 99.9%)

For specimens P_0, fatigue crack initiation sites were detected at their surface. Some specimens tested at higher alternated stress ranges (740 MPa) manifested multiple initiation sites. Conversely, at lower stress ranges, all specimens manifested single initiation sites, and pores were not observed in these sites (see Figure 4.13 a) and b). This indicates that the measured

fatigue behavior of these specimen sets was not affected by the presence of defects. Pores were also observed within the fractured surfaces (Figure 4.13 e); their size was of the order of tens of micrometers, which agrees with the results of CT scans.

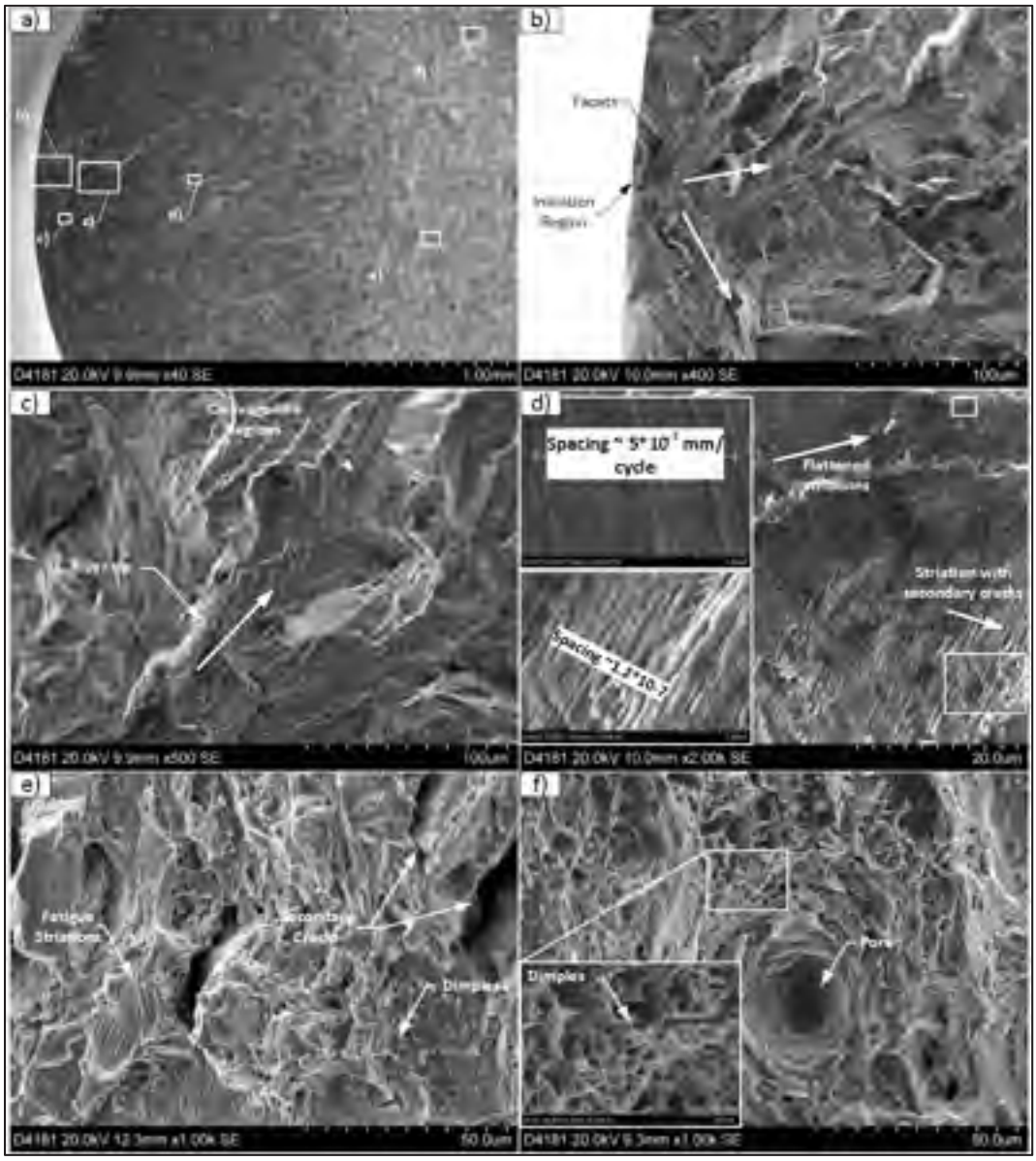

Figure 4.13 Typical example of fracture surfaces and features observed for specimens P_0

Moreover, in the vicinity of the crack initiation sites, highly faceted fracture surfaces were observed as a result of the crystallographic crack growth along the persistent slip bands, which align with closely packed crystallographic planes in the early stage of propagation (Stage I) (Balachandramurthi et al., 2019) (see Figure 4.13 b) and c). Farther from the crack initiation site with the increasing stress intensity factor, stable crack propagation (Stage II) depicts fatigue striations as the main features, and cleavage-like regions, to a lesser extent, which is expected for this material under these conditions (Pereira et al., 2018).

As shown in Figure 4.13 d), in some grains, striations appear to be highly flattened as a result of plasticity-induced crack closure, which is an indication of a very ductile material. In other areas, very well defined fatigue striations with regular secondary cracks appear with a significantly different spacing (Lynch, 2017). Similar well-defined striations were documented under nearly identical testing conditions for wrought IN625 (Pereira et al., 2018) and Incoloy X750 at high stress intensity factors (*Fractography*, 1987). In this case, an unfavorably oriented grain might be exposed to a higher SIF range, than are their neighbors, and this translates to a different aspect of fatigue striations when compared to the neighboring grains.

In the transition region, a mix of fatigue striations and dimples were observed with larger and frequent secondary cracks as shown in Figure 4.13 f). The fractured specimens also exhibit large shear lips and a significant reduction of the fracture area, which is typical for very ductile materials (Ma et al., 2010). SEM observations of final fracture regions revealed that they are populated with fine dimples resulting from tensile overload (Figure 4.13 f).

Specimen sets with seeded porosity (0.3-2.7%)

For specimens P_1, P_2 and P_3, fractographic observations confirmed that crack nucleation sites were at the near-the-surface LOF defects. These observations were verified by the presence of unfused powder in the pores at which fatigue cracks nucleated as well as smooth surfaces that appear as melt pool regions solidified with no cohesion, as shown in the red region of Figure 4.14 b) and c). When comparing the defect at which fatigue crack initiated for specimens from

the same set tested to rupture with replication, it was not always found larger than for specimen having a shorter fatigue life. This suggests that, for a given porosity level, the initial defect size within a specimen is not the sole parameter driving the fatigue life; other variables, such as the distance separating defects, could also play a significant role (i.e., interaction of defects). Among specimen sets P_2 and P_3, some exhibited multiple initiation regions at defects located in different planes, which resulted in the concurrent growth of multiple fatigue cracks with no river lines joining the cracks (see Figure 4.15). Close to the defects leading to the fatigue crack initiation in specimens P_2 (P_3), crystallographic features, such as facets, appear to be finer than in the case of specimens P_0. This appears to be related to a generally finer microstructure of specimens with higher porosity, as well as to the presence of clusters of fine grains in the vicinity of the defects (Figure 4.14 b).

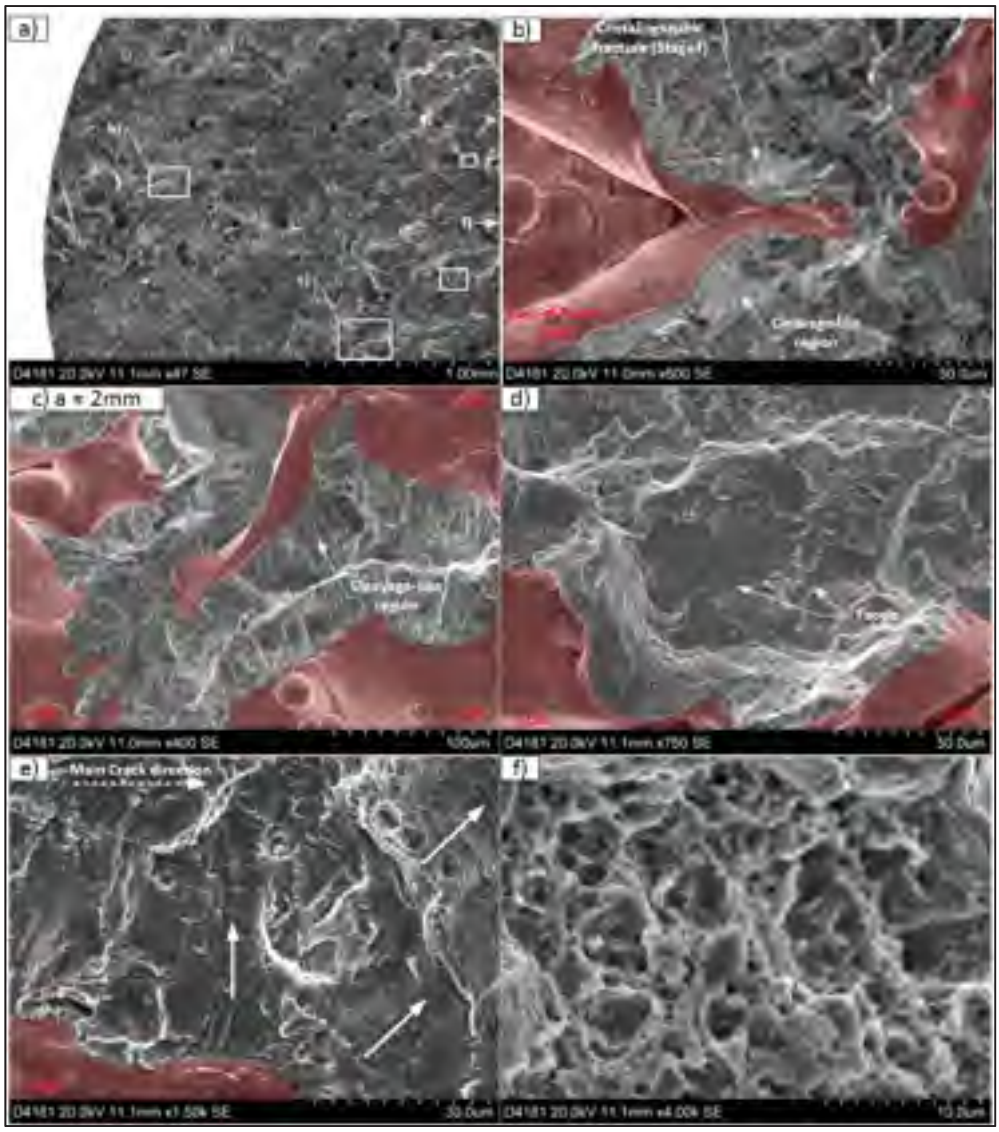

Figure 4.14 Fractographic observation of porous specimen (P_2-2)

Farther from the initiation site, SEM observations reveal more features typical of Stage I crack growth (near-threshold). Quasi-cleavage and highly faceted features are observed at the expense of fatigue striations, especially near the defects (Figure 4.14 c and d). This trend becomes more compelling when the porosity level increases, and is believed to result either from a complex triaxial stress state at the root of defects (Committee, 1990), which can induce multiple failure modes, or from multiple crack arrest-and-reinitiation events caused by the presence of defects. The limited regions where fatigue striations are observed also depict a

very erratic crack growth behavior (i.e. striation spacing and orientation), especially in the vicinity of defects (Figure 4.14 e) (*Fractography*, 1987). Therefore, the microscopic and macroscopic crack growths can be expected to have very distinct orientations. With respect to these observations, in the finite life region, the fatigue crack growth stage can be expected to occupy a larger portion of the total specimen life than what is typically reported, and Stage I mechanisms must be well understood to accurately predict the fatigue life of porosity-contained specimens.

Due to the lower load levels employed, areas of the final rupture (tensile overload) also become narrower. There is also very limited shear lips (reduction of area) for P_1 specimens when compared to P_0 specimens, as shown in Figure 4.13. This is even more compelling for the specimen sets P_2 and P_3, where the final fracture region appears flat with no area reduction. This is a result of the strongly impeded ductility in the presence of LOF type defects and confirms observations made in a previous paper (Poulin et al., 2019). The final fracture regions exhibit a significant amount of incohesive regions (i.e. defects), with a mix of elongated dimples and hemispherical dimples resulting from a complex stress state in the vicinity of the defect.

4.7 Discussion

Despite the differences in the microstructure and fracture mechanisms revealed by the fractographic analysis, the fatigue life predictions based on the use of El-Haddad's model and Murakami's parameter were found in good agreement with the trend observed experimentally (less than 8% error for porosity ranging from 0.3 to 3%). While this approach does not take into account the geometry and interaction of defects and the material microstructure, stress-controlled fatigue testing results were found in good agreement with the predicted values, albeit slightly conservative. It is worth mentioning that in the presence of defects significantly larger than grain size, the literature reports that the fatigue strength is more impacted by defects than it is sensitive to the microstructure (Yadollahi et Shamsaei, 2017). In fact, laser scanning

parameters employed to generate porosity have also been shown to produce a finer and more equiaxed microstructure and, simultaneously, larger defects, which would both contribute to making the direct LEFM-based prediction appropriate. Moreover, close to the defects, the microstructure was finer than in the dense regions of the same specimens. In fact, when comparing the constant stress fatigue testing results to those obtained with El-Haddad's model, a better agreement was found with the direct application of the LEFM approach. However, this is not a contradiction, since the size of defects in our specimens was significantly greater than the material's intrinsic flaw size (El Haddad, Topper et Smith, 1979).

Notwithstanding the preceding, testing specimens with less porosity and smaller defects (closer to the short crack regime) would provide deeper insight into the fatigue resistance in the short cracks-to-long cracks transition region. With respect to the conservatism of the approach, it is worth mentioning that the fatigue life prediction based on the largest of the defects found in multiple specimens can be conservative in some cases. As an example, for specimens P_1, the prediction was based on a defect size of 350 μm, while the largest defects specimens found in specimens P_1-1 and P_1-3 were respectively 291 and 326 μm. In this paper, Murakami's parameter was selected as the metric to characterize defects, since it is widely employed in the literature. However, using a different metric, namely, the mean ferret diameter, would have resulted in better agreement with the experimental results, with a maximum discrepancy below 3% for specimen set P_2 instead of 7%. However, as suggested by previous works focussing on casting shrinkage defects (Nicoletto, Konečná et Fintova, 2012), the use of the maximum ferret diameter would significantly increase conservatism in our case, since the large defects resulting from an increase in laser scanning speed are small highly-ramified LOF pores interlaced between multiple melt pool/layers (see Figure 4.15). In the light of this, it is somewhat difficult to fully characterize such complex and large LOFs with a single parameter, and we believe this is a key aspect to focus on to improve the applicability of this approach. To support this assertion, it can be shown that some specimens showed multiple defects initiating fatigue cracks, with each defect being characterized by a different Murakami parameter (see Figure 4.15).

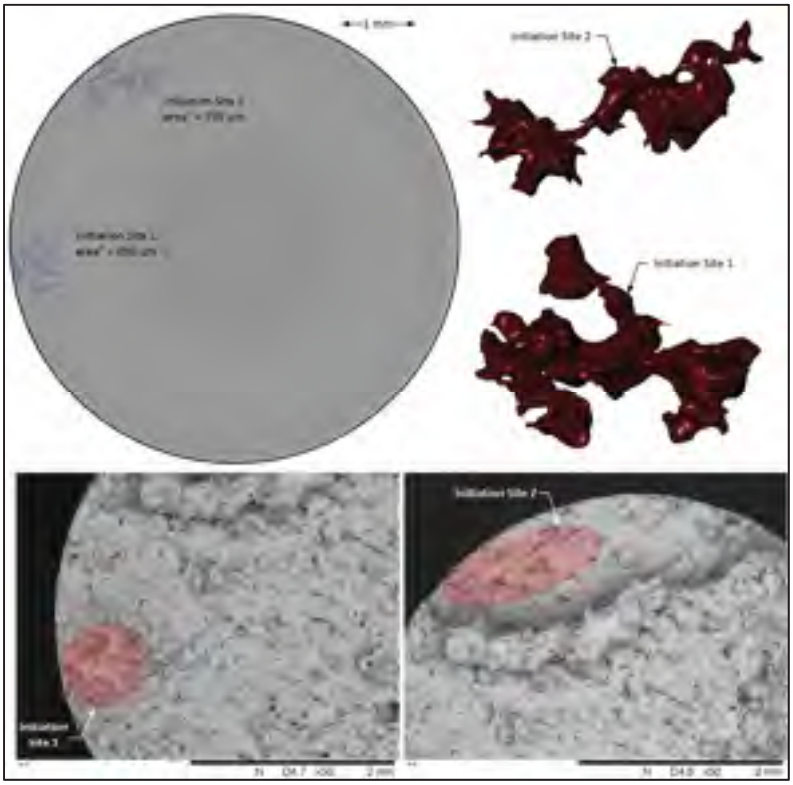

Figure 4.15 Specimen P_2-02 ($\Delta\sigma$=240MPa, n=4.87*10^6), showing multiple initiation sites

4.7.1 Finite Life Prediction

While this manuscript is focused on the fracture mechanics-based fatigue strength prediction (conditions for unpropagating cracks or safe-life), designers must generally consider different load cases, some being in the finite life region. In addition, some engineering components are designed to serve in the low cycle fatigue region. In this context, the methodology proposed in this manuscript provides only a limited framework to support commissioning LPBF built components, and more work is required to link the finite life to the defect distribution. We believe however that this approach can be extended to finite life applications (Ciavarella et Monno, 2006; Karlén et al., 2012; Maierhofer, Gänser et Pippan, 2015) and implemented in a probabilistic framework (Correia et al., 2016; Gagnon et al., 2013; Pessard et al., 2013).

Although our results depict a strong relationship between the defect size and the fatigue life, in accordance with what was reported in (Sheridan et al., 2018), direct correlation of fatigue lives with the Paris diagram appears difficult. This can be explained by the fact that after crack nucleation, physically short and long crack propagation regimes manifest very different propagation rates under the same SIF. When it comes to long cracks, the NASGRO model (Bao et Zhang, 2010; Forman et al., 2005) appears to be the most robust since it represents all three regions of the Paris diagram. In Figure 4.16, the fatigue crack propagation curves based on the NASGRO model fitted with the least square method are given for specimens sets P_0-P_3. In the near-threshold region (Stage I), the crack propagation appears to be retarded with increasing porosity. This is expected to result from both the interaction of cracks with defects and from a finer microstructure. Nevertheless, as indicated in Figure 4.12, specimens with intentionally-seeded defects spend longer time in this slow growth region, which is counterintuitive, since the presence of defects is expected to shorten the initiation phase. Consequently, a combined approach for the finite life prediction accounting for both the physically short and long crack propagation in porosity-contained components becomes especially valuable.

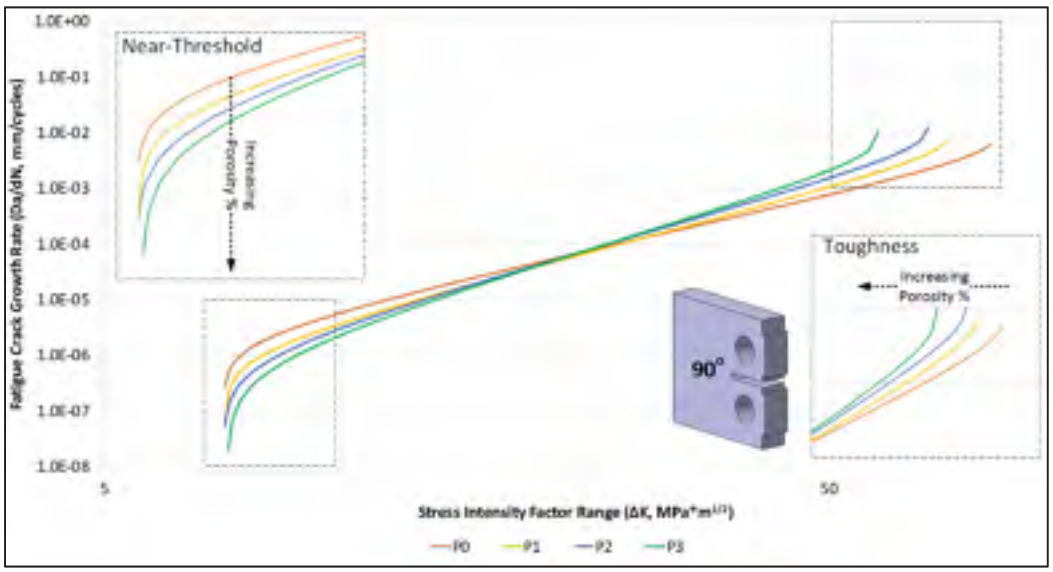

Figure 4.16 NASGROW Curves fitted from experimental data (Poulin et al., 2019) for specimens P_0-P_3

In addition, our results depict very significant scatter in the finite life of specimens with intentionally-seeded defects, which is considered to be a combined result of variations in the initial flaw size, microstructurally-dominated fatigue crack nucleation and initial fatigue crack propagation stages (physically short cracks). To successfully predict the fatigue crack growth in this regime, models including more detailed retardation effects (i.e., crack closure) should be employed (Bang, Ince et Noban, 2019; Maierhofer, Pippan et Gänser, 2014; Wang et al., 2014). This is especially important for nickel superalloys, for which crack closure plays a significant role in the crack propagation behavior (Li et al., 2018; Poulin, Brailovski et Terriault, 2018).

4.8 Conclusion

In this manuscript, the fatigue strengths of specimens with various levels of intentionally-seeded porosity were predicted with a reasonable accuracy, using El-Haddad's model. It must be acknowledged that testing specimens with defect sizes closer to the calculated intrinsic flaw size would have been interesting to validate the model's ability to deal with short cracks. In addition, that would have been more representative of the defects which are typically observed in specimens produced using optimized processing and post-processing conditions.

The fractographic analysis of specimens with finite lives illustrates the importance of Stage I crack propagation when specimens contain a certain amount of seeded defects. Moreover, it is shown that LPBF-built IN625, which is a very ductile material, becomes fragile in the presence of porosity. Furthermore, it is also shown that the fatigue behavior of LPBF components cannot be correlated solely to the porosity level, but rather, to the size and geometry of individual (critical) defects. In this manuscript, Murakami's parameter was employed, but other metrics can be calculated when specimens are inspected, and more work must be done to identify the most relevant metrics.

Considering the challenges in detecting LPBF-induced defects using traditional NDT techniques, due to their very small size, their high aspect ratio and rough as-built surfaces, CT appears as a valuable technology. Although CT inspection still faces many technological challenges to full implementation in the industrial quality control chain, we believe it represents a very powerful tool for the defect identification and measurements, and that CT data could be extrapolated to larger specimens or parts using statistics of extreme, as proposed in (Masuo et al., 2017; Romano et al., 2017)

4.9 Acknowledgement

The authors would like to thank the Fonds de Recherche du Québec – Nature et Technologie (FRQNT) and the National Science and Engineering Research Council (NSERC) for their support in financing the present study. The authors would also like to thank Firas Koubaa, Alexandre Szymanski and Serge Lalonde for their support through this project.

4.10 Annex

Table 4.9 List of all stress-controlled fatigue tests performed

P_0 Specimens					
ID	Porosity (%)	Alternated Stress	Cycles	Defect Size (Area 1/2)	Comment
P0-1	≤0.1	560	10^7	56 (CT)	Gauge Failure
P0-2	≤0.1	680	1.68×10^5	60	Gauge Failure
P0-3	≤0.1	650	3.13×10^5	60	Gauge Failure
P0-4	≤0.1	740	5.73×10^4	47 (CT)	Gauge Failure
P0-5	≤0.1	650	2.53×10^5	60	Gauge Failure
P0-6*	≤0.1	740	4.52×10^4	60	Gauge Failure
P0-7	≤0.1	620	4.03×10^6	60	Gauge Failure (Excluded)
P0-8	≤0.1	590	10^7	60	Runout
P0-9	≤0.1	590	10^7	60	Runout
P0-10	≤0.1	650	2.93×10^5	60	Gauge Failure
P0-11	≤0.1	680	1.22×10^5	60	Gauge Failure
P0-12	≤0.1	620	1.01×10^6	60	Gauge Failure

P0-13	≤0.1	590	10^7	60	Runout
P0-14	≤0.1	605	3.78×10^6	60	Gauge Failure
P0-15	≤0.1	605	2.93×10^6	60	Gauge Failure
P0-16	≤0.1	605	5.17×10^6	60	Gauge Failure
P0-17	≤0.1	740	6.25×10^4	60	Gauge Failure
P0-18	≤0.1	620	7.86×10^5	51 (CT)	Gauge Failure
P0-19*	≤0.1	620	1.25×10^5	60	Blend Defects Failure (Excluded)
P0-20	≤0.1	680	1.71×10^5	60	Runout
P_1 Specimens					
P1-01	0.3	280	10^7	291 (CT)	Runout
P1-02	0.3	310	10^7	347 (CT)	Runout
P1-03	0.3	340	2.65×10^6	326(CT)	Gauge Failure
P1-04	0.3	310	10^7	350	Gauge Failure
P1-05	0.3	400	2.17×10^5	350	Gauge Failure
P1-06	0.3	400	6.58×10^5	350	Gauge Failure
P1-07	0.3	340	1.07×10^6	350	Gauge Failure
P1-08	0.3	520	6.03×10^4	350	Gauge Failure
P_2 Specimens					
P2-01	0.9	200	10^7	900	Runout
P2-02	0.9	220	10^7	801 (CT)	Runout
P2-03	0.9	240	4.87×10^6	896 (CT)	Gauge Failure
P2-04	0.9	220	10^7	900	Runout
P2-05	0.9	400	5.08×10^4	688 (CT)	Gauge Failure
P2-06	0.9	240	2.28×10^6	900	Gauge Failure
P2-07	0.9	280	3.77×10^5	900	Gauge Failure
P2-08	0.9	280	6.77×10^5	900	Gauge Failure
P_3 Specimens					
P3-01	3	161	10^7	980 (CT)	Runout
P3-02	3	180	3.15×10^6	1400	Gauge Failure
P3-03	3	180	10^7	1400	Runout
P3-04	3	240	2.97×10^5	1400	Gauge Failure
P3-05	3	200	2.96×10^5	1400	Gauge Failure
P3-06	3	240	1.96×10^5	1393 (CT)	Gauge Failure
P3-07	3	280	1.24×10^5	1370 (CT)	Gauge Failure
P3-08	3	200	1.01×10^6	1400	Gauge Failure

* Specimens were excluded for curve fitting

CONCLUSION

Les travaux réalisés dans le cadre de cette thèse visaient à évaluer la possibilité d'employer une approche basée sur la mécanique de la rupture pour guider l'application de l'approche de tolérance aux dommages de pièces obtenues par fabrication additive.

Dans la première portion des travaux, il a été montré que l'alliage Inconel 625 obtenu par fabrication additive possède une résistance à la propagation de fissure longue similaire à celle de l'alliage corroyé. Toutefois, suivant un recuit de relaxation des contraintes, la microstructure anisotrope et grossière lui confère un avantage dans certaines directions à cause de la fermeture de fissure induite par la rugosité. Ce mécanisme est également observé suivant un traitement de pressage isostatique à chaud, mais est indépendant de la direction, puisque la microstructure est plus homogène après un tel traitement. En excluant les mécanismes de fermeture de fissure, le comportement de l'alliage obtenu par fabrication additive est toutefois trouvé équivalent à celui de l'alliage corroyé.

Dans la seconde portion des travaux, des échantillons sont fabriqués avec différents niveaux de porosité en modifiant la vitesse du laser. Se faisant, il a été montré que la densité d'énergie a un impact significatif sur le taux de porosité résultant de la LPBF. Les essais mécaniques sur les échantillons poreux révèlent que la ductilité est la propriété la plus fortement affectée par la porosité, particulièrement lorsque le chargement est appliqué dans l'axe perpendiculaire au plan de fabrication. Par contre, les propriétés élastiques du matériau sont très peu impactées par la présence de porosité. De même, l'étude du comportement des fissures de fatigue révèle que la présence de porosité a un impact négligeable sur la propagation des fissures lorsque le facteur d'intensité de contrainte est proche du seuil. L'impact de la porosité se fait sentir lorsque le facteur d'intensité de contrainte augmente et est fortement dépendant de l'orientation de fabrication puisque ces dernières sont accélérées lorsque la fissure se propage de manière parallèle au plan de fabrication et ralenties lorsqu'elles se propagent perpendiculairement. Cet effet est toutefois observable lorsque le taux de porosité est significatif (1% et plus).

Enfin, le troisième article scientifique a permis de montrer qu'il est possible d'utiliser le comportement en propagation de fissure pour déterminer la taille de défauts qui peuvent être tolérés dans un alliage obtenu par fabrication additive tout en évitant les ruptures par fatigue. Pour y parvenir, des échantillons de fatigue avec porosité variable dans la section d'essai ont été fabriqués et testés en fatigue en contrôlant la contrainte alternée. Les propriétés des échantillons ayant une densité supérieure ont été utilisées afin de prédire la limite de fatigue des échantillons comprenant des taux de porosité supérieurs (0.3, 0.9 et 2.7%) et ce, grâce au modèle d'El-Haddad. Les résultats expérimentaux ont montré que le modèle est assez fidèle pour l'utilisation en ingénierie alors que l'erreur entre la limite de fatigue prédite et la limite expérimentale est inférieure à 10%, ce qui est généralement acceptable en ingénierie. De surcroit, l'observation des faciès de rupture a permis de mettre en évidence l'importance grandissante de la phase de propagation de fissure pour les échantillons dans la zone de vie finie.

Pour terminer, les travaux présentés dans cette thèse ont été concentrés sur la relation entre la limite de fatigue et les défauts. Toutefois, la conception de pièces requiert généralement de considérer un grand nombre de cas de chargements, lesquels peuvent être dans une zone de vie finie où le nombre de cycles est plus faible. En ce sens, il reste un grand nombre de défis à relever afin d'implémenter de manière rigoureuse la méthode en question pour mettre en service des pièces obtenues par LPBF.

RECOMMANDATIONS

À la lumière des travaux présentés dans cette thèse, il est possible d'identifier certains aspects qui devront être approfondis afin de développer l'approche de tolérance aux dommages de manière rigoureuse dans un contexte industriel. Dans cet ordre d'idée, une liste non exhaustive de recommandations est proposée dans les paragraphes suivants.

Premièrement, les résultats expérimentaux présentés dans cette thèse constituaient principalement une étude de faisabilité et ont été réalisés à température ambiante. Or, l'alliage Inconel 625 est destiné aux applications à haute température. Il serait donc impératif de réaliser des essais de caractérisation aux températures de service typiques pour cet alliage avant de viser une application réelle.

Dans le même ordre d'idée, il est important de mentionner que les applications en aérospatiale requièrent généralement la considération de plusieurs types de chargements. Par exemple, les charges correspondant aux décollages/atterrissages sont généralement les plus importantes, mais le nombre de cycles a considérer est tel qu'ils constituent généralement des cas de chargement en fatigue à bas nombre de cycles. Pour ces chargements, la méthode proposée dans cette thèse qui consiste à prédire une durée de vie infinie risque d'être trop conservatrice et rendre le procédé de fabrication additive inintéressant. Il apparait donc essentiel de complémenter cette méthode pour permettre une corrélation de la vie finie avec les défauts de fabrication.

Au niveau du contrôle de la qualité, les travaux présentés ici ont tiré profit de la tomographie à rayons X pour caractériser les matériaux. Bien que la technologie ait été employée ici comme un outil performant en caractérisation des matériaux, il reste plusieurs défis à relever en ce qui concerne les applications industrielles. D'une part, le cout de l'équipement et les temps d'acquisition en font une technologie prohibitive. D'autre part, certains verrous technologiques doivent encore être levés. Par exemple, il difficile d'obtenir une résolution adéquate pour

l'inspection de pièces de grande taille. Par ailleurs, il existe également des difficultés associées aux artéfacts de reconstruction obtenus avec des géométries complexes ou de matériaux denses. Une avenue intéressante pourrait être l'emploi de méthodes statistiques pour prédire la distribution de taille de défaut obtenu pour différents volumes de pièces. Il faudrait également s'assurer de considérer comment les défauts sont distribués en tenant compte des facteurs géométriques intrinsèques à la géométrie de la pièce, ainsi qu'au procédé (paramètres laser pour les différentes surfaces et hauteurs de fabrication par exemple). Ensuite, à partir des distributions de défauts anticipés, il pourrait être intéressant de prédire la taille de défaut anticipé sur la base de statistiques inférentielles.

Dans un autre ordre d'idée, afin de donner une valeur supplémentaire à la tomographie aux rayons X, il pourrait également être intéressant de superposer défauts observés aux résultats d'une analyse par éléments finis afin d'appliquer la tolérance aux dommages de manière locale. De cette manière, il est possible de croire qu'un moins grand nombre de pièces risquerait d'être rejeté, ce qui limiterait les couts associés à la non-qualité.

Enfin, il est important de réitérer que les travaux présentés ici se sont intéressés à la porosité résultant d'une fusion sous une énergie sous-optimale. En ce sens, les défauts observés étaient majoritairement des porosités de basse énergie, qui ont généralement une apparence similaire à une fissure. Dans bien des cas, l'apport en énergie lors de la fusion est plutôt au-delà de la valeur optimale, de sorte que la porosité observée prend une forme beaucoup plus sphérique. Pour de tels cas, il est attendu que l'impact de la porosité est moins important et il est possible que la méthode proposée soit trop conservatrice. Il serait donc intéressant d'évaluer l'impact de porosités créé à haute énergie sur le comportement mécanique de l'alliage. Dans de tels cas, il est possible que l'utilisation d'un modèle basé sur l'effet d'entaille soit plus appropriée.

ANNEXE I

INFLUENCE OF INTENTIONNALY-INDUCED POROSITY AND POST-PROCESSING CONDITIONS ON THE MECHANICAL PROPERTIES OF LASER POWDER BED FUSED INCONEL 625

J-R. Poulin[1], M. Letteneur[1], P. Terriault[1], V. Brailovski[1,*]

[1] Jean-Rene Poulin, Department of Mechanical Engineering, École de technologie supérieure, 1100 Notre-Dame Street West, Montreal, Quebec, Canada, H3C 1K3

[1,*]Corresponding author: Vladimir Brailovski, Department of Mechanical Engineering, École de technologie supérieure, 1100 Notre-Dame Street West, Montreal, Quebec, Canada, H3C 1K3 (vladimir.brailovksi@etsmtl.ca, tel: 514-396-8594)

Cet article a été présenté à la conférence :

3rd ASTM Symposium on structural Integrity of Additively Manufactured Parts

Washington, DC, USA, November 6-8 2018

1. Abstract

Additive manufacturing (AM) technologies, such as laser powder bed fusion (LPBF), have gained significant attention due to their capacity to manufacture near-net shape complex metallic components. Although LPBF components can manifest static mechanical properties comparable to those of their wrought counterparts, processing-induced defects, such as porosity and lack of fusion, are regularly observed within the build and are of particular concern for the structural integrity of printed components. In this work, the impact of LPBF-induced defects on the static mechanical properties of Inconel 625 specimens is studied. To establish the relationship between the level of such defects and the specific combinations of LPBF parameters, coupons with porosities of up to 20% were manufactured by varying the laser power from 70 to 360 W, the scanning speed, from 720 to 3840 mm/s, and the hatching

space, from 0.08 to 0.33 mm (a constant layer thickness of 40 microns was used). To measure the level of processing-induced porosity, the computed microtomography (micro-CT) and Archimedes' techniques were concurrently applied. The micro-CT was also used to evaluate the nature and morphology of defects and their distributions resulting from different combinations of processing parameters. Next, tensile specimens with porosities of up to 3% with two build orientations (0^o and 90^o) were manufactured, subjected to stress relief annealing and hot isostatic pressing, and then tested to measure the impact of the prosessing-induced porosity, build orientation and post-processing conditions on the static mechanical properties of Inconel 625 specimens. Our results indicate that the presence of pores strongly reduces the ductility of the material, especially when stresses are applied along the build direction. Although hot isostatic pressing allowed a significant reduction in porosity, this post-processing was ineffective in improving the ductility of specimens with as-printed porosities exceeding 0.3%.

Keywords: Additive manufacturing, Laser powder bed fusion, Selective laser melting, Nickel-based superalloy, Processing-induced porosity, Tensile properties.

2. Introduction

Metal additive manufacturing (AM) has emerged as the best-designated technology for manufacturing complex metallic components from various metallic materials, such as stainless steel, aluminium, titanium and nickel-based alloys (DebRoy et al., 2018; Herzog et al., 2016; Murr et al., 2012). The laser powder bed fusion (LPBF) technology is particularly interesting because the mechanical properties of the majority of LPBF-processed alloys are close to those of their wrought counterparts (Hanzl et al., 2015; Vrancken et al., 2012). However, significant amounts of processing-induced defects are regularly observed within the builds of the former. These defects have been shown to result from a complex interaction of multiple material and processing characteristics, such as the alloy composition, powder particle morphology and recoating techniques, laser exposure parameters, scanning strategy, temperature of the build

plate, protective gas flow, etc. (Criales et al., 2017; Fox, Moylan et Lane, 2016; Kamath et al., 2014; Koutiri et al., 2018). LPBF components present build orientation-dependent irregular surface topographies, and may contain partially bonded particles (Mumtaz et Hopkinson, 2009; Strano et al., 2013). Furthermore, these components may contain volumetric defects, such as pores, zones with a lack of fusion, and inclusions (Kasperovich et al., 2016; Koutiri et al., 2018; Ziółkowski et al., 2014).

While surface defects can be reduced or removed by conventional machining, polishing or shot peening operations, volumetric defects are difficult to quantify and repair. Their presence has been shown to be strongly related to laser exposure parameters, namely, the laser power (P) and speed (v), the hatching space (h), and the layer thickness (t) (Kasperovich et al., 2016; Koutiri et al., 2018). These parameters can be combined to calculate the volumetric energy density VED=P/vht, a metric frequently used to define the LPBF processing conditions (Letenneur et al., 2017). For example, VED has been successfully correlated to the porosity level of Ti6Al4V LPBF components (Kasperovich et al., 2016). At higher energy densities, the keyholing effect has been shown to be responsible for creating spherical pores (Criales et al., 2017; Montgomery et al., 2015; Simonelli et al., 2015). Conversely, lower energy densities tend to cause lack-of-fusion defects, which are typically crack-like elongated voids sometimes containing unfused powder (Khairallah et al., 2016; Qiu et al., 2015).

When the main laser exposure parameters (laser power and scanning speed) ensure a stable melt pool throughout the build, very low porosity levels can be obtained after LPBF (below 0.1%) (Khairallah et al., 2016; Li, Guo et Zhao, 2017; Qiu et al., 2015). Both laser exposure parameters influence the melt pool size and the temperature distribution, strongly impacting the cooling rates and the thermal gradients in zones surrounding the exposed region, which, in turn, significantly affect the resulting microstructure. Typically, the higher the energy density (higher laser power or lower scanning speed), the lower the cooling rate, and the coarser and the more textured the microstructure (Li, Guo et Zhao, 2017). Conversely, a lower power and a higher scanning speed decrease the size of a melt pool, which, under these conditions,

solidifies faster and promotes the formation of a more random and finer microstructure (Kreitcberg et al., 2017; Yadroitsev et al., 2013).
The hatching strategy also has a strong influence on the defects and microstructure of the printed material, as multiple remelting helps to reduce the occurrence of unmelted regions within the build (Tang, Pistorius et Beuth, 2017). Remelting is promoted when the melt pool depth and width are significantly greater than the layer thickness and the hatching space, respectively.

Studies have shown that the quality of components can also be significantly affected by other variables, such as the geometry of the component and the part location on the build plate, since all these strongly affect the heat transfer conditions (Khairallah et al., 2016; Parry, Ashcroft et Wildman, 2016). Other variables affecting the quality of the components are the temperature of the build plate and the powder recoating and protective gas flow conditions (Ferrar et al., 2012). Because of these complex interactions, optimising LPBF processing parameters constitutes a difficult task; rather, they are defined in terms of processing windows, and can be suboptimal in some areas of the build. Since LPBF of entirely defect-free components appears to be a nearly impossible task, a better understanding of how these defects affect the mechanical behaviour of printed component is required.

3. Materials and methods

To begin, defects are intentionally generated by varying three processing parameters (laser power, scanning speed and hatching space). The defects are then detected and quantified using the computed tomography (CT) and Archimedes' density measurement techniques. (The results obtained are also validated via the metallography observations, but the results of this validation are not presented here.) Next, tensile specimens with a porosity level of up to 3% are built, subjected to stress relief annealing and hot isostatic pressing, and, finally, mechanically tested. Finally, the CT technique is used to analyse the near-to-rupture zone of tensile specimens with a goal to better understand the results obtained.

3.1 Manufacturing intentionally flawed specimens

Firstly, 6.25 mm-diameter, 35 mm-height cylindrical coupons oriented at 90^{o} to the build plate were manufactured with various parameter sets to create different levels of porosity; manufacturing was carried out under argon protective atmosphere using an EOSINT M 280 system equipped with a 400 W Yttrium laser. An Inconel 625 powder, provided by EOS, whose composition corresponds to the UNS N06625 specifications was used (wt.%): ≥58%Ni; 20-23%Cr; 8-10%Mo; 3.15-4.15%Nb; ≤5%Fe; ≤0.40%Ti; ≤0.40%Al; ≤1.0%Co; ≤0.10%C; ≤0.05%Ta; ≤0.50%Si; ≤0.50%Mn, ≤0.15%P, and ≤0.15%S. To generate various levels of porosity, three laser exposure parameters were varied independently: the laser power was varied from 71 to 356 W (specimens P1-P4), the scanning speed, from 240 to 3840 mm/s (V1-V9), and the hatching space, from 0.03 to 0.44 mm (H1-H9). All 18 LPBF parameter sets are shown on the Power-Speed-Hatching Space process map in Figure A 1, and given in Table A 1 in the Annex. (Note that the layer thickness is kept constant at t=40 μm and the Reference case (R) corresponds to a point common for all three parameter sets: V, P and H.)

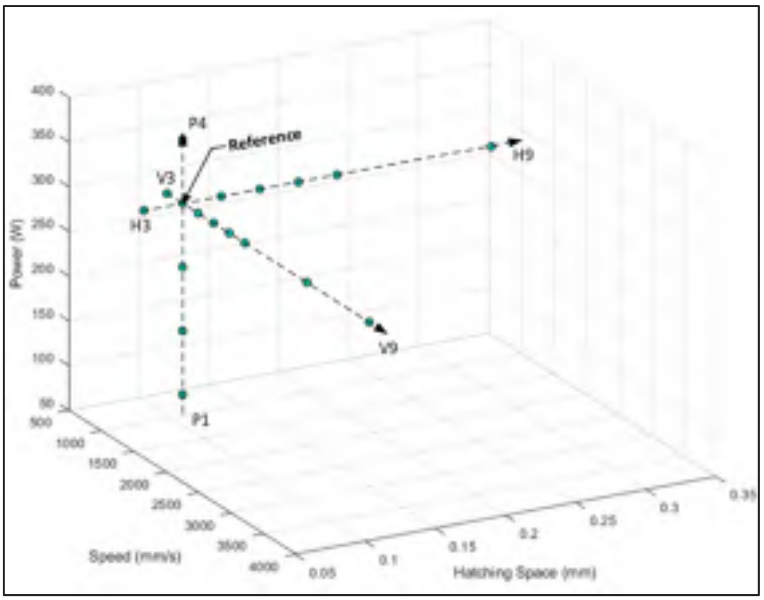

Figure A 1: 18 LPBF parameter sets employed
for the defect generation

In two subsequent builds, 6 mm-diameter, 80 mm-long blanks were manufactured in the vertical (90º) and horizontal (0º) orientations using the following four parameter sets: R, V5, V6, and V7 (see one of the build plates in Figure A 2). In total, eight blanks were manufactured for each parameter set. Following the build, a stress relief (SR) annealing was performed on the build plate according to the manufacturer's recommendation (870 ºC for 1 h, under argon atmosphere). Next, the blanks were cut off the build plate and machined to produce 4 mm-gauge diameter, 30 mm-gauge length tensile specimens (30 mm gauge length, instead of the E8 25 mm gauge length recommended by ASTM, was preferred to facilitate the extensometer mounting procedure). Four specimens per parameter set were tensile-tested in this state (SR), while the other four were additionally subjected to HIP before testing. During HIP, the specimens were heated at a constant rate of 10 ºC/min, maintained in argon atmosphere for 4h at 1120 ºC & 100 MPa, and furnace-cooled (it takes ~1h30 to cool the HIP chamber from 1120 to 200 ºC).

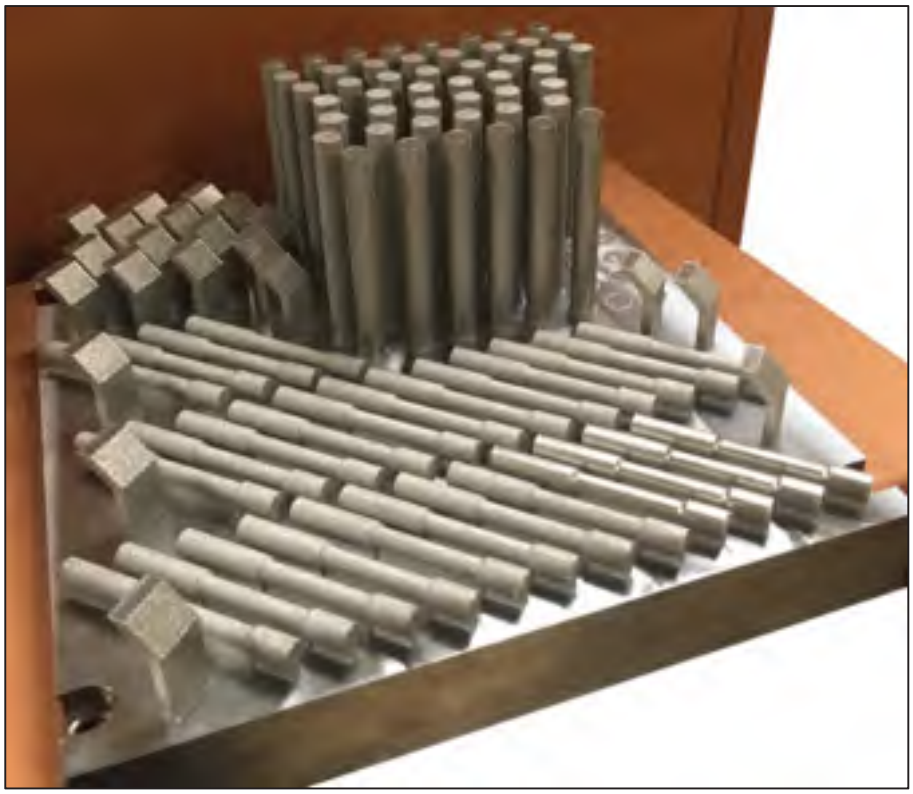

Figure A 2: Image of the build plate with 0° and 90°-oriented tensile blanks series

3.2 Porosity measurement

After the first build, 6.25 mm-diameter 35 mm-long coupons are subjected to porosity evaluation using two complementary methods. Next, the specimens are manually separated from the build plate and the remaining support structures removed using abrasive paper. First, the Archimedes' density measurement technique is applied to all the manufactured specimens. Next, CT observations are carried out on at least one specimen for each parameter set.

3.3 Archimede's method

The porosity measurements by the Archimedes' method are performed according to the ASTM B962-17 standard using a Sartorius YDK03 density determination kit with a measurement uncertainty of 0.05%. At least four measurements are carried out for each manufacturing parameter set.

3.4 Computed tomography (CT)

3.5

Computed tomography analysis on at least one 6.25 mm-diameter x 5 mm-height sections of the coupons belonging to each parameter set was performed using a Nikon XT-H225 CT system with a 225 kV reflection X-Ray source. The specimens were scanned with a voxel size of 5x5x5 (µm), a beam energy of 200 kV and a current of 50 mA using a 1 mm-thick copper sheet filter. A total of 2634 projections with an exposure time of two seconds were acquired.

The images were reconstructed using the CT PRO 3D software provided by Nikon Metrology, and the post-processing was performed using the ORS Dragonfly image treatment software. To avoid false detections associated with noise, a lower bound threshold of above 8 contiguous 5x5x5 (µm) voxels was considered, which corresponds to a volume of 1000 μm^3 and an equivalent minimal spherical defect ~12.4 µm in diameter. The validity of the CT analysis was assessed by comparing the results obtained with two different specimens produced using the same parameter set V5 (Specimen 1 and 2, CT1) and by analysing the same specimen twice (Specimen 1, CT1 and CT2). A good agreement is found in all the cases, as shown in Figure A 3.

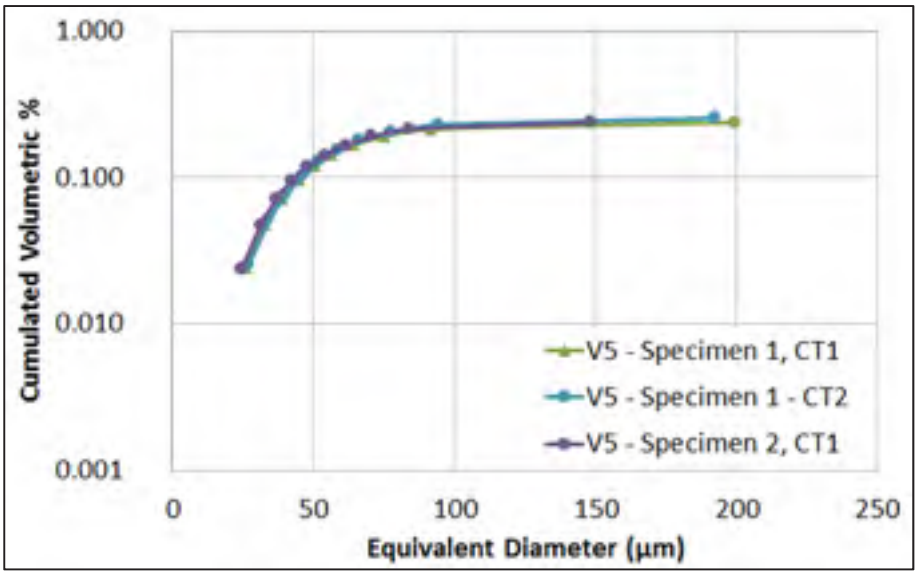

Figure A 3: The pore size distributions obtained by multiple CT analyses of the V5 parameter set specimens

3.6 Tensile Testing

Room-temperature tensile testing to failure is performed at a constant strain rate of 10^{-3} s^{-1} on a 15 kN MTS 810 servo-hydraulic tensile machine equipped with an MTS 634.12 mechanical extensometer. During testing, time, strain and force are recorded at an acquisition rate of 20Hz. The Young's modulus is calculated in the 100-250 MPa stress range, the yield stress (YS) is determined on the basis of a 0.2% offset strain, the ultimate tensile strength (UTS) corresponds to the maximum force reached during testing, and the elongation at break (δ) corresponds to the maximum strain reached during testing (without elastic component).

4. Results

4.1 Porosity measurements

4.1.1 Archimede's method

Porosity levels of up to 20% were generated by varying the principal laser exposure parameters (power, scanning speed and hatching space). Some of the specimens with the highest energy levels: VED≥90 J/mm^3 (V1, V2, H1 and H2) could not be manufactured successfully, and their build had to be aborted after only 4 layers, since they were impeding the recoater movement and generating excessive particle splattering on the powder bed. As a result, only specimens with VED levels ranging from 17 to 90 J/mm^3 were built.

The porosity level measured by the Archimedes' method are plotted as functions of each processing parameter in Figure A 4 a,b,c. It can be noted that certain ranges of processing conditions led to relatively low levels of processing-induced porosity (≤0.5%): laser power ranging from 56 to 214 W, scanning speed ranging from 720 to 1440 mm/s, and hatching space, ranging from 0.08 to 0.14 mm.

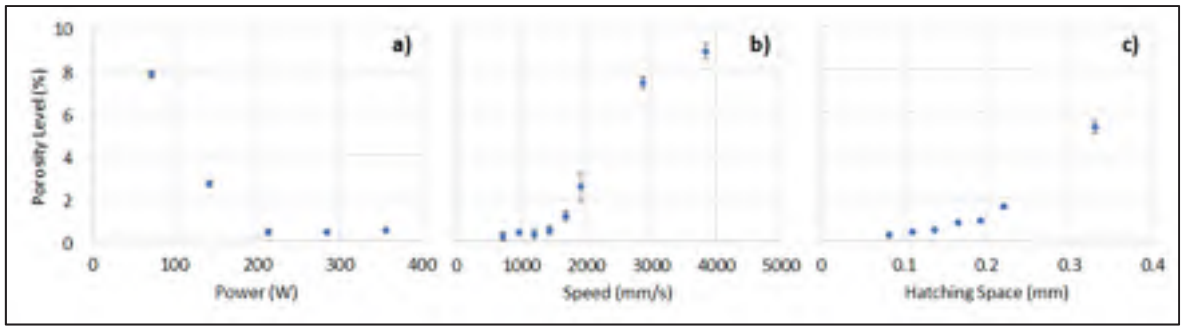

Figure A 4 Archimedes' porosity as a function of (a) laser power, (b) scanning speed, and (c) hatching space

4.1.2 Computed tomography

Typical results of the CT analyses for R, V5 and V7 specimens are shown in Figure A 5 a to c. For these specimens, the CT porosities after SR correspond to 0.07, 0.25 and 2.67%, respectively (Figure A 5), while after SR+HIP, they correspond to ~0.03, 0.05 and 0.33%, respectively (V5-HIP and V7-HIP specimens are shown in Figure A 5 d and e, while R-HIP is omitted because of its similarity to the R-SR specimen in Figure A 5 a). For specimens R-HIP, V5-HIP and V6-HIP, the final porosity levels are quite close, while for V7-HIP, the remaining porosity is relatively high, and some of the pores are interconnected and open to the surface. The open pores are permeable to high-pressure argon during HIP, while their closed counterparts contain gases entrapped during processing, and the largest of them shrink, but still remain after HIP.

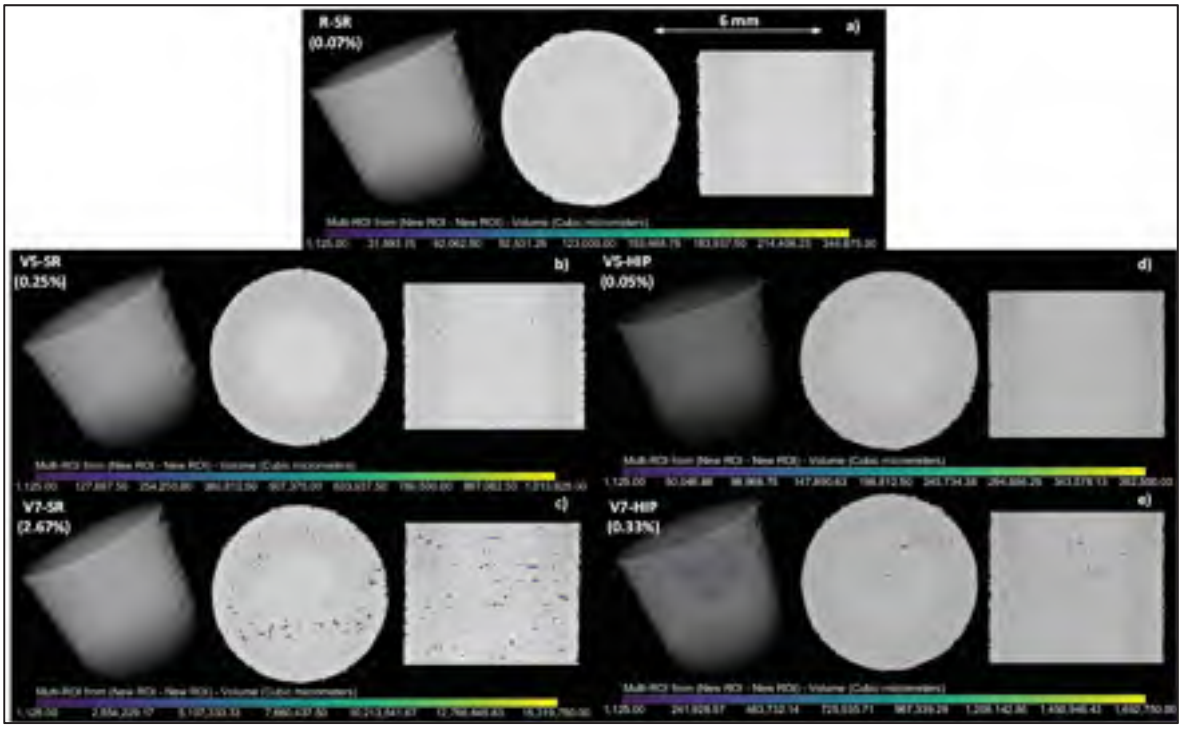

Figure A 5 CT-observed porosities after SR in specimens: a) R, b) V5 and c) V7; after SR+HIP: d) V5 and e) V7

Figure A 6 a) shows the pore size distribution obtained via CT analysis for specimens R, V5, V6 and V7. In this figure, the pore equivalent diameter is plotted against the cumulated porosity on a log scale, showing that when the scanning speed increases, both the pore size and the porosity level increase drastically. Note that the porosity values indicated in Figure A 5 and Figure A 6 correspond to those resulting from the CT measurements, and that they differ from those obtained by the Archimedes' technique (see section 4.1.3 for discussion about the sources of this discrepancy).

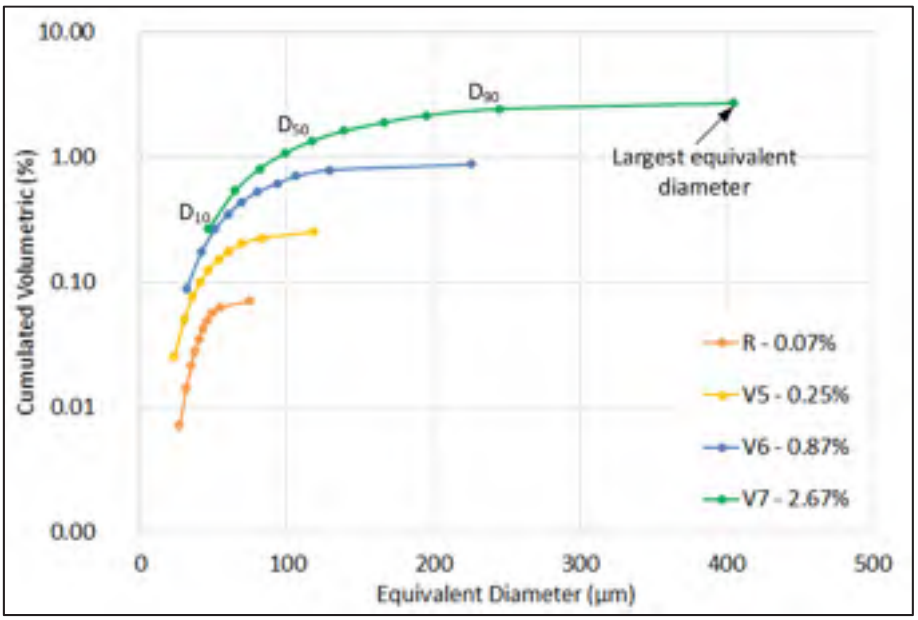

Figure A 6 Porosity distributions obtained by CT analysis for specimens R, V5, V6 and V7

4.1.3 CT vs Archimedes' measured porosity

The levels of the CT- and Archimedes'-measured porosities are shown as a function of VED in Figure A 7 for all SR specimens. For specimens having a porosity level below 2%, there appears to be a significant underestimation (0.3 ± 0.1% on average) of the CT porosity when compared to its Archimedes' equivalent. This discrepancy is mainly related to the presence of a certain quantity of pores smaller than the CT detection threshold of ~12.4 µm. Moreover,

variations in the alloy compositions could result in a density level different from the theoretical value used in Archimedes' calculations. An incomplete wetting of the LPBF surfaces could also influence the Archimedes' measurement. For specimens having a porosity level above 2%, the tendency is inversed and the Archimedes' porosity is smaller than its CT equivalent (see Figure A 7 and numerical values in Table A 1 of the Annex). This discrepancy is due to the fact that CT analysis does not allow partially fused and tightly packed particles inside large pores to be distinguished from entirely fused materials.

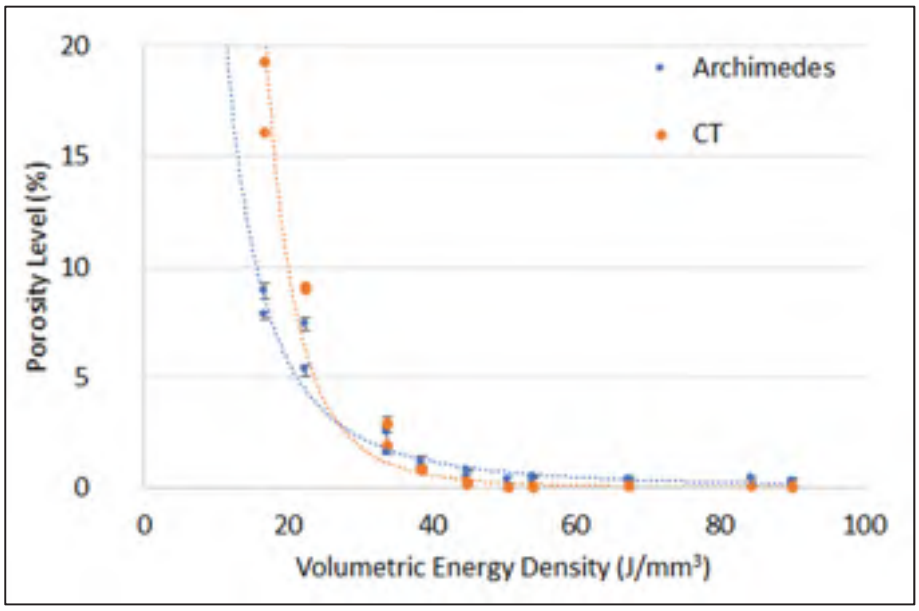

Figure A 7 :Archimedes' and CT-measured porosities as functions of VED (SR specimens)

Note that in the next sections of this work, porosity values measured by CT are mentioned when the aspects of pore morphology and special distribution are discussed. Otherwise, Archimedes' porosity values are preferred since they are believed to be more statistically representative.

3.3 Tensile Properties

Figure A 8 shows typical tensile diagrams of the 0- and 90°-oriented R, V5, V6 and V7 specimens produced by varying the scanning speed (V) from 960 to 1920 m/s (P=285 W and h=0.11 mm), and subjected to SR and SR+HIP post-processing. The mechanical properties and the porosity levels of all the tested specimens are presented in Table A 2 of the Annex.

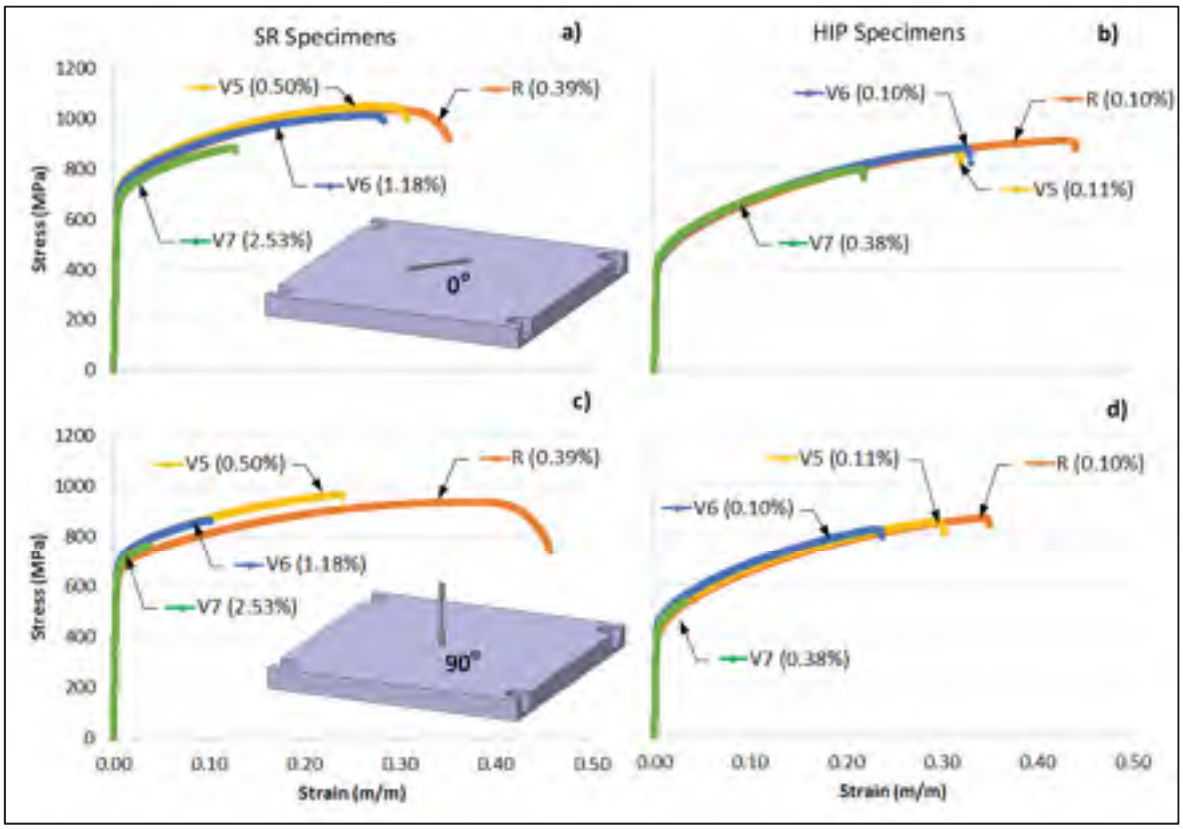

Figure A 8 Typical tensile stress-strain diagrams obtained for R, V5, V6 and V7 specimens with build orientation 0°: a) SR, b) HIP, and 90°: c) SR, d) HIP; the porosity values are Archimedes'-measured

5. Discussion

5.1 Effect of laser exposure parameters on material density and pores distribution

VED appears to be a determining factor driving the level of porosity and a wide range of the VED levels [from 45 to 90 J/mm^3], which result in fairly low porosities (≤0.5%). Therefore, the process appears to be robust and to leave enough room for optimisation using other considerations than just the material density.

For example, the process could be further optimised to improve the microstructure, dimensional accuracy, surface roughness, build rate, etc. It should be emphasised that when the VED decreases below 45 J/mm^3, the porosity level increases rapidly. Typically, a similar trend is expected when the VED exceeds 90 J/mm^3 due to the keyholing melting mode generating a significant amount of porosity (Kasperovich et al., 2016). However, in the framework of this study, the latter effect was not observed, given the limitations of the EOS system: specimens with high energy levels impeded the recoater movement and their build needed to be aborted.

The CT observations also showed that the pores resulting from the decreasing laser power P and increasing scanning speed v (while the hatching space and layer thickness are maintained constant) are distributed randomly and stretched horizontally: for example, in the build plane of specimens V7 and P2 (Figure A 9), the cumulative pore area is 40-50% greater than in the normal plane. When the P/v ratio decreases (this metric, called linear energy density, is frequently used in conventional welding), the volume of the melt pool decreases and its stability is affected, which has been shown to promote the development of stretched and interconnected pores (Kasperovich et al., 2016).

On the other hand, when the hatching space is increased while the P/v ratio is maintained constant (specimen H7), the pores are mainly distributed along the tracks and organised in a sort of chess pattern (Figure A 9). In this case, defects obtained by increasing the hatching space are essentially caused by a decreasing overlap between the melt tracks, causing a porosity distribution defined by the hatching strategy (track rotation, stripe width, etc.) (Tang, Pistorius et Beuth, 2017). Unlike with variations in power and speed, the cumulative areas of pores in the build and normal planes in this case are equivalent, and the pores are less interconnected.

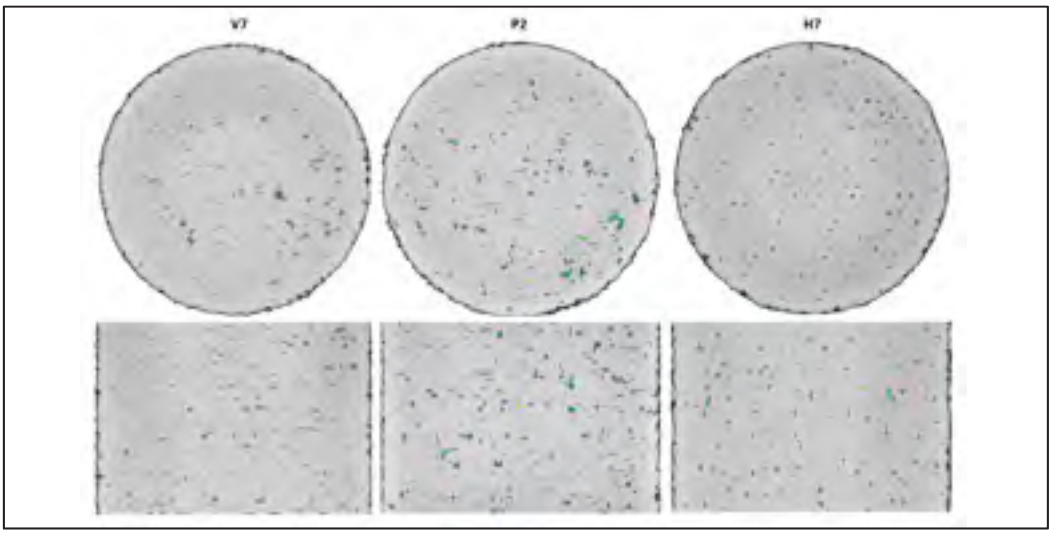

Figure A 9 Typical defects observed by CT in the build and normal planes for specimens manufactured with a constant VED of 34 J/mm^3, V7 (2.67%), P2 (2.93%), H7 (1.92%); the porosity values are CT-measured

4.2 Effect of porosity and post-processing on the tensile mechanical properties

In Figure A 10, normalised mechanical properties from Table A 2 of the Annex, namely, the Young's modulus E, the yield stress YS, the ultimate tensile strength UTS, and the elongation to failure δ, are plotted as functions of the build orientation, porosity and post-processing conditions (SR or SR+HIP). In Figure A 10 a) and b), the mechanical properties are normalised using the corresponding values of the 0^o-oriented SR specimens, while in Figure A 10 c) and d), they are normalised using those of the 90^o-oriented SR specimens.

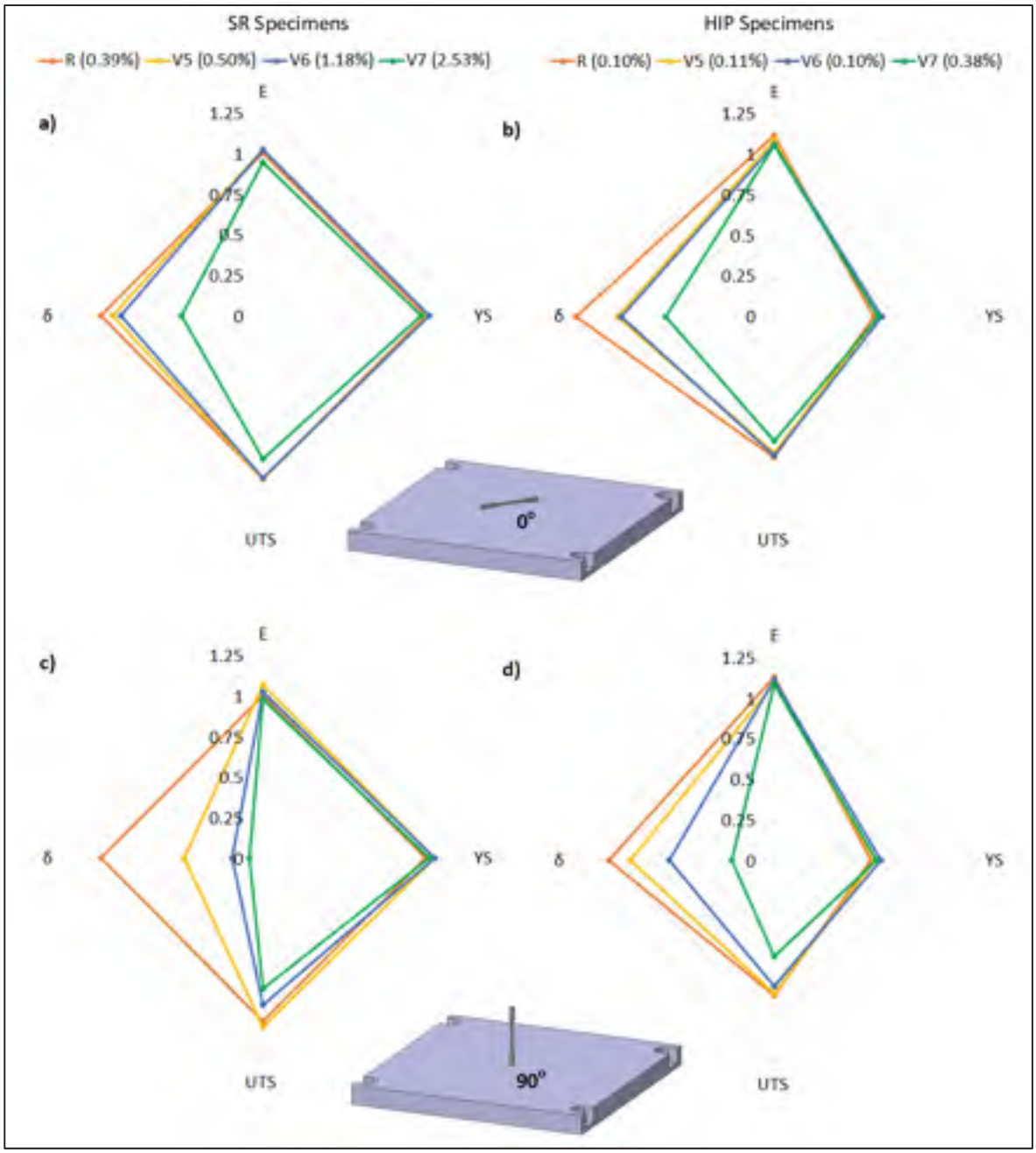

Figure A 10 Normalised mechanical properties (SR as the reference conditions): build orientation 0º: a) SR and b) HIP; build orientation 90º: c) SR and d) HIP; the porosity values are Archimedes'-measured

When comparing the properties of the SR specimens manufactured with various laser scanning speeds, it can be seen that the E and YS values remain close for all the porosity levels (Figure A 10 a) and c)). More than that, a simple Anova analysis confirms that the YS values for specimens V5 and V6 are even slightly higher than those of the Reference specimens (p-values ≤0.05), despite their higher porosity (see Table A 2 of the Annex for numerical values). This apparent discrepancy can be explained by the fact that an increase in scanning speed at a constant laser power (Reference, V5, V6 and V7 specimens) increases the cooling rate, thus resulting in a finer microstructure (Kreitcberg et al., 2017), and that in this case, the strengthening effect of the structure refinement outweighs the weakening effect of the porosity increase.

In the plastic deformation regime however, a significant drop in elongation at break indicates that the material ductility is much more severely affected by porosity than the material resistance, and this effect is strongly build orientation-dependent. In the case of specimens built at 0° (Figure A 10 a), the reduction in elongation at break is relatively weak, while for those built at 90°, this decrease is drastic, even at low porosity levels (compare specimens V5 and V6 in Figure A 10 b) and c)). Furthermore, the UTS of 0° specimens decreases to a lower extent as a function of the processing-induced porosity as compared to their 90° counterparts (Figure A 10 b) and c)). As discussed previously, pores in V5, V6 and V7 specimens are stretched in the build plane, which could explain a greater negative impact of porosity on the mechanical properties of 90° specimens. The mechanical properties of the 0° and 90°-oriented specimens subjected to HIP are shown in Figure A 10 b) and d). It can be seen that both the processing-induced porosity and the material resistance (YS and UTS) are reduced for all the specimens subjected to HIP, and that the material softening observed is accompanied by an increase in ductility. Both phenomena are expected, since on the one hand, HIP exposes the parts to high temperatures and pressures, thus partially closing the processing-induced pores (Tillmann et al., 2017). On the other hand, HIP triggers the grain coarsening phenomenon, thus decreasing the mechanical resistance (Kreitcberg, Brailovski et Turenne, 2017a) (Kreitcberg, Brailovski et Turenne, 2017b; Poulin, Brailovski et Terriault, 2018).

It is worth mentioning that although specimens R, V5 and V6 have an equivalent post-HIP porosity of ~0.1% (Figure A 11), their properties differ, especially their ductility. For example, after HIP, the elongations at break of 0°-oriented V5 and V6 specimens remain lower than those of 0°-oriented R specimens (31.6, 32.3 and 40.9%, respectively). Furthermore, the ductility of V7 specimens after HIP is not the same as that of R specimens before HIP, despite their equivalent porosity of ~0.4% (Figure A 11). For example, for the build orientation of 0°, the elongation at break of V7-HIP specimens is 22.5%, whereas for R-SR specimens, it is 33.4%. Both phenomena are even more accentuated for 90° specimens (see Table A 2 in the Annex).

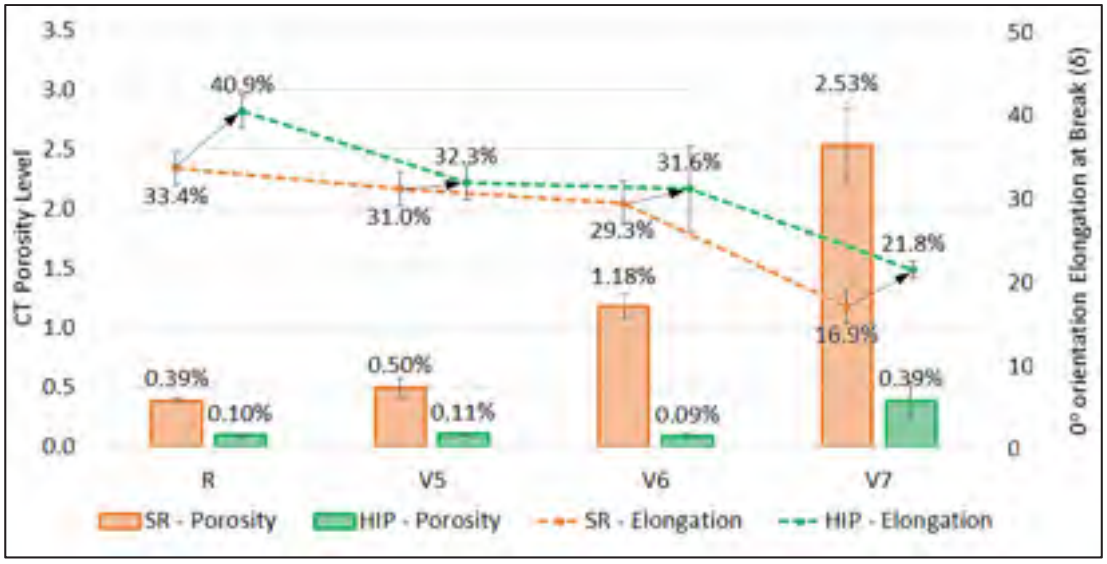

Figure A 11: Porosity (Archimedes') and elongation at break for R, V5, V6, and V7 specimens before and after HIP

The lower ductility of pore-containing specimens even after their HIP post-processing could be explained by the nature of residual pores in these specimens, which are especially critical for V7 specimens, where pores represent large clusters of interconnected lack-of-fusion type defects connected to the surface (see Figure A 12). To support this assertion, the CT scans and SEM fracture surface images from V7-90° specimens subjected to SR and SR+HIP post-processing are shown in Figure A 12. Failures of these two specific specimens occurred at an

elongation of 4%, with no reduction of area. Also for both specimens, the CT observations reveal the presence of multiple cracks which had already been initiated on the surface. For both specimens, the SEM images reveal that in addition to dimpled regions, some zones of the fracture surfaces contain unmelted powder and demonstrate a lack of cohesion.

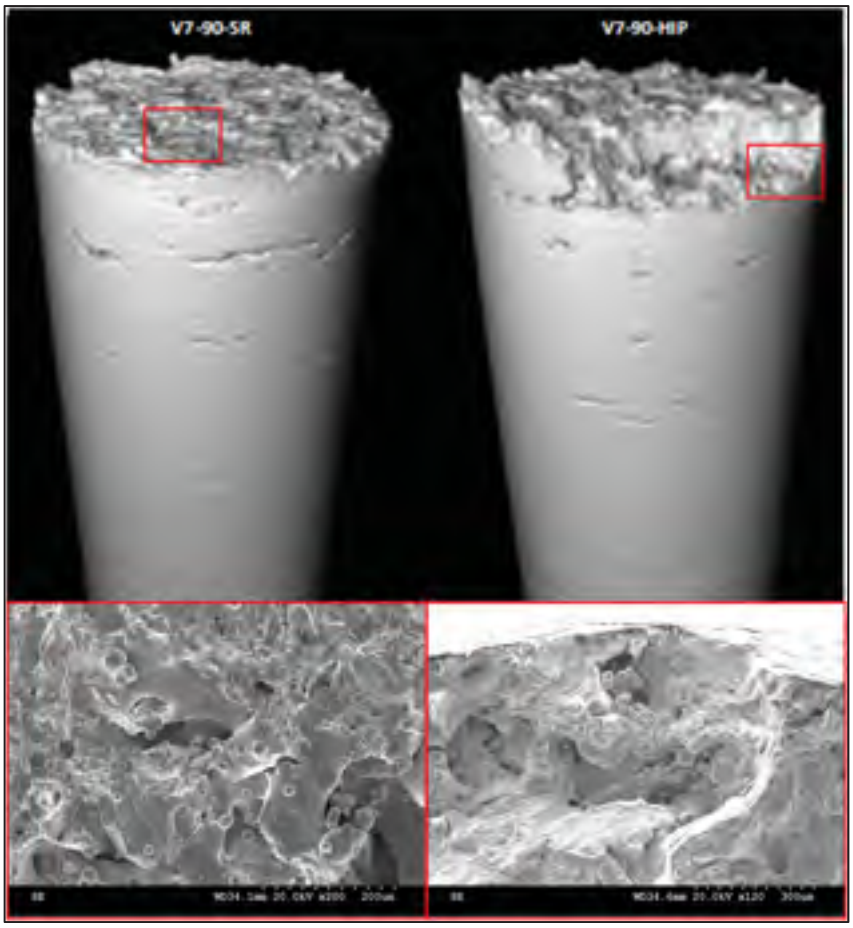

Figure A 12 CT and SEM fracture surface observations of the tensile-tested specimens (V7-90°): a) SR (Archimedes' porosity 2.53%) and b) SR+HIP (porosity 0.38%); elongation at break of both specimens ~4%

Given the above observations, the as-built porosity level appears to play a definitive role as far as the mechanical properties are concerned. Moreover, even though HIP increases the elongation at break of flawed LPBF specimens, this positive effect is limited to specimens

containing as-built porosities that are less than ~1%. Surprisingly, the elongation at break of specimens obtained with the reference parameters was lower following the HIP, with no striction observed**.** Obviously, a plan of experiments with more specimens is required to increase the statistical significance of the results obtained.

6. Conclusions

In this study, porosities were generated in LPBF Inconel 625 specimens by varying the laser power, scanning speed and hatching space. Specimens containing up to 20% of porosity were successfully built when increasing the speed and the hatching distance, or reducing power. Comparing each parameter set for VEDs ranging from 45 to 90 J/mm^3, the porosity level was consistently found below 0.5%, and increased rapidly below 45 J/mm^3. Tensile testing on specimens containing up to ~3% porosity manufactured by increasing the scanning speed from 960 to 1920 mm/s revealed strong sensitivity of elongation at break and, to a lesser extent, of UTS, to the level of porosity. This was especially true for 90^o-oriented specimens. The results of mechanical testing of HIP specimens attest that this post-processing can provide significant improvement in the ductility of specimens with as-built porosities below ~1% (V5 and V6). More work is however required to obtain more statistically significant results regarding the defects characterisation. More work is also required to separate the influence of porosity on the mechanical properties from that of the microstructure. Following such work, the influence of LPBF-induced defects on the fatigue behaviour of IN625 specimens should be evaluated in the context of a damage-tolerant approach (fatigue crack propagation).

7. Acknowledgements

The author would like to thank the Fonds de Recherche du Québec - Nature et Technologie (FRQNT), and the Natural Science and Engineering Research Council of Canada (NSERC) for their support in financing the present study. Contribution of Alexandre Bocher in the realisation of porosity analysis is also recognised.

8. Annex

Table A 1 : Parameters employed for the porosity generation and measured Archimedes' and CT porosity

Parameter Set	Power (W)	Speed (mm/s)	Hatching Space (mm)	VED (J/mm^3)	Archimedes Porosity (%)	CT Porosity (%)
V1	285	240	0.11	270	-	-
V2	285	480	0.11	135	-	-
V3	285	720	0.11	90.0	0.26	0.08
Reference	285	960	0.11	67.5	0.39	0.07
V4	285	1200	0.11	54.0	0.30	0.11
V5	285	1440	0.11	45.0	0.50	0.25
V6	285	1680	0.11	38.6	1.18	0.87
V7	285	1920	0.11	33.7	2.53	2.67
V8	285	2880	0.11	22.5	7.42	8.99
V9	285	3840	0.11	16.9	8.90	19.32
P1	71	960	0.11	16.9	7.83	16.11
P2	143	960	0.11	33.7	2.67	2.93
P3	214	960	0.11	50.6	0.47	0.10
Reference	285	960	0.11	67.5	0.39	0.07
P4	356	960	0.11	84.3	0.46	0.05
H1	285	960	0.03	270	-	-
H2	285	960	0.05	135	-	-
H3	285	960	0.08	90.0	0.23	0.03
Reference	285	960	0.11	67.5	0.39	0.07
H4	285	960	0.14	54.0	0.50	0.06
H5	285	960	0.17	45.0	0.82	0.30
H6	285	960	0.19	38.6	0.94	0.76
H7	285	960	0.22	33.7	1.78	1.92
H8	285	960	0.33	22.5	5.31	9.09

Table A 2 : Mechanical properties of SR and HIP specimens (0º and 90º orientation)

Parameter Set	Porosity (%)	E (GPa)	YS (MPa)	UTS (MPa)	Elongation (%)
SR Specimens					
Reference – 0º	0.39	194 ± 5	689 ± 4	1035 ± 7	33.4 ± 2
V5 – 0º	0.50	199 ± 1	704 ± 2	1036 ± 3	31.0 ± 2
V6 – 0º	1.18	198 ± 5	707 ± 4	1030 ± 18	29.3 ± 5
V7 – 0º	2.53	184 ± 3	672 ± 4	909 ± 16	16.9 ± 1
Reference – 90º	0.39	189 ± 3	637 ± 1	934 ± 2	46.0 ± 1
V5 – 90º	0.50	202 ± 5	676 ± 4	966 ± 18	22.3 ± 5
V6 – 90º	1.18	193 ± 4	673 ± 3	840 ± 58	8.8 ± 4
V7 – 90º	2.53	185 ± 4	651 ± 4	749 ± 17	4.3 ± 1
HIP Specimens					
Reference – 0º	0.10	216 ± 13	422 ± 3	894 ± 11	40.9 ± 2
V5 – 0º	0.11	211 ± 3	439 ± 9	868 ± 12	32.3 ± 2
V6 – 0º	0.09	206 ± 11	456 ± 15	883 ± 17	31.6 ± 3
V7 – 0º	0.38	204 ± 3	441 ± 7	795 ± 25	22.5 ± 2
Reference – 90º	0.10	219 ± 4	408 ± 2	858 ± 11	44.2 ± 2
V5 – 90º	0.11	211 ± 9	425 ± 1	850 ± 11	29.7 ± 1
V6 – 90º	0.09	216 ± 2	450 ± 2	804 ± 26	21.8 ± 3
V7 – 90º	0.38	211 ± 12	433 ± 5	609 ± 129	8.8 ± 9

LISTE DE RÉFÉRENCES BIBLIOGRAPHIQUES

Akita, Masayuki, Yoshihiko Uematsu, Toshifumi Kakiuchi, Masaki Nakajima et Ryosei Kawaguchi. 2016. « Defect-dominated fatigue behavior in type 630 stainless steel fabricated by selective laser melting ». *Materials Science and Engineering: A,* vol. 666, p. 19-26.

Amato, Krista, J Hernandez, LE Murr, E Martinez, SM Gaytan, PW Shindo et S Collins. 2012. « Comparison of microstructures and properties for a Ni-base superalloy (alloy 625) fabricated by electron beam melting ». *Journal of Materials Science Research,* vol. 1, nº 2, p. 3.

Anderson, T.L. 2017. *Fracture Mechanics: Fundamentals and Applications, Fourth Edition*. CRC Press.

Atzeni, Eleonora, et Alessandro Salmi. 2012. « Economics of additive manufacturing for end-usable metal parts ». *The International Journal of Advanced Manufacturing Technology,* vol. 62, nº 9-12, p. 1147-1155.

Baicheng, Zhang, Lee Xiaohua, Bai Jiaming, Guo Junfeng, Wang Pan, Sun Chen-nan, Nai Muiling, Qi Guojun et Wei Jun. 2017. « Study of selective laser melting (SLM) Inconel 718 part surface improvement by electrochemical polishing ». *Materials & Design,* vol. 116, p. 531-537.

Balachandramurthi, Arun Ramanathan, Johan Moverare, Nikhil Dixit, Dunyong Deng et Robert Pederson. 2019. « Microstructural influence on fatigue crack propagation during high cycle fatigue testing of additively manufactured Alloy 718 ». *Materials Characterization*.

Bang, DJ, A Ince et M Noban. 2019. « Modeling approach for a unified crack growth model in short and long fatigue crack regimes ». *International Journal of Fatigue,* vol. 128, p. 105182.

Bao, Rui, et Xiang Zhang. 2010. « Fatigue crack growth behaviour and life prediction for 2324-T39 and 7050-T7451 aluminium alloys under truncated load spectra ». *International Journal of Fatigue,* vol. 32, nº 7, p. 1180-1189.

Beretta, S., M. Carboni et M. Madia. 2009. « Modelling of fatigue thresholds for small cracks in a mild steel by "Strip-Yield" model ». *Engineering Fracture Mechanics,* vol. 76, nº 10, p. 1548-1561.

Beretta, S., et S. Romano. 2017. « A comparison of fatigue strength sensitivity to defects for materials manufactured by AM or traditional processes ». *International Journal of Fatigue,* vol. 94, Part 2, p. 178-191.

Bidare, P, I Bitharas, RM Ward, MM Attallah et AJ Moore. 2018. « Fluid and particle dynamics in laser powder bed fusion ». *Acta Materialia,* vol. 142, p. 107-120.

Biswal, Romali, Xiang Zhang, Abdul Khadar Syed, Mustafa Awd, Jialuo Ding, Frank Walther et Stewart Williams. 2019. « Criticality of porosity defects on the fatigue performance of wire+ arc additive manufactured titanium alloy ». *International Journal of Fatigue,* vol. 122, p. 208-217.

Blackwell, P. L. 2005. « The mechanical and microstructural characteristics of laser-deposited IN718 ». *Journal of Materials Processing Technology,* vol. 170, nº 1, p. 240-246.

Boyer, Howard E. 1985. *Atlas of fatigue curves*. Asm International.

Brackett, D, I Ashcroft et R Hague. 2011. « Topology optimization for additive manufacturing ». In *Proceedings of the solid freeform fabrication symposium, Austin, TX*. p. 348-362.

Brandl, Erhard, Ulrike Heckenberger, Vitus Holzinger et Damien Buchbinder. 2012. « Additive manufactured AlSi10Mg samples using Selective Laser Melting (SLM): Microstructure, high cycle fatigue, and fracture behavior ». *Materials & Design,* vol. 34, p. 159-169.

Caiazzo, Fabrizia, Vittorio Alfieri, Gaetano Corrado et Paolo Argenio. 2017. « Laser powder-bed fusion of Inconel 718 to manufacture turbine blades ». *The International Journal of Advanced Manufacturing Technology*.

Caton, M. J., et S. K. Jha. 2010. « Small fatigue crack growth and failure mode transitions in a Ni-base superalloy at elevated temperature ». *International Journal of Fatigue,* vol. 32, nº 9, p. 1461-1472.

Chen, Bo, Jun Jiang et Fionn P. E. Dunne. 2017. « Microstructurally-sensitive fatigue crack nucleation in Ni-based single and oligo crystals ». *Journal of the Mechanics and Physics of Solids,* vol. 106, p. 15-33.

Ciavarella, M., et F. Monno. 2006. « On the possible generalizations of the Kitagawa–Takahashi diagram and of the El Haddad equation to finite life ». *International Journal of Fatigue,* vol. 28, nº 12, p. 1826-1837.

Committee, ASM International. Handbook. 1990. *ASM Handbook*. vol. 12. ASM International.

Conner, Brett P, Guha P Manogharan, Ashley N Martof, Lauren M Rodomsky, Caitlyn M Rodomsky, Dakesha C Jordan et James W Limperos. 2014. « Making sense of 3-D printing: Creating a map of additive manufacturing products and services ». *Additive Manufacturing,* vol. 1, p. 64-76.

Correia, JAFO, Abílio MP De Jesus, Alfonso Fernández-Canteli, Roberto Brighenti, PMGP Moreira et R Calçada. 2016. « A procedure to obtain the probabilistic kitagawa-takahashi diagram ». *UPB Sci. Bull. Ser. Mech. Eng,* vol. 78, p. 3-12.

Cotteleer, Mark, et Jim Joyce. 2014. « 3D opportunity: Additive manufacturing paths to performance, innovation, and growth ». *Deloitte Review,* vol. 14, p. 5-19.

Criales, Luis, Yigit Arisoy, Brandon Lane, Shawn Moylan, M. Donmez et Tuğrul Özel. 2016. *Predictive Modeling and Optimization of Multi-Track Processing for Laser Powder Bed Fusion of Nickel Alloy 625*.

Criales, Luis E, Yiğit M Arısoy, Brandon Lane, Shawn Moylan, Alkan Donmez et Tuğrul Özel. 2017. « Laser powder bed fusion of nickel alloy 625: experimental investigations of effects of process parameters on melt pool size and shape with spatter analysis ». *International Journal of Machine Tools and Manufacture,* vol. 121, p. 22-36.

de los Rios, E. R., A. Walley, M. T. Milan et G. Hammersley. 1995. « Fatigue crack initiation and propagation on shot-peened surfaces in A316 stainless steel ». *International Journal of Fatigue,* vol. 17, nº 7, p. 493-499.

DebRoy, T., H. L. Wei, J. S. Zuback, T. Mukherjee, J. W. Elmer, J. O. Milewski, A. M. Beese, A. Wilson-Heid, A. De et W. Zhang. 2018. « Additive manufacturing of metallic components – Process, structure and properties ». *Progress in Materials Science,* vol. 92, p. 112-224.

Deng, Dunyong, Johan Moverare, Ru Lin Peng et Hans Söderberg. 2017. « Microstructure and anisotropic mechanical properties of EBM manufactured Inconel 718 and effects of post heat treatments ». *Materials Science and Engineering: A,* vol. 693, p. 151-163.

Dubey, S., A. B. O. Soboyejo et W. O. Soboyejo. 1997. « AN INVESTIGATION OF THE EFFECTS OF STRESS RATIO AND CRACK CLOSURE ON THE MICROMECHANISMS OF FATIGUE CRACK GROWTH IN Ti-6Al-4V ». *Acta Materialia,* vol. 45, nº 7, p. 2777-2787.

Edwards, P., et M. Ramulu. 2014. « Fatigue performance evaluation of selective laser melted Ti–6Al–4V ». *Materials Science and Engineering: A,* vol. 598, p. 327-337.

Edwards, P., et M. Ramulu. 2015. « Effect of build direction on the fracture toughness and fatigue crack growth in selective laser melted Ti-6Al-4 V ». *Fatigue & Fracture of Engineering Materials & Structures,* vol. 38, nº 10, p. 1228-1236.

El Haddad, MH, KN Smith et TH Topper. 1979. « Fatigue crack propagation of short cracks ». *Journal of Engineering Materials and Technology,* vol. 101, nº 1, p. 42-46.

El Haddad, MH, TH Topper et KN Smith. 1979. « Prediction of non propagating cracks ». *Engineering fracture mechanics,* vol. 11, nº 3, p. 573-584.

Elber, Wolf. 1971. « The significance of fatigue crack closure ». In *Damage tolerance in aircraft structures*. ASTM International.

Ferrar, B., L. Mullen, E. Jones, R. Stamp et C. J. Sutcliffe. 2012. « Gas flow effects on selective laser melting (SLM) manufacturing performance ». *Journal of Materials Processing Technology,* vol. 212, nº 2, p. 355-364.

Fleck, NA, et RA Smith. 1981a. « Effect of density on tensile strength, fracture toughness, and fatigue crack propagation behaviour of sintered steel ». *Powder Metallurgy,* vol. 24, nº 3, p. 121-125.

Fleck, NA, et RA Smith. 1981b. « Use of simple models to estimate effect of density on fracture behaviour of sintered steel ». *Powder Metallurgy,* vol. 24, nº 3, p. 126-130.

Ford, Sharon LN. 2014. « Additive manufacturing technology: Potential implications for US manufacturing competitiveness ». *Journal of International Commerce and Economics*.

Ford, Simon, et Mélanie Despeisse. 2016. « Additive manufacturing and sustainability: an exploratory study of the advantages and challenges ». *Journal of Cleaner Production,* vol. 137, p. 1573-1587.

Forman, RG, V Shivakumar, JW Cardinal, LC Williams et PC McKeighan. 2005. « Fatigue crack growth database for damage tolerance analysis ».

Forman, RG, V Shivakumar, SR Mettu et JC Newman. 2000. « Fatigue crack growth computer program NASGRO version 3.0 ». *Reference Manual, NASA JSC-22267B*.

Forman, Royce G, VE Kearney et RM Engle. 1967. « Numerical analysis of crack propagation in cyclic-loaded structures ».

Fox, Jason C., Shawn P. Moylan et Brandon M. Lane. 2016. « Effect of Process Parameters on the Surface Roughness of Overhanging Structures in Laser Powder Bed Fusion Additive Manufacturing ». *Procedia CIRP,* vol. 45, p. 131-134.

Fractography. 1987. ASM International.

Gagnon, Martin, Antoine Tahan, Philippe Bocher et Denis Thibault. 2013. « A probabilistic model for the onset of High Cycle Fatigue (HCF) crack propagation: Application to hydroelectric turbine runner ». *International Journal of Fatigue,* vol. 47, p. 300-307.

Ganesh, P., R. Kaul, C. P. Paul, Pragya Tiwari, S. K. Rai, R. C. Prasad et L. M. Kukreja. 2010. « Fatigue and fracture toughness characteristics of laser rapid manufactured Inconel 625 structures ». *Materials Science and Engineering: A,* vol. 527, nº 29, p. 7490-7497.

Gao, Wei, Yunbo Zhang, Devarajan Ramanujan, Karthik Ramani, Yong Chen, Christopher B. Williams, Charlie C. L. Wang, Yung C. Shin, Song Zhang et Pablo D. Zavattieri. 2015. « The status, challenges, and future of additive manufacturing in engineering ». *Computer-Aided Design,* vol. 69, p. 65-89.

Gao, Yong, R. O. Ritchie, Mukul Kumar et R. K. Nalla. 2005. « High-cycle fatigue of nickel-based superalloy ME3 at ambient and elevated temperatures: Role of grain-boundary engineering ». *Metallurgical and Materials Transactions A,* vol. 36, nº 12, p. 3325-3333.

Gao, Yong, J. S. Stölken, Mukul Kumar et R. O. Ritchie. 2007. « High-cycle fatigue of nickel-base superalloy René 104 (ME3): Interaction of microstructurally small cracks with grain boundaries of known character ». *Acta Materialia,* vol. 55, nº 9, p. 3155-3167.

Garb, Christian, Martin Leitner, Bernhard Stauder, Dirk Schnubel et Florian Grün. 2018. « Application of modified Kitagawa-Takahashi diagram for fatigue strength assessment of cast Al-Si-Cu alloys ». *International Journal of Fatigue,* vol. 111, p. 256-268.

Gong, Haijun, Khalid Rafi, Hengfeng Gu, G. D. Janaki Ram, Thomas Starr et Brent Stucker. 2015. « Influence of defects on mechanical properties of Ti–6Al–4 V components produced by selective laser melting and electron beam melting ». *Materials & Design,* vol. 86, p. 545-554.

Gong, Haijun, Khalid Rafi, Hengfeng Gu, Thomas Starr et Brent Stucker. 2014. « Analysis of defect generation in Ti–6Al–4V parts made using powder bed fusion additive manufacturing processes ». *Additive Manufacturing,* vol. 1-4, p. 87-98.

Gorelik, Michael. 2017. « Additive manufacturing in the context of structural integrity ». *International Journal of Fatigue,* vol. 94, Part 2, p. 168-177.

Greitemeier, Daniel, Frank Palm, Freerk Syassen et Tobias Melz. 2017. « Fatigue performance of additive manufactured TiAl6V4 using electron and laser beam melting ». *International Journal of Fatigue,* vol. 94, p. 211-217.

Griffith, Alan Arnold. 1921. « VI. The phenomena of rupture and flow in solids ». *Philosophical transactions of the royal society of london. Series A, containing papers of a mathematical or physical character,* vol. 221, nº 582-593, p. 163-198.

Günther, J., D. Krewerth, T. Lippmann, S. Leuders, T. Tröster, A. Weidner, H. Biermann et T. Niendorf. 2017. « Fatigue life of additively manufactured Ti–6Al–4V in the very high cycle fatigue regime ». *International Journal of Fatigue,* vol. 94, p. 236-245.

Gusarov, AV, I Yadroitsev, Ph Bertrand et I Smurov. 2009. « Model of radiation and heat transfer in laser-powder interaction zone at selective laser melting ». *Journal of heat transfer,* vol. 131, nº 7, p. 072101.

Hack, Harvey, Richard Link, Erik Knudsen, Brad Baker et Scott Olig. 2017. « Mechanical properties of additive manufactured nickel alloy 625 ». *Additive Manufacturing,* vol. 14, p. 105-115.

Hadrboletz, A, et B Weiss. 1997. « Fatigue behaviour of iron based sintered material: a review ». *International materials reviews,* vol. 42, nº 1, p. 1-44.

Han, Qi-Nan, Wenhui Qiu, Zhiwu He, Yue Su, Xianfeng Ma et Hui-Ji Shi. 2018. « The effect of crystal orientation on fretting fatigue crack formation in Ni-based single-crystal superalloys: In-situ SEM observation and crystal plasticity finite element simulation ». *Tribology International,* vol. 125, p. 209-219.

Hanzl, Pavel, Miroslav Zetek, Tomáš Bakša et Tomáš Kroupa. 2015. « The Influence of Processing Parameters on the Mechanical Properties of SLM Parts ». *Procedia Engineering,* vol. 100, p. 1405-1413.

Hertzberg, R.W., R.P. Vinci et J.L. Hertzberg. 2012. *Deformation and Fracture Mechanics of Engineering Materials, 5th Edition*. Wiley.

Herzog, Dirk, Vanessa Seyda, Eric Wycisk et Claus Emmelmann. 2016. « Additive manufacturing of metals ». *Acta Materialia,* vol. 117, p. 371-392.

Hrabe, Nikolas, Thomas Gnäupel-Herold et Timothy Quinn. 2017a. « Fatigue properties of a titanium alloy (Ti–6Al–4V) fabricated via electron beam melting (EBM): Effects of internal defects and residual stress ». *International Journal of Fatigue,* vol. 94, p. 202-210.

Hrabe, Nikolas, Thomas Gnäupel-Herold et Timothy Quinn. 2017b. « Fatigue properties of a titanium alloy (Ti–6Al–4V) fabricated via electron beam melting (EBM): Effects of internal defects and residual stress ». *International Journal of Fatigue,* vol. 94, Part 2, p. 202-210.

Hwang, K. S. 2012. « 10 - Common defects in metal injection molding (MIM) ». In *Handbook of Metal Injection Molding*, sous la dir. de Heaney, Donald F., p. 235-253. Woodhead Publishing. < http://www.sciencedirect.com/science/article/pii/B9780857090669500108 >.

Irwin, George R. 1957. « Analysis of stresses and strains near the end of a crack transversing a plate ». *Trans. ASME, Ser. E, J. Appl. Mech.,* vol. 24, p. 361-364.

ISO 12108, BS. 2002. « Metallic Material—Fatigue Testing—Fatigue Crack Growth Method ».

Jia, Qingbo, et Dongdong Gu. 2014. « Selective laser melting additive manufacturing of Inconel 718 superalloy parts: Densification, microstructure and properties ». *Journal of Alloys and Compounds,* vol. 585, p. 713-721.

Jiang, J., J. Yang, T. Zhang, J. Zou, Y. Wang, F. P. E. Dunne et T. B. Britton. 2016. « Microstructurally sensitive crack nucleation around inclusions in powder metallurgy nickel-based superalloys ». *Acta Materialia,* vol. 117, p. 333-344.

Kamath, Chandrika, Bassem El-dasher, Gilbert F. Gallegos, Wayne E. King et Aaron Sisto. 2014. « Density of additively-manufactured, 316L SS parts using laser powder-bed fusion at powers up to 400 W ». *The International Journal of Advanced Manufacturing Technology,* vol. 74, nº 1, p. 65-78.

Karlén, Kristoffer, Mårten Olsson, Hamidreza Ahmadi et Gunnar Härkegård. 2012. « On the effect of random defects on the fatigue notch factor at different stress ratios ». *International Journal of Fatigue,* vol. 41, p. 179-187.

Kasperovich, Galina, Jan Haubrich, Joachim Gussone et Guillermo Requena. 2016. « Correlation between porosity and processing parameters in TiAl6V4 produced by selective laser melting ». *Materials & Design,* vol. 105, p. 160-170.

Kasperovich, Galina, et Joachim Hausmann. 2015. « Improvement of fatigue resistance and ductility of TiAl6V4 processed by selective laser melting ». *Journal of Materials Processing Technology,* vol. 220, p. 202-214.

Katayama, Seiji. 2013. *Handbook of laser welding technologies*. Elsevier.

Khairallah, Saad A., Andrew T. Anderson, Alexander Rubenchik et Wayne E. King. 2016. « Laser powder-bed fusion additive manufacturing: Physics of complex melt flow and formation mechanisms of pores, spatter, and denudation zones ». *Acta Materialia,* vol. 108, p. 36-45.

Kimura, Takahiro, et Takayuki Nakamoto. 2016. « Microstructures and mechanical properties of A356 (AlSi7Mg0.3) aluminum alloy fabricated by selective laser melting ». *Materials & Design,* vol. 89, nº Supplement C, p. 1294-1301.

Kitagawa, H. 1976. « Applicability of fracture mechanics to very small cracks or the cracks in the early stage ». *Proc. of 2nd ICM, Cleveland, 1976*, p. 627-631.

Kobayashi, M, T Matsui et Y Murakami. 1998. « Mechanism of creation of compressive residual stress by shot peening ». *International Journal of Fatigue,* vol. 20, nº 5, p. 351-357.

Kolitsch, S., H. P. Gänser, J. Maierhofer et R. Pippan. 2016. « Fatigue crack growth threshold as a design criterion - statistical scatter and load ratio in the Kitagawa-Takahashi diagram ». *IOP Conference Series: Materials Science and Engineering,* vol. 119.

Konečná, R., L. Kunz, G. Nicoletto et A. Bača. 2016. « Long fatigue crack growth in Inconel 718 produced by selective laser melting ». *International Journal of Fatigue,* vol. 92, p. 499-506.

Koutiri, Imade, Etienne Pessard, Patrice Peyre, Ouafae Amlou et Thibaut De Terris. 2018. « Influence of SLM process parameters on the surface finish, porosity rate and fatigue behavior of as-built Inconel 625 parts ». *Journal of Materials Processing Technology,* vol. 255, p. 536-546.

Kozar, R.W., A. Suzuki, W.W. Milligan, J.J. Schirra, M.F. Savage et T.M. Pollock. 2009. « Strengthening Mechanisms in Polycrystalline Multimodal Nickel-Base Superalloys ». *Metallurgical and Materials Transactions A,* vol. 40, nº 7, p. 1588-1603.

Kreitcberg, A., V. Brailovski, V. Sheremetyev et S. Prokoshkin. 2017. « Effect of Laser Powder Bed Fusion Parameters on the Microstructure and Texture Development in Superelastic Ti–18Zr–14Nb Alloy ». *Shape Memory and Superelasticity,* vol. 3, nº 4, p. 361-372.

Kreitcberg, Alena, Vladimir Brailovski et Sylvain Turenne. 2017a. « Effect of heat treatment and hot isostatic pressing on the microstructure and mechanical properties of Inconel 625 alloy processed by laser powder bed fusion ». *Materials Science and Engineering: A,* vol. 689, p. 1-10.

Kreitcberg, Alena, Vladimir Brailovski et Sylvain Turenne. 2017b. « Elevated temperature mechanical behavior of IN625 alloy processed by laser powder-bed fusion ». *Materials Science and Engineering: A,* vol. 700, p. 540-553.

Krupp, U. 2007. *Fatigue Crack Propagation in Metals and Alloys: Microstructural Aspects and Modelling Concepts*. Wiley.

Kruth, J. P., L. Froyen, J. Van Vaerenbergh, P. Mercelis, M. Rombouts et B. Lauwers. 2004. « Selective laser melting of iron-based powder ». *Journal of Materials Processing Technology,* vol. 149, nº 1–3, p. 616-622.

Kruth, Jean-Pierre, Jan Deckers, Evren Yasa et Ruben Wauthlé. 2012. « Assessing and comparing influencing factors of residual stresses in selective laser melting using a novel analysis method ». *Proceedings of the Institution of Mechanical Engineers, Part B: Journal of Engineering Manufacture,* vol. 226, nº 6, p. 980-991.

Kruth, Jean-Pierre, Peter Mercelis, J Van Vaerenbergh, Ludo Froyen et Marleen Rombouts. 2005. « Binding mechanisms in selective laser sintering and selective laser melting ». *Rapid prototyping journal,* vol. 11, nº 1, p. 26-36.

Lampman, S.R., N.D. DiMatteo et ASM International. Handbook Committee. 1996. *Fatigue and Fracture*. ASM International.

Lass, Eric A, Mark R Stoudt, Michael B Katz et Maureen E Williams. 2018. « Precipitation and dissolution of δ and γ ″during heat treatment of a laser powder-bed fusion produced Ni-based superalloy ». *Scripta Materialia,* vol. 154, p. 83-86.

Lavery, N. P., J. Cherry, S. Mehmood, H. Davies, B. Girling, E. Sackett, S. G. R. Brown et J. Sienz. 2017. « Effects of hot isostatic pressing on the elastic modulus and tensile properties of 316L parts made by powder bed laser fusion ». *Materials Science and Engineering: A,* vol. 693, p. 186-213.

Letenneur, Morgan, Vladimir Brailovski, Alena Kreitcberg, Vladimir Paserin et Ian Bailon-Poujol. 2017. « Laser Powder Bed Fusion of Water-Atomized Iron-Based Powders: Process Optimization ». *Journal of Manufacturing and Materials Processing,* vol. 1, nº 2, p. 23.

Letenneur, Morgan, Alena Kreitcberg et Vladimir Brailovski. 2019. « Optimization of Laser Powder Bed Fusion Processing Using a Combination of Melt Pool Modeling and Design of Experiment Approaches: Density Control ». *Journal of Manufacturing and Materials Processing,* vol. 3, nº 1, p. 21.

Leuders, S., M. Thöne, A. Riemer, T. Niendorf, T. Tröster, H. A. Richard et H. J. Maier. 2013. « On the mechanical behaviour of titanium alloy TiAl6V4 manufactured by selective laser melting: Fatigue resistance and crack growth performance ». *International Journal of Fatigue,* vol. 48, p. 300-307.

Li, C., Y. B. Guo et J. B. Zhao. 2017. « Interfacial phenomena and characteristics between the deposited material and substrate in selective laser melting Inconel 625 ». *Journal of Materials Processing Technology,* vol. 243, p. 269-281.

Li, C., R. White, X. Y. Fang, M. Weaver et Y. B. Guo. 2017. « Microstructure evolution characteristics of Inconel 625 alloy from selective laser melting to heat treatment ». *Materials Science and Engineering: A,* vol. 705, p. 20-31.

Li, H. Y., H. L. Sun, P. Bowen et J. F. Knott. 2018. « Effects of compressive residual stress on short fatigue crack growth in a nickel-based superalloy ». *International Journal of Fatigue,* vol. 108, p. 53-61.

Li, P., D. H. Warner, A. Fatemi et N. Phan. 2016. « Critical assessment of the fatigue performance of additively manufactured Ti–6Al–4V and perspective for future research ». *International Journal of Fatigue,* vol. 85, p. 130-143.

Li, Shuai, Qingsong Wei, Yusheng Shi, Zicheng Zhu et Danqing Zhang. 2015. « Microstructure characteristics of Inconel 625 superalloy manufactured by selective laser melting ». *Journal of Materials Science & Technology,* vol. 31, n^{o} 9, p. 946-952.

Li, Yali, et Dongdong Gu. 2014. « Parametric analysis of thermal behavior during selective laser melting additive manufacturing of aluminum alloy powder ». *Materials & Design,* vol. 63, p. 856-867.

Liaw, P. 1988. « Overview of Crack Closure at Near-Threshold Fatigue Crack Growth Levels ». In *Overview of Crack Closure at Near-Threshold Fatigue Crack Growth Levels*.

Liu, C. M., H. M. Wang, X. J. Tian, H. B. Tang et D. Liu. 2013. « Microstructure and tensile properties of laser melting deposited Ti–5Al–5Mo–5V–1Cr–1Fe near β titanium alloy ». *Materials Science and Engineering: A,* vol. 586, p. 323-329.

Liu, Qian Chu, Joe Elambasseril, Shou Jin Sun, Martin Leary, Milan Brandt et Peter Khan Sharp. 2014. « The Effect of Manufacturing Defects on the Fatigue Behaviour of Ti-6Al-4V Specimens Fabricated Using Selective Laser Melting ». *Advanced Materials Research,* vol. 891-892, p. 1519-1524.

Luo, YW, Bin Zhang, CP Li, GF Chen et Guang-Ping Zhang. 2019. « Detecting void-induced scatter of fatigue life of selective laser melting-fabricated inconel 718 using miniature specimens ». *Materials Research Express*.

Lynch, Stan. 2017. « Some fractographic contributions to understanding fatigue crack growth ». *International Journal of Fatigue,* vol. 104, p. 12-26.

Ma, Xian-feng, Zheng Duan, Hui-ji Shi, Ryosuke Murai et Eiichi Yanagisawa. 2010. « Fatigue and fracture behavior of nickel-based superalloy Inconel 718 up to the very high cycle regime ». *Journal of Zhejiang University-SCIENCE A,* vol. 11, nº 10, p. 727-737.

Maierhofer, J., H. P. Gänser et R. Pippan. 2015. « Modified Kitagawa–Takahashi diagram accounting for finite notch depths ». *International Journal of Fatigue,* vol. 70, p. 503-509.

Maierhofer, J., R. Pippan et H. P. Gänser. 2014. « Modified NASGRO equation for physically short cracks ». *International Journal of Fatigue,* vol. 59, nº Supplement C, p. 200-207.

Makhlouf, Kamel, et J. W. Jones. 1993. « Effects of temperature and frequency on fatigue crack growth in 18% Cr ferritic stainless steel ». *International Journal of Fatigue,* vol. 15, nº 3, p. 163-171.

Marchese, Giulio, Massimo Lorusso, Simone Parizia, Emilio Bassini, Ji-Won Lee, Flaviana Calignano, Diego Manfredi, Mathieu Terner, Hyun-Uk Hong et Daniele Ugues. 2018a. « Influence of heat treatments on microstructure evolution and mechanical properties of Inconel 625 processed by laser powder bed fusion ». *Materials Science and Engineering: A,* vol. 729, p. 64-75.

Marchese, Giulio, Massimo Lorusso, Simone Parizia, Emilio Bassini, Ji-Won Lee, Flaviana Calignano, Diego Manfredi, Mathieu Terner, Hyun-Uk Hong, Daniele Ugues, Mariangela Lombardi et Sara Biamino. 2018b. « Influence of heat treatments on microstructure evolution and mechanical properties of Inconel 625 processed by laser powder bed fusion ». *Materials Science and Engineering: A,* vol. 729, p. 64-75.

Masuo, Hiroshige, Yuzo Tanaka, Shotaro Morokoshi, Hajime Yagura, Tetsuya Uchida, Yasuhiro Yamamoto et Yukitaka Murakami. 2017. « Effects of Defects, Surface Roughness and HIP on Fatigue Strength of Ti-6Al-4V manufactured by Additive Manufacturing ». *Procedia Structural Integrity,* vol. 7, p. 19-26.

Masuo, Hiroshige, Yuzo Tanaka, Shotaro Morokoshi, Hajime Yagura, Tetsuya Uchida, Yasuhiro Yamamoto et Yukitaka Murakami. 2018. « Influence of defects, surface roughness and HIP on the fatigue strength of Ti-6Al-4V manufactured by additive manufacturing ». *International Journal of Fatigue,* vol. 117, p. 163-179.

Mayer, H. 1999. « Fatigue crack growth and threshold measurements at very high frequencies ». *International Materials Reviews,* vol. 44, nº 1, p. 1-34.

Mazur, Maciej, Martin Leary, Shoujin Sun, Martin Vcelka, Darpan Shidid et Milan Brandt. 2015. « Deformation and failure behaviour of Ti-6Al-4V lattice structures manufactured by selective laser melting (SLM) ». *The International Journal of Advanced Manufacturing Technology*.

McCarver, J. F., et R. O. Ritchie. 1982. « Fatigue crack propagation thresholds for long and short cracks in René 95 Nickel-base superalloy ». *Materials Science and Engineering,* vol. 55, nº 1, p. 63-67.

McLouth, Tait D, Glenn E Bean, David B Witkin, Scott D Sitzman, Paul M Adams, Dhruv N Patel, Woonsup Park, Jenn-Ming Yang et Rafael J Zaldivar. 2018. « The effect of laser focus shift on microstructural variation of Inconel 718 produced by selective laser melting ». *Materials & Design,* vol. 149, p. 205-213.

Meggiolaro, M. A., A. C. O. Miranda, J. T. P. Castro et L. F. Martha. 2005. « Stress intensity factor equations for branched crack growth ». *Engineering Fracture Mechanics,* vol. 72, nº 17, p. 2647-2671.

Meneghetti, G., D. Rigon et C. Gennari. 2019. « An analysis of defects influence on axial fatigue strength of maraging steel specimens produced by additive manufacturing ». *International Journal of Fatigue,* vol. 118, p. 54-64.

Mercelis, Peter, et Jean-Pierre Kruth. 2006. « Residual stresses in selective laser sintering and selective laser melting ». *Rapid Prototyping Journal,* vol. 12, nº 5, p. 254-265.

Messner, Mark C. 2016. « Optimal lattice-structured materials ». *Journal of the Mechanics and Physics of Solids,* vol. 96, p. 162-183.

Miao, Jiashi, Tresa M. Pollock et J. Wayne Jones. 2012. « Microstructural extremes and the transition from fatigue crack initiation to small crack growth in a polycrystalline nickel-base superalloy ». *Acta Materialia,* vol. 60, nº 6, p. 2840-2854.

Miller, Keith J. 1997. « The three thresholds for fatigue crack propagation ». In *Fatigue and Fracture Mechanics: 27th volume*. ASTM International.

Miller, KJ. 1982. « The short crack problem ». *Fatigue & Fracture of Engineering Materials & Structures,* vol. 5, nº 3, p. 223-232.

Montgomery, Colt, Jack Beuth, Luke Sheridan et Nathan Klingbeil. 2015. « Process mapping of Inconel 625 in laser powder bed additive manufacturing ». In *Solid Freeform Fabrication Symposium*. p. 1195-1204.

Morrison, D. J., et J. C. Moosbrugger. 1997. « Effects of grain size on cyclic plasticity and fatigue crack initiation in nickel ». *International Journal of Fatigue,* vol. 19, nº 93, p. 51-59.

Mukherjee, T., et T. DebRoy. 2018. « Mitigation of lack of fusion defects in powder bed fusion additive manufacturing ». *Journal of Manufacturing Processes,* vol. 36, p. 442-449.

Mukherjee, T., W. Zhang et T. DebRoy. 2017. « An improved prediction of residual stresses and distortion in additive manufacturing ». *Computational Materials Science,* vol. 126, p. 360-372.

Mumtaz, Kamran, et Neil Hopkinson. 2009. « Top surface and side roughness of Inconel 625 parts processed using selective laser melting ». *Rapid Prototyping Journal,* vol. 15, nº 2, p. 96-103.

Murakami, Yukitaka. 2019. *Metal fatigue: effects of small defects and nonmetallic inclusions*. Academic Press.

Murakami, Yukitaka, et M Endo. 1994. « Effects of defects, inclusions and inhomogeneities on fatigue strength ». *International journal of fatigue,* vol. 16, nº 3, p. 163-182.

Murr, Lawrence E., Sara M. Gaytan, Diana A. Ramirez, Edwin Martinez, Jennifer Hernandez, Krista N. Amato, Patrick W. Shindo, Francisco R. Medina et Ryan B. Wicker. 2012. « Metal Fabrication by Additive Manufacturing Using Laser and Electron Beam Melting Technologies ». *Journal of Materials Science & Technology,* vol. 28, nº 1, p. 1-14.

Newman, J. C. 1984. « A crack opening stress equation for fatigue crack growth ». *International Journal of Fracture,* vol. 24, nº 4, p. R131-R135.

Nicoletto, Gianni. 2017. « Anisotropic high cycle fatigue behavior of Ti–6Al–4V obtained by powder bed laser fusion ». *International Journal of Fatigue,* vol. 94, p. 255-262.

Nicoletto, Gianni, Radomila Konečná et Stanislava Fintova. 2012. « Characterization of microshrinkage casting defects of Al–Si alloys by X-ray computed tomography and metallography ». *International Journal of Fatigue,* vol. 41, p. 39-46.

Paris, Paul C. 1961. « A rational analytic theory of fatigue ». *The trend in engineering,* vol. 13, p. 9.

Parry, L., I. A. Ashcroft et R. D. Wildman. 2016. « Understanding the effect of laser scan strategy on residual stress in selective laser melting through thermo-mechanical simulation ». *Additive Manufacturing,* vol. 12, p. 1-15.

Patriarca, L., M. Filippini et S. Beretta. 2018. « Short-crack thresholds and propagation in an AISI 4340 steel under the effect of SP residual stresses ». *Fatigue & Fracture of Engineering Materials & Structures,* vol. 41, nº 6, p. 1275-1290.

Pavlou, DG, NV Vlachakis, MG Pavlou et VN Vlachakis. 2004. « Estimation of fatigue crack growth retardation due to crack branching ». *Computational materials science,* vol. 29, nº 4, p. 446-452.

Pereira, Fábio Gustavo Lima, Jorge Magner Lourenço, Rubens Maribondo do Nascimento et Nicolau Apoena Castro. 2018. « Fracture Behavior and Fatigue Performance of Inconel 625 ». *Materials Research,* vol. 21, nº 4.

Pereira, Marcos Venicius Soares, Fathi Aref Ibrahim Darwish, Arnaldo Freitas Camarão et Sérgio Henrique Motta. 2007. « On the prediction of fatigue crack retardation using Wheeler and Willenborg models ». *Materials Research,* vol. 10, nº 2, p. 101-107.

Pessard, Etienne, Daniel Bellett, Franck Morel et Imade Koutiri. 2013. « A mechanistic approach to the Kitagawa–Takahashi diagram using a multiaxial probabilistic framework ». *Engineering Fracture Mechanics,* vol. 109, p. 89-104.

Peters, J. O., B. L. Boyce, X. Chen, J. M. McNaney, J. W. Hutchinson et R. O. Ritchie. 2002. « On the application of the Kitagawa–Takahashi diagram to foreign-object damage and high-cycle fatigue ». *Engineering Fracture Mechanics,* vol. 69, nº 13, p. 1425-1446.

Pippan, Reinhard. 1991. « Threshold and effective threshold of fatigue crack propagation in ARMCO iron I: The influence of grain size and cold working ». *Materials Science and Engineering: A,* vol. 138, nº 1, p. 1-13.

Poulin, J-R, V Brailovski et P Terriault. 2018. « Long fatigue crack propagation behavior of Inconel 625 processed by laser powder bed fusion: Influence of build orientation and post-processing conditions ». *International Journal of Fatigue,* vol. 116, p. 634-647.

Poulin, J. R., A. Kreitcberg, P. Terriault et V. Brailovski. 2019. « Long fatigue crack propagation behavior of laser powder bed-fused inconel 625 with intentionally-seeded porosity ». *International Journal of Fatigue,* vol. 127, p. 144-156.

Prashanth, K. G., S. Scudino, H. J. Klauss, K. B. Surreddi, L. Löber, Z. Wang, A. K. Chaubey, U. Kühn et J. Eckert. 2014. « Microstructure and mechanical properties of Al–12Si

produced by selective laser melting: Effect of heat treatment ». *Materials Science and Engineering: A,* vol. 590, nº Supplement C, p. 153-160.

Prithivirajan, Veerappan, et Michael D. Sangid. 2018. « The role of defects and critical pore size analysis in the fatigue response of additively manufactured IN718 via crystal plasticity ». *Materials & Design,* vol. 150, p. 139-153.

Products, Special Metals Corporation. « INCONEL® alloy 625 ». < www.specialmetals.com/products >.

Qiu, Chunlei, Chinnapat Panwisawas, Mark Ward, Hector C. Basoalto, Jeffery W. Brooks et Moataz M. Attallah. 2015. « On the role of melt flow into the surface structure and porosity development during selective laser melting ». *Acta Materialia,* vol. 96, p. 72-79.

Rafi, H. K., N. V. Karthik, Haijun Gong, Thomas L. Starr et Brent E. Stucker. 2013. « Microstructures and Mechanical Properties of Ti6Al4V Parts Fabricated by Selective Laser Melting and Electron Beam Melting ». *Journal of Materials Engineering and Performance,* vol. 22, nº 12, p. 3872-3883.

Rafi, H. Khalid, Thomas L. Starr et Brent E. Stucker. 2013. « A comparison of the tensile, fatigue, and fracture behavior of Ti–6Al–4V and 15-5 PH stainless steel parts made by selective laser melting ». *The International Journal of Advanced Manufacturing Technology,* vol. 69, nº 5-8, p. 1299-1309.

Rahman, M., W. K. H. Seah et T. T. Teo. 1997. « The machinability of inconel 718 ». *Journal of Materials Processing Technology,* vol. 63, nº 1, p. 199-204.

Rehme, Olaf, Friedrich G. Bachmann, Claus Emmelmann, Willem Hoving, Yongfeng Lu et Kunihiko Washio. 2006. « Rapid manufacturing of lattice structures with selective laser melting ». vol. 6107, p. 61070K.

Reschetnik, W., J. P. Brüggemann, M. E. Aydinöz, O. Grydin, K. P. Hoyer, G. Kullmer et H. A. Richard. 2016. « Fatigue crack growth behavior and mechanical properties of additively processed EN AW-7075 aluminium alloy ». *Procedia Structural Integrity,* vol. 2, p. 3040-3048.

Riemer, A., S. Leuders, M. Thöne, H. A. Richard, T. Tröster et T. Niendorf. 2014. « On the fatigue crack growth behavior in 316L stainless steel manufactured by selective laser melting ». *Engineering Fracture Mechanics,* vol. 120, p. 15-25.

Ritchie, R. O., F. A. McClintock, H. Nayeb-Hashemi et M. A. Ritter. 1982. « Mode III fatigue crack propagation in low alloy steel ». *Metallurgical Transactions A,* vol. 13, nº 1, p. 101-110.

Ritchie, Robert O. 1999. « Mechanisms of fatigue-crack propagation in ductile and brittle solids ». *International Journal of Fracture,* vol. 100, nº 1, p. 55-83.

Romano, S., A. Brandão, J. Gumpinger, M. Gschweitl et S. Beretta. 2017. « Qualification of AM parts: Extreme value statistics applied to tomographic measurements ». *Materials & Design,* vol. 131, p. 32-48.

Romano, S., A. Brückner-Foit, A. Brandão, J. Gumpinger, T. Ghidini et S. Beretta. 2018. « Fatigue properties of AlSi10Mg obtained by additive manufacturing: Defect-based modelling and prediction of fatigue strength ». *Engineering Fracture Mechanics,* vol. 187, p. 165-189.

Sallica-Leva, E., A. L. Jardini et J. B. Fogagnolo. 2013. « Microstructure and mechanical behavior of porous Ti-6Al-4V parts obtained by selective laser melting ». *J Mech Behav Biomed Mater,* vol. 26, p. 98-108.

Schönbauer, B. M., K. Yanase et M. Endo. 2017. « Influences of small defects on torsional fatigue limit of 17-4PH stainless steel ». *International Journal of Fatigue,* vol. 100, p. 540-548.

Seede, Raiyan, Ahmad Mostafa, Vladimir Brailovski, Mohammad Jahazi et Mamoun Medraj. 2018. « Microstructural and Microhardness Evolution from Homogenization and Hot Isostatic Pressing on Selective Laser Melted Inconel 718: Structure, Texture, and Phases ». *Journal of Manufacturing and Materials Processing,* vol. 2, nº 2, p. 30.

Seifi, Mohsen, Michael Gorelik, Jess Waller, Nik Hrabe, Nima Shamsaei, Steve Daniewicz et John J. Lewandowski. 2017. « Progress Towards Metal Additive Manufacturing Standardization to Support Qualification and Certification ». *JOM,* vol. 69, nº 3, p. 439-455.

Seifi, Mohsen, Ayman Salem, Jack Beuth, Ola Harrysson et John J. Lewandowski. 2016. « Overview of Materials Qualification Needs for Metal Additive Manufacturing ». *JOM,* vol. 68, nº 3, p. 747-764.

Sergueeva, AV, J Zhou, BE Meacham et DJ Branagan. 2009. « Gage length and sample size effect on measured properties during tensile testing ». *Materials Science and Engineering: A,* vol. 526, nº 1-2, p. 79-83.

Shao, Shuai, Mohammad J. Mahtabi, Nima Shamsaei et Scott M. Thompson. 2017. « Solubility of argon in laser additive manufactured α-titanium under hot isostatic pressing condition ». *Computational Materials Science,* vol. 131, p. 209-219.

Sheridan, Luke, Onome E. Scott-Emuakpor, Tommy George et Joy E. Gockel. 2018. « Relating porosity to fatigue failure in additively manufactured alloy 718 ». *Materials Science and Engineering: A,* vol. 727, p. 170-176.

Shiomi, M., K. Osakada, K. Nakamura, T. Yamashita et F. Abe. 2004. « Residual Stress within Metallic Model Made by Selective Laser Melting Process ». *CIRP Annals - Manufacturing Technology,* vol. 53, nº 1, p. 195-198.

Siddique, Shafaqat, Muhammad Imran, Miriam Rauer, Michael Kaloudis, Eric Wycisk, Claus Emmelmann et Frank Walther. 2015. « Computed tomography for characterization of fatigue performance of selective laser melted parts ». *Materials & Design,* vol. 83, p. 661-669.

Siddique, Shafaqat, Muhammad Imran et Frank Walther. 2017. « Very high cycle fatigue and fatigue crack propagation behavior of selective laser melted AlSi12 alloy ». *International Journal of Fatigue,* vol. 94, p. 246-254.

Simonelli, M., Y. Y. Tse et C. Tuck. 2014. « Effect of the build orientation on the mechanical properties and fracture modes of SLM Ti–6Al–4V ». *Materials Science and Engineering: A,* vol. 616, p. 1-11.

Simonelli, Marco, Chris Tuck, Nesma T Aboulkhair, Ian Maskery, Ian Ashcroft, Ricky D Wildman et Richard Hague. 2015. « A study on the laser spatter and the oxidation reactions during selective laser melting of 316L stainless steel, Al-Si10-Mg, and Ti-6Al-4V ». *Metallurgical and Materials Transactions A,* vol. 46, nº 9, p. 3842-3851.

Skorupa, M. 1998. « Load interaction effects during fatigue crack growth under variable amplitude loading—a literature review. Part I: empirical trends ». *Fatigue & Fracture of Engineering Materials & Structures,* vol. 21, nº 8, p. 987-1006.

Spagnoli, Andrea. 2004. « Fractality in the threshold condition of fatigue crack growth: an interpretation of the Kitagawa diagram ». *Chaos, Solitons & Fractals,* vol. 22, nº 3, p. 589-598.

Standard Practice for Conducting Force Controlled Constant Amplitude Axial Fatigue Tests of Metallic Materials. 2015. ASTM International. Consulté le 09 Jan 2017.

Standard Practice for Statistical Analysis of Linear or Linearized Stress-Life (S-N) and Strain-Life (ε-N) Fatigue Data. 2015. ASTM International. Consulté le 09 Jan 2019.

Standard Test Method for Linear-Elastic Plane-Strain Fracture Toughness of Metallic Materials. 2012. ASTM International. Consulté le 09 Jan 2017.

Standard Test Method for Measurement of Fatigue Crack Growth Rates. 2015. ASTM International. Consulté le 09 Jan 2017.

Standard Test Methods for Tension Testing of Metallic Materials. 2016. ASTM International. Consulté le 09 Jan 2017.

Stephens, Ralph I, Ali Fatemi, Robert R Stephens et Henry O Fuchs. 2000. *Metal fatigue in engineering*. John Wiley & Sons.

Stephens, Ralph I, Joshua J Horn, Dente D Poland et Eric A Sager. 1998. « Influence of density and porosity size and shape on fatigue and fracture toughness of high strength FL4405 P/M steel ». In *Effects of product quality and design criteria on structural integrity*. ASTM International.

Sterling, Amanda, Nima Shamsaei, Brian Torries et Scott M. Thompson. 2015. « Fatigue Behaviour of Additively Manufactured Ti-6Al-4V ». *Procedia Engineering,* vol. 133, p. 576-589.

Strano, Giovanni, Liang Hao, Richard M. Everson et Kenneth E. Evans. 2013. « Surface roughness analysis, modelling and prediction in selective laser melting ». *Journal of Materials Processing Technology,* vol. 213, nº 4, p. 589-597.

Suave, Lorena Mataveli, Jonathan Cormier, Denis Bertheau, Patrick Villechaise, Aurélie Soula, Zéline Hervier et Florence Hamon. 2016. « High temperature low cycle fatigue properties of alloy 625 ». *Materials Science and Engineering: A,* vol. 650, p. 161-170.

Suresh, S. 1998. *Fatigue of Materials*. Cambridge University Press.

Tammas-Williams, S, PJ Withers, I Todd et PB Prangnell. 2017. « The influence of porosity on fatigue crack initiation in additively manufactured titanium components ». *Scientific reports,* vol. 7, nº 1, p. 7308.

Tammas-Williams, S., P. J. Withers, I. Todd et P. B. Prangnell. 2016a. « Porosity regrowth during heat treatment of hot isostatically pressed additively manufactured titanium components ». *Scripta Materialia,* vol. 122, p. 72-76.

Tammas-Williams, Samuel, Philip J. Withers, Iain Todd et Philip B. Prangnell. 2016b. « The Effectiveness of Hot Isostatic Pressing for Closing Porosity in Titanium Parts

Manufactured by Selective Electron Beam Melting ». *Metallurgical and Materials Transactions A,* vol. 47, nº 5, p. 1939-1946.

Tang, Ming, et P. Chris Pistorius. 2017. « Oxides, porosity and fatigue performance of AlSi10Mg parts produced by selective laser melting ». *International Journal of Fatigue,* vol. 94, p. 192-201.

Tang, Ming, P. Chris Pistorius et Jack L. Beuth. 2017. « Prediction of lack-of-fusion porosity for powder bed fusion ». *Additive Manufacturing,* vol. 14, p. 39-48.

Tenkamp, Jochen, Alexander Koch, Stephan Knorre, Ulrich Krupp, Wilhelm Michels et Frank Walther. 2018. « Defect-correlated fatigue assessment of A356-T6 aluminum cast alloy using computed tomography based Kitagawa-Takahashi diagrams ». *International Journal of Fatigue,* vol. 108, p. 25-34.

Theriault, A., L. Xue et J. R. Dryden. 2009. « Fatigue behavior of laser consolidated IN-625 at room and elevated temperatures ». *Materials Science and Engineering: A,* vol. 516, nº 1, p. 217-225.

Thijs, Lore, Frederik Verhaeghe, Tom Craeghs, Jan Van Humbeeck et Jean-Pierre Kruth. 2010. « A study of the microstructural evolution during selective laser melting of Ti–6Al–4V ». *Acta Materialia,* vol. 58, nº 9, p. 3303-3312.

Thomas, Douglas S, et Stanley W Gilbert. 2014. « Costs and cost effectiveness of additive manufacturing ». *NIST Special Publication,* vol. 1176, p. 12.

Tillmann, W., C. Schaak, J. Nellesen, M. Schaper, M. E. Aydinöz et K. P. Hoyer. 2017. « Hot isostatic pressing of IN718 components manufactured by selective laser melting ». *Additive Manufacturing,* vol. 13, p. 93-102.

Torres, M. A. S., et H. J. C. Voorwald. 2002. « An evaluation of shot peening, residual stress and stress relaxation on the fatigue life of AISI 4340 steel ». *International Journal of Fatigue,* vol. 24, nº 8, p. 877-886.

Torries, Brian, Aidin Imandoust, Stefano Beretta, Shuai Shao et Nima Shamsaei. 2018. « Overview on Microstructure- and Defect-Sensitive Fatigue Modeling of Additively Manufactured Materials ». *Jom,* vol. 70, nº 9, p. 1853-1862.

Tradowsky, U., J. White, R. M. Ward, N. Read, W. Reimers et M. M. Attallah. 2016. « Selective laser melting of AlSi10Mg: Influence of post-processing on the microstructural and tensile properties development ». *Materials & Design,* vol. 105, nº Supplement C, p. 212-222.

Trester, P. W., J. L. Kaae et R. Gallix. 1985. « Fatigue strength of inconel 625 plate and weldments used in the DIII-D configuration vacuum vessel ». *Journal of Nuclear Materials,* vol. 133-134, p. 347-350.

Trosch, Tanja, Johannes Strößner, Rainer Völkl et Uwe Glatzel. 2016. « Microstructure and mechanical properties of selective laser melted Inconel 718 compared to forging and casting ». *Materials Letters,* vol. 164, nº Supplement C, p. 428-431.

Urlea, V., et V. Brailovski. 2017. « Electropolishing and electropolishing-related allowances for IN625 alloy components fabricated by laser powder-bed fusion ». *The International Journal of Advanced Manufacturing Technology,* vol. 92, nº 9, p. 4487-4499.

Van Hooreweder, Brecht, David Moens, Rene Boonen, Jean-Pierre Kruth et Paul Sas. 2012. « Analysis of Fracture Toughness and Crack Propagation of Ti6Al4V Produced by Selective Laser Melting ». *Advanced Engineering Materials,* vol. 14, nº 1-2, p. 92-97.

Vilaro, T., C. Colin et J. D. Bartout. 2011. « As-Fabricated and Heat-Treated Microstructures of the Ti-6Al-4V Alloy Processed by Selective Laser Melting ». *Metallurgical and Materials Transactions A,* vol. 42, nº 10, p. 3190-3199.

Vrancken, Bey, Lore Thijs, Jean-Pierre Kruth et Jan Van Humbeeck. 2012. « Heat treatment of Ti6Al4V produced by Selective Laser Melting: Microstructure and mechanical properties ». *Journal of Alloys and Compounds,* vol. 541, p. 177-185.

Wan, Hualiang, Qizhi Wang, Chenxue Jia et Zheng Zhang. 2016. « Multi-scale damage mechanics method for fatigue life prediction of additive manufacture structures of Ti-6Al-4V ». *Materials Science and Engineering: A,* vol. 669, p. 269-278.

Wang, K, F Wang, W Cui, T Hayat et B Ahmad. 2014. « Prediction of short fatigue crack growth of Ti-6Al-4V ». *Fatigue & Fracture of Engineering Materials & Structures,* vol. 37, nº 10, p. 1075-1086.

Wang, T., Y. Y. Zhu, S. Q. Zhang, H. B. Tang et H. M. Wang. 2015. « Grain morphology evolution behavior of titanium alloy components during laser melting deposition additive manufacturing ». *Journal of Alloys and Compounds,* vol. 632, p. 505-513.

Wang, Zemin, Kai Guan, Ming Gao, Xiangyou Li, Xiaofeng Chen et Xiaoyan Zeng. 2012. « The microstructure and mechanical properties of deposited-IN718 by selective laser melting ». *Journal of Alloys and Compounds,* vol. 513, p. 518-523.

Westergaard, Harold M. 1939. « Bearing pressures and cracks ». *Trans AIME, J. Appl. Mech.,* vol. 6, p. 49-53.

Wilkinson, Angus J. 2001. « Modelling the effects of texture on the statistics of stage I fatigue crack growth ». *Philosophical Magazine A,* vol. 81, nº 4, p. 841-855.

Wilson, David, et Fionn PE Dunne. 2019. « A mechanistic modelling methodology for microstructure-sensitive fatigue crack growth ». *Journal of the Mechanics and Physics of Solids,* vol. 124, p. 827-848.

Witkin, David B., Dhruv N. Patel, Henry Helvajian, Lee Steffeney et Agustin Diaz. 2019. « Surface Treatment of Powder-Bed Fusion Additive Manufactured Metals for Improved Fatigue Life ». *Journal of Materials Engineering and Performance,* vol. 28, nº 2, p. 681-692.

Wohlers, Terry. 2016. *Wohlers report 2016*. Wohlers Associates, Inc.

Wohlers, Terry, et Tim Caffrey. 2013. « Additive manufacturing: going mainstream ». *Manufacturing Eng,* vol. 151, nº 6, p. 67-73.

Wohlers, Terry, Tim Caffrey, Robert Ian Campbell, Olaf Diegel et Joseph Kowen. 2018. *Wohlers Report 2018: 3D Printing and Additive Manufacturing State of the Industry; Annual Worldwide Progress Report*. Wohlers Associates.

Wong, Kaufui V., et Aldo Hernandez. 2012. « A Review of Additive Manufacturing ». *ISRN Mechanical Engineering,* vol. 2012, p. 1-10.

Wu, Ming-Wei, et Pang-Hsin Lai. 2016. « The positive effect of hot isostatic pressing on improving the anisotropies of bending and impact properties in selective laser melted Ti-6Al-4V alloy ». *Materials Science and Engineering: A,* vol. 658, p. 429-438.

Wu, Ming-Wei, Pang-Hsin Lai et Jhewn-Kuang Chen. 2016. « Anisotropy in the impact toughness of selective laser melted Ti–6Al–4V alloy ». *Materials Science and Engineering: A,* vol. 650, p. 295-299.

Wycisk, Eric, Claus Emmelmann, Shafaqat Siddique et Frank Walther. 2013. « High Cycle Fatigue (HCF) Performance of Ti-6Al-4V Alloy Processed by Selective Laser Melting ». *Advanced Materials Research,* vol. 816-817, p. 134-139.

Wycisk, Eric, Andreas Solbach, Shafaqat Siddique, Dirk Herzog, Frank Walther et Claus Emmelmann. 2014. « Effects of Defects in Laser Additive Manufactured Ti-6Al-4V on Fatigue Properties ». *Physics Procedia,* vol. 56, p. 371-378.

Yadollahi, Aref, et Nima Shamsaei. 2017. « Additive manufacturing of fatigue resistant materials: Challenges and opportunities ». *International Journal of Fatigue,* vol. 98, p. 14-31.

Yadollahi, Aref, Nima Shamsaei, Scott M. Thompson, Alaa Elwany et Linkan Bian. 2017. « Effects of building orientation and heat treatment on fatigue behavior of selective laser melted 17-4 PH stainless steel ». *International Journal of Fatigue,* vol. 94, p. 218-235.

Yadroitsev, I, M Pavlov, Ph Bertrand et I Smurov. 2009. « Mechanical properties of samples fabricated by selective laser melting ». *14èmes Assises Européennes du Prototypages & Fabrication Rapide, Paris*.

Yadroitsev, I., P. Krakhmalev, I. Yadroitsava, S. Johansson et I. Smurov. 2013. « Energy input effect on morphology and microstructure of selective laser melting single track from metallic powder ». *Journal of Materials Processing Technology,* vol. 213, nº 4, p. 606-613.

Yamashita, Yoichi, Takao Murakami, Rei Mihara, Masami Okada et Yukitaka Murakami. 2018. « Defect analysis and fatigue design basis for Ni-based superalloy 718 manufactured by selective laser melting ». *International Journal of Fatigue,* vol. 117, p. 485-495.

Yan, Chunze, Liang Hao, Ahmed Hussein, Philippe Young, Juntong Huang et Wei Zhu. 2015. « Microstructure and mechanical properties of aluminium alloy cellular lattice structures manufactured by direct metal laser sintering ». *Materials Science and Engineering: A,* vol. 628, p. 238-246.

Yuen, BKC, et F Taheri. 2006. « Proposed modifications to the Wheeler retardation model for multiple overloading fatigue life prediction ». *International journal of fatigue,* vol. 28, nº 12, p. 1803-1819.

Zaeh, Michael F., et Gregor Branner. 2010. « Investigations on residual stresses and deformations in selective laser melting ». *Production Engineering,* vol. 4, nº 1, p. 35-45.

Zegard, Tomás, et Glaucio H Paulino. 2016. « Bridging topology optimization and additive manufacturing ». *Structural and Multidisciplinary Optimization,* vol. 53, nº 1, p. 175-192.

Zerbst, U., et C. Klinger. 2019. « Material defects as cause for the fatigue failure of metallic components ». *International Journal of Fatigue*.

Zerbst, Uwe, Michael Vormwald, Reinhard Pippan, Hans-Peter Gänser, Christine Sarrazin-Baudoux et Mauro Madia. 2016. « About the fatigue crack propagation threshold of metals as a design criterion – A review ». *Engineering Fracture Mechanics,* vol. 153, p. 190-243.

Zhai, Yuwei, Haize Galarraga et Diana A. Lados. 2016. « Microstructure, static properties, and fatigue crack growth mechanisms in Ti-6Al-4V fabricated by additive manufacturing: LENS and EBM ». *Engineering Failure Analysis,* vol. 69, p. 3-14.

Ziółkowski, G., E. Chlebus, P. Szymczyk et J. Kurzac. 2014. « Application of X-ray CT method for discontinuity and porosity detection in 316L stainless steel parts produced with SLM technology ». *Archives of Civil and Mechanical Engineering,* vol. 14, nº 4, p. 608-614.

Zok, Frank W., Ryan M. Latture et Matthew R. Begley. 2016. « Periodic truss structures ». *Journal of the Mechanics and Physics of Solids,* vol. 96, p. 184-203.